PACIFIC EARTHQUAKE ENGINEERING
RESEARCH CENTER

Partially Non-Ergodic Ground-Motion Model for Subduction Regions using the NGA-Subduction Database

Nicolas Kuehn

Yousef Bozorgnia

Department of Civil and Environmental Engineering
University of California, Los Angeles

Kenneth W. Campbell

Core Logic, Inc.

Nicholas Gregor

Nicholas Gregor Consulting

PEER Report 2020/04
Pacific Earthquake Engineering Research Center
Headquarters, University of California at Berkeley

September 2020

PEER 2020/04
August 2020

Partially Non-Ergodic Ground-Motion Model for Subduction Regions using the NGA-Subduction Database

Nicolas Kuehn

Yousef Bozorgnia

Department of Civil and Environmental Engineering
University of California, Los Angeles

Kenneth W. Campbell

CoreLogic, Inc.

Nicholas Gregor

Nicholas Gregor Consulting

PEER Report No. 2020/04

Pacific Earthquake Engineering Research Center
Headquarters, University of California, Berkeley
September 2020

ABSTRACT

This report presents a summary of the development, evaluation, and comparison of a new subduction ground-motion model (GMM), now known as Kuehn-Bozorgnia-Campbell-Gregor (KBCG20) model. This GMM was developed as part of the Next Generation Attenuation for Subduction Regions (NGA-Sub) program using a comprehensive compilation of subduction interface and intraslab ground-motion recordings and metadata compiled in the NGA-Sub database. The KBCG20 model includes ground-motion scaling terms for magnitude, distance, site amplification, and basin amplification. Some of these terms are adjustable to accommodate differences between interface and intraslab earthquakes, and differences among seven subduction-zone regions for which data were compiled as part of the NGA-Sub program. These regions include Alaska (AK), Central America and Mexico (CAM), Cascadia (CASC), Japan (JP), New Zealand (NZ), South America (SA), and Taiwan (TW). Some of these regions are further divided into sub-regions to account for differences in anelastic attenuation between the subduction forearc and backarc, and differences in breakpoint magnitude (the magnitude at which magnitude scaling rate decreases) between segments of a larger subduction zone.

This study uses an innovative Bayesian regression approach to incorporate informative prior distributions of model coefficients and formally estimate the uncertainty in their posterior estimates. The posterior distributions of coefficients together with their co-variance matrix can be used to estimate epistemic uncertainty in the median ground-motion predictions for a given earthquake scenario. Partial non-ergodicity was achieved by accounting for the regional differences in overall amplitude (constants) of prediction, anelastic attenuation, linear site amplification, and basin amplification. Because of the expanded database and innovative regression approach that includes median, aleatory variability, and epistemic uncertainty models, this new GMM represents a significant improvement in the understanding and prediction of subduction ground motion. Furthermore, the Bayesian approach used to develop the model will facilitate update of this innovative GMM as new data become available.

ACKNOWLEDGMENTS

This study was supported by FM Global, the U.S. Geological Survey (USGS), and the California Department of Transportation (Caltrans). The authors would like to acknowledge the generous support of the Pacific Earthquake Engineering Research Center (PEER).

The opinions, findings, conclusions or recommendations expressed in this publication are those of the author(s) and do not necessarily reflect the views of the study sponsor(s), PEER, or the Regents of the University of California.

Following the tradition of previous NGA research projects, the ground-motion modeling teams as well as database developers have had continuous technical interactions that resulted in a higher quality of the final products than each researcher could achieve individually. We especially would like to thank Drs. Tadahiro Kishida and Silvia Mazzoni for their dedication on the development of the NGA-Sub database. Special thanks should also be given to over thirty-two junior and senior researchers who worked on various pieces of NGA-Sub research program. Their contributions, dedicatio, and teamwork are greatly appreciated.

We would like to thank Professor Pedro Arduino and his group at the University of Washington as well as Professor Filip Filippou of UC Berkeley for making the LaTeX style file for PEER reports available.

CONTENTS

LIST OF TABLES

LIST OF FIGURES

1 Introduction

1.1 OVERVIEW

The Next Generation Attenuation (NGA) research program for subduction earthquakes (NGA-Sub) is the latest component of the NGA research series. The NGA-Sub project is a large multidisciplinary and multi-researcher initiative to develop a comprehensive ground-motion database and multiple ground-motion models (GMMs) for subduction earthquakes. In the NGA-Sub project, a database of ground motions recorded in worldwide subduction events was developed (Stewart et al., 2020). The database includes the processed recordings and supporting source, path, and site metadata from Alaska (AK), Central America and Mexico (CAM), Cascadia (CASC), Japan (JP), New Zealand (NZ), South America (SA), and Taiwan (TW). The NGA-Sub database includes 1880 events with moment magnitudes ranging from 4.0 to 9.1. Subduction events are classified as interface, intraslab, or outer-rise events. The NGA-Sub ground-motion database has 214,020 individual ground-motion components. This is by far the largest ground-motion database developed in any previous NGA project. Multiple GMMs have been developed by NGA-Sub developers using this empirical ground-motion database and supporting ground-motion simulations. This report discusses the GMM developed by the NGA-Sub team, referred to within as Kuehn-Bozorgnia-Campbell-Gregor (KBCG20).

In the KBCG20 model, special attention has been given to distinguish GMMs for seven different subduction regions, including Japan and the Pacific Northwest (Cascadia). A subset of the full database was selected for use in the analysis. The details of data selection and rejection are presented in Chapter 2. The methodology for computation of median, aleatory variability, and epistemic uncertainty models are discussed in Chapters 4, 5, and 6, respectively. The KBCG20 model evaluation, including the analysis of residuals and model predictions, is presented in Chapter 7, followed by a discussion of the applicability and limitations of the GMM in Chapter 8. Electronic Appendices include the Record Sequence Numbers (RSNs) of the selected recordings, model coefficients, and implementation guidelines.

The GMM is developed as a partially non-ergodic model (Stafford, 2014), which means that there are different values of coefficients—in this case: constant, anelastic attenuation, linear site scaling, and basin amplification—for different regions. This is explained in detail in Chapter 3 and Section 4.2. As indicated above, in general, there are seven different main regions (see Chapter 2) for which different coefficients were estimate different coefficients; see Kishida et al. (2018) and Bozorgnia et al. (2020).

In addition, some of the median regions were subdivided to account for differences in the age and geometry of the subduction zones within the regions; this has consequences for the break in the magnitude scaling rate, as explained in Sections 8.2.2 and 8.2.3. These subdivisions are referred to as subregions. These subregions are from the same main region have the same constant, anelastic attenuation, linear site scaling, and basin amplification, but a different magnitude break point.

Furthermore, the anelastic attenuation model accounts for differences in attenuation when crossing an volcanic arc. This requires an additional subdivision depending on where the source/site is relative to the volcanic arc. These subdivisions are called "subregions relative to the volcanic arc." (The traditional forearc/backarc nomenclature becomes too simplistic if there is more than one arc, as is the case for Japan.)

1.2 PREVIOUS STUDIES

Several empirical and simulation-based GMMs have been developed over the years for both interface and intraslab subduction earthquakes. The models based on ground-motion simulations are typically developed for a specific application to a localized region such as Cascadia, whereas the empirically based models are typically developed for global applications. The dataset of available strong ground-motion recordings has increased over time; thus, the later GMMs are mostly based on the recent recordings, whereas the previous GMMs are based on the more limited, older datasets. More recent models generally update and supersede the previous models.

The listing and discussion of previous subduction GMMs would be expansive and is outside of the scope of this report. Instead, the discussion and comparisons presented in this report are focused on the more recent GMMs. The reader is referred to the comprehensive compilation of GMMs maintained by John Douglas at the following website: http://www.gmpe.org.uk The selected set of GMMs used for comparison includes those used in the current USGS National Seismic Hazard Maps Project (Petersen et al., 2014) for application to subduction earthquakes originating in the Cascadia region. This section presents a short description of each of these GMMs.

Atkinson and Boore (2003, 2008) developed a globally based GMM using a database of worldwide subduction events available at the time. This model was defined for a suite of eight spectral periods from PGA to 3.0 sec. Site classification was defined in terms of the NEHRP site categories of B, C, D, and E site conditions (Building Seismic Safety Council, 2001). The dataset associated with this model was primarily from events in Japan, Mexico, and Central America. Both the 2001 Nisqually (**M**6.8) and 1999 Satsop (**M**5.9) Cascadia intraslab events were included in the dataset. This GMM is defined for both interface and intraslab events. Regional variations of the intraslab model were defined for Cascadia and Japan in addition to a global model.

Zhao et al. (2006) developed a GMM for both crustal events and subduction events based primarily on strong ground-motion data recorded in Japan. Additional non-Japanese events were included in the dataset but do not make up a significant number of the total database. This model is defined for a spectral period range from PGA to 5.0 sec. Site classification is based on five site classes from hard rock to soft soil. Zhao et al. (2006) provides an associated mapping of these five site classifications to NEHRP site classifications and approximate V_{S30} values. Zhao et al. (2016b,a) provided an update to this GMM based on the development of a more recent and expanded dataset. Similar to the Zhao et al. (2006) study, the bulk of the data in the 2006 study is from events recorded in Japan. The same site-classification scheme was used in the updated version of the model.

Atkinson and Macias (2009) developed a Cascadia-specific GMM for interface events based on ground-motion simulations. As part of this study, the simulation methodology was validated with the numerous recordings from the 2003 Tokachi-Oki (**M**8.1) earthquake, and regional adjustments were implemented to develop a simulation dataset for Cascadia events. Simulations were performed for magnitudes 7.5, 8.0, 8.5, and 9.0 given the expected engineering focus on these larger interface events in the Pacific Northwest region. All of the simulations were computed for a NEHRP B/C site category corresponding to a V_{S30} value of 760 m/sec. The model is defined for a suite of 25 spectral periods from PGA to 10 sec. The recommended standard deviation (sigma) for this model is adopted from the sigma model of Campbell and Bozorgnia (2008).

As part of a large SSHAC Level 3 study conducted by BC Hydro (2012) for the seismic hazard assessment of their facilities, Abrahamson et al. (2016) developed a new global subduction model that employed a contemporary database of subduction ground-motion recordings. This GMM has been cited variously as BC Hydro (2012), Abrahamson et al. (2012), and Abrahamson et al. (2016), causing confusion about the potential differences between these models. The two 2012 citations refer to the BC Hydro (2012) report. The only difference between them and the 2016 citation is that the latter refers to a journal paper. Otherwise, the GMM is identical between these publications. In the report herein, this model will be referred to as the BC Hydro model or by its formal citation Abrahamson et al. (2016).

The compiled database for the BC Hydro model included the data used in previous empirical models as well as more recently recorded events. In addition, a reassessment of the station and earthquake metadata was performed. The majority of the subduction data in the database came from Japan and Taiwan, with additional data from other global subduction regions. During the development of the model, two significant large magnitude interface events, the 2010 Maule Chile (**M**8.8) and 2011 Tohuku Japan (**M**9.1), occurred after the deadline for inclusion in the database. Although occurring too late to use in the direct development of the model, adjustments were developed to account for the observed residuals from these two events. The BC Hydro model was developed for a suite of 25 spectral periods from PGA to 10 sec. In addition, the site-response term in the model was based on a continuous model for V_{S30} following the site response terms developed for the NGA-West1 GMMs by Walling et al. (2008). This GMM is a global model that also includes a term for the separation of backarc and forearc site locations. For application as part of the BC Hydro (2012) SSHAC Level 3 study, a spectral period-dependent modification for intraslab events occurring in Cascadia was proposed. This was based on the residual analysis of the limited number of intraslab events recorded in the Cascadia region.

As part of the NGA-Sub program, a preliminary GMM per (Abrahamson et al., 2018) was developed specifically for the Cascadia forearc region for potential use by the USGS in its update of its national seismic hazard maps. This "Updated BC Hydro" model implemented the same functional form as the original BC Hydro model except for the removal of the backarc term in the model. Given the larger dataset developed as part of the NGA-Sub program, this updated GMM includes a regionalization for Cascadia of the model constant, the linear distance term, and the

V_{S30} scaling term Abrahamson et al. (2018). This preliminary GMM for Cascadia is expected to be superseded by the final set of NGA-Sub GMMs.

Comparisons of KBCG20 with the previous GMMs discussed above will be presented later in this report. As noted earlier, the selection of these specific GMMs for the comparisons with KBCG20 was not meant to represent the large number of available GMMs for subduction events in such regions as Japan, Chile, Mexico, Taiwan, etc. More information about these regional models can be found in the global compilation of GMMs maintained by John Douglas (http://www.gmpe.org.uk).

2 Database

2.1 PEER NGA-SUBDUCTION DATABASE

The NGA-Subduction (NGA-Sub) database contains 1880 subduction events with moment magnitudes ranging from 4.0 to 9.1 that have occurred in Japan, Taiwan, the Pacific Northwest (Cascadia), Alaska, New Zealand, Mexico, and South and Central America (Kishida et al., 2018; Bozorgnia et al., 2020). The database contains 71,340 three-component time series (214,020 individual components) from about over 6000 recording stations compiled from various data sources. Figure 2.1a shows the distribution of the epicenters in the NGA-Sub database. Figure 2.1b presents the overall distribution of the recording stations.

The unprocessed ("raw") waveforms were processed using a uniform set of instrument-correction, filtering, and baseline-correction algorithms developed by previous NGA research programs (Chiou et al., 2008; Ancheta et al., 2014; Kishida et al., 2018) from which acceleration time series and peak ground-motion parameters were determined. Ground-motion parameters in the database include peak ground acceleration (PGA), peak ground velocity (PGV), and pseudo-spectral acceleration (PSA) for horizontal and vertical components. The PSA periods range from 0.01 to 10 sec.

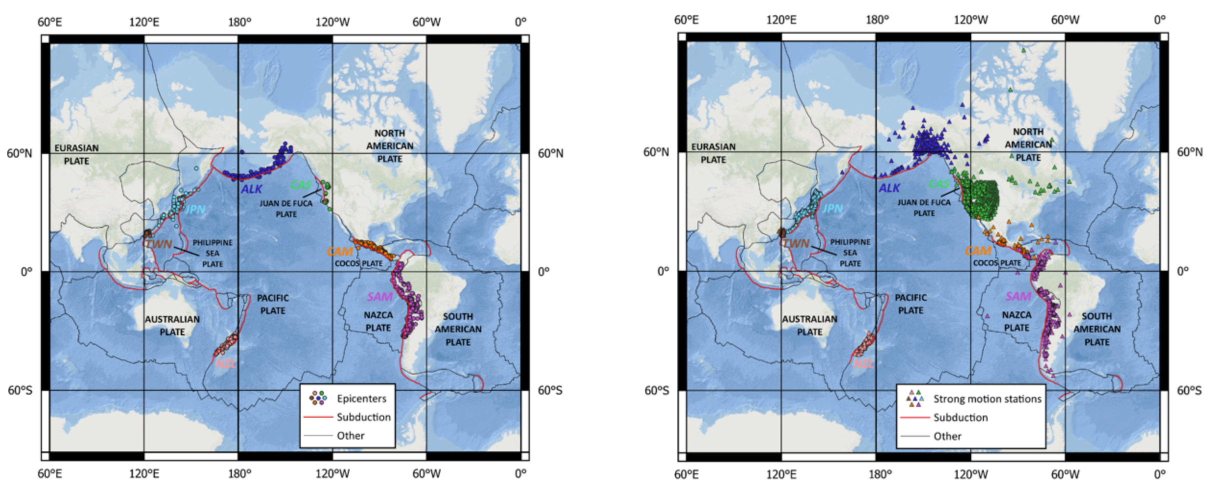

Figure 2.1: (a) Map of the distribution of epicenters in the NGA-Sub overall database; and (b) map of the distribution of the recording stations in the NGA-Sub overall database (figure courtesy of Victor Contreras).

Figure 2.2 shows the regional distribution of events, recordings, and stations. Figure 2.2(a) shows that Japan and Taiwan provide the largest number of recordings. Figure 2.2(b) shows that South and Central America is the region with the largest number of subduction earthquakes; however, they are recorded by a relatively small number of stations. Figure 2.2(c) shows that Japan, Cascadia in the Pacific Northwest, South America, and Taiwan have the largest number of recording stations.

In the database are 88 events with documented finite-fault models. The identification of foreshocks and aftershocks are also provided based on previous studies and the method described in Wooddell and Abrahamson (2014). The site database includes station name, station ID, recording network, geographic coordinates, instrument location, geology and geomorphology information, and soil profile characteristics, such as V_{S30} and depths to various V_S (shear-wave velocity) horizons (e.g., $Z_{1.0}$ and $Z_{2.5}$). Details of the NGA-Sub database are documented in a separate report (Stewart et al., 2020).

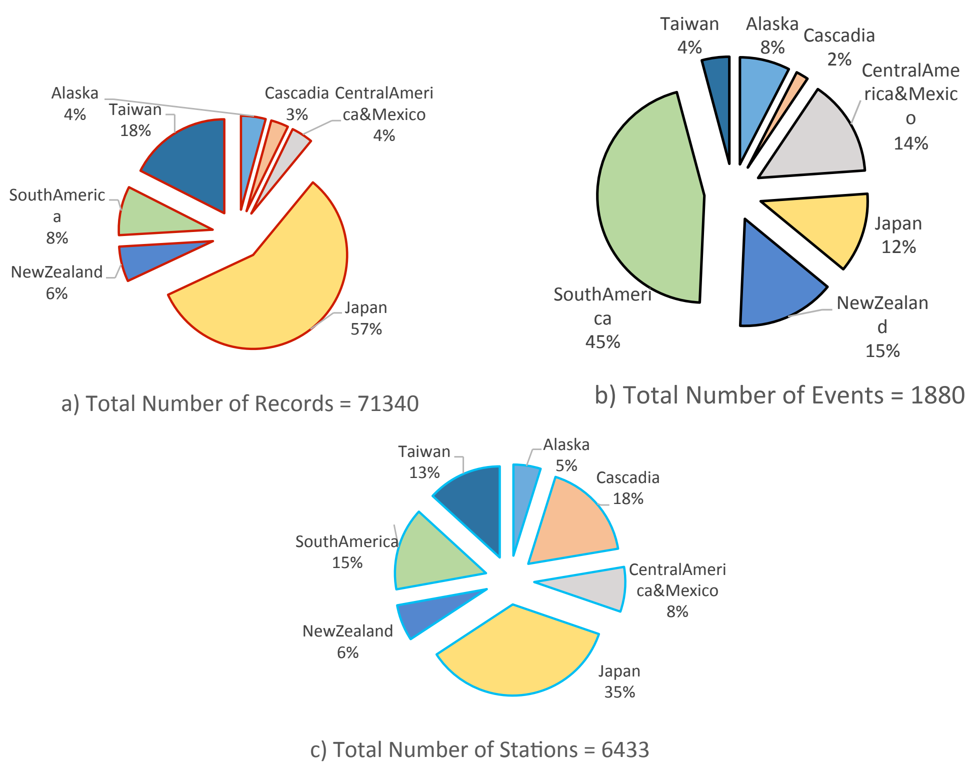

Figure 2.2: Regional distributions of the NGA-Sub database; (a) number of recordings, (b) number of events, and (c) number of stations (figure courtesy of Silvia Mazzoni).

2.2 DATA SELECTION CRITERIA

The data selection criteria are designed to select only data that are deemed to be accurate, reliable, and usable for GMM development. Hence, data that might bias the model are screened out.

In a first step, only those data including the numerical values of the main predictor variables were selected. Table 2.1 lists the predictor variables used in the model and their definitions. The variables with required numerical values are as follows: moment magnitude (**M**), rupture distance (R_{RUP}), time-averaged shear-wave velocity in the upper 30 m of the site (V_{S30}), and depth to the top of the rupture surface (Z_{TOR}). Data from stations for which no estimate of the depth to a shear-wave velocity horizon of 1 km/sed (Z_1) or 2.5 km/sed ($Z_{2.5}$) is available are not discarded, since these quantities are only available for a small number of stations and are not available at all for some regions; discarding these stations would severely reduce the number of usable data. Only data that have a positive value of PGA in the database were selected to screen out data that are not reliable.

Table 2.1: Definition of predictor variables.

Variable	Definition
M	Moment magnitude
R_{RUP}	Closest distance to rupture plane (km)
V_{S30}	Time-averaged shear-wave velocity in upper 30 m (m/sec)
Z_{TOR}	Depth to top of rupture (km)
$Z_{1.0}$	Depth to 1.0 km/sec shear-wave velocity horizon below site (km)
$Z_{2.5}$	Depth to 2.5 km/sec shear-wave velocity horizon below site (km)
F_S	Flag indicating interface event ($F_S = 0$) or intraslab event ($F_S = 1$)
F_X	Flag indicating no arc-crossing path ($F_X = 0$) or arc-crossing path ($F_X = 1$)
R_1	Distance (R_{RUP}) within Subregion 1 (Backarc) relative to volcanic arc (km)
R_2	Distance (R_{RUP}) within Subregion 2 (Forearc; Global, Japan Trench) (km)
R_3	Distance (R_{RUP}) within Subregion 3 (Forearc; Japan Nankai Trough) (km)

The NGA-Sub database classifies events into six different types; see Contreras et al. (2020) for details. The ground-motion model presented herein has been developed for two subduction event types: interface and intraslab. Type-0 events were selected for the interface earthquake dataset. For intraslab earthquakes, Type-1 (intraslab) and Type 5 events were selected (i.e., events from the lower part of a double seismic zone).

Earthquakes with a magnitude larger than 4.0 were selected. Although this threshold includes magnitudes that may not be of engineering interest, including the smaller magnitudes increases the number of recordings, which helps constrain the regression parameters of the model. For Cascadia, two events were classified as interface earthquakes in the database. Located off the central Oregon coast, they have magnitudes of $\mathbf{M} = 4.7$ and $\mathbf{M} = 4.9$. These earthquakes were excluded from the analysis because a special correction to Cascadia interface events (see Section 4.2.1) cannot be applied as it would be difficult to do for only two small interface events.

We excluded the October 4, 1994 $\mathbf{M} = 8.28$ Kuril event, which is unique in its characteristics (Tanioka et al., 1995a) and does not behave like other intraslab events included in the database.

We also excluded data based on the following quality criteria:

- Recordings with a multiple event flag equal to 1 (time histories that include more than one earthquake)
- Stations with instrument depth > 2 m
- Recordings with a visual quality flag not equal to 2 or 9
- Recordings with GMX 1st letter of N, Z, or F (non-free-field stations)

There are some records for which the PGA value in the database is very large ($PGA > 100$g); because these are obvious outliers, recordings that have $PGA > 10$g were removed.

We selected only recordings for which $R_{RUP} < R_{MAX}$. R_{MAX} is the maximum distance for each event that is introduced to avoid biasing the model with non-triggered recordings, which arises when an instrument triggers only above a certain amplitude threshold; see Section 4.5.2 of Contreras et al. (2020). Since very long distances do not contribute significantly to hazard, only recordings with $R_{RUP} < 800$ km were selected even if the value of R_{MAX} was larger. To make sure that each event has a reasonable distance range, events for which the ratio of the largest to smallest rupture distance is larger than 2 were also selected.

Based on an initial regression, there were several recordings considered to be outliers and were subsequently removed from the dataset. For example, we removed all recordings with absolute residuals that deviated more than four times the within-event standard deviation from the median prediction at eight selected periods of engineering interest. Finally, after all of the aforementioned criteria were applied, only those events that had a minimum number of five recordings were selected.

The selection criteria lead to the selection of 16,045 recordings from 238 events and 3769 stations for PGA. At long periods, the number of recordings was reduced due to the useable bandwidth. The number of recordings, events, and stations for each period is shown in Figure 2.3. A list of the Record Sequence Numbers (RSNs) for the recordings used in the development of this model is available in an electronic supplement to this report.

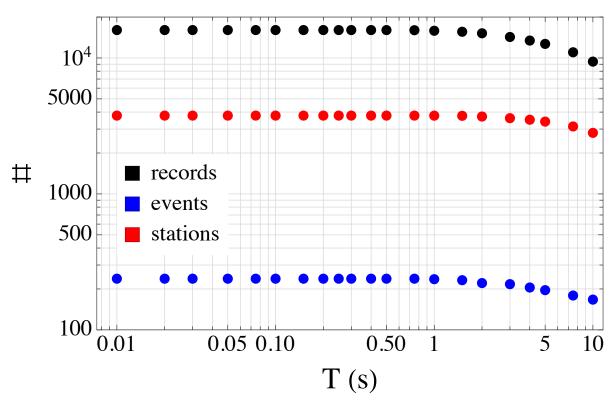

Figure 2.3: Number of recordings, events, and stations for each period used in the analysis.

2.3 DATA DISTRIBUTION

The NGA-Sub database identifies seven database regions: Alaska, Cascadia (Pacific Northwest), Central America and Mexico, Japan, New Zealand, South America, and Taiwan. Table 2.2 lists the number of recordings, number of events, and number of stations for each of the database regions for the subset of data selected for analysis; see previous section. Japan dominates the dataset with over 50% of the recordings. Taiwan and South America also have a significant number of events but fewer recordings. For Cascadia, Central America and Mexico, and New Zealand, the number of available recordings is relatively sparse.

The magnitude-distance distribution of the selected recordings is shown in Figure 2.4 for interface events and intraslab events. The number of events at large magnitudes ($\mathbf{M} > 8.0$ for interface, $\mathbf{M} > 7.0$ for intraslab) is limited. The largest events are the $\mathbf{M} = 8.81$ Maule earthquake in Chile and the $\mathbf{M} = 9.12$ Tohoku-Oki earthquake in Japan.

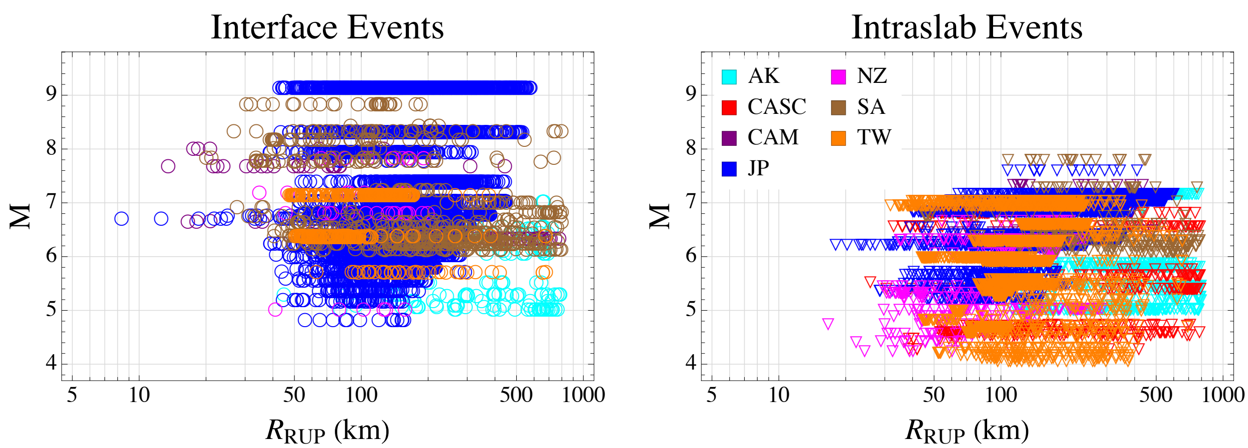

Figure 2.4: Magnitude/distance scatterplot.

The distribution of V_{S30} values is shown in Figures 2.5 and 2.6. For regions with a small number of recordings, the range of V_{S30} values is limited.

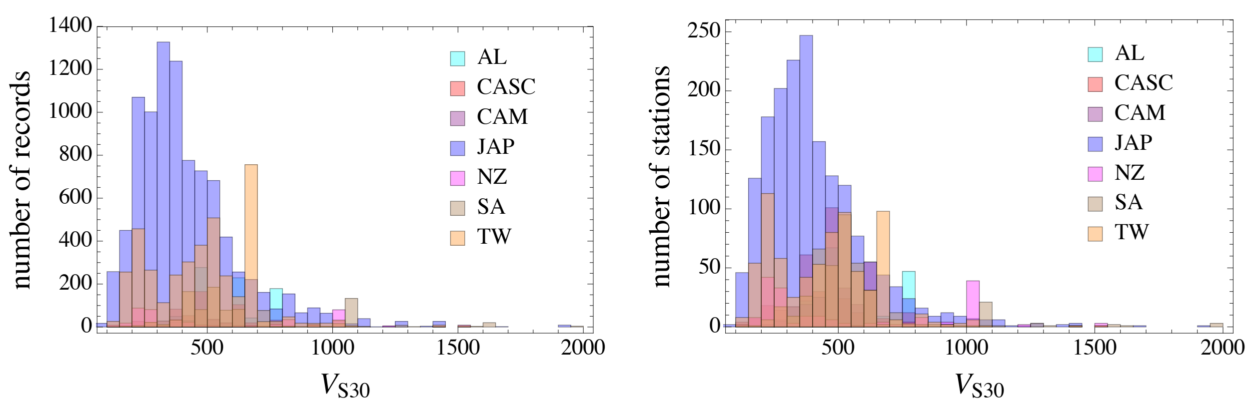

Figure 2.5: Distribution of V_{S30} values: (left) number of recordings and (right) number of stations.

Table 2.2: Selected number of recordings by region.

Region	Region abbreviation	No. of recordings	No. of events	No. of Stations
All	–	16,045	238	3,769
Alaska	AK	822	33	205
Cascadia	CASC	604	12	365
Central America & Mexico	CAM	120	9	110
Japan	JAP	9,217	63	1,745
New Zealand	NZ	441	21	185
South America	SA	953	51	415
Taiwan	TW	3,888	49	744

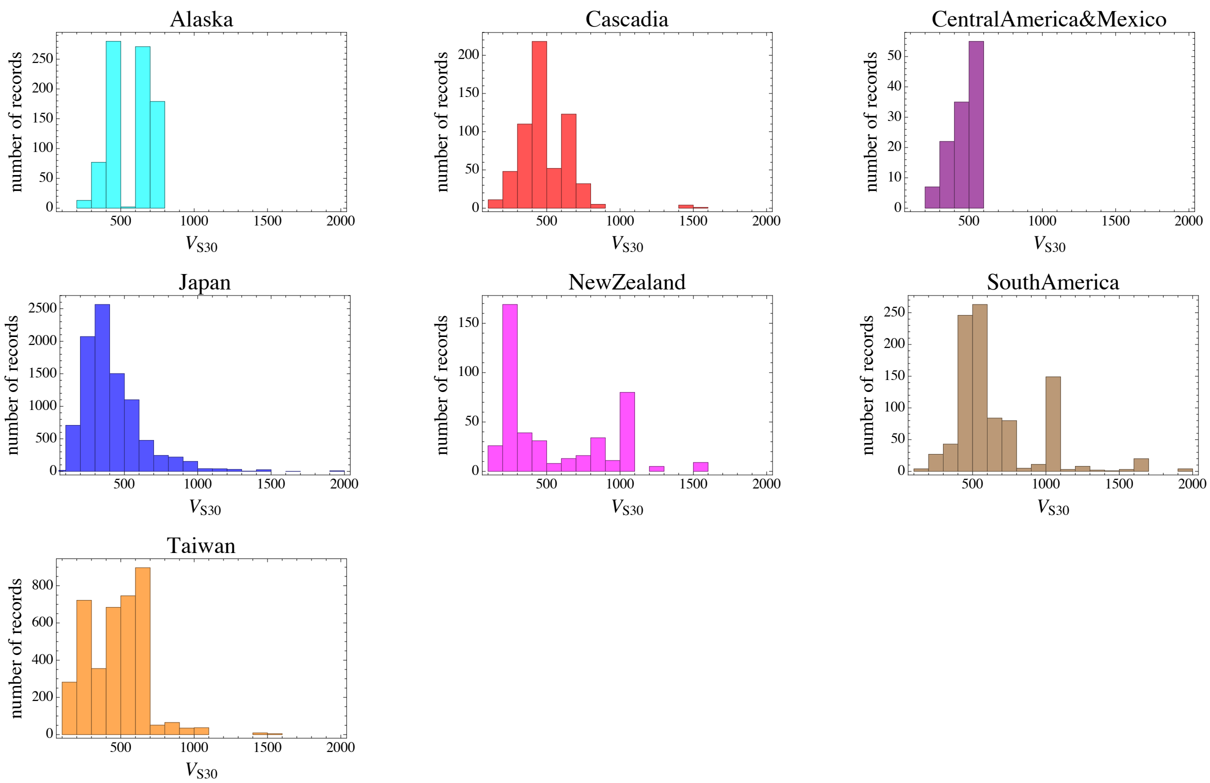

Figure 2.6: Distribution of V_{S30} values per region.

Figure 2.7 shows the distribution of recordings versus the depth to the top of the rupture surface, Z_{TOR}. The depths of interface events range from $0 \leq Z_{TOR} \leq 59$ km. The intraslab events have a depth range of $16 \leq Z_{TOR} \leq 177$ km.

Figure 2.8 shows the number of recordings per event and station. As described in the

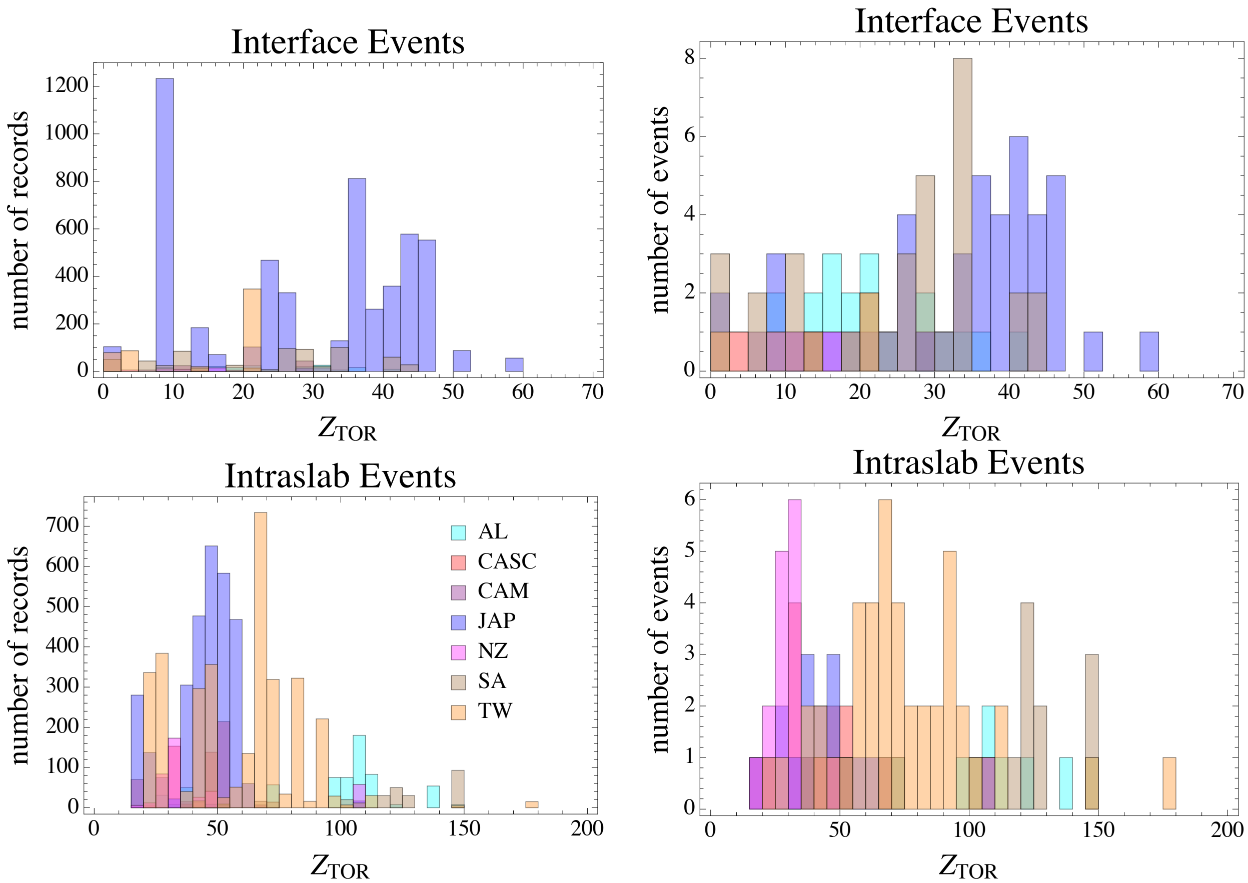

Figure 2.7: Distribution of Z_{TOR} values: (left) number of recordings and (right) number of events.

previous section, only those events with at least five recordings were selected. Because there are a number of stations with only one recording, the criterion that there be a minimum number of recordings per station was disregarded.

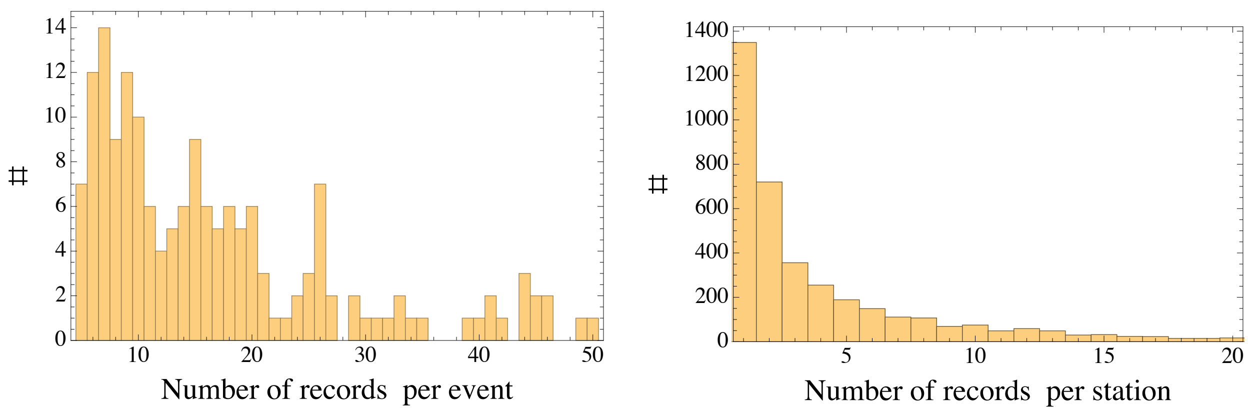

Figure 2.8: Number of recordings per event and station. The maximum number of recordings per event is 980 (Tohoku-Oki earthquake) and the maximum number of recordings per station is 46.

3 Methodology

An important consideration during the model development was to take into account regional differences in ground-motion scaling. In particular, the GMM is a partially non-ergodic model (Stafford, 2014) in which some coefficients are regionalized (i.e., have different values for different regions), while others have the same value across all regions (i.e., are global). This is important, since it allowed the project team to relax the ergodic assumption (Anderson and Brune, 1999), which leads to a better estimate of the median predictions and smaller aleatory variability. At the same time, it is important to account for the epistemic uncertainty in the regional coefficients since these are estimated from a smaller dataset. Not accounting for this added uncertainty would lead to an underestimate of hazard (e.g. Abrahamson et al., 2019).

Several previous GMMs have taken into account regional differences; for example, some of the models developed in the NGA-West2 project include regional differences (Bozorgnia et al., 2014; Abrahamson et al., 2014; Boore et al., 2014; Campbell and Bozorgnia, 2014; Chiou and Youngs, 2014). These models estimated adjustment coefficients based on regional residual trends. A more statistical approach is to estimate these regression parameters as regional random effects (e.g., Stafford, 2014; Kotha et al., 2016; Sedaghati and Pezeshk, 2017). This approach has the advantage that the regional regression parameters can influence each other via their global mean and that a global distribution for the regression parameters is estimated. This global distribution can be used to extend the model to new regions that are not included in the development of the GMM. Often, such a model is called a multilevel or hierarchical model (Gelman and Hill, 2006; Betancourt and Girolami, 2015), since there is a hierarchy from global to regional to event-specific levels. In Bayesian terms, one can imagine that the global level provides a prior distribution for the regional level (e.g., a global attenuation coefficient can serve as a prior mean for a regional attenuation coefficient).

The regression model has the form

$$\ln Y_{es} = f_{base}(\vec{\theta}; \vec{x}_{es}) + \delta B_e + \delta W_{es} \tag{3.1}$$

where f_{base} represents the base median model, $\vec{\theta}$ is a vector of coefficients (some of which are regionalized), $\vec{x}_{es}$ is a vector of predictor variables (cf. Table 2.1), and subscripts e and s are indices representing event e and station s, respectively. δB_e denotes the between-event residual (i.e., source term) and δW_{es} the within-event residual. Systematic site effects (i.e., site terms) are not accounted for in the regression and are usually denoted δS_s; for each station, the term δS is a systematic difference from the average site scaling (dependent on V_{S30}). The subduction data exhibit strong path effects that, if not completely modeled, would map into the systematic site terms. In addition, there are many stations with only one recording, which does not provide much confidence when estimating a systematic station term.

The functional form of the base model and the regionalization of the coefficients are described in Chapter 4. The aleatory variability model is described in Chapter 5. Chapter 6 describes how to estimate epistemic uncertainty associated with the median predictions.

3.1 REGRESSION APPROACH

The regression parameters (i.e., coefficients, standard deviations, etc.) of the model are estimated via Bayesian inference (e.g., Spiegelhalter and Rice, 2009). The goal in Bayesian inference is to calculate the *posterior distribution* of the regression parameters given the data. The posterior distribution can be calculated as the product of the *likelihood* and the *prior distribution* according to Bayes' rule:

$$P(\vec{\theta}|D) = \frac{P(D|\vec{\theta})P(\vec{\theta})}{P(D)} \tag{3.2}$$

where $\vec{\theta}$ denotes the vector of regression parameters of the model, and D is the observed data. The marginal probability of the data, $P(D)$, is a constant, which can be calculated from the prior distribution and the likelihood by the expression $P(D) = \int P(D|\vec{\theta})P(\vec{\theta})d\vec{\theta}$. The prior distribution, $P(\vec{\theta})$, makes it possible to incorporate prior information in the estimation of the regression parameters as well as constrain the range of values the regression parameters can take. The posterior distribution, $P(\vec{\theta}|D)$, describes the full uncertainty of all of the regression parameters.

The Bayesian approach is also useful for building a model that can be easily updated once a new earthquake occurs (Stafford, 2019). In such cases, the posterior distribution of the existing model becomes the prior distribution for the newly observed data.

Since solving Equation (3.2) is analytically intractable, a Markov Chain Monte Carlo (MCMC) sampling is employed to estimate the posterior distribution of the regression parameters using the program "Stan" (Carpenter et al., 2017), which employs Hamiltonian Monte Carlo sampling (Betancourt, 2017; Neal, 2011). The output of the MCMC algorithm are samples from the posterior distribution, which can be used to estimate the mean, median, standard deviation, and other statistics of the posterior distribution of each regression parameter. It can also be used to assess the correlation between regression parameters.

Chapter 6 describes how the samples from the posterior distribution are used to assess the epistemic uncertainty of the median predictions, which is an important quantity in probabilistic seismic hazard analysis (PSHA). Simply speaking, one can calculate a median prediction for each sample from the posterior distribution, thus providing a distribution of median predictions for a specific earthquake scenario. Similar to the model of Al-Atik and Youngs (2014), this distribution describes the epistemic uncertainty associated with these median predictions.

During the initial regression, outliers were discovered in the selected database. Section 2.2 describeshow some recordings that were obvious outliers based on the residuals of an early trial

regression were discarded; however, there may be still undetected outliers in the database. Such outlier recordings will have undue influence on the regression, resulting in a biased median prediction and inflated aleatory variability. To avoid potential biases due to remaining outliers, a robust Bayesian regression was performed (see e.g. https://jrnold.github.io/bayesian_notes/robust-regression.html or https://solomonkurz.netlify.com/post/robust-linear-regression-with-the-robust-stud
Thus, instead of modeling the within-event variability with a normal distribution (as is traditionally the case), a Student's t-distribution, or simply t-distribution was used. The t-distribution has heavier tails than the normal distribution and can accommodate outliers better than the normal distribution. Compared to the normal distribution, the t-distribution has an additional parameter, $\nu > 0$, defined as the degrees-of-freedom. For $\nu \to \infty$, the t-distribution approaches the normal distribution; for small values of ν it has heavier tails and is less susceptible to outliers. Chapter 5 describes the robust Bayesian regression model in more detail.

3.1.1 Regression Details

The regression is run independently for each period. Ideally, the model parameters for all periods should be estimated at the same time since that would allow for an estimate of their correlations of both of the spectral accelerations as well as the parameters during the regression; however, this approach is computationally challenging due to the large number of recordings.

For each period, all regression parameters (e.g., coefficients, standard deviations, and event terms) of the model are estimated simultaneously with the prior distributions balancing trade-offs between parameters. Estimating all regression parameters simultaneously has the advantage that it is possible to determine the co-variance between them, which is important if one wants to calculate the epistemic uncertainty of the median predictions per Al-Atik and Youngs (2014).

As explained previously, the regression parameters of the model are estimated via the MCMC method. In an MCMC sampling, four Markov Chains for each regression were run to assess convergence. For each chain, the first 200 samples of the posterior distribution were discarded as "burn-in." An additional 200 samples from the posterior distribution were run four times, resulting in 800 samples for each regression parameter.

4 Median Model

4.1 BASE MODEL

The functional form of the base median model is similar to that of the BC Hydro GMM (Abrahamson et al., 2016) and its 2018 update (Abrahamson et al., 2018). Differences from the BC Hydro model include: (1) replacing the sharp breakpoints in the bilinear magnitude and source-depth terms with a smoother transition function; (2) adding a source-depth term for interface events; (3) replacing the anelastic attenuation term with a new term that does not depend on the location of the site to define forearc and backarc attenuation but instead depends on the lengths of the travel path to the site within the forearc and backarc regions; and (4) incorporating more geographic areas in the regionalized model.

The general regression model is defined in Equation (3.1). The base median model in that equation has the following form

$$
\begin{aligned}
f_{base}(\vec{\theta};\vec{x}) = (1-F_S)\theta_{1,if} + F_S\theta_{1,slab} + f_{mag}(\mathbf{M},F_S) + f_{geom}(R_{RUP},\mathbf{M},F_S) + f_{depth}(Z_{TOR},F_S) \\
+ f_{attn}(R_{RUP},R_1,R_2,R_3,F_X) + f_{site}(V_{S30},PGA_{1100}) + f_{basin}(Z_{1.0}|Z_{2.5}) \qquad (4.1)
\end{aligned}
$$

where $\vec{x} = \{\mathbf{M}, R_{RUP}, V_{S30}, Z_{TOR}, F_S, F_X, R_1, R_2, R_3, Z_{1.0}|Z_{2.5}\}$ is the vector of predictor variables (cf. Table 2.1), and where the vertical bar in $Z_{1.0}|Z_{2.5}$ means that either one depth parameter or the other is included in the model. Interface and intraslab events are distinguished by the flag F_S, which is $F_S = 1$ for intraslab events and 0 otherwise. The remaining terms and parameters of the model are defined in the following sections in the order that they appear in Equation (4.1). For brevity, the terms and parameters are only defined once and are not defined again the next time they are used. The regression coefficients $\theta_{1,if}$ and $\theta_{1,slab}$ are the constants for interface events and intraslab events, respectively, and were found to vary by geographic region; see Section 4.2. The subscripts "if" and "$slab$" identify parameters and coefficients representing interface events and intraslab events, respectively.

To ensure a physically meaningful spectrum, the predicted median PSA at short periods are not allowed to be smaller than PGA:

$$
\mu = \begin{cases} \ln PGA(\vec{x}) & PSA < PGA \text{ and } T \leq 0.1s \\ f_{base}(\vec{\theta}(T),\vec{x}) & else \end{cases} \qquad (4.2)
$$

where $\vec{\theta}(T)$ is the set of coefficients for period T, and $\ln PGA(\vec{x})$ is the (logarithmic) median prediction for PGA for scenario $\vec{x}$.

Table 4.1 lists the model coefficients, their purpose, and whether the coefficient is regionalized; see the following sections for details.

Table 4.1: Description of model coefficients.

Coefficient	Description	Regionalized
$\theta_{1,if}$	Interface constant	Yes
$\theta_{1,slab}$	Intraslab constant	Yes
$\theta_{2,if}$	Interface geometrical spreading	No
$\theta_{2,slab}$	Intraslab geometrical spreading	No
θ_3	Magnitude-dependent geometrical spreading	No
$\theta_{4,if}$	Interface small-magnitude scaling rate MSR	No
$\theta_{4,slab}$	Intraslab small-magnitude scaling rate MSR	No
θ_5	Large magnitude MSR	No
$\theta_{6,xc}$	Arc-crossing constant	No
$\theta_{6,x1}$	Anelastic attenuation, arc-crossing subregion relative to arc 1	Yes
$\theta_{6,x2}$	Anelastic attenuation, arc-crossing subregion relative to arc 2	Yes
$\theta_{6,x3}$	Anelastic attenuation, arc-crossing subregion relative to arc 3	Yes
$\theta_{6,1}$	Anelastic attenuation, non arc-crossing subregion relative to arc 1	Yes
$\theta_{6,2}$	Anelastic attenuation, non arc-crossing subregion relative to arc 2	Yes
$\theta_{6,3}$	Anelastic attenuation, non arc-crossing subregion relative to arc 3	Yes
θ_7	Linear site amplification (V_{S30} scaling)	Yes
$\theta_{9,if}$	Interface source-depth scaling rate DSR (Z_{Tor} scaling)	No
$\theta_{9,slab}$	Intraslab source-depth scaling rate DSR (Z_{Tor} scaling)	No
$\theta_{10} = 0$	Source-depth scaling rate for deep events ($Z_{TOR} > z_B$) fixed to zero	No
θ_{11}	Constant of basin-depth scaling	Yes
θ_{12}	Slope of basin depth scaling	Yes
$\theta_{nft,1}$	Coefficient for near-fault term	No
$\theta_{nft,2}$	Coefficient for near-fault term	No
$\delta Z_{B,if}$	Adjustment to depth break point for interface events	No
$\delta Z_{B,slab}$	Adjustment to depth break point for interface events	No

4.1.1 Logistic Hinge Function

The logistic hinge function is used to model the magnitude and source-depth terms. It is a bilinear function with a smooth transition between two linear regimes given by the function

$$lh(x, x_0, a, b_0, b_1, \delta) = a + b_0(x - x_0) + (b_1 - b_0)\delta \ln\left[1 + \exp\left(\frac{x - x_0}{\delta}\right)\right] \quad (4.3)$$

The breakpoint between the two linear regimes is defined by the parameters x_0 and δ, which determine the smoothness of the transition. Smaller values of δ lead to a sharper breakpoint. The parameters b_0 and b_1 are the slopes of the linear regimes below and above the breakpoint, respectively, and a is an offset at the breakpoint. Figure 4.1 shows an example logistic hinge function with a breakpoint at $x_0 = 7.5$, a slope below the breakpoint of $b_0 = 1$, a slope above the breakpoint of $b_1 = 0.2$, and two different values of δ. The offset in Figure 4.1 is set to $a = 1$.

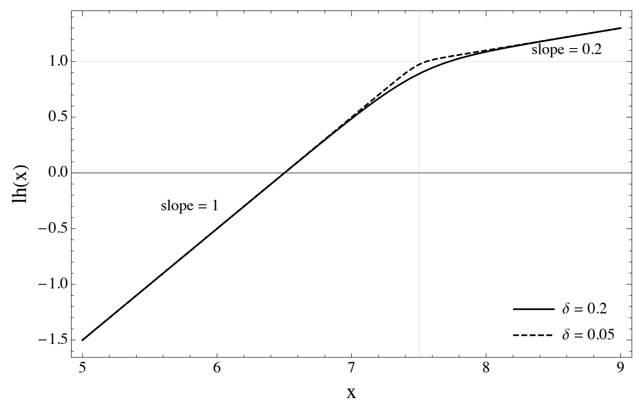

Figure 4.1: Logistic hinge function.

4.1.2 Magnitude Term

The magnitude term is given by the bilinear function

$$\begin{aligned} f_{mag} = (1 - F_S)\ & lh(\mathbf{M}, \mathbf{M}_{B,if}, \theta_{4,if}(\mathbf{M}_{B,if} - \mathbf{M}_{ref}), \theta_{4,if}, \theta_5, \delta_M) \\ &+ F_S\ lh(\mathbf{M}, \mathbf{M}_{B,slab}, \theta_{4,slab}(\mathbf{M}_{B,slab} - \mathbf{M}_{ref}), \theta_{4,slab}, \theta_5, \delta_M) \end{aligned} \quad (4.4)$$

where $\mathbf{M}$ is moment magnitude, $\mathbf{M}_{ref}$ is a reference magnitude to center, and δ_M is a transition smoothness parameter. The bilinear magnitude scaling has breakpoints at $\mathbf{M}_{B,if}$ and $\mathbf{M}_{B,slab}$ that are assigned based on the geometry of the subduction zone. They are different for different subduction zones and types of event. For interface events, they are assigned based on the study of Campbell (2020) and for intraslab events based on the study of Ji and Archuleta (2018), as summarized in Section 8.2.2.

The slope defining the magnitude scaling rate (MSR) below the magnitude breakpoint is given by regression coefficients $\theta_{4,if}$ and $\theta_{4,slab}$. The MSR above the magnitude breakpoint, θ_5, was constrained to be the same for both interface and intraslab events. There are not enough data above the magnitude breakpoints of each subduction zone to empirically constrain the large-magnitude MSR coefficients, which is why both subduction types are used to define the large-magnitude MSR.

The smoothness of the transition between the two linear MSR regimes is fixed at $\delta_M = 0.1$. Preliminary trials to estimate this parameter demonstrated that it was not well constrained, and that its posterior distribution was almost unchanged compared to its prior distribution. Thus, the selected value leads to a reasonably smooth transition between the two linear regimes. The offset is chosen so that the magnitude term is centered at magnitude $M_{ref} = 6.0$.

During an initial regression, it became apparent that at long periods ($T > 1$ sec) the event terms for interface events at large magnitudes were not centered but biased low. As a result, an adjustment to $\mathbf{M}_{B,if}$ for interface events at $T > 1$ sec was included per Abrahamson et al. (2016, 2018). This adjustment is zero at $T \leq 1$ sec and -0.4 at $T \geq 4$ sec, with a log-linear interpolation in between. The values are shown in Figure 4.2.

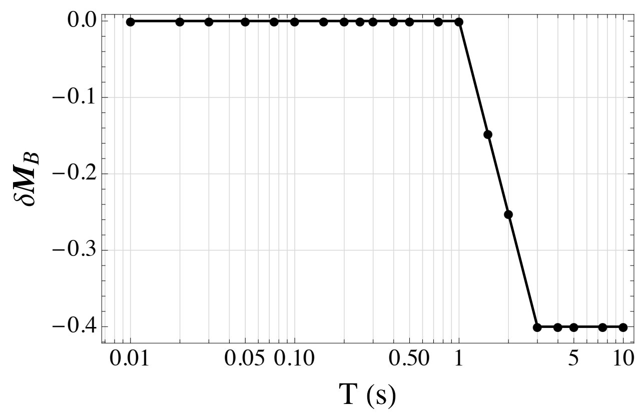

Figure 4.2: Adjustment to the magnitude breakpoint for interface events.

To check whether a different magnitude slope for interface and intraslab events makes sense, the posterior distribution of the magnitude scaling coefficients was examined $\theta_{4,if}$ and $\theta_{4,slab}$, as shown in Figure 4.3. The majority of the two posterior distributions do not overlap, which indicates that the two coefficients should have different values.

To statistically test whether a magnitude term with different MSRs for interface and intraslab events performs better than one with the same MSR, the data was split into a training dataset and a test dataset. Two regression analyses were performed on the training dataset: one using the same MSR and one using different MSRs for interface and intraslab events. Their performance was then evaluated using the test dataset. Thirty interface and 30 intraslab events from the full KBCG20 database were randomly selected to define the test dataset. The training dataset was defined by removing all of the recordings from the test dataset, leaving 178 events.

The mean-squared error of the residuals of the regression on the test dataset, calculated as $MSE = \frac{1}{N}\sum_{i=1}^{N}(\ln PGA_i - \mu_i)^2$, is 0.727 for the model with the same MSR and 0.722 for the model with different MSRs. These results suggest that there is basically no difference in predictive performance between the two models, indicating that both models are valid. Given the results

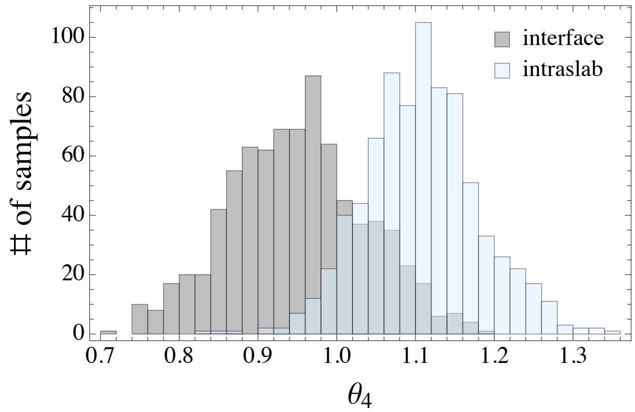

Figure 4.3: Posterior distributions of the PGA magnitude-scaling coefficients $\theta_{4,if}$ and $\theta_{4,slab}$ for interface and intraslab events, respectively.

in Figure 4.3, it is assumed there is value in using different magnitude scaling coefficients for interface and intraslab events, and we adopted this approach in the regressions.

4.1.3 Geometrical Attenuation Term

The geometrical attenuation term (i.e., geometrical spreading) is modeled by the function

$$f_{geom} = (1 - F_S)(\theta_{2,if} + \theta_3\mathbf{M})(\ln[R_{RUP} + h(\mathbf{M})]) + F_S(\theta_{2,slab} + \theta_3\mathbf{M})(\ln[R_{RUP} + h(\mathbf{M})]) \tag{4.5}$$

where R_{RUP} (km) is the shortest distance between the site and the fault rupture surface; $h(\mathbf{M})$ (km) is a magnitude-dependent finite-fault term (a.k.a. fictitious depth) that accounts for ground-motion saturation at small distances; and $\theta_{2,if}$ and $\theta_{2,slab}$ are magnitude-independent regression coefficients. The regression coefficient θ_3 is the same for both subduction event types and was adopted from the geometrical attenuation term of Abrahamson et al. (2016, 2018) because of insufficient data to constrain it.

The finite-fault term is given by the function

$$h(\mathbf{M}) = 10^{\theta_{nft,1} + \theta_{nft,2}(\mathbf{M} - 6.0)} \tag{4.6}$$

in which the regression coefficients $\theta_{nft,1}$ and $\theta_{nft,2}$ were given a strong prior distribution in the regression because they were not well constrained by data.

4.1.4 Source-Depth Term

The source-depth term is given by the bilinear function

$$f_{depth} = (1 - F_S)\ lh(Z_{TOR}, Z_{B,if} + \delta Z_{B,if}, \theta_{9,if}(z_{B,if} + \delta Z_{B,if} - Z_{if,ref}), \theta_{9,if}, \theta_{10}, \delta_Z) + F_S\ lh(Z_{TOR}, Z_{B,slab} + \delta Z_{B,slab}, \theta_{9,slab}(Z_{B,slab} + \delta Z_{B,slab} - Z_{slab,ref}), \theta_{9,slab}, \theta_{10}, \delta_Z) \tag{4.7}$$

where Z_{TOR} is the depth (km) to the top of the fault rupture surface, $Z_{if,ref}$ and $Z_{slab,ref}$ are reference depths (km), and δ_Z is the smoothness transition parameter between the two linear regimes. The bilinear depth scaling has breakpoints at $Z_{B,if} + \delta Z_{B,if}$ and $Z_{B,slab} + \delta Z_{B,slab}$ that were determined from the regression. The source-depth breakpoints were initially set to $Z_{B,if} = 30$ km and $Z_{B,slab} = 80$ km. The period-dependent adjustment coefficients $\delta Z_{B,if}$ and $\delta Z_{B,slab}$ were determined by regression because the depth breakpoints have no theoretical basis in constrast to the magnitude breakpoints. Therefore, the effective source depth breakpoints become $Z_{B,if} + \delta Z_{B,if}$ and $Z_{B,slab} + \delta Z_{B,slab}$.

The parameter δ_Z determines the smoothness of transition in the bilinear form and was set to $\delta Z = 1$.

The coefficients for the source-depth scaling rates (DSR) up to the depth breakpoints are $\theta_{9,if}$ and $\theta_{9,slab}$. Both of the coefficients for the DSRs above the breakpoints were fixed at $\theta_{10} = 0$. This is consistent with Abrahamson et al. (2016, 2018) because there are not many events with depths larger than these breakpoints, and the depths that do exist do not show any systematic trend with ground-motion amplitude.

4.1.5 Site Amplification Term

The site-amplification term is given by the function

$$f_{site}(V_{S30}) = \begin{cases} \theta_7(reg)\ln\left(\frac{V_{S30}}{k_1}\right) + k_2\left\{\ln\left[PGA_{1100} + c\ln\left(\frac{V_{S30}}{k_1}\right)^n\right] - \ln\left[PGA_{1100} + c\right]\right\} & V_{S30} \le k_1 \\ (\theta_7(reg) + k_2 n)\ln\left(\frac{V_{S30}}{k_1}\right) & V_{S30} > k_1 \end{cases} \tag{4.8}$$

where V_{S30} (m/sec) is the time-averaged shear-wave velocity in the top 30 m of the site, and PGA_{1100} is the median predicted value of PGA (g) for a rock site with $V_{S30} = 1100$ m/sec. The function defining the site amplification term was taken from Campbell and Bozorgnia (2014), as were the period-dependent parameters k_1 and k_2, and the period-independent parameters c and n. The linear scaling of ground motion with V_{S30} is given by the regression coefficient $\theta_7(reg)$, which varies by geographic region; see Section 4.2. It is assumed that nonlinear site amplification for subduction events is similar to that for crustal events, which is consistent with Abrahamson et al. (2016) and Montalva et al. (2017).

4.1.6 Anelastic Attenuation Term

The anelastic attenuation (i.e., arc-crossing) term varies by geographic region and, in some cases, by subregions within these broader geographic regions; see Section 4.2. For the geographic regions of Japan (JP), Central America and Mexico (CAM), and South America (SA), differences in anelastic attenuation for travel paths within the forearc and backarc subregions were taken into account, whereas they were not for Alaska (AK), Cascadia (CASC), New Zealand (NZ), and Taiwan (TW). The difference in how these regions were treated was based on inspection of residual plots and ground-motion scaling of trial regressions for each region without including forearc and backarc attenuation coefficients.

For each identified geographic region, the anelastic attenuation can depend on whether the travel path passes through the volcanic arc (i.e., the transition between the forearc and backarc subregions). Subregion i determines whether the travel path passes through the backarc subregion (Subregion 1), the forearc subregion except the forearc of southwestern Japan (Subregion 2), and the forearc subregion of southwestern Japan (Subregion 3). The northeastern forearc of Japan is adjacent to the Japan Trench, whereas the southwestern forearc of Japan is adjacent to the Nankai Trough.

The rupture distance that falls within a given Subregion i is denoted R_i and is defined as the fractional part of the total rupture distance that falls within each of the subregions, where $\sum_i R_i = R_{RUP}$. After preliminary regression analyses, the NGA-Sub GMM developers defined three global attenuation regions: (1) JP, (2) CAM and SA, and (3) AK, CASC, NZ, and TW. Taking into account the three subregions for JP and the two subregions each for CAM and SA (Kishida et al., 2018; Bozorgnia et al., 2020), there are a total of 11 regional anelastic attenuation coefficients. This subregional anelastic attenuation model is a generalized version of the cell-specific attenuation model of Dawood and Rodriguez-Marek (2013) and Kuehn et al. (2019).

Because the regression coefficient θ_6 was found to be different for different geographic regions and subregions, it was regionalized (see Section 4.2) according to the anelastic attenuation term

$$f_{attn} = \begin{cases} F_X(\theta_{6,xc} + \theta_{6,x1}(reg)R_1 + \theta_{6,x2}(reg)R_2 + \theta_{6,x3}(reg)R_3) & \\ \quad +(1-F_X)(\theta_{6,1}(reg)R_1 + \theta_{6,2}(reg)R_2 + \theta_{6,3}(reg)R_3) & \text{JP} \\ F_X(\theta_{6,xc} + \theta_{6,x1}(reg)R_1 + \theta_{6,x2}(reg)R_2) & \\ \quad +(1-F_X)(\theta_{6,1}(reg)R_1 + \theta_{6,2}(reg)R_2) & \text{CAM,SA} \\ \theta_{6,2}(reg)R_{RUP} & \text{AK,CASC,NZ,TW} \end{cases} \tag{4.9}$$

where $F_X = 1$ is for backarc travel paths and 0 otherwise, and R_i is the travel distance through subregion i for a given geographic region. The regression coefficient $\theta_{6,i}$ represents the anelastic attenuation coefficient for subregion i. An x before the subregion index indicates that the travel path has crossed a volcanic arc from the forearc into the backarc. The coefficient $\theta_{6,xc}$ is a regionalized constant that accounts for lower overall ground-motion amplitudes (an offset) when the travel path crosses the volcanic arc from the forearc into the backarc.

In the regression, all six coefficients ($\theta_{6,x1}, \theta_{6,x2}, \theta_{6,x3}, \theta_{6,1}, \theta_{6,2}, \theta_{6,3}$) for all three geographic regions were estimated. Based on preliminary analyses that indicate that these regions have the same anelastic attenuation in the forearc and backarc subregions, $R_2 = R_{RUP}$ and $R_1 = R_3 = 0$ for AK, CASC, NZ, and TW. Therefore, the posterior distributions for the geographic regions without different forearc and backarc subregions are defined by their prior distributions.

4.1.7 Basin-Depth Term

The effect of the deep structure beneath the site is modeled by the depth (km) to the 1.0 km/sec or 2.5 km/sec shear-wave velocity horizons (i.e., basin depths) beneath the site, referred to as $Z_{1.0}$ or $Z_{2.5}$, respectively. These basin-depth parameters are not available for all geographic regions or for all recording sites within a given region. For CASC sites, only $Z_{2.5}$ is available. For NZ and TW sites, only $Z_{1.0}$ is available. For JP sites, both $Z_{1.0}$ and $Z_{2.5}$ are available. For CAM and SA neither depth is available.

The basin-depth term is given by the function

$$f_{basin}(Z) = \theta_{11} + \theta_{12}\delta_{\ln Z} \tag{4.10}$$

where Z is either $Z_{1.0}$ or $Z_{2.5}$, $\delta_{\ln Z} = \ln Z_{obs} - \ln Z_{ref}$, Z_{obs} is the observed value of basin depth, and $Z_{ref} = f(V_{S30})$ is the reference value of basin depth for a given geographic region and V_{S30} value. Practically, the value of θ_{11} is small; thus, when $\delta \ln Z$ goes to zero the f_{basin} approaches a small value. For CASC, the basin depth term in Equation (4.10) is only applied if the site for which one wants to calculate median predictions is in a designated basin. We describe the application to CASC in more detail in section 4.2.1. Z_{ref} is given by the function

$$\ln Z_{ref} = \theta_{z1} + (\theta_{z2} - \theta_{z1}) \frac{\exp\left(\frac{\ln V_{S30} - \theta_{z3}}{\theta_{z4}}\right)}{1 + \exp\left(\frac{\ln V_{S30} - \theta_{z3}}{\theta_{z4}}\right)} \tag{4.11}$$

where $\theta_{z1}, \ldots, \theta_{z4}$ vary by geographic region for CASC, JP, NZ, and TW, respectively. Figure 4.4 shows scatterplots of V_{S30} and $Z_{1.0}|Z_{2.5}$ for the regions for which data is available, together with the fitted models according to Equation (4.11).

For CASC, estimating all parameters of Equation 4.11 is not possible due to the very limited number of stations with associated V_{S30} and $Z_{2.5}$ values at hard rock sites in particular . Hence, in this case the model is constrained to approach a value of $Z_{ref} = 10$ m for large values of V_{S30} ($V_{S30} > 2000$ m/sec).

There is considerable scatter in the values of $Z_{2.5}|Z_{1.0}$ around the $Z_{ref}(V_{S30})$ line. Hence, in the application of the model it is not appropriate to just apply the Z_{ref} value if $Z_{2.5}|Z_{1.0}$ is unknown; the uncertainty of the predicted value should be considered. There are two ways to do this: (1) the uncertainty in $Z_{2.5}|Z_{1.0}$ can be modeled with a logic tree with a central branch corresponding to $Z_{ref}(V_{S30})$ and an upper/lower branch that takes into account the scatter seen in Figure 4.4; or (2) larger aleatory variability can be used together with the default value $Z_{ref}(V_{S30})$. Chapter 5 describes how the basin-depth model decreases the value of the aleatory within-event variability ϕ. For method (2), one would use the larger value of ϕ.

4.1.8 Prior Distributions of Regression Coefficients

It would have been ideal to incorporate information from prior subduction GMMs (e.g., the mean and standard errors of their regression coefficients) to set the prior distributions for the regression

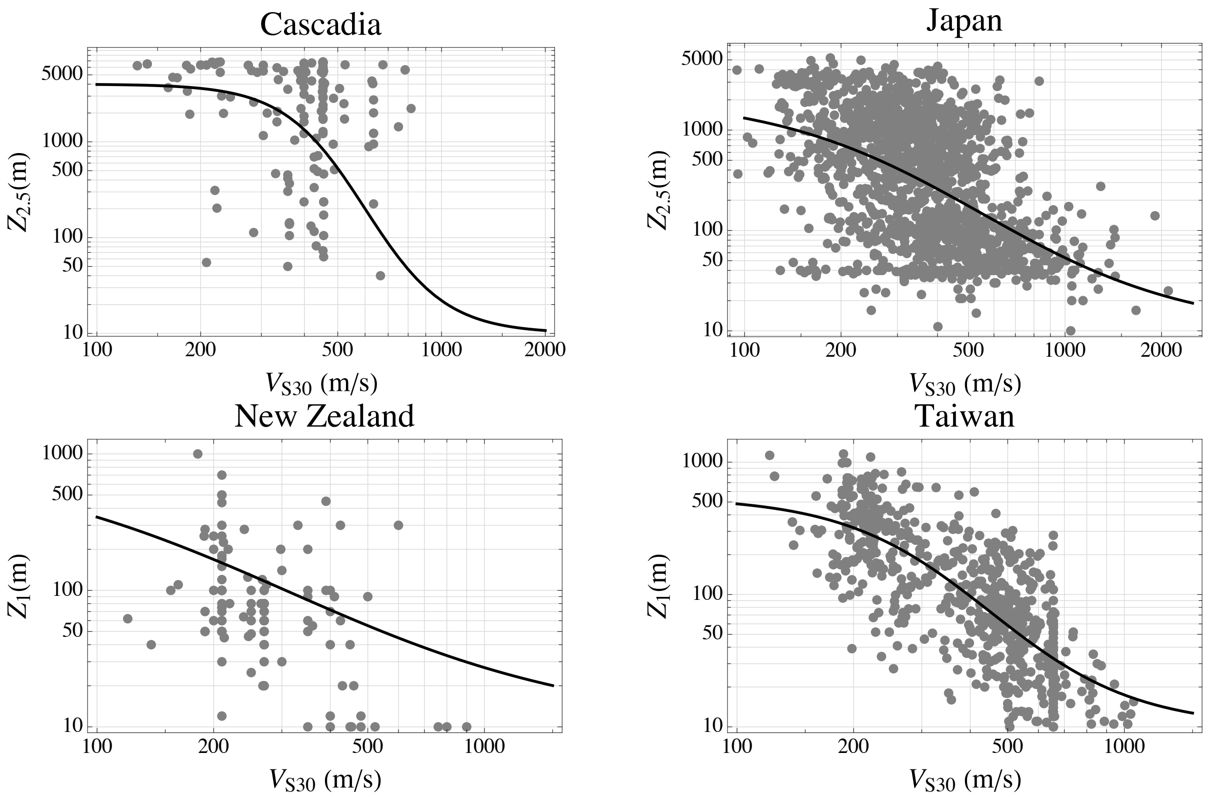

Figure 4.4: Scaling of $Z_{2.5}$ (for Cascadia and Japan) and $Z_{1.0}$ (for New Zealand and Taiwan) with V_{S30}, together with fitted models.

coefficients presented here; however, because most GMMs do not report the full distributions of their coefficients, this information is not available. Furthermore, there is probably an overlap between the dataset used to develop KBCG20 and those used in previous subduction GMMs, running the risk of double-counting much of the data. As a result, prior distributions for the regression coefficients were set as a mix of weakly informative and more strongly informative prior distributions, with the stronger informative prior based on physical considerations and physics-based simulation models. For those regression coefficients that were not well constrained by data, it is important to set informative prior distributions for the results to be meaningful. For example, this is especially true for the large-magnitude MSR coefficient θ_5, which is derived from only a few earthquakes in the dataset. After research and preliminary regressions, the prior distributions for the regression coefficients defined in the previous sections were set as follows:

$$
\begin{aligned}
\mu_{\theta 1,if} &\sim N(0,10)\\
\mu_{\theta 1,slab} &\sim N(0,10)\\
\theta_{2,if} &\sim N(0,5)\\
\theta_{2,slab} &\sim N(0,1)\\
\theta_3 &\sim N(0.1,0.05)\\
\theta_{4,if} &\sim N(1,0.5)\ T(0,)\\
\theta_{4,slab} &\sim N(1,0.5)\ T(0,)\\
\theta_5 &\sim N(0,0.2)\ T(0,\theta_{4,if})\\
\mu_{\theta 6,A} &\sim N(0,0.01)\ T(,0)\\
\mu_{\theta 6,B} &\sim N(0,0.01)\ T(,0)\\
\mu_{\theta 7} &\sim N(CB14,0.5)\\
\theta_{9,if} &\sim N(0,0.1)\\
\theta_{9,slab} &\sim N(0,0.1)\\
\theta_{6,xc} &\sim N(0,1)\\
\theta_{nft,1} &\sim N(0.875,0.02)\\
\theta_{nft,2} &\sim N(0.201,0.005)\\
\delta Z_{B,if} &\sim N(0,10)\\
\delta Z_{B,slab} &\sim N(0,10)
\end{aligned}
$$

where $T(a, b)$ means that the prior normal distribution is truncated with a lower bound of a and an upper bound of b. If one bound is empty, it is unconstrained. The coefficients $\mu_{\theta x}$ are the global mean coefficients for the regionalized coefficients; see Table 4.2 and Section 4.2.

The prior distribution for μ_{theta7} (the global mean of the linear site amplification coefficient) is centered on the values from Campbell and Bozorgnia (2014)'s model. Thus, it is assumed that the linear site scaling is similar for shallow crustal and subduction regions.

The prior distribution for the large-magnitude MSR coefficient θ_5 is based on the simulation-based models of Gregor et al. (2002) and Atkinson and Morrison (2009). The effective MSRs of these two models at large magnitudes is shown in Figure 4.5. For comparison, we also plot the slope estimated by Ghofrani and Atkinson (2014) for empirical data from large-magnitude events in Japan; note that at long periods, the slope coefficient for their model is not statistically significant. To enforce magnitude saturation but not allow oversaturation to occur at short distances, we constrain θ_5 to be positive and smaller than $\theta_{4,if}$, for the small-magnitude MSR coefficients of interface events, . The standard deviation of the prior distribution is set to 0.2, corresponding to the range of MSRs across different periods.

We use the same prior distribution for the two small-magnitude MSR coefficients $\theta_{4,if}$ and $\theta_{4,slab}$, although the regression leads to different values for these two coefficients, as discussed previously. The prior distributions are taken from the physics-based simulations for slab events per Ji and Archuleta (2018). We performed a simple regression on the simulation data and found the

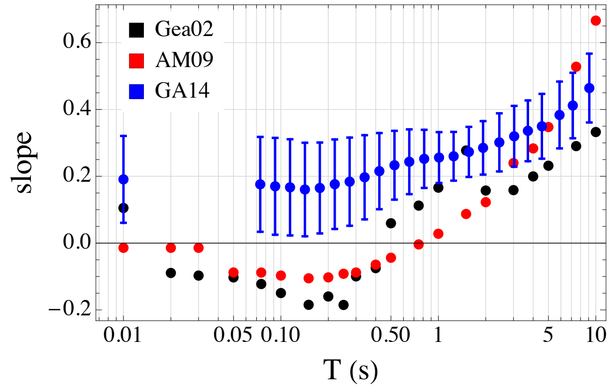

Figure 4.5: Large-magnitude MSRs for the GMMs of Gregor et al. (2002) (Gea02), Atkinson and Macias (2009) (AM09), and Ghofrani and Atkinson (2014) (GA14).

estimated MSR to be similar to unity across all periods. Since the simulated data range is rather limited, we used the regression results as guidance to impart a wider standard deviation on the prior distribution coming from the regression. The GMMs of Gregor et al. (2002) and Atkinson and Macias (2009) are valid for $\mathbf{M} > 7.5$, so they cannot be used to determine the MSRs at small magnitudes.

4.2 REGIONAL ADJUSTMENTS

We observed strong regional differences in ground-motion scaling for some of the scaling terms in the GMM. As discussed previously, regional differences can be geographic (i.e., different for different subduction zones) or subregional (i.e., different for subregions within a geographic region). We found strong regional differences in anelastic attenuation, presumably related to differences in Q, and in the linear site amplification (i.e., V_{S30} scaling) and basin-depth terms, the latter two presumably related to regional differences in shear-wave velocity profiles. We also found regional differences in the overall level of ground-motion amplitudes modeled by allowing regional differences in the constants in the GMM. Regional differences were incorporated in the model as partially nonergodic adjustments. Partially nonergodic models are an improvement from fully ergodic global models because they are one step closer to becoming source and site specific—the "holy grail" of ground-motion modeling.

We model regional adjustments to the global regression coefficients using the hierarchical/multilevel approach of Gelman and Hill (2006). In this approach, we define a global level, a regional level, and an event and record level and regression coefficients are different for each level, albeit connected via higher levels. This hierarchical/multilevel approach is the same as a regional random-effects model, where the global coefficients are the fixed effects and the regional adjustments are the random effects, each having a global mean and standard deviation.

The regionalized regression coefficients adopted for our GMM are the constants $\theta_{1,if}$ and $\theta_{1,slab}$, the linear site amplification coefficient θ_7, and the anelastic attenuation coefficients $\theta_{6,1}$, $\theta_{6,2}$, $\theta_{6,3}$, $\theta_{6,x1}$, $\theta_{6,x2}$, and $\theta_{6,x3}$. For each geographic region and subregion, the regional coefficient

Table 4.2: Description of Regional Model Coefficients

Coefficient	Description	Regions	Global parameters
$\theta_{1,if}$	Interface constant	All	$\mu_{\theta 1,if}, \psi_{\theta 1,if}$
$\theta_{1,slab}$	Intraslab constant	All	$\mu_{\theta 1,slab}, \psi_{\theta 1,slab}$
$\theta_{6,x1}$	Anelastic attenuation, arc-crossing subregion relative to arc 1	CAM, JP, SA	$\mu_{\theta 6,A}, \psi_{\theta 6,A}$
$\theta_{6,x2}$	Anelastic attenuation, arc-crossing subregion relative to arc 2	CAM, JP, SA	$\mu_{\theta 6,A}, \psi_{\theta 6,A}$
$\theta_{6,x3}$	Anelastic attenuation, arc-crossing subregion relative to arc 3	JP	$\mu_{\theta 6,A}, \psi_{\theta 6,A}$
$\theta_{6,1}$	anelastic attenuation, non arc-crossing subregion relative to arc 1	CAM, JP, SA	$\mu_{\theta 6,A}, \psi_{\theta 6,A}$
$\theta_{6,2}$	Anelastic attenuation, non arc-crossing subregion relative to arc 2	All	$\mu_{\theta 6,B}, \psi_{\theta 6.B}$
$\theta_{6,3}$	Anelastic attenuation, non arc-crossing subregion relative to arc 3	JP	$\mu_{\theta 6,A}, \psi_{\theta 6,A}$
θ_7	Linear site amplification (V_{S30} scaling)	All	$\mu_{\theta 6}, \psi_{\theta 7}$
θ_{11}	Constant of basin depth scaling	CASC, JP, NZ, TW	–
θ_{12}	Slope of basin depth scaling	CASC, JP, NZ, TW	–

are calculated by the functions

$$\begin{aligned}
\theta_{1,if}(reg) &= \mu_{\theta 1,if} + \delta\theta_{1,if}(reg) \\
\theta_{1,slab}(reg) &= \mu_{\theta 1,slab} + \delta\theta_{1,slab}(reg) \\
\theta_7(reg) &= \mu_{\theta 7} + \delta\theta_7(reg) \\
\theta_{6,x1}(reg) &= \mu_{\theta 6,A} + \delta\theta_{6,x1}(reg) \\
\theta_{6,x2}(reg) &= \mu_{\theta 6,A} + \delta\theta_{6,x2}(reg) \\
\theta_{6,x3}(reg) &= \mu_{\theta 6,A} + \delta\theta_{6,x3}(reg) \\
\theta_{6,1}(reg) &= \mu_{\theta 6,A} + \delta\theta_{6,1}(reg) \\
\theta_{6,2}(reg) &= \mu_{\theta 6,B} + \delta\theta_{6,2}(reg) \\
\theta_{6,3}(reg) &= \mu_{\theta 6,B} + \delta\theta_{6,3}(reg)
\end{aligned} \tag{4.12}$$

where μ_θ is the global value of the regression coefficient before regionalization, and $\delta\theta$ is the regional adjustment coefficient.

We model the distribution of the adjustment coefficients according to the multivariate normal distribution

$$\overrightarrow{\delta R} \sim MVN(0, \Sigma_R) \tag{4.13}$$

where $\overrightarrow{\delta R} = \{\delta\theta_{1,if}, \delta\theta_{1,slab}, \delta\theta_7, \delta\theta_{6,1}, \delta\theta_{6,2}, \delta\theta_{6,3}, \delta\theta_{6,x1}, \delta\theta_{6,x2}, \delta\theta_{6,x3}\}$ is the vector of regional adjustment coefficients with covariance matrix Σ_R. The entries of the covariance matrix are

$\Sigma_{R,ij} = \rho_{ij}\psi_i\psi_j$, where ρ_{ij} is the correlation coefficient between the different regional coefficients i and j, ψ_i is the standard deviation of the ith regional coefficient and ψ_j is the standard deviation of the jth regional coefficient. The values of ψ_i and ψ_j describe the range the regression coefficient θ_i, and θ_j can range across different geographic regions and subregions.

The list of regional coefficients, and which regions they apply to is given in Table 4.2. In addition to the aforementioned coefficients, the coefficients for the basin depth scaling are also regional (cf. Section 4.1.7). However, the basin-depth coefficients are not modeled as random effects (and hence have no associated global mean and standard deviation), because due to missing data they are only estimated on a subset of the within-event residuals. Furthermore, they are estimated for only two regions (CASC, JP) for $Z_{2.5}$ and two regions (NZ, TW) for $Z_{1.0}$, which does not allow to reliably estimate a multilevel structure.

To calculate the median predicted value of ground motion for a geographic region or subregion, one needs to replace the global regression coefficients $\mu_{\theta 1,if}, \mu_{\theta 1,slab}, \mu_{\theta 7}, \ldots, \mu_{\theta 6,B}$ with their appropriate regional values. The global coefficients should be used if one wants to exclude regional adjustments for a modeled geographic region or subregion or wants to apply the GMM to a subduction zone that is not included in the geographic regionalization. For a new region, the values of the regional adjustment coefficients are not known; therefore, additional epistemic uncertainty needs to be taken into account. The uncertainty for each regional coefficient is described by its regional standard deviation ψ. Chapter 6 describs how the total epistemic uncertainty associated with median predictions can be can be calculated for a new region.

For each region, there are 6 regression coefficients to model subregional anelastic attenuation: $\theta_{6,x1}$, $\theta_{6,x2}$, $\theta_{6,x3}$, $\theta_{6,1}$, $\theta_{6,2}$, and $\theta_{6,3}$. For AK, CASC, NZ, and TW, only coefficient $\theta_{6,2}$ is relevant for the median predictions, while for CAM, JP and SA all six coefficients are relevant. Hence, there are seven regional coefficients $\delta\theta_{6,2}$ to constrain corresponding global regression parameters ($\mu_{\theta 6,B}$ and $\psi_{\theta 6,B}$), similar to the constants for the linear site amplification terms. For the other anelastic attenuation coefficients, there are only three regions to constrain the global coefficients, with very limited data in the case of CAM and SA. Hence, we set the global coefficients for $\theta_{6,x1}$, $\theta_{6,x2}$, $\theta_{6,x3}$, $\theta_{6,1}$, and $\theta_{6,3}$ to be the same.

Equation 4.13 connects the regional adjustment coefficients from different geographic regions and subregions through their global hyperparameters (mean and covariance). Thus, data from one region can have an indirect effect on the coefficients of another region. The formulation of regionalization with a random-effects model also has the effect that regions with sparse data need a strong regional signal in the data to move their coefficients far from the global mean.

We statistically tested the effect of regionalizing most of the regression coefficients. The results are shown in Figure 4.6. The regionalized coefficients that were tested are $\theta_{1,if}$, $\theta_{1,slab}$, $\theta_{2,if}$, $\theta_{2,slab}$, $\theta_{4,if}$, $\theta_{4,slab}$, $\theta_{6,x1}$, $\theta_{6,x2}$, $\theta_{6,x3}$, $\theta_{6,1}$, $\theta_{6,2}$, $\theta_{6,3}$, θ_7, $\theta_{9,if}$, and $\theta_{9,slab}$. We also tested the effect of using different prior distributions on the values of the standard deviations by using either an exponential distribution or a Half-Cauchy probability density function (PDF) as a prior on the regionalized standard deviations. The distributions are scaled differently for each coefficient, but their parameters are calculated so that they have the same mean value.

Figure 4.6 shows that the standard deviations for the coefficients of the MSR and DSR coefficients have their mode at zero, meaning that there is no evidence in the data for regional effects for these coefficients. For the coefficients of the geometrical attenuation term, the highest posterior density does not include zero, which indicates that there is possible regional variation in geometrical attenuation. However, we do not allow regional variability in geometrical spreading because physically the geometrical spreading of a point source should not change between regions. Furthermore, we do not think that possible differences in finite-fault effects can be resolved based on the limited data we have with small distances.

Figure 4.6 also shows that the values of the regional standard deviations are larger when a Half-Cauchy PDF is used as the prior distribution as compared to an exponential distribution; because the Half-Cauchy PDF has wider tails than the exponential distribution, it allows larger values. This has the effect of leading to larger regional deviations from the global mean parameters. Since there is only a small number of regions that this applies to, we decided that it is better to place a stronger prior on the values of the regional coefficient standard deviation and only allow for regional deviations if there is strong evidence in the data. Therefore, we decided to use an exponential distribution as the prior for the regionalized standard deviations. We explain how the parameters for the exponential distributions are set in Section 4.2.2.

4.2.1 Regional Adjustments for Cascadia

Observed short-period ground-motion amplitudes for CASC intraslab earthquakes are low compared to the global mean and to the other geographic regions. This has also been observed by Atkinson (1997), Atkinson and Boore (2003), and Abrahamson et al. (2016, 2018). On the other hand, the two largest events in the CASC region closer to the global mean exhibit larger event terms compared to the smaller CASC events. This makes estimating a separate regional constant term for CASC problematic.

Because of the relatively small magnitudes and small number of events that exhibit low amplitudes, we decided to use only the two largest events from CASC to estimate a CASC-specific constant term. We also calculated a separate regional constant for the smaller CASC events to center their event terms. Centering allows these small-magnitude earthquakes to be used to estimate CASC-specific anelastic attenuation, linear site amplification, and basin-amplification terms that are assumed to be event-independent. The small-magnitude constant is not used in the multilevel structure; therefore, it does not affect the between-event standard deviation nor the correlation with other regional regression parameters. In other words, it does not affect the co-variance matrix Σ_R in Equation (4.13).

For CASC, basin margins for the Seattle, Tacoma, and Everett basins are available in digital form (Ahdi et al., 2020); therefore, we know which stations are located in a basin. Figure 4.7 shows the $Z_{2.5}$ values for CASC against V_{S30}, which is color-coded to identify the different basins. We took this information into account to derive the basin-depth term for CASC.

As seen in Figure 4.7, there is no correlation between V_{S30} and $Z_{2.5}$ for the Seattle basin over a wide range of V_{S30} values. Hence, for the Seattle basin, we estimated a constant amplification, which is calculated as the mean of the within-event residuals for stations within the Seattle basin. For the other basins, we estimated the dependence of basin amplification on $\delta \ln Z_{2.5}$ as described in Section 4.1.7 since they do not have enough stations to reliably estimate a separate

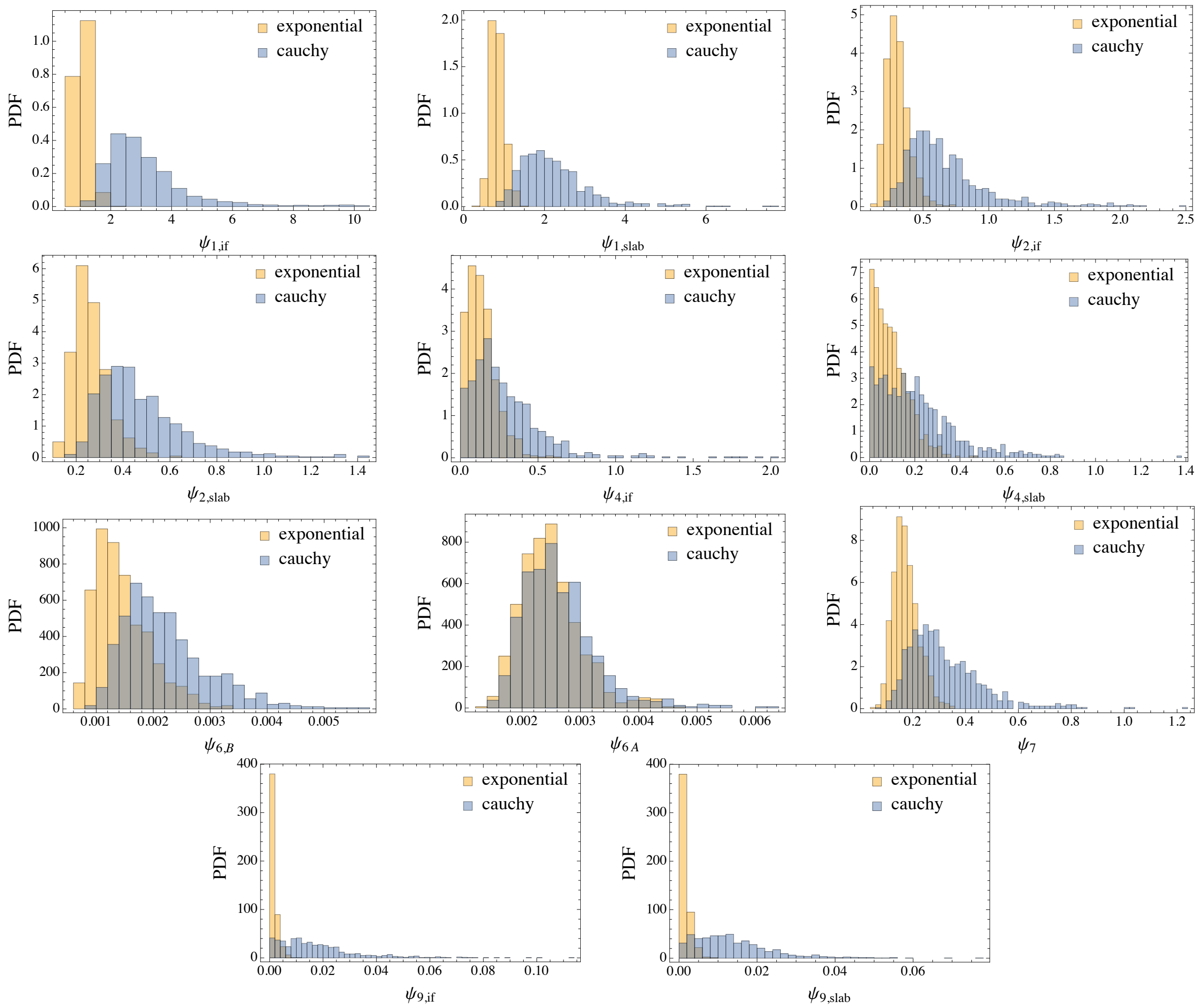

Figure 4.6: Posterior distributions of the regional standard deviations for those coefficients that were regionalized in the regression. Results for two different prior distributions are shown, an exponential distribution and a Half-Cauchy PDF.

basin-amplification term. Since the other basins are not as deep as the Seattle basin, we limited the amplification to be smaller than that for the Seattle basin. Therefore, the model for basin amplification for CASC is given by the function

$$f_{basin}(Z) = \begin{cases} \theta_{11,SEA} & \text{site in Seattle basin} \\ \min(\theta_{11} + \theta_{12}\delta_{\ln Z_{2.5}}, \theta_{11,SEA}) & \text{site in other basins} \\ 0 & \text{site outside of basin} \end{cases} \tag{4.14}$$

4.2.2 Prior Distributions

The use of Bayesian regression analysis required that we set parameters for the prior distributions of the components of the multivariate normal distribution (mean and co-variance matrix) given by

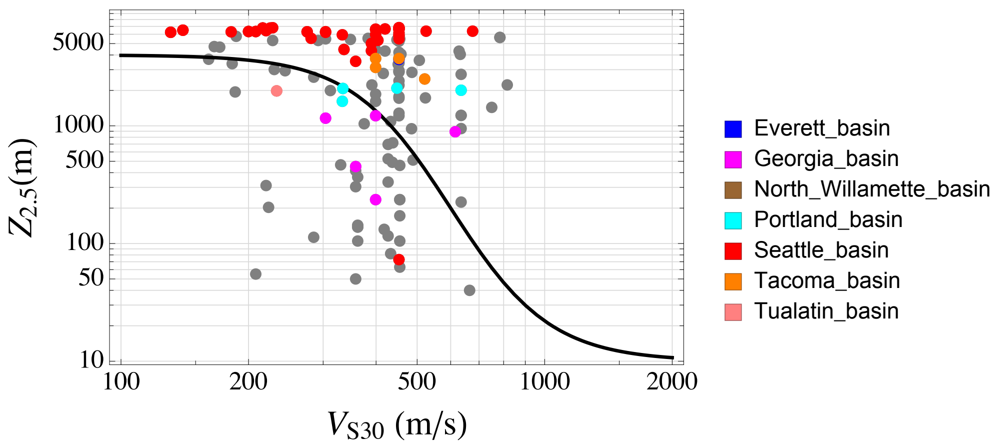

Figure 4.7: $Z_{2.5}$ vs. V_{S30} for Cascadia, with different basin highlighted. Non-basin sites are shown in gray.

Equation (4.13). The co-variance matrix can be decomposed into standard deviations and correlations using the function

$$\Sigma_R = \text{diag\_matrix}(\vec{\psi}_R)\ C\ \text{diag\_matrix}(\vec{\psi}_R) \tag{4.15}$$

where $\vec{\psi}_R = \{\psi_{1,if}, \psi_{1,slab}, \psi_7, \psi_{6,A}, \psi_{6,A}, \psi_{6,A}, \psi_{6,A}, \psi_{6,B}, \psi_{6,A}\}$ are the standard deviations of the regional adjustment coefficients [cf. Equation 4.12 and Table 4.2]. Recall that we model the anelastic attenuation coefficients with only two standard deviations, one for $\theta_{6,2}$ and one for the other coefficients.

The matrix $C_{ij} = \frac{\Sigma_{R,ij}}{\psi_i \psi_j}$ is the correlation matrix that describes the correlation between the different regional adjustments; the term diag_matrix($\vec{\psi}_R$) describes a diagonal matrix whose diagonal elements are the elements of $\vec{\psi}_R$. This formulation allows one to decouple the standard deviations and correlations of the regional adjustment coefficients and place separate prior distributions on each of them. For the correlation matrix C, we use an LKJ prior distribution (Lewandowski et al., 2009) with a parameter value of 2.

For the standard deviations, we used a Half-Cauchy PDF as a prior distribution per Gelman (2006). The Half-Cauchy PDF places a lot of mass at large values, which can lead to large values of the standard deviation and, in turn, large regional effects; see Figure 4.6. This is particularly important in our case since the number of regions is quite small from a statistical point of view. Thus, as discussed previously, we use an exponential distribution as the prior for the regional standard deviations ψ_R, which places a lot of mass at zero, allowing for deviations from the global model *only* if the signal in the data is relatively strong. This distribution is given by the equation

$$\psi_i \sim \mathcal{E}(\lambda_i) \tag{4.16}$$

where i is the index representing the region. The parameters λ for the exponential distribution were set in a way to discourage large values of the standard deviation ψ. This was done by assigning a low probability that ψ can be larger than what we believe should be the maximum regional adjustment effect. The maximum regional effect was estimated from the regional coefficients of the

NGA-West2 GMMs (Abrahamson et al., 2014; Boore et al., 2014; Campbell and Bozorgnia, 2014; Chiou and Youngs, 2014), which provide regional anelastic attenuation and/or site-amplification (V_{S30}-scaling) coefficients for Japan, California, Taiwan, China, Turkey, and Italy.

Once the maximum effects for these regions were calculated, we were able to estimate the parameter λ of the exponential distribution according to the equation

$$1 - \text{CDF}[\mathcal{E}(\lambda)](\text{maxeffect}) = 0.05 \tag{4.17}$$

This approach makes the implicit assumption that the range of regional adjustments is similar between crustal and subduction events; in the absence of other prior information, we believe is a reasonable approach. After estimating the parameters of the exponential distributions, we fit simple piece-wise linear functions to them so that their function with period varies smoothly. Not all of the NGA-West2 GMMs have a regionally varying constant term, so we assume a possible maximum effect for the regional constant at short periods of 0.3, which decreases at long periods to 0.05.

The maximum regional effects from the NGA-West2 GMMs and inferred λ values are shown in Figures 4.8, 4.9, and 4.10 for the constant terms, linear site-amplification coefficients, and anelastic attenuation coefficients, respectively. Lacking any specific information to the contrary, we assume the same prior distribution for the standard deviations of these terms apply to both interface and intraslab events.

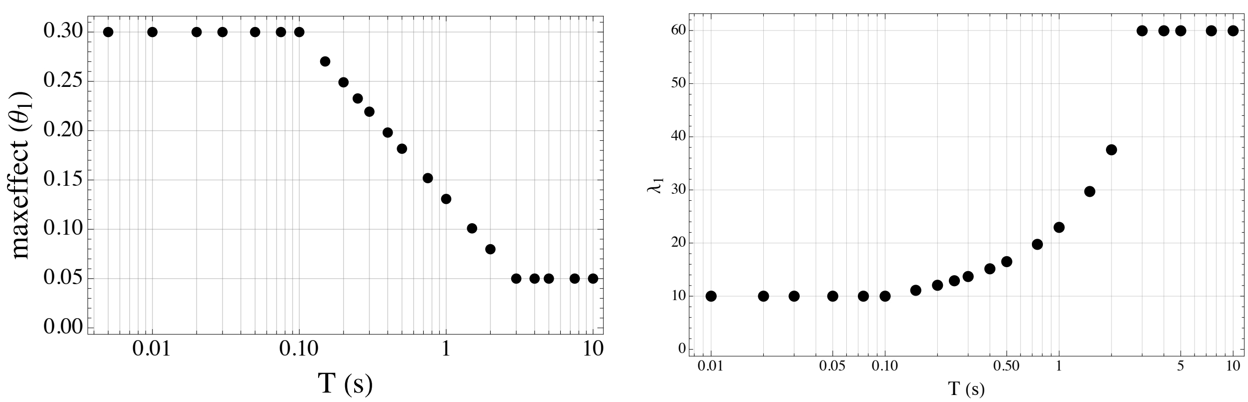

Figure 4.8: Regional prior on the standard deviations of the constant terms θ_1: (left) maximum effect; (right) parameter of the exponential distribution.

In the actual implementation of the maximum regional effects in Stan, the LKJ prior was placed on the Cholesky decomposition matrix L of the correlation matrix C. Then, the vector of regional adjustment coefficients $\delta\vec{R}$ [Equation (4.13)] was calculated from the equation

$$\delta\vec{R} = (\text{diag\_matrix}(\vec{\psi}_R)\ L)\vec{z} \tag{4.18}$$

where $\vec{z} = \{z_{1,if}, z_{1,slab}, \ldots, z_{6,3}\}$ is a vector of independent random variables, each of which has prior distribution, and is a standard normal distribution with mean 0 and standard deviation 1. This implementation is more efficient than a direct implementation of the multivariate normal distribution and its co-variance matrix.

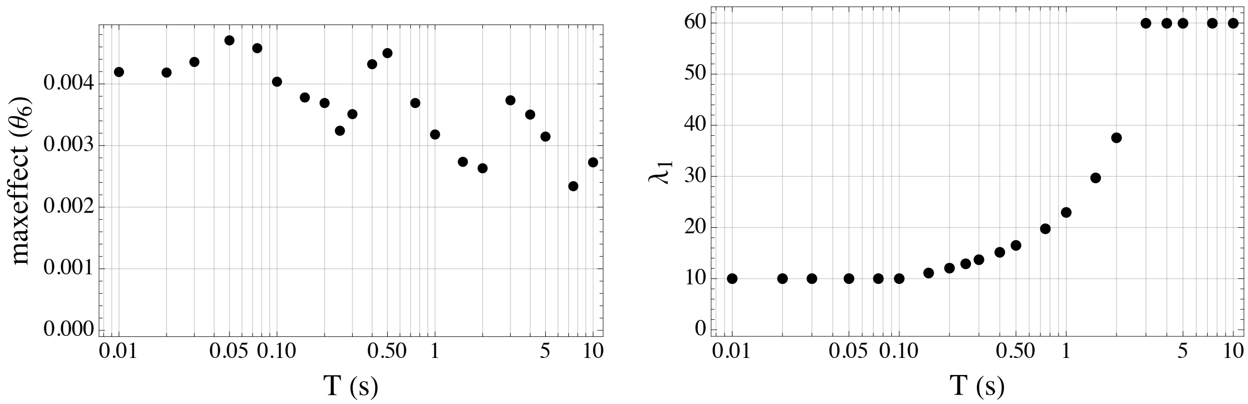

Figure 4.9: Regional prior on the standard deviations of the anelastic attenuation coefficients θ_6: (left) maximum effect; (right) parameter of the exponential distribution.

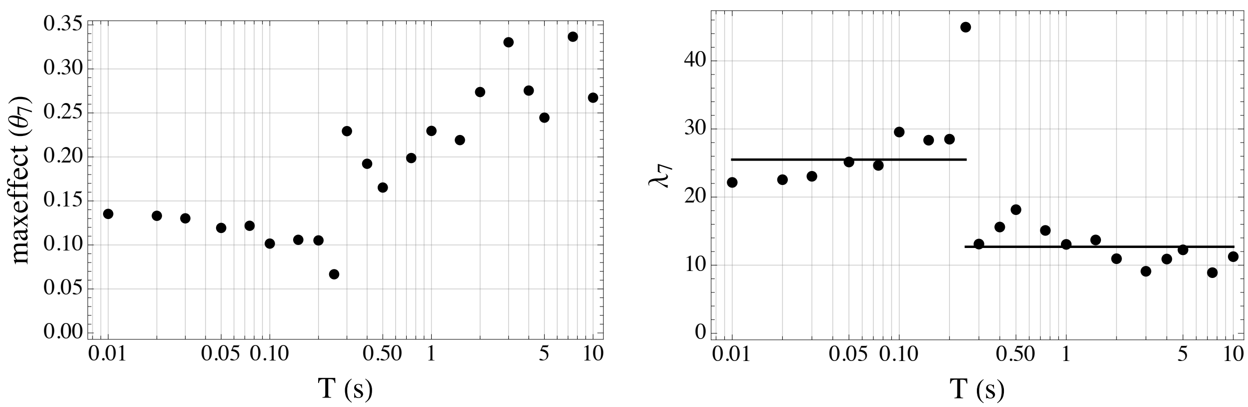

Figure 4.10: Regional prior on the standard deviations of the linear site-amplification coefficients θ_7: (left) maximum effect; (right) parameter of the exponential distribution.

The parameters for the anelastic attenuation coefficients, $z_{6,x1}, \ldots, z_{6,3}$, were constrained by the function

$$z_{6,x1} < \frac{-\mu_{\theta 6,B}}{\psi_{6,B}} \tag{4.19}$$

This ensures that the final attenuation coefficient, $\theta_{6,x1} = \mu_{\theta 6b} + z_6 \psi_{6b}$, is negative. The other attenuation coefficients are constrained in the same way, with the appropriate means and standard deviations ($\mu_{\theta 6,B}, \psi_{\theta 6,B}$ for $z_{6,2}$, and $\mu_{\theta 6,A}, \psi_{6,B}$ for the other attenuation coefficients).

4.3 REGRESSION COEFFICIENTS

4.3.1 Smoothing

To ensure a smooth predicted response spectrum, the coefficients of the model are slightly smoothed. We smoothed the mean coefficients (the mean of the 800 posterior samples for each coefficient) using a Gaussian process (GP) regression (Rasmussen and Williams, 2006). This model assumes that the coefficients should be a smooth function of $x = \ln T$ (logarithmic period); the (mean) coefficients estimated by regression are noisy observations of this function. Since the exact functional form is unknown, we place a GP prior on it; in Bayesian non-parametrics (Hjort et al., 2010), a GP is a prior over functions. Thus, the model becomes

$$\theta = f(x) + \epsilon \tag{4.20}$$

$$\epsilon \sim N(0, \sigma) \tag{4.21}$$

$$f \sim GP(\mu, k(x, x')) \tag{4.22}$$

$$k(x, x') = \eta^2 \exp\left(-\frac{1}{2}\frac{(x - x')^2}{\rho}\right) \tag{4.23}$$

Here, σ describes the variation of the coefficient around the smoothed function, η describes the overall variability of the coefficient $theta$ across periods, and ρ is a length-scale that describes how how close similar points in $\ln T$ should be. We use a squared exponential co-variance function because it leads to very smooth functions. The mean function of the GP, μ, is a constant and is given by the mean of θ across all periods. For details on GP regression, see Rasmussen and Williams (2006).

We smoothed all coefficients $\theta_{1,if}, \ldots, \theta_{9,slab}$ (global and regional values), as well as τ and ϕ. The regional standard deviations ψ were not smoothed since they do not affect the predicted median spectrum. Likewise, the parameters of the correlation matrix for the regional coefficients were not smoothed.

In an initial smoothing run, we estimated η, ρ, and σ for each coefficient. We found that the estimated length-scales ρ vary between 1 and 2. Based on the initial regression, we fixed the length-scales to $\rho = 2$ for all coefficients (and τ and ϕ) except for the linear site-scaling coefficients θ_7 (global value $\mu_{\theta 7}$ and regional θ_7 values).

The smoothing was applied to the mean of the posterior distribution for each coefficient. Thus, we re-centered the posterior distribution of each coefficient by subtracting the mean and adding the smoothed value. Not only does this retain the range of the posterior distribution, but it also retains the correlation between the posterior distributions of different coefficients.

4.3.2 Results

The global regression coefficients are shown as a function of period in Figures 4.11 to 4.16. Shown are the (unsmoothed) mean of the posterior distributions, the smoothed coefficient values, and the 5% and 95% percentiles of the re-centered posterior distributions.

The correlation among the coefficients is shown in Figure 4.17 for PGA ($T = 0$) and $T = 0.2$, 1.0, and 3.0 sec. The correlations are estimated from the samples from the posterior distributions. These correlations are found to be quite stable across periods.

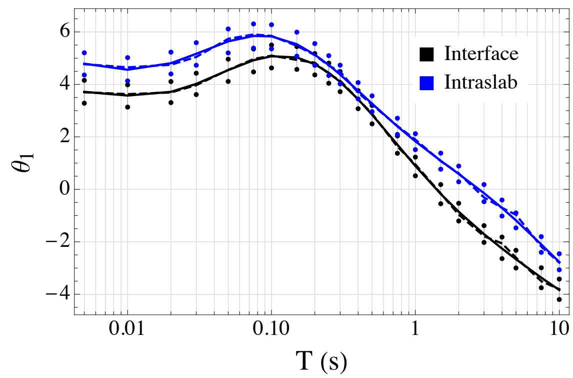

Figure 4.11: Estimated global regression constant coefficient for interface events (black) and intraslab events (blue) as a function of period. Shown are the mean of the posterior distribution (dashed line), the smoothed coefficients (solid line), and the 5% and 95% percentiles of the posterior distribution (vertical lines).

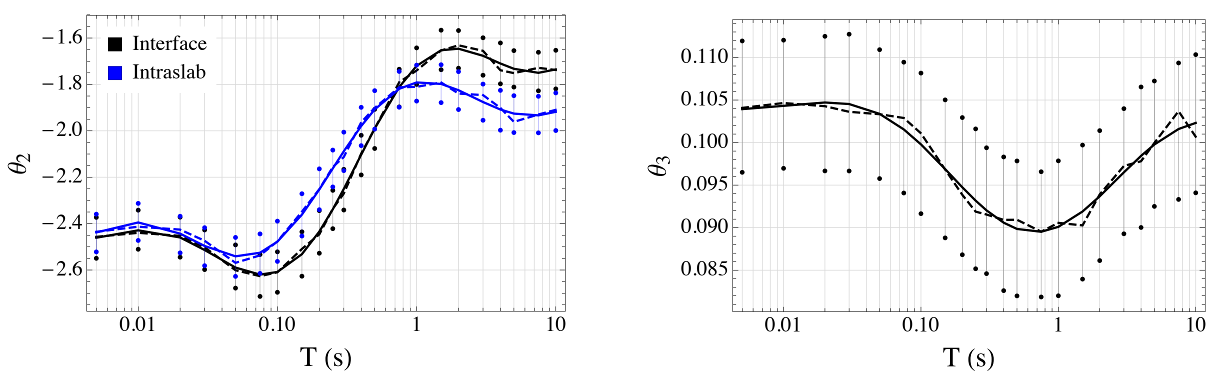

Figure 4.12: Estimated global regression geometrical spreading coefficient for interface events (black) and intraslab events (blue) as a function of period (left), and global regression coefficient modeling the magnitude dependency of the geometrical spreading (right), applicable to both event types. Shown are the mean of the posterior distribution (dashed line), the smoothed coefficients (solid line), and the 5% and 95% percentiles of the posterior distribution (vertical lines).

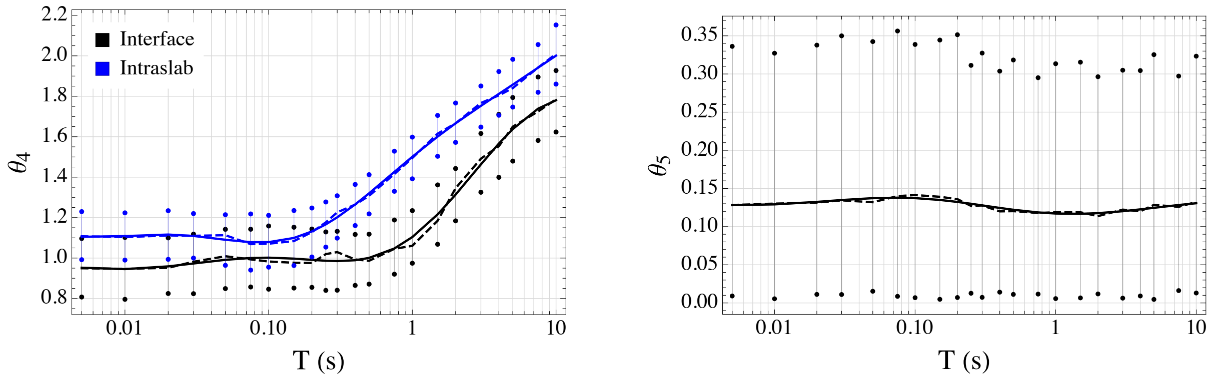

Figure 4.13: Estimated global magnitude scaling regression coefficients for interface events (black) and intraslab events (blue) as a function of period. Left: magnitude slope below the break point; Right: magnitude slope above the break point. Shown are the mean of the posterior distribution (dashed line), the smoothed coefficients (solid line), and the 5% and 95% percentiles of the posterior distribution (vertical lines).

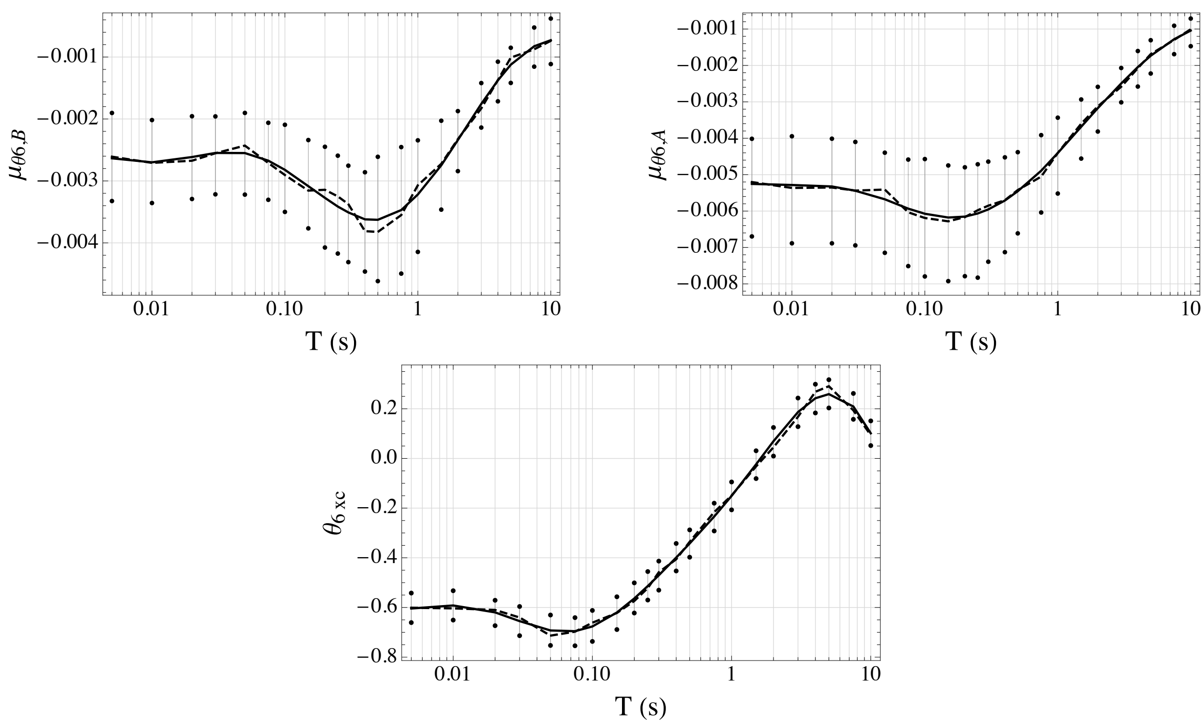

Figure 4.14: Estimated global regression coefficients for the anelastic attenuation model as a function of period. Shown are the mean of the posterior distribution (dashed line), the smoothed coefficients (solid line), and the 5% and 95% percentiles of the posterior distribution (vertical lines).

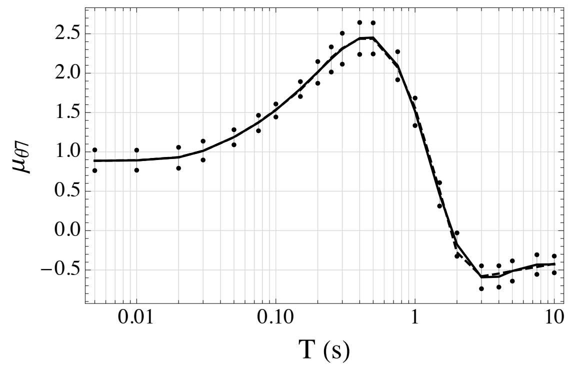

Figure 4.15: Estimated global V_{S30}-scaling regression coefficients as a function of period. Shown are the mean of the posterior distribution (dashed line), the smoothed coefficients (solid line), and the 5% and 95% percentiles of the posterior distribution (vertical lines).

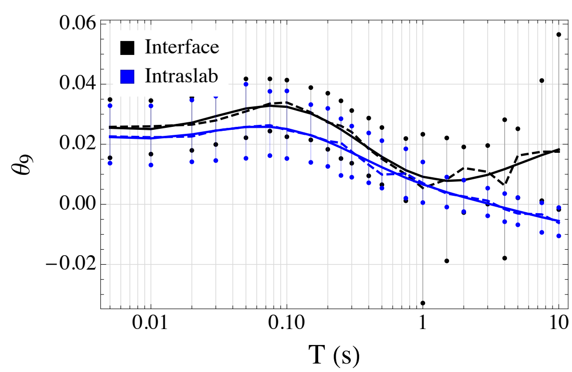

Figure 4.16: Estimated global Z_{TOR}-scaling regression coefficients for interface events (black) and intraslab events (blue) as a function of period. Shown are the mean of the posterior distribution (dashed line), the smoothed coefficients (solid line), and the 5% and 95% percentiles of the posterior distribution (vertical lines).

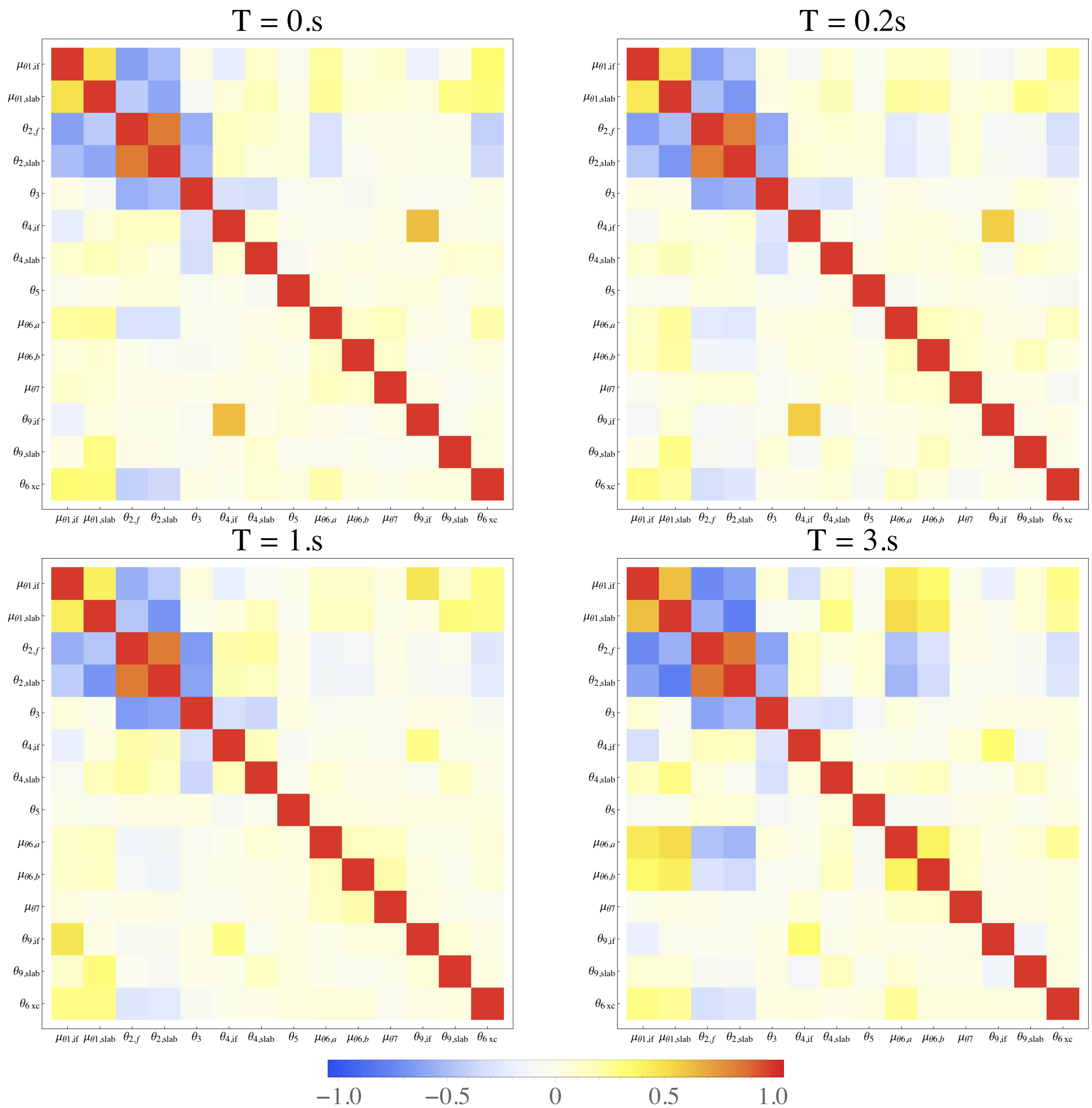

Figure 4.17: Empirical correlations among the global regression coefficients for PGA ($T = 0$) and periods $T = 0.2$, 1.0, and 3.0 sec estimated from samples of their posterior distributions.

4.3.3 Regional Adjustments

The regional regression adjustment coefficients for the interface and intraslab constant, and linear site-amplification terms are shown in Figure 4.18. At short periods, the regional differences can be quite large. The differences at long periods are mainly due to differences in the linear site-amplification (V_{S30}-scaling) terms. The regional regression adjustment coefficients for the anelastic attenuation terms are shown in Figure 4.19. For most of the regions, only $\delta\theta_{6,2}$ is used, in which case the other anelastic adjustment coefficients are close to zero.

The standard deviations ψ of the regional adjustment coefficients are shown in Figure 4.20. Similar to the mean regional adjustment coefficients, their standard deviations are relatively large at short periods and decrease at long periods, with the exception of the linear site-amplification adjustment coefficient. If one wants to apply the model to a new region, its regional adjustment coefficients will not be known. In this case, the regionalized coefficients can be set to their mean global values, and their epistemic uncertainty can be set to to the corresponding values of ψ. We elaborate on this in Chapter 6.

As defined in Equation (4.13), the regional adjustment coefficients are distributed according to a multivariate normal distribution whose covariance matrices are partitioned into matrices of standard deviations and correlation coefficients; see Equation (4.15). The correlation matrices of the regional coefficients are shown in Figure 4.21 for PGA ($T = 0$) and $T = 0.2$, 1.0, and 3.0 sec.

4.3.4 Basin-Depth Coefficients

The coefficients for the basin-depth term (Section 4.1.7) are shown in Figure 4.22. The left part of Figure 4.22 shows the intercept θ_{11}, while the right part shows the slope with $\delta \ln Z$, θ_{12}. For events at short periods, the intercept is not zero in most cases, indicating a small offset in the residuals of stations for which $Z_{2.5}/Z_{1.0}$ is available; however, because this offset is small, it does not strongly affect the median predictions. The basin-depth coefficients are already rather smooth; therefore, we do not think that there is a need to apply a smoothing operator.

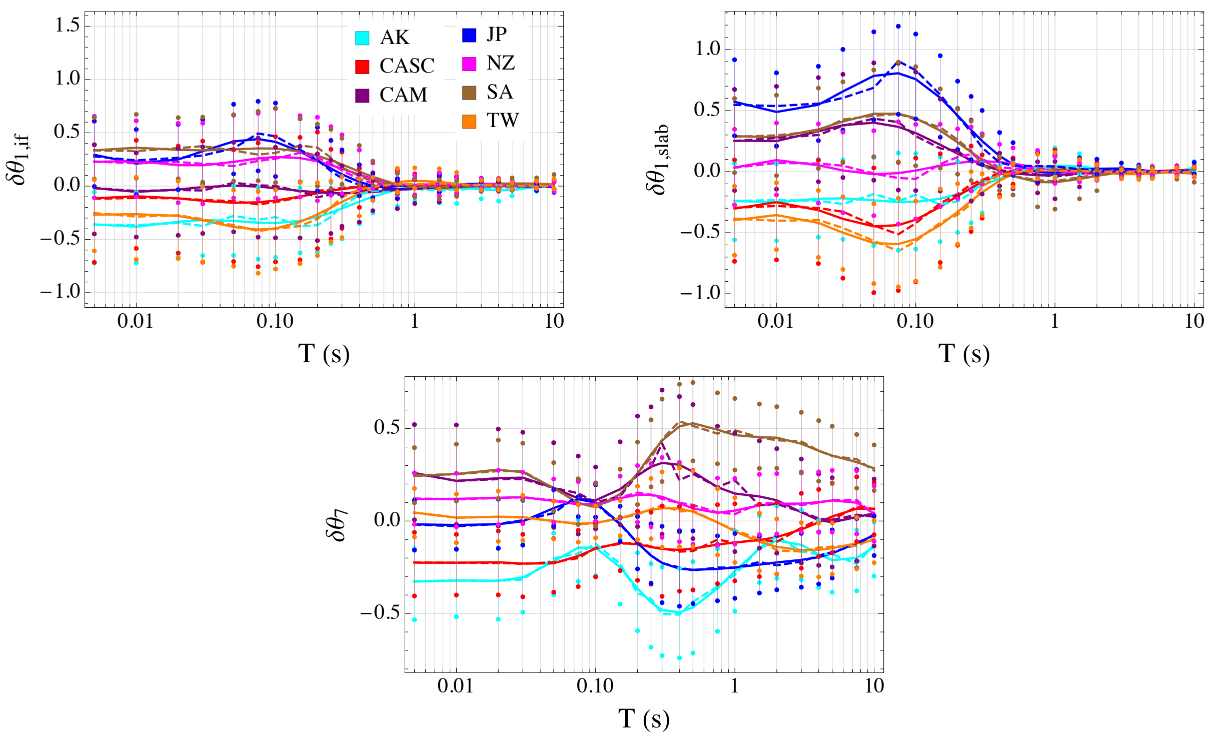

Figure 4.18: Regional regression adjustment coefficients for the interface and intraslab constants, and the linear site-amplification coefficient. Shown are the means of the posterior distributions (solid line), the smoothed coefficients (dashed line), and the 5% and 95% percentiles of the posterior distribution (vertical lines).

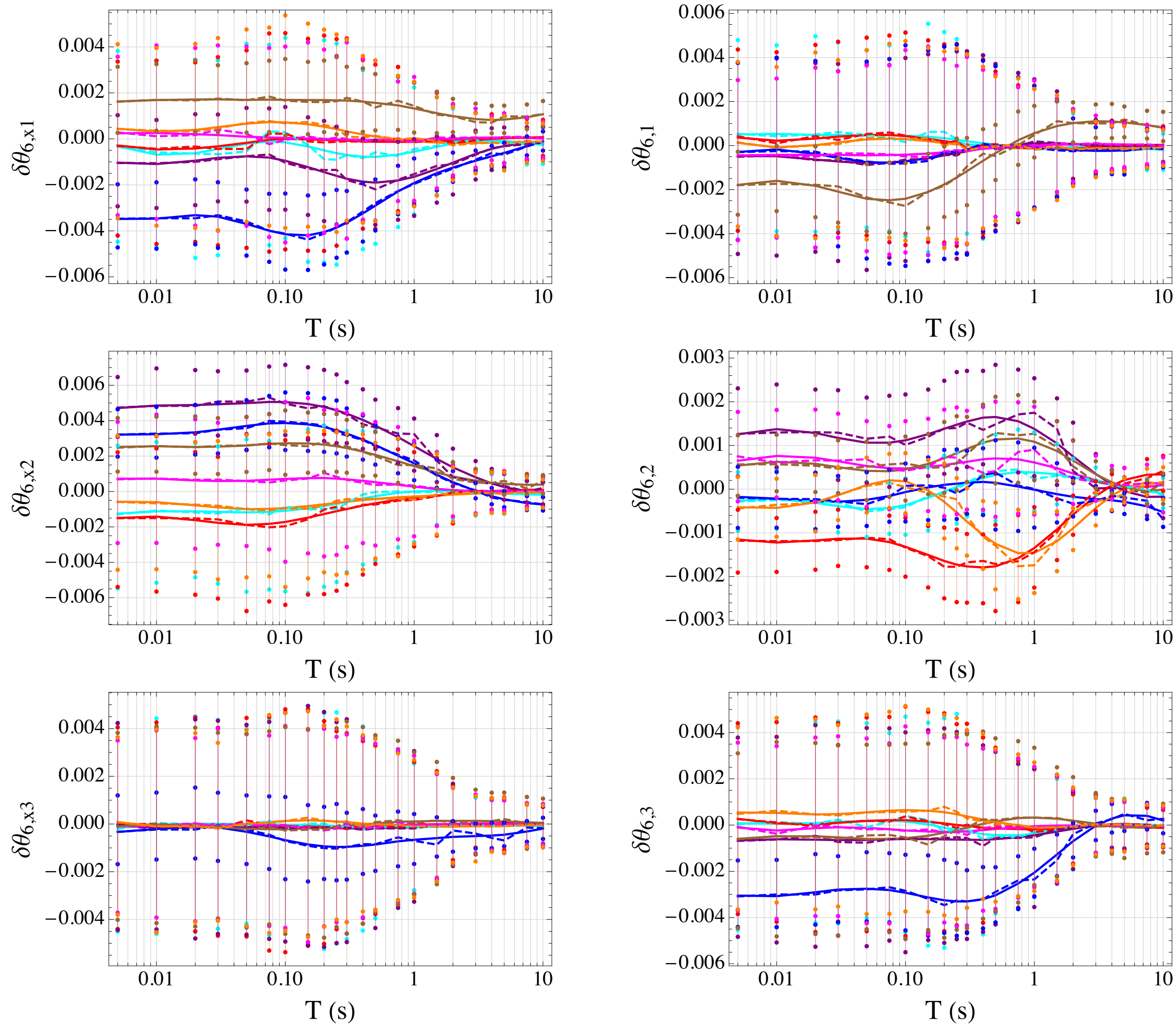

Figure 4.19: Regional regression adjustment coefficients for the anelastic attenuation coefficients. Shown are the means of the posterior distributions (solid line), the smoothed adjustment coefficients (dashed line), and the 5% and 95% percentiles of the posterior distributions.

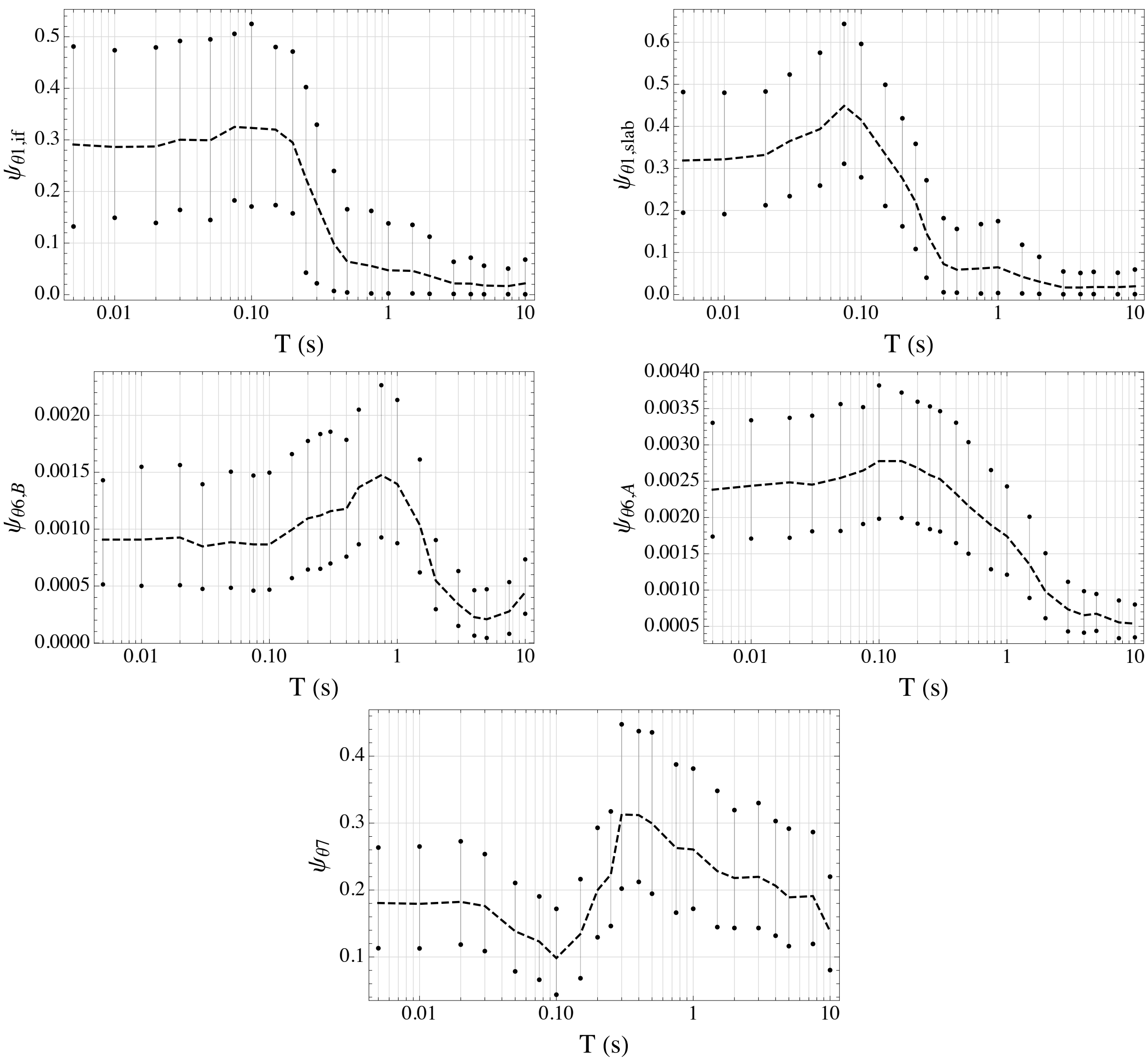

Figure 4.20: Standard deviations ψ of regional adjustment coefficients. Shown are the means of the posterior distributions (dashed line), and the 5% and 95% percentiles of the posterior distributions.

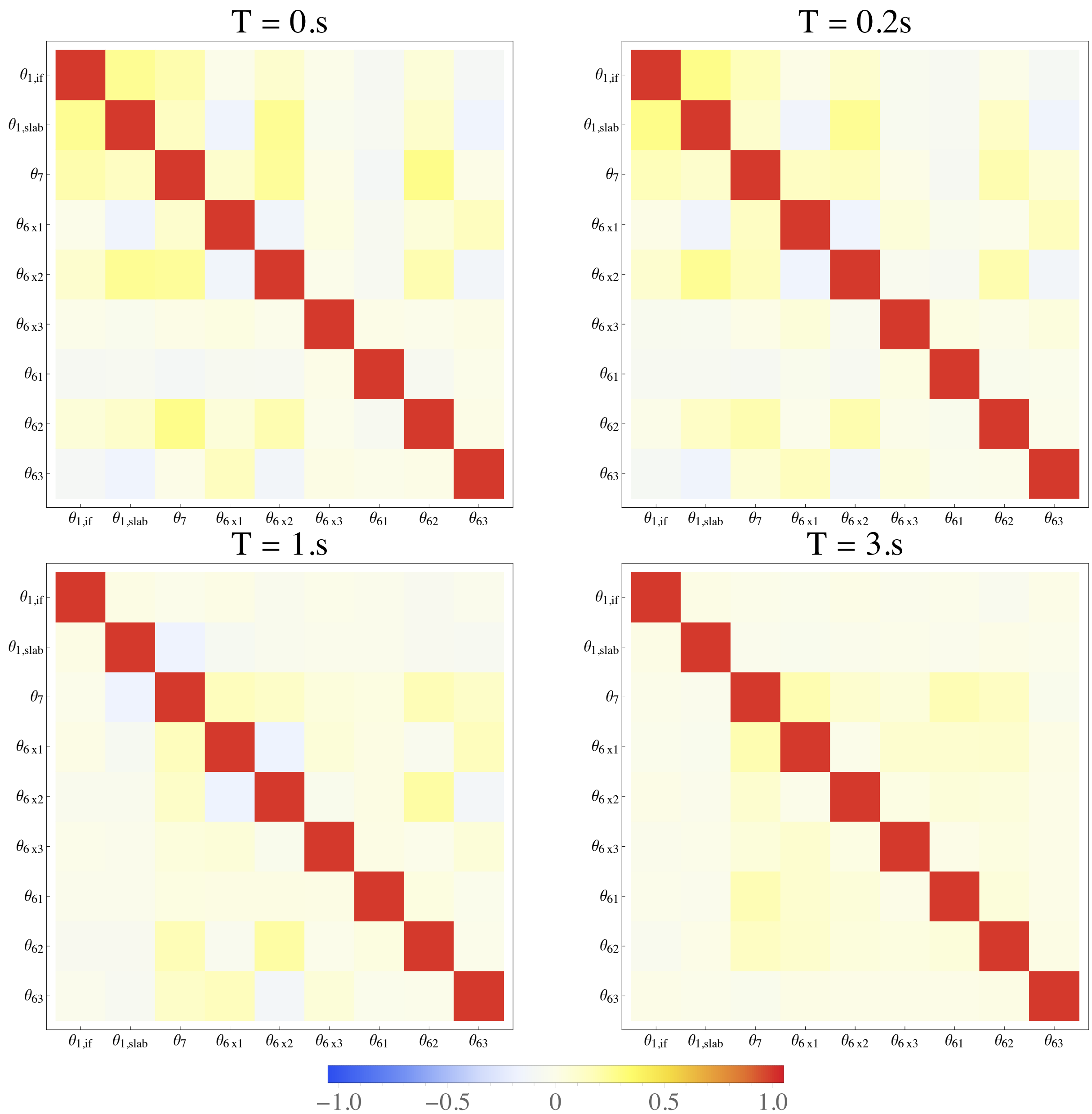

Figure 4.21: Correlation coefficients between the regional adjustment coefficients.

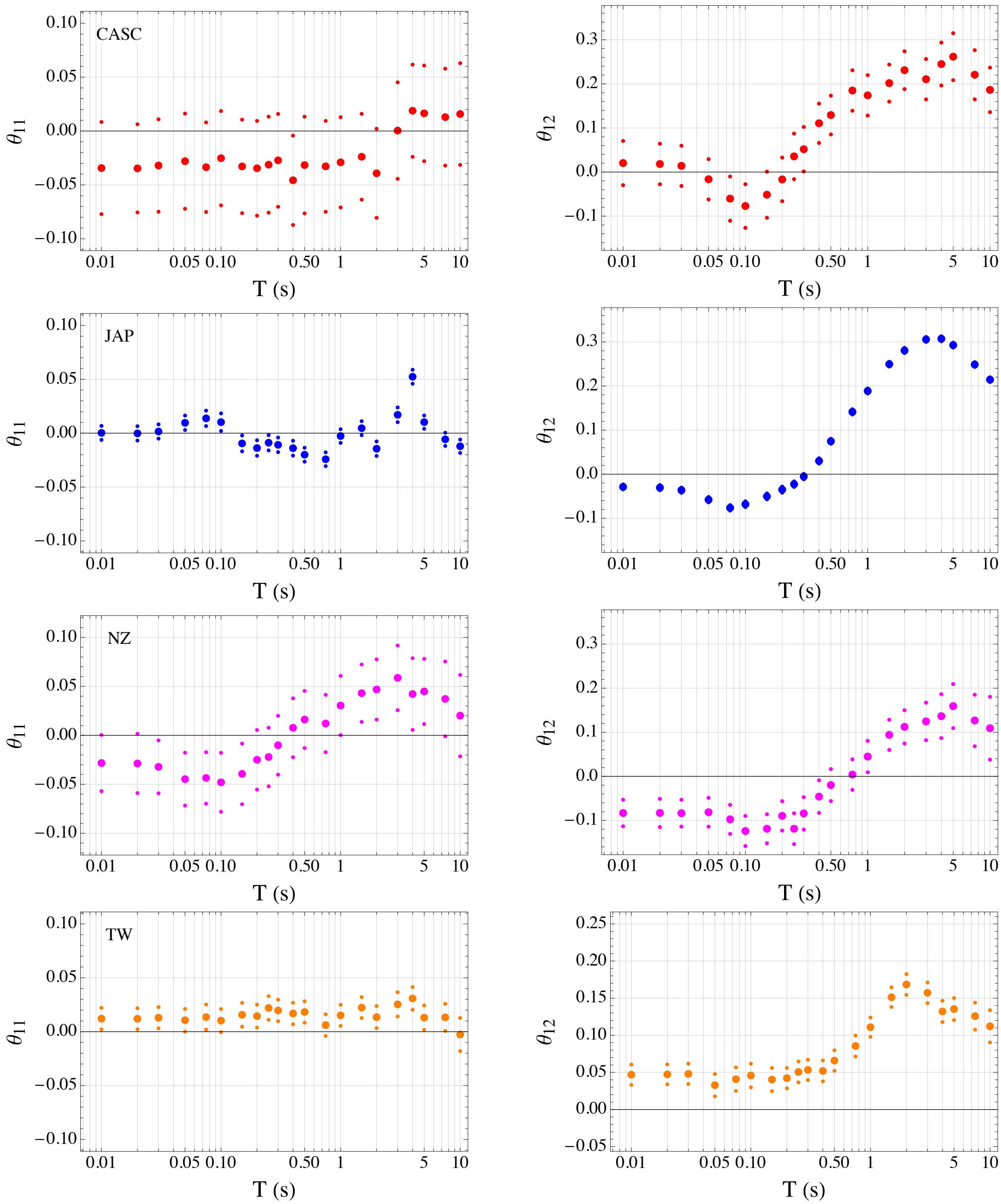

Figure 4.22: Coefficients θ_{11} (intercept) and θ_{12} (slope) for the basin-depth scaling against period T. Note that for Cascadia (CASC) and Japan (JP), the scaling is with $Z_{2.5}$, while for New Zealand (NZ) and Taiwan (Tw) the scaling is with $Z_{1.0}$.

5 Aleatory Variability

5.1 BASE MODEL

The statistical model of the GMM was presented in Equation(3.1). It includes a function for the median prediction (explained in detail in Chapter 4), an event term δB_e, and a between-event residual δW_{es}. The event terms are modeled by a normal distribution with mean zero and standard deviation τ. Usually, the within-event residuals are assumed to have a normal distribution with mean zero and standard deviation ϕ; however, as described in Section 3.1, Bayesian robust regression was used to minimize the effect of potential outliers on the mean regression estimates and aleatory variability. This means that there was a likelihood that that the model would adopt a t-distribution, which has wider tails than the normal distribution, making it less sensitive to outliers. In this case, the statistical model is given by the equations

$$\mu = f_{base}(\vec{\theta}; \vec{x}) + \delta B_e \tag{5.1}$$

$$\delta B_e \sim N(0, \tau) \tag{5.2}$$

$$\ln Y \sim S_T(\mu, \phi, \nu) \tag{5.3}$$

Equations (5.1) to (5.3) are interpreted as follows:

- The median μ is calculated as the base median function [Equation 4.1] plus the event term δB_e.
- The event term is distributed according to a normal distribution with mean zero and standard deviation τ.
- The observation $\ln Y$ is distributed according to a t-distribution with location parameter μ, scale parameter ϕ, and degrees-of-freedom ν.

The regression analysis estimated different values of ν for the seven different database regions, as data from different regions have different qualities and quantities of recordings. The prior distribution for ν is the Gamma distribution

$$\nu \sim G(2, 0.1) \tag{5.4}$$

where the parameters of the Gamma distribution are set based on Juárez and Steel (2010). This distribution is capable of assigning a broad range of possible values to ν.

The value of ν is only estimated for PGA. For the other periods, ν was fixed to the mean of the posterior value estimated for PGA. In this way, possible strong basin effects at long periods do not show up as outliers and affect the estimate of ν.

Also estimated during the regression were τ and ϕ. The prior distributions for these regression parameters are defined as the Half-Cauchy PDFs (Gelman, 2006)

$$\tau \sim HC(0, 0.5) \tag{5.5}$$

$$\phi \sim HC(0, 0.5) \tag{5.6}$$

Preliminary analyses showed that the posterior distributions of τ and ϕ were not strongly sensitive to the choice of the prior distribution.

Equations (5.2) and (5.3) partition the residual variance into a between-event part (τ^2) and a within-event part (ϕ^2). The role of the t-distribution is to diminish the effect of outliers (due to data quality and quantity) on the value of ϕ, however, in a forward application of the model, there are no outliers. Hence, the total variance for a forward application of the model can be calculated as follows:

$$\sigma^2 = \tau^2 + \phi^2 \tag{5.7}$$

assuming that the ground-motion distribution follows a normal distribution.

The NGA-West2 GMMs suggested a possible magnitude dependence of τ, thus warranting further investigation. This potential magnitude dependence in the regression was modeled with the logistic function

$$\tau = \tau_1 + (\tau_2 - \tau_1)\frac{\exp\left[(\mathbf{M} - m_0)/\delta\right]}{1 + \exp\left[(\mathbf{M} - m_0)/\delta\right]} \tag{5.8}$$

This function reaches τ_1 at small magnitudes and τ_2 at large magnitudes, with a smooth transition in between. The estimated values of τ_1 and τ_2 were found to be similar with overlapping posterior distributions; therefore, a magnitude dependence of τ was not included in the model.

It was found that because the standard deviations of the event terms between interface and intraslab events were similar, a difference in τ between these two types of events was not accounted for. One problem when estimating different τ values for different groups (e.g., intraslab versus interface or different regions) is that the number of events is quite small. Therefore, the same value of τ was adopted for all events regardless of the region.

Frankel et al. (2018) found a larger within-event variability at short rupture distances in their physics-based simulation of ground motions from a **M**9.0 Cascadia megathrust earthquake. Since the number of recordings at short distances in our dataset is small (Figure 2.4), we do not see this effect in our results. Furthermore, the effect seen in the simulations is probably because the distances to the subevents (asperities on the rupture surface) are more important than the distances to the rupture surface at short distances, which increases the variability at short distances because the asperities are spread out along the rupture length. This implies that this effect does not apply to the smaller-magnitude events included in our analysis. This effect was not included in our model because there is not enough empirical data at short distances to constrain it, nor enough simulations to constrain its magnitude dependence.

5.2 REGIONAL ADJUSTMENTS

KBCG20 was developed under the assumption that aleatory variability is the same for all regions. Due to the very different number of events and recordings in the different regions (Table 2.2), this is a reasonable assumption as it would be difficult to get a good estimate of variability for regions such as CASC or CAM where data is sparse. The regionalization of the parameter ν of the t-distribution, used for the Bayesian robust regression [Equation (5.3)] takes care of some regional differences in the variability.

Additional regional adjustments to aleatory variability (in particular, adjustments to ϕ) were accounted for by regionalizing the basin-depth terms involving $Z_{1.0}$ and $Z_{2.5}$. Including these terms leads to a decrease in the value of ϕ, which is regionally dependent. The regionalization of aleatory variability also depends on the parameter that is regionalized. Since basin depths are not available for all regions (see Section 4.1.7), a basin-depth term using $Z_{2.5}$ was developed for CASC and JP, while a basin-depth term using $Z_{1.0}$ was developed for TW and NZ, which can lead to different within-event standard deviations.

5.3 STANDARD DEVIATIONS

Figure 5.1 shows the estimated values of the between-event standard deviations τ and the within-event standard deviations ϕ, as well as the total standard deviation $\sigma = \sqrt{\tau^2 + \phi^2}$. The standard deviations were smoothed as a function of period, applying the same method as that used for the mean regression coefficients. The uncertainty associated with τ was found to be significantly larger than that of ϕ because it is estimated from fewer data.

Figure 5.2 shows the ratio of the standard deviation of within-event residuals before and after the basin-depth scaling is applied.

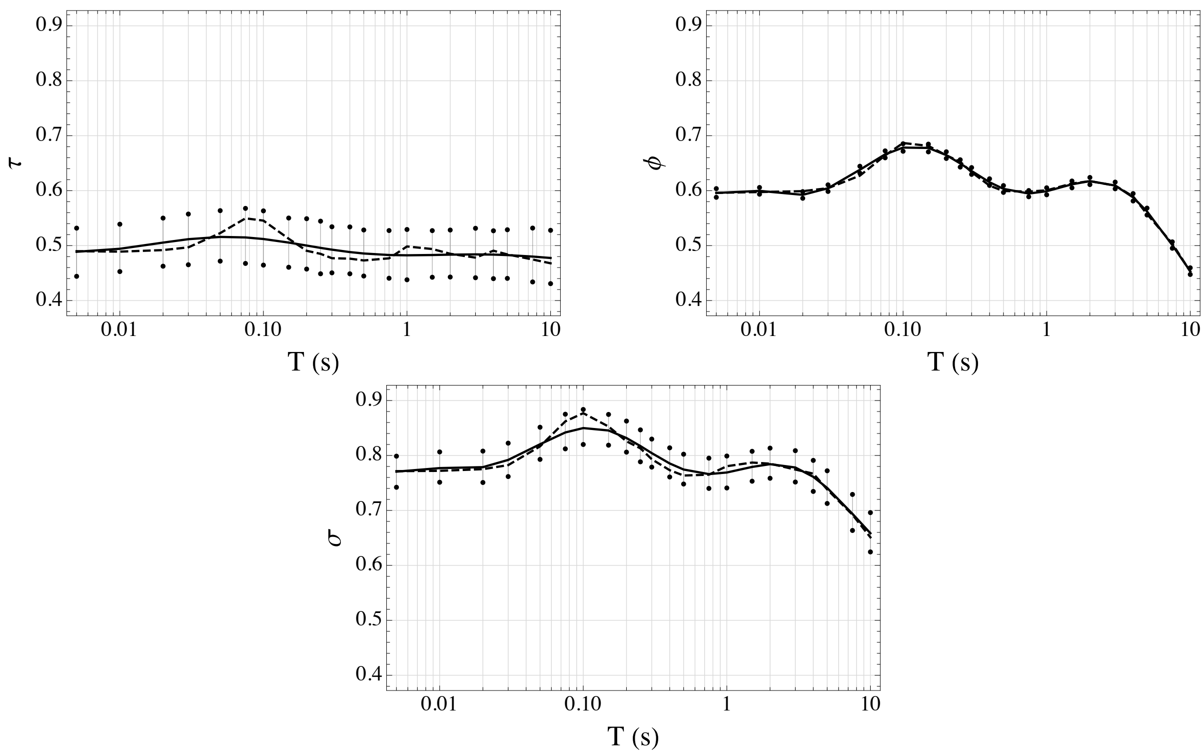

Figure 5.1: Aleatory standard deviations as a function of period for (top left) between-event terms (τ) and (top right) within-event residuals (ϕ), and total standard deviation σ (bottom). Shown are mean values of the posterior distributions (dashed lines), smoothed mean values (solid lines), and 5% and 95% percentiles of the posterior distributions (vertical lines).

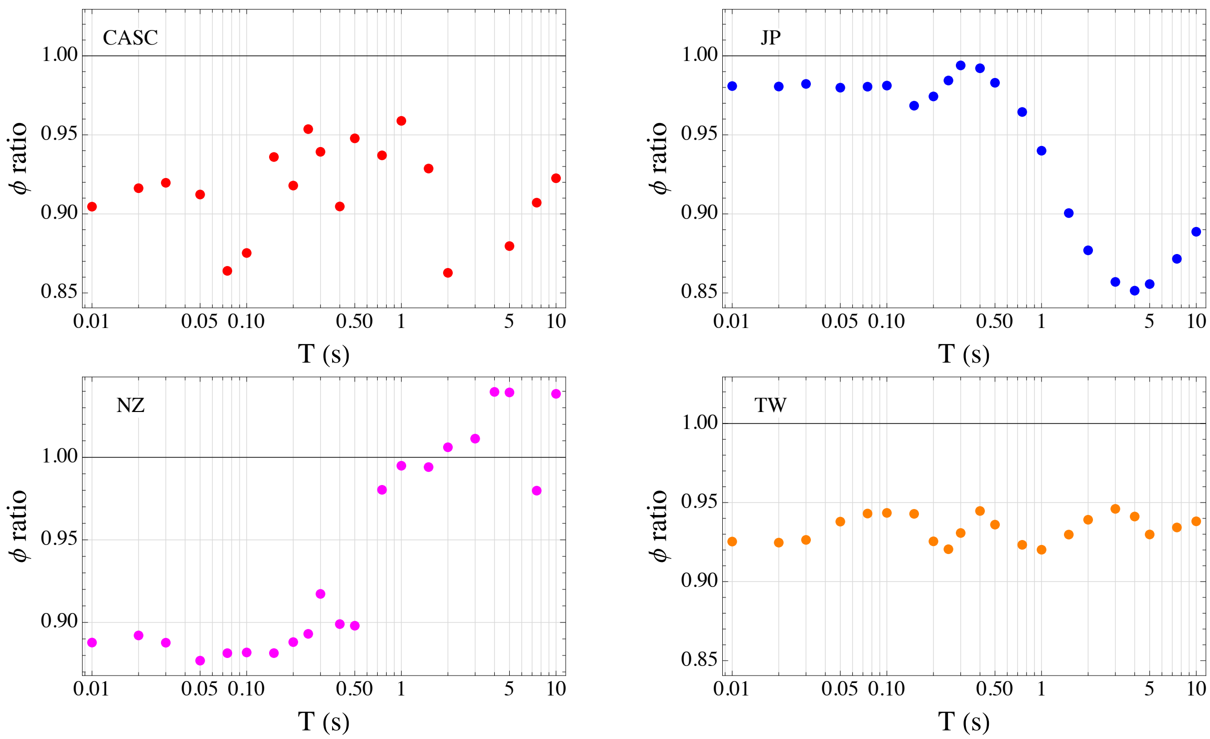

Figure 5.2: Ratio of standard deviations ϕ of within residuals after applying the basin depth scaling for those regions for which basin-depth terms are available.

6 Epistemic Uncertainty Model

Since the regression parameters of the KBCG20 GMM were estimated from a dataset limited in the ranges of related predictor variables, these regression parameters are subject to uncertainty, which translates into epistemic uncertainty in the median predictions. One example of such uncertainty is given in Al-Atik and Youngs (2014), which provides a model for the epistemic standard deviations associated with median predictions from the NGA-West2 GMMs. Using the same methodology, Lanzano et al. (2019) provided standard deviations of the epistemic uncertainty within different magnitude-distance combinations for their GMM, which was developed for shallow crustal earthquakes in Italy.

The Bayesian approach is particularly well suited for calculating epistemic uncertainty, since the outcome is not just a point estimate of the regression parameters but their entire posterior distributions. In our case, the posterior distributions of each regression parameter consists of 800 samples drawn using the MCMC methodology. Hence, there are 800 sets of regression parameters $\vec{\theta}$ comprising all of the coefficients, standard deviations, event terms, correlations, etc. For each set of coefficients, one can calculate median predictions for a particular scenario, resulting in 800 values of the median prediction of a given ground-motion parameter. These 800 median predictions provide an estimate of the epistemic uncertainty distribution associated with the scenario. One can calculate the mean, standard deviation, and fractiles of the median prediction of ground motion using this epistemic distribution.

There are different ways one can use the posterior distribution in PSHA calculations. The most comprehensive way is to use all 800 samples (or a large subset of them) to calculate the hazard using a logic tree. This would correspond to a logic tree with 800 branches for the GMM. This approach was applied by Abrahamson et al. (2019) who used 100 samples from an epistemic uncertainty distribution of regression coefficients to calculate non-ergodic seismic hazard in California. The advantage of this approach is that it does not discard any information or make any approximations. In particular, it retains the correlation between the median predictions over multiple scenarios; however, running hazard calculations for 800 combinations of coefficients is computationally demanding.

Figure 6.1(a) shows a histogram of the median predictions for one scenario for Japan calculated using the 800 sets of coefficients. The 800 different models span a range of median predictions, concentrated around the prediction calculated with the mean coefficients. Figure 6.1(b) shows an approximation to the density of the median distributions for all regions, calculated as a smooth kernel histogram. One can clearly see that there are regional differences in the location and range between the different distributions – median predictions are on average larger for Japan and South America, while the range of epistemic uncertainty is higher for regions with less data (e.g., Cascadia, Central America, and Mexico).

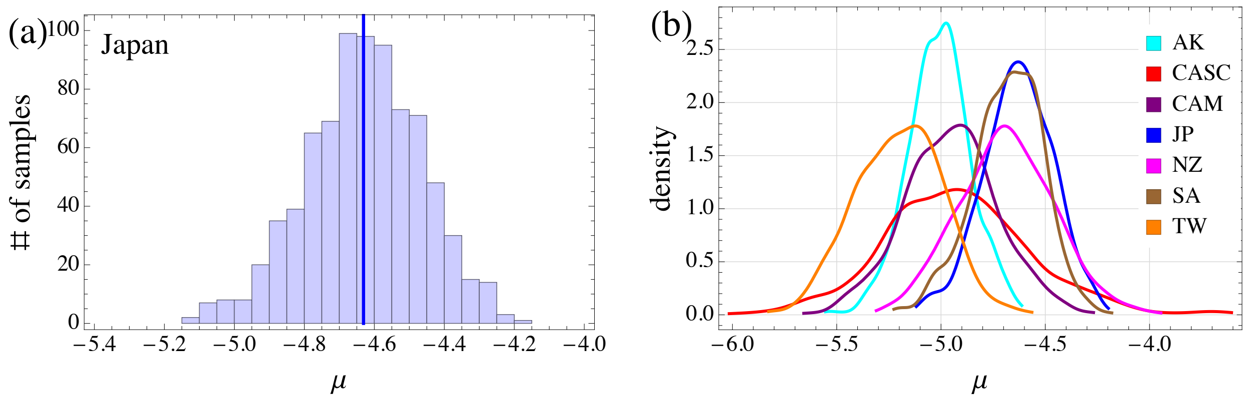

Figure 6.1: Left: Histogram of 800 calculated median predictions for Japan, for M $= 6$, $R_{RUP} = 100$ **km,** $V_{S30} = 400$, $Z_{TOR} = 10$ **km,** $F_S = 0$ **and** $F_X = 0$**. The vertical line is the median prediction using the mean coefficients. Right: Smoothed kernel density of 800 median predictions for all regions.**

A way to reduce the computational burden of a large number of samples is to approximate the distribution associated with epistemic uncertainty in the median predictions. If one makes the assumption that the median prediction of a ground-motion parameter for each scenario is Gaussian (Normal), then its mean and standard deviation is sufficient to fully specify the distribution; this is the approach used by Lanzano et al. (2019). One can then use this distribution to scale a backbone GMM using a reasonably small number of estimated fractiles (Atkinson et al., 2014; García-Fernández et al., 2019) or the polynomial chaos method to perform PSHA (Lacour and Abrahamson, 2019). We provide an *R*-function that calculates median predictions for the 800 sets of coefficients, and provides summary statistics such as median, standard deviation and some fractiles at `https://github.com/nikuehn/KBCG20`.

Figure 6.2 shows the scaling of median PSA with magnitude for Japan (interface events) and the associated epistemic uncertainty. The solid line shows the prediction using the mean coefficients, while the light blue lines show 10 individual samples (each line is calculated using one set of coefficients out of the 800 in the posterior distribution). The dashed lines represent a scaled backbone model calculated from the 5% and 95% of the distribution of the 800 median predictions at different magnitude values. Figure 6.2 shows that the individual samples behave differently than a simple scaled backbone; they have different slopes with magnitude. This behavior is lost in a backbone model.

We emphasize the importance of including epistemic uncertainty in the application of our GMM. This is because it was developed as a partially nonergodic model, meaning that some of the aleatory variability is traded-off with epistemic uncertainty compared to an ergodic model, i.e., we get less aleatory variability at the expense of more epistemic uncertainty compared to a fully ergodic model. This reduction must be offset by increased epistemic uncertainty. This is especially important for regionalized coefficients estimated from limited data. For example,

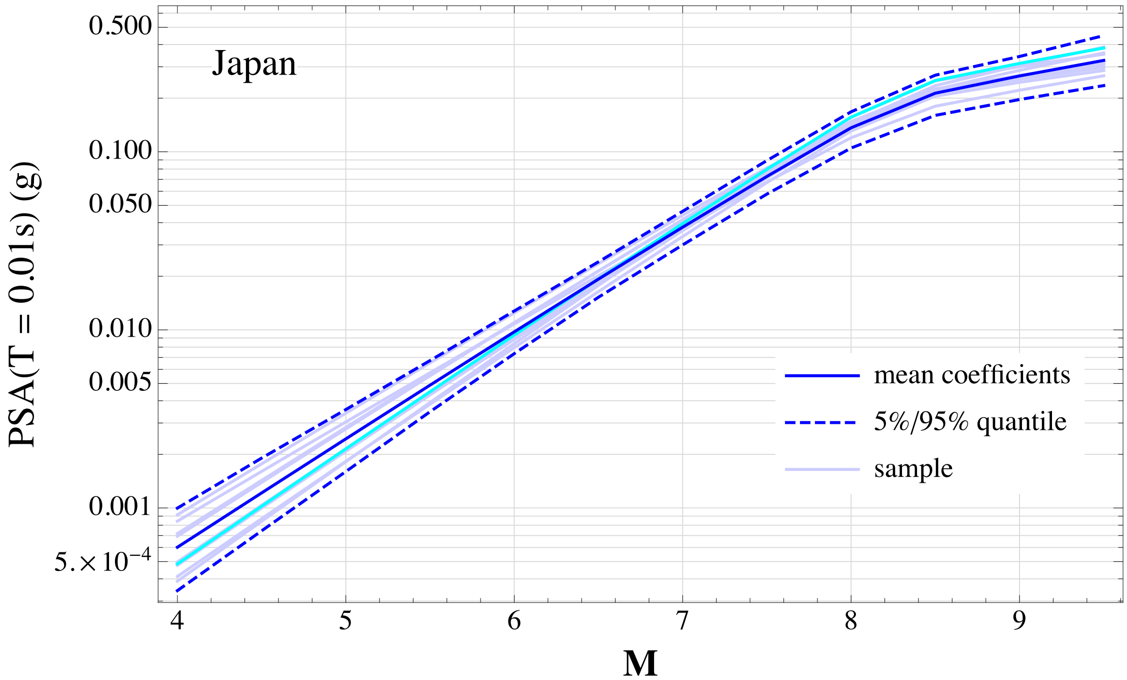

Figure 6.2: Scaling of PSA ($T = 0.01$sec) against magnitude for 10 individual samples from the posterior distribution (light blue), mean coefficients (blue), and 5% and 95% quantiles of all 800 sets of coefficients (dashed). Predictions are made for $R_{RUP} = 100$ km, $Z_{TOR} = 10$ km, $V_{S30} = 400$ km, and $F_S = 0$ (interface).

regions with a relatively small number of events and recordings, such as CASC or CAM, will have larger epistemic uncertainty in the median predictions than regions with a much larger dataset, such as JP and TW. As demonstrated in Abrahamson et al. (2019), this uncertainty must be included in hazard calculations, otherwise the estimated hazard will be underestimated.

Figures 6.3 and 6.4 show the epistemic standard deviations (ψ_μ) associated with the median predictions of PSA for a few scenarios, for interface and intraslab events. As one can see, the value of ψ_μ depends strongly on the region. Regions with a smaller number of events and recordings have larger uncertainty. This uncertainty also increases at the extremes of the data (e.g., large magnitudes and large distances), where the data are sparse. For Cascadia, one can see that the epistemic uncertainty associated with median predictions is higher for interface than for intraslab events. This is because there are no interface events in Cascadia, so the regional constant is not well constrained, while there is some intraslab data to estimate the intraslab constant. For longer periods, regional differences become less pronounced, i.e., the uncertainty decreases.

The black line in Figure 6.3 represents the uncertainty that should be associated when the model is applied to a new subduction region, i.e., one that is not covered by the seven regions used for KBCG20. In this case, one has to account for the regional differences in the constant, V_{S30}-scaling, and anelastic attenuation. For a new region, the regional adjustments are unknown, so each regional adjustment coefficient $\delta\theta$ should be assumed to have mean zero, and standard deviation ψ_θ (or, equivalently, the regional coefficient θ should have global mean μ_θ and standard deviation ψ_θ), as elaborated below. As described in Section 4.2, the regional coefficients are modeled as

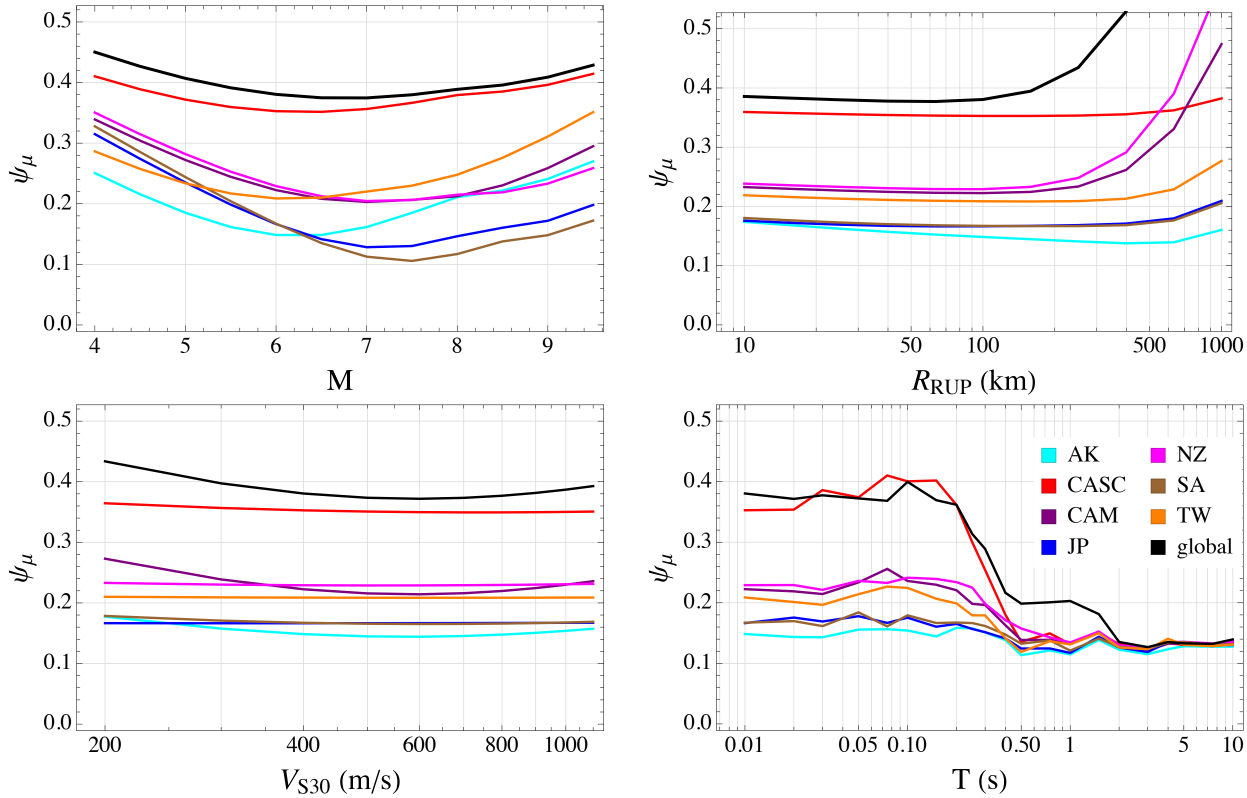

Figure 6.3: Standard deviations ψ_μ of the epistemic uncertainty associated with median predictions of ground motion, for interface events: (upper left) PGA versus magnitude M, (upper right) PGA versus distance R_{RUP}, (bottom left) PGA versus V_{S30}, and (bottom right) PSA versus period T. The values of the predictor variables used to calculate the median ground motions are M $= 6$, $R_{RUP} = 100$ km, $V_{S30} = 400$, $Z_{TOR} = 50$ km, $F_S = 1$ and $F_X = 0$. The black line represents uncertainty in global parameters plus regional uncertainty.

correlated. Hence, the distribution describing the epistemic uncertainty of the regional adjustment coefficients for a new region is a multivariate normal distribution

$$\overrightarrow{\delta R} \sim MVN(0, \Sigma_R) \tag{6.1}$$

To illustrate the effect of the regionalization on the epistemic uncertainty, Table 6.1 compares the aleatory standard deviations (ϕ and τ) and the epistemic uncertainty associated with median predictions (ψ_μ) for the different regions and a separate ergodic model. The ergodic model uses the same functional form and Bayesian regression methodology as KBCG20, but none of the coefficients is regionalized. For the ergodic model, the coefficients are determined by all records in the dataset, which leads to a very small value of the epistemic uncertainty. However, this is offset by larger values for τ and ϕ. The total variability, which combines the aleatory variability and epistemic uncertainty and describes the full range of possible ground motions, can be calculated as $\sigma_{total} = \sqrt{\tau^2 + \phi^2 + \psi_\mu^2}$. The total variability of the KBCG20 model, applied to a new region, is very close to the total variability of the ergodic model, but a larger part of the total variability is epistemic uncertainty for the KBCG20 model. This is an example of the trade-off between

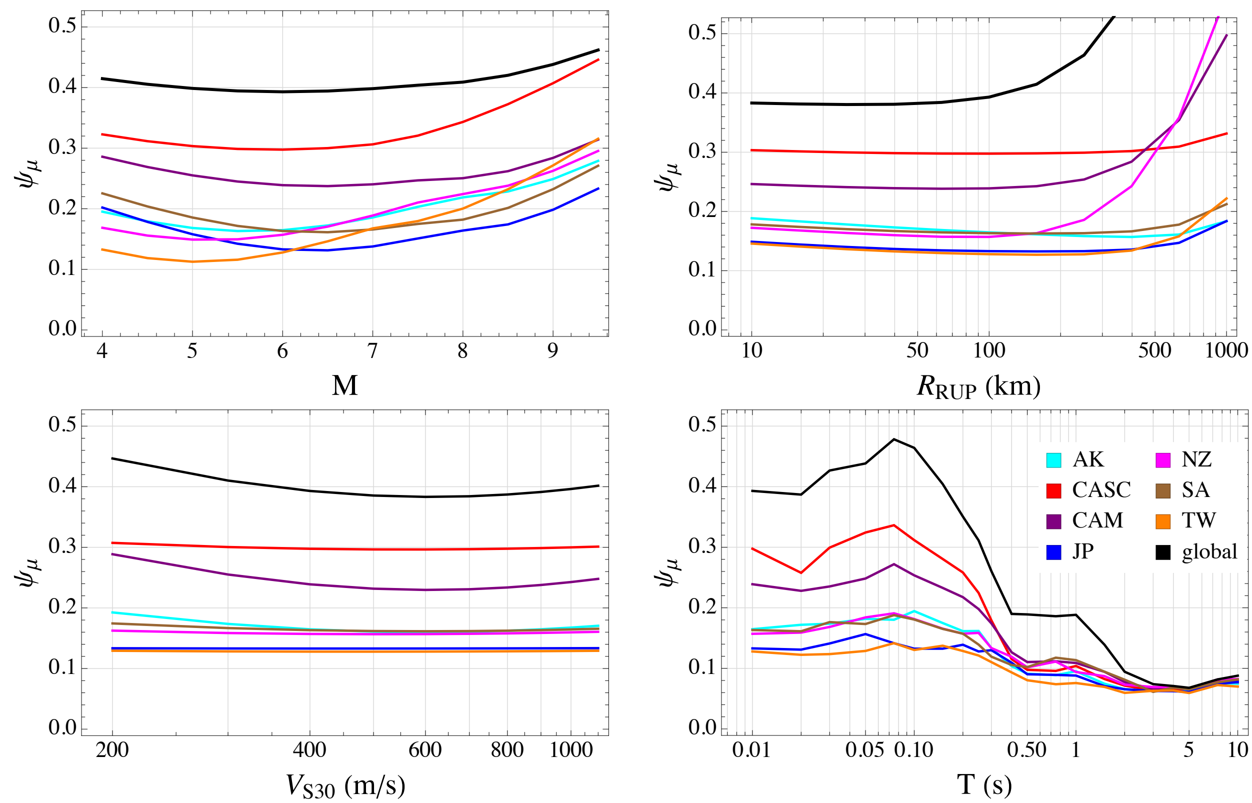

Figure 6.4: Standard deviations ψ_μ of the epistemic uncertainty associated with median predictions of ground motion, for intraslab events: (upper left) PGA versus magnitude M, (upper right) PGA versus distance R_{RUP}, (bottom left) PGA versus V_{S30}, and (bottom right) PSA versus period T. The values of the predictor variables used to calculate the median ground motions are M $= 6$, $R_{RUP} = 100$ km, $V_{S30} = 400$, $Z_{TOR} = 10$ km, $F_S = 0$ and $F_X = 0$. The black line represents uncertainty in global parameters plus regional uncertainty.

epistemic uncertainty and aleatory variability; the value of the aleatory variability is reduced, but there is a penalty because we are more uncertain about the median predictions. For regions with some amount of data, this trade-off is beneficiary, as the value of σ_{total} is reduced compared to the ergodic model.

6.1 CALCULATION OF EPISTEMIC UNCERTAINTY

To calculate the epistemic uncertainty associated with an earthquake-site scenario $\vec{x}_*$ and a given region, we calculate a prediction for each of the 800 sets of coefficients:

$$\mu_k = f_{base}(\vec{\theta}_k; \vec{x}_*) \tag{6.2}$$

where k indexes the samples from the posterior distribution. We then loop over the 800 samples, which results in 800 values of median predictions from which we can calculate statistics such as the standard deviation or some fractiles.

Table 6.1: Aleatory variability (τ and ϕ) and epistemic uncertainty (ψ_μ) for the different regional models, and an ergodic (not regionalized) model. The epistemic uncertainty σ_{mu} is calculated for M $= 7$, $R_{RUP} = 100$ km, $V_{S30} = 400$, $Z_{TOR} = 10$ km, and $F_S = 0$ (interface) for PGA.

Region	ϕ	τ	ψ_μ	σ_{total}
Alaska	0.5958	0.4887	0.1613	0.7873
Cascadia	0.5958	0.4887	0.3699	0.8548
CentralAmerica & Mexico	0.5958	0.4887	0.2205	0.8015
Japan	0.5958	0.4887	0.1351	0.7823
New Zealand	0.5958	0.4887	0.2169	0.8005
South America	0.5958	0.4887	0.1254	0.7807
Taiwan	0.5958	0.4887	0.2034	0.797
Global	0.5958	0.4887	0.3625	0.8516
Ergodic	0.6265	0.5966	0.0155	0.8652

For a new region, we need to add epistemic uncertainty according to Equation (6.1). In this case, for each iteration k we sample a vector of regional adjustment coefficients $\overrightarrow{\delta R}$ from its joint distribution. Then, we add the adjustment coefficient to the global value; the following shows the interface constant as an example:

$$\theta_{1,if;newregion;k} = \mu_{\theta 1,if;k} + \delta\theta_{1,if;sampled} \tag{6.3}$$

where $\delta\theta_{1,ig;sampled}$ is part of the sampled δR.

To sample a new vector $\overrightarrow{\delta R}$, we need the co-variance matrix Σ_R, which is calculated as

$$\Sigma_R = \text{diag\_matrix}(\vec{\psi}_{R,k})\ C_k\ \text{diag\_matrix}(\vec{\psi}_{R,k}) \tag{6.4}$$

where $\vec{\psi}_{R,k} = \{\psi_{1,if;kk}, \psi_{1,slab;k}, \psi_{7;k}, \psi_{6,g1;k}, \psi_{6,g1;k}, \psi_{6,g1;k}, \psi_{6,g1;k}, \psi_{6,g2;k}, \psi_{6,g1;k}\}$ is the kth sample from the posterior distribution of the standard deviations of the regional adjustment coefficients [cf. Equation 4.12; Table 4.2]. C_k is the kth sample of the regional correlation matrix. In the regression, we do not estimate the components of the correlation matrix C but its Cholesky decomposition L. Hence, we calculate C_k as

$$C_k = L_k^T L \tag{6.5}$$

Calculating the distribution of median predictions in this way takes into account epistemic uncertainty in the regional standard deviations $\vec{\psi}_R$ and the correlation matrix C. In practice, we find that this has only a minor effect on the overall epistemic uncertainty for a new region.

We have sampled 800 values of regional adjustment coefficients for a new region according to the methodology outlined in the previous paragraphs; see electronic appendix.

7 MODEL EVALUATION

7.1 RESIDUAL ANALYSES

Event terms (between-event residuals, δB_e) for interface and intraslab events are plotted versus magnitude in Figure 7.1 and versus depth to top of rupture in Figure 7.2 for PGA ($T = 0$) and PSA at $T = 0.2$, 1.0 and 3.0 sec. Global subduction regions are identified by different colors. In general, both the interface and intraslab event terms appear to be relatively unbiased.

Within-event residuals (δW_{es}) are plotted versus rupture distance for all regions in Figure 7.3. Each region is plotted separately in Figures 7.4 to 7.10. Note: when reviewing these plots, remember that a Bayesian robust regression analysis was used, assuming a t-distribution for the residuals, which minimized the influence of outliers on the regression results. The apparent outliers on these plots do not have the same impact as they would in a more typical least-squares regression. Similar plots for site-amplification terms (V_{S30}-scaling) and basin-depth terms ($Z_{1.0}$ and $Z_{2.5}$ scaling) can be found at `https://github.com/nikuehn/KBCG20/`.

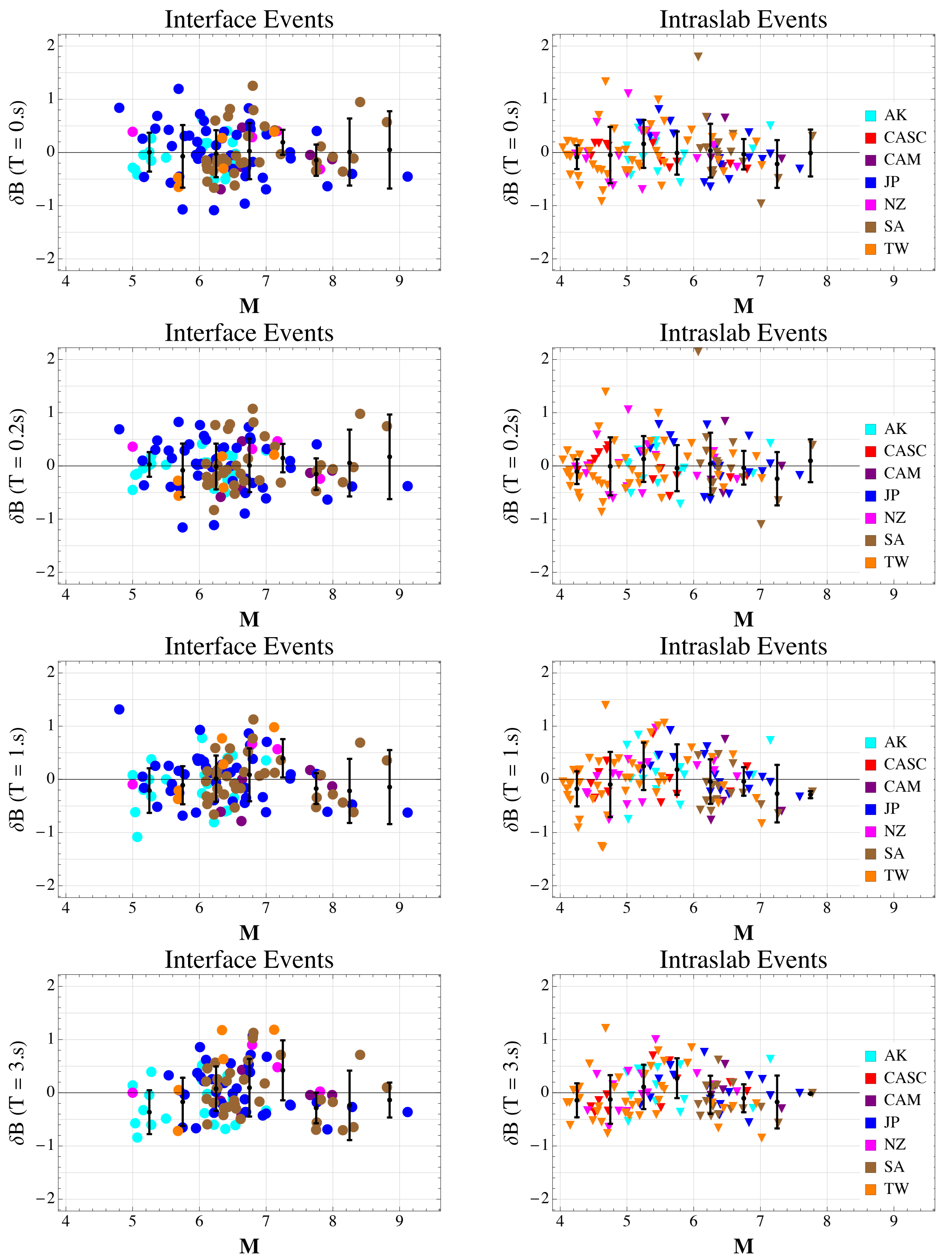

Figure 7.1: Plot of event terms versus magnitude M for PGA ($T = 0$) and PSA at $T = 0.2$, 1.0 and 3.0 sec: (left) interface events; (right) intraslab events.

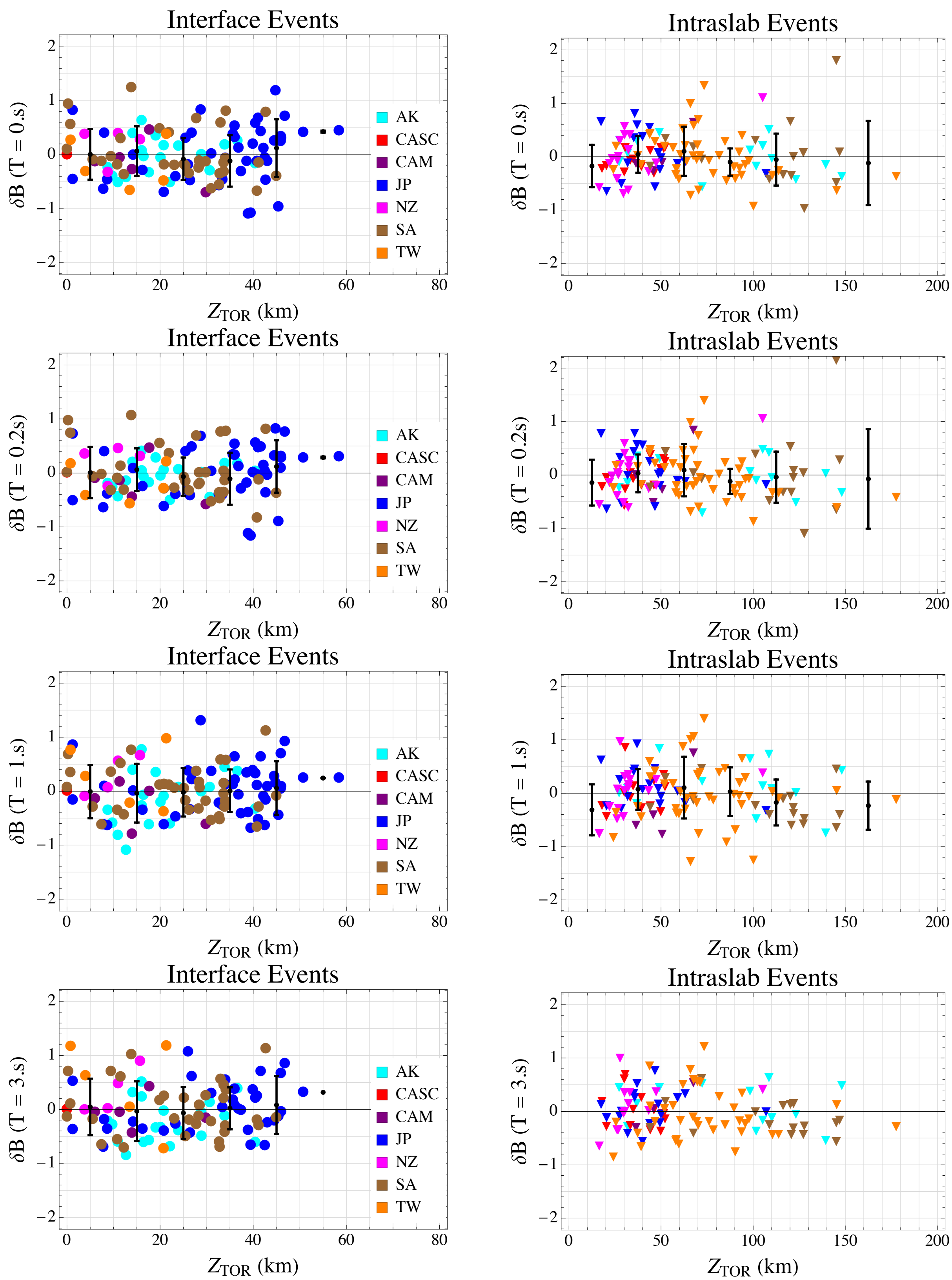

Figure 7.2: Plot of event terms versus depth to top of rupture Z_{TOR} for PGA ($T = 0$) and PSA at $T = 0.2$, 1.0 and 3.0 sec: (left) interface events; (right) intraslab events.

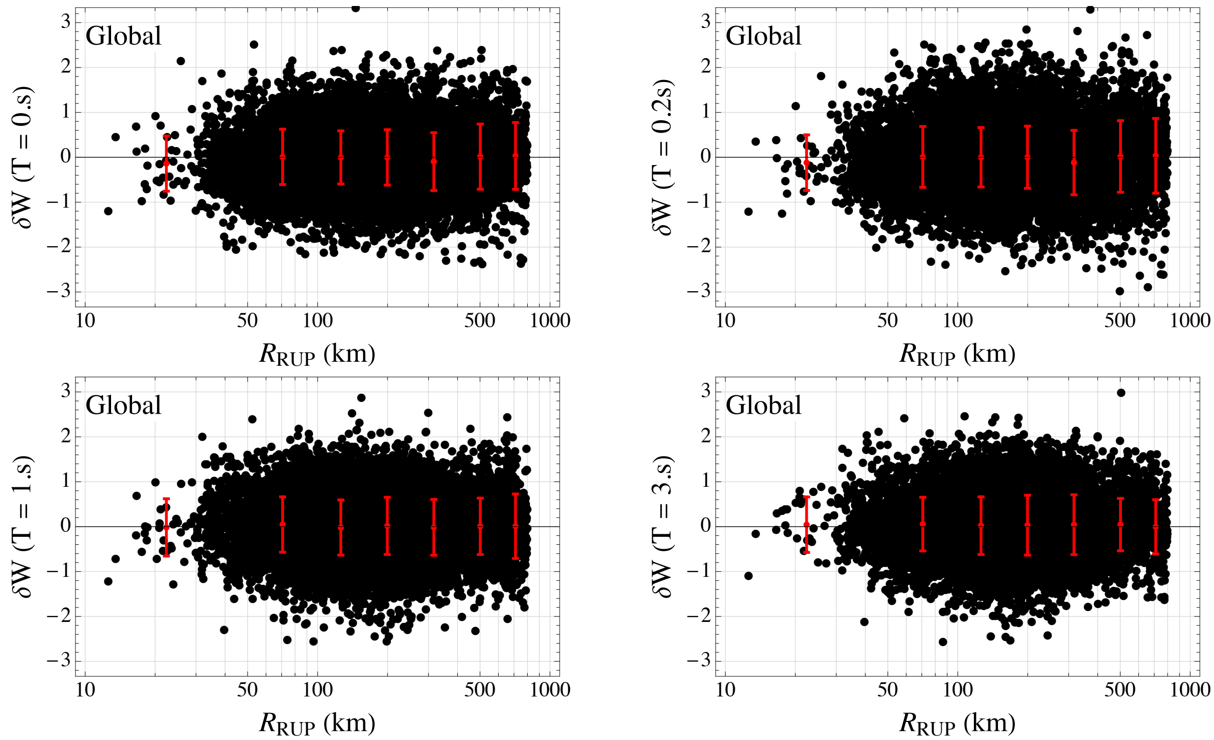

Figure 7.3: Plot of within-event residuals versus rupture distance R_{RUP} for PGA ($T = 0$) and PSA at $T = 0.2$, 1.0, and 3.0 sec for the Global model.

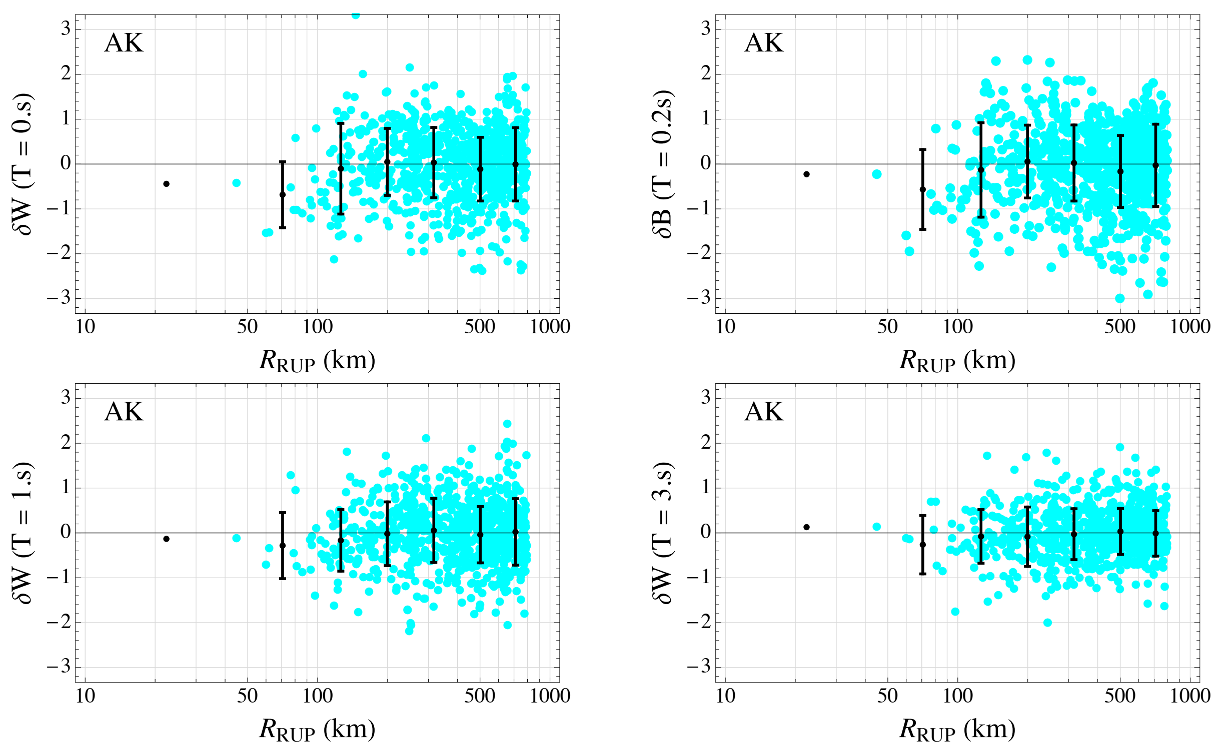

Figure 7.4: Plot of within-event residuals versus rupture distance R_{RUP} for PGA ($T = 0$) and PSA at $T = 0.2$, 1.0, and 3.0 sec for Alaska (AK).

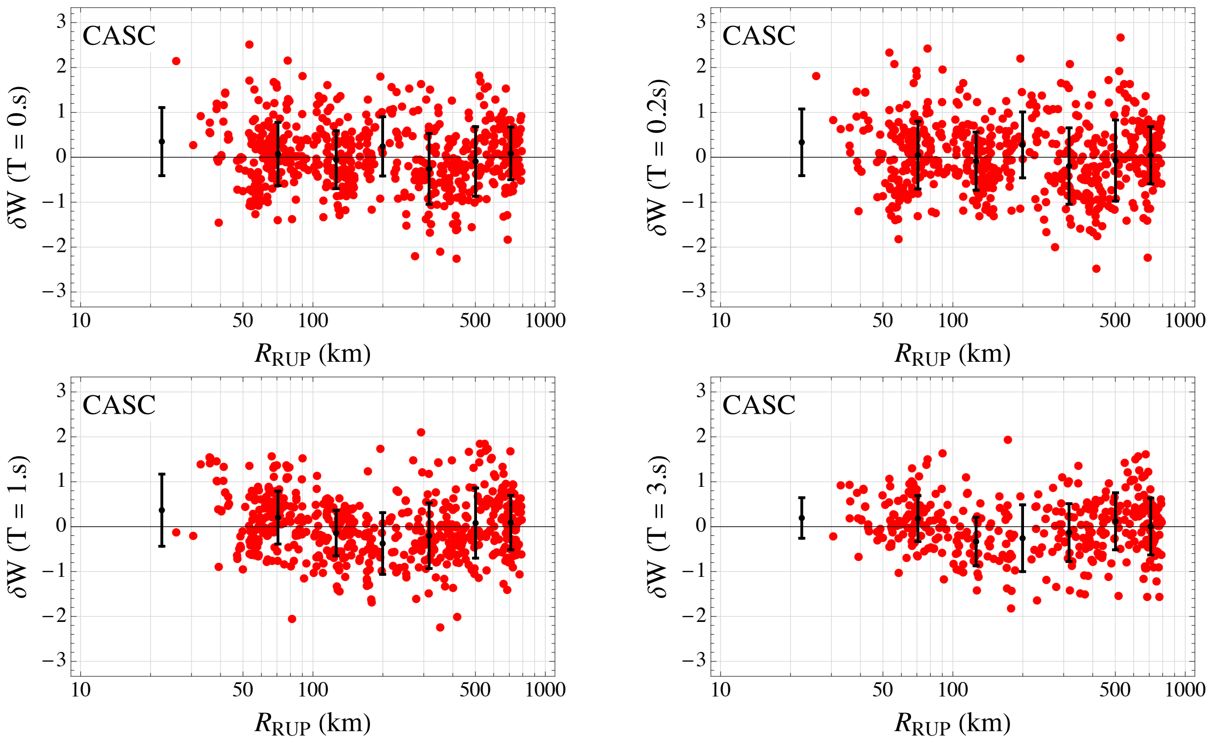

Figure 7.5: Plot of within-event residuals versus rupture distance R_{RUP} for PGA ($T = 0$) and PSA at $T = 0.2$, 1.0, and 3.0 sec for Cascadia (CASC).

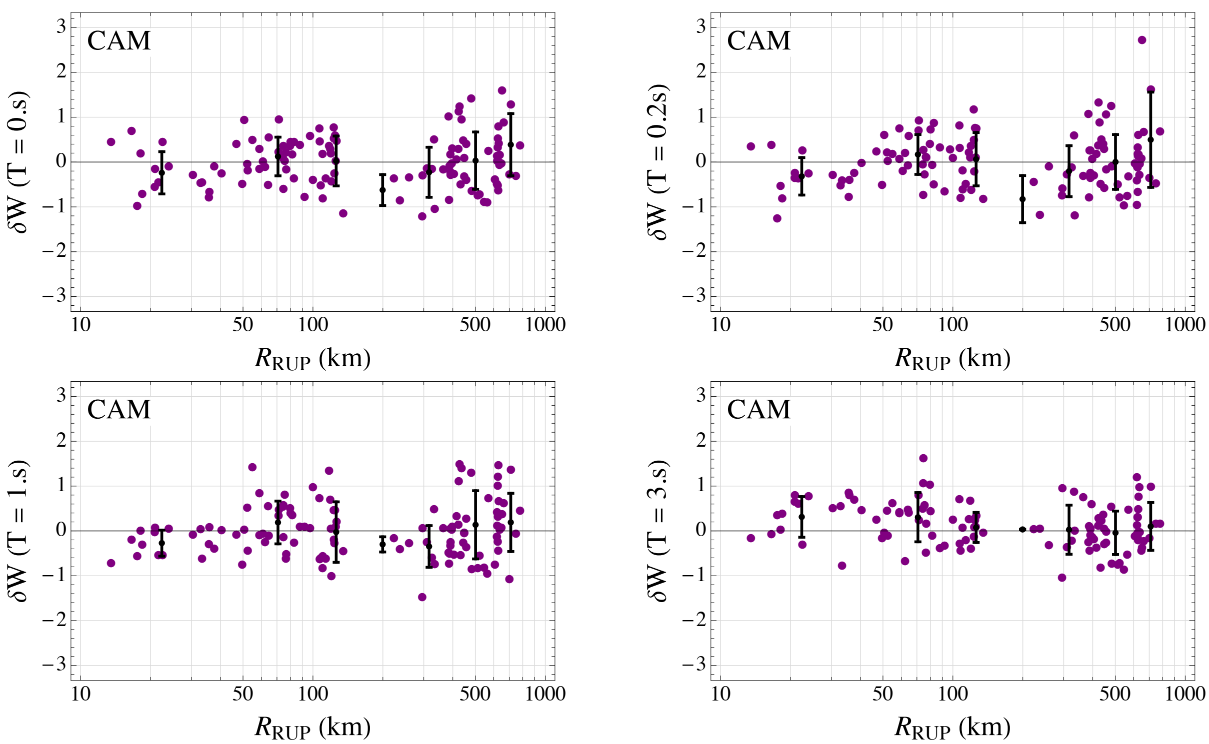

Figure 7.6: Plot of within-event residuals versus rupture distance R_{RUP} for PGA ($T = 0$) and PSA at $T = 0.2$, 1.0, and 3.0 sec for Central America and Mexico (CAM).

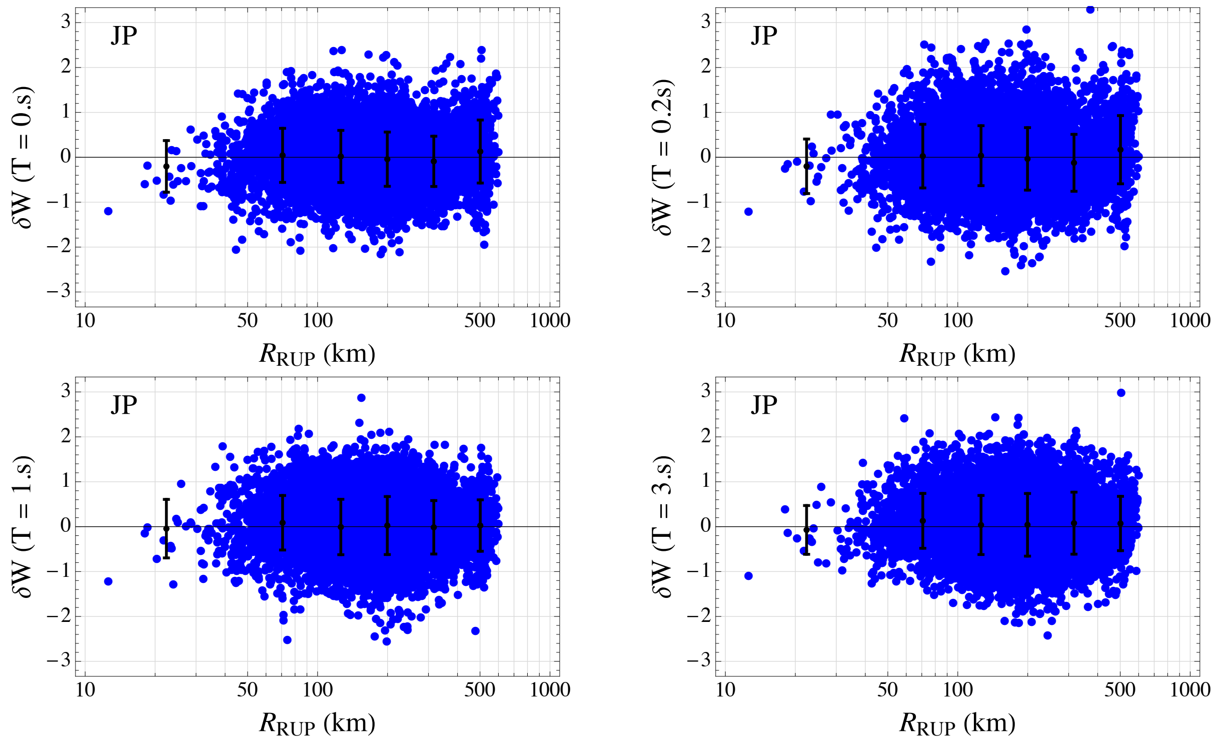

Figure 7.7: Plot of within-event residuals versus rupture distance R_{RUP} for PGA ($T = 0$) and PSA at $T = 0.2$, 1.0, and 3.0 sec for Japan (JP).

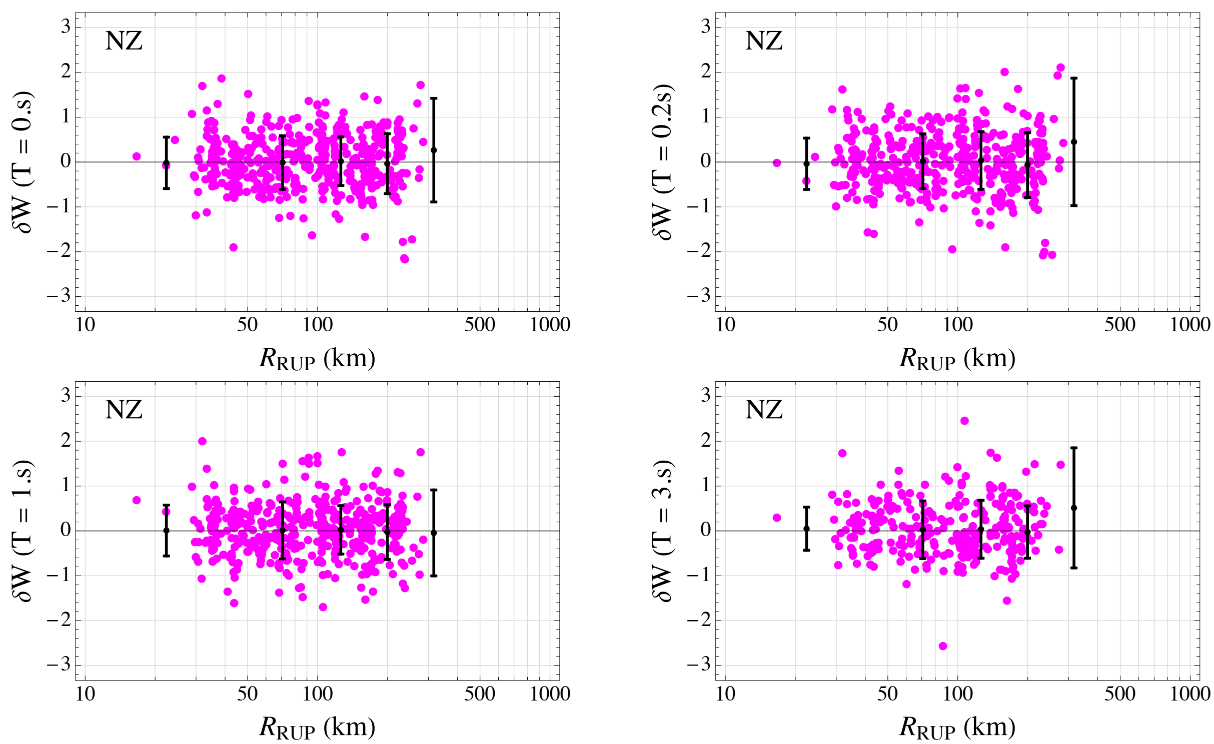

Figure 7.8: Plot of within-event residuals versus rupture distance R_{RUP} for PGA ($T = 0$) and PSA at $T = 0.2$, 1.0 and 3.0 sec for New Zealand (NZ).

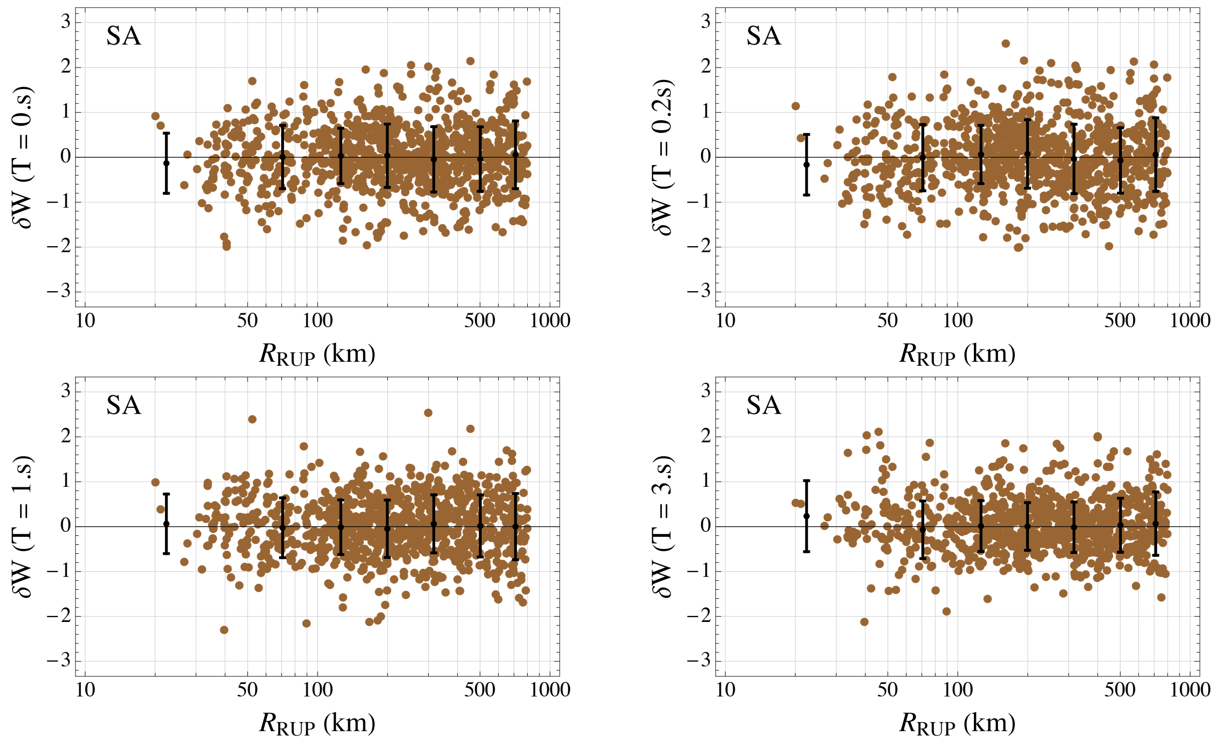

Figure 7.9: Plot of within-event residuals versus rupture distance R_{RUP} for for PGA ($T = 0$) and PSA at $T = 0.2$, 1.0, and 3.0 sec for South America (SA).

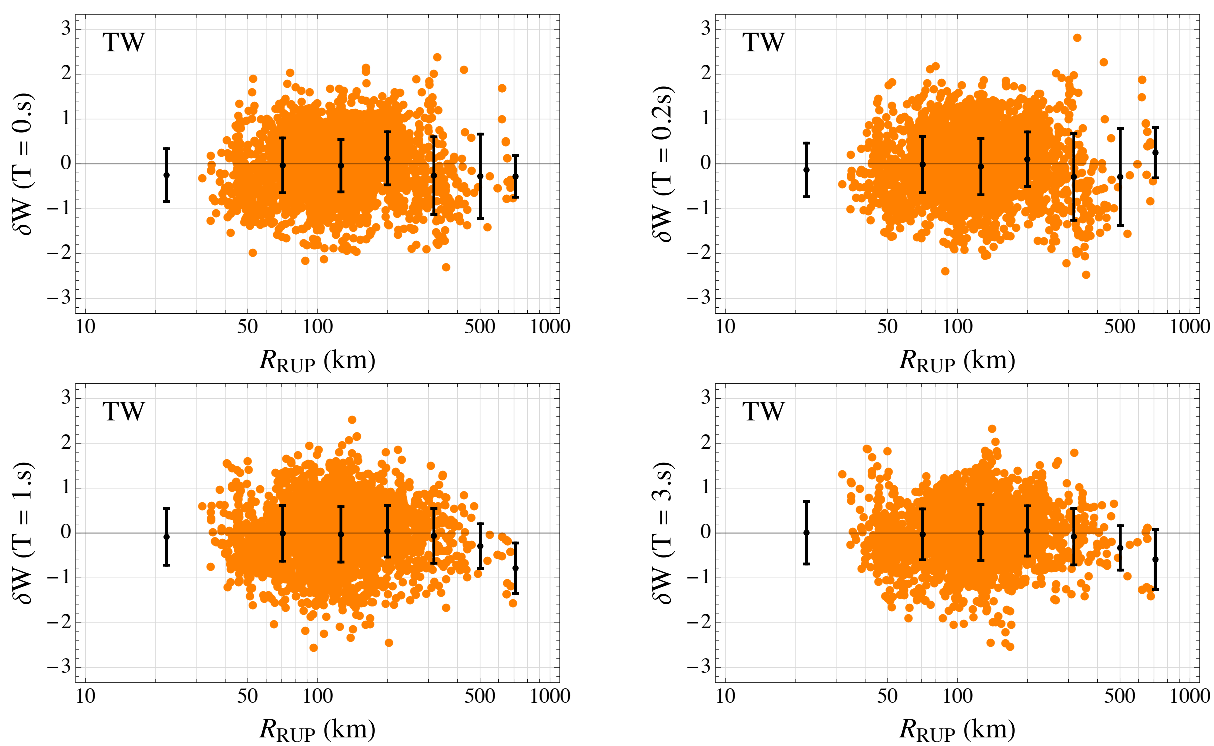

Figure 7.10: Plot of within-event residuals versus rupture distance R_{RUP} for PGA ($T = 0$) and PSA at $T = 0.2$, 1.0, and 3.0 sec for Taiwan (TW).

7.2 MODEL PREDICTIONS

This section presents plots of median predicted values from KBCG20 for representative scenarios with a focus on the different features and parameterization of our GMM. All of the plots are for the forearc region since this region exists in all of the subduction zones. In the selection of these scenarios, no attempt was made to cover the broad applicable range of the model; additional plots, if desired, are left to the user. Scenario plots are presented for the following cases:

- Attenuation
- Response spectra
- Magnitude
- Source depth
- Basin amplification (CASC, JP, TW, NZ)
- Site amplification

For both attenuation and response spectra, plots are presented for V_{S30} values of 760 m/sec and a 400 m/sec. The larger value is representative of the common reference-site condition corresponding to NEHRP B/C boundary. The smaller value is representative of soft rock-site conditions.

Plots are presented for 12 forearc areas (not to be confused with the specific geographic regions and sub-regions discussed previously), which account for differences in estimated interface ($\mathbf{M}_{B,if}$) and intraslab ($\mathbf{M}_{B,slab}$) breakpoint magnitudes as follows:

- Global ($\mathbf{M}_{B,if} = 7.9$, $\mathbf{M}_{B,slab} = 7.6$)
- Alaska ($\mathbf{M}_{B,if} = 8.6$, $\mathbf{M}_{B,slab} = 7.2$)
- Alaska: Aleutians ($\mathbf{M}_{B,if} = 8.0$, $\mathbf{M}_{B,slab} = 8.0$)
- Cascadia ($\mathbf{M}_{B,if} = 8.0$, $\mathbf{M}_{B,slab} = 7.2$)
- Northern Central America and Mexico ($\mathbf{M}_{B,if} = 7.4$, $\mathbf{M}_{B,slab} = 7.4$)
- Southern Central America ($\mathbf{M}_{B,if} = 7.5$, $\mathbf{M}_{B,slab} = 7.6$)
- Japan: Pacific Plate ($\mathbf{M}_{B,if} = 8.5$, $\mathbf{M}_{B,slab} = 7.6$)
- Japan: Philippine Sea Plate ($\mathbf{M}_{B,if} = 7.7$, $\mathbf{M}_{B,slab} = 7.6$)
- Northern South America ($\mathbf{M}_{B,if} = 8.5$, $\mathbf{M}_{B,slab} = 7.3$)
- Southern South America ($\mathbf{M}_{B,if} = 8.6$, $\mathbf{M}_{B,slab} = 7.2$)
- Taiwan ($\mathbf{M}_{B,if} = 7.1$, $\mathbf{M}_{B,slab} = 7.7$)

- New Zealand ($\mathbf{M}_{B,if} = 8.3$, $\mathbf{M}_{B,slab} = 7.6$)

For a subduction sub-region with multiple breakpoint magnitudes (i.e., AK, JP, CAM, and SA), the only difference are the breakpoint magnitudes. Therefore, for magnitudes less than the breakpoint magnitude, the median predicted ground motions are the same for these regions.

7.2.1 Attenuation

Attenuation curves are shown for each area to demonstrate their regional differences. Plots are presented for $\mathbf{M} = 7.0$, 8.0, and 9.0 for interface events and for $\mathbf{M} = 6.0$, 7.0, and 8.0 for intraslab events. These magnitudes span the full range of breakpoint magnitudes for all regions. The depth to the top of the rupture (Z_{TOR}) is 10 km for interface events and 50 km for intraslab events.

For the four regions that include basin amplification terms (CASC, JP, TW, and NZ), the attenuation curves are for the default values of $Z_{1.0}$ and $Z_{2.5}$ (i.e., $\delta Z_{1.0} = \delta Z_{2.5} = 0$). A separate plot demonstrating the basin amplification features of the model for these four regions is presented in a later section of this report.

The attenuation curves for PGA are shown in Figure 7.11 for the "soft-rock" site condition ($V_{S30} = 400$ m/sec). There is overall good agreement over different areas, especially for the smaller magnitudes. For the larger **M**8.0 and 9.0 interface scenarios, the impact from the variation in breakpoint magnitudes for the different areas is clearly observed. For example, the TW attenuation curve falls below the other attenuation curves for the **M**8.0 and 9.0 scenarios because of its relatively low breakpoint magnitude of 7.1. Differences in attenuation are also observed for those areas with similar breakpoint magnitudes. For example, the attenuation curve for CASC attenuates faster for the longer distances than the global attenuation curve, both of which have a similar breakpoint magnitude. This difference in attenuation is attributable to the difference in anelastic attenuation between CASC and the global model.

Similar attenuation curves for PSA at $T = 0.2$, 1.0, and 3.0 sec are presented in Figures 7.12 to 7.14. The observations for $T = 0.2$ sec are similar to those for PGA. For $T = 1.0$ sec and distances less than about 100 km, there is relatively strong agreement among the suite of attenuation curves for the **M**7.0 interface scenario; however, for the larger distances and larger magnitude scenarios shown in the figure, the suite of attenuation curves exhibit a wider range in values based on the regional differences in both breakpoint magnitude and anelastic attenuation. Similar observations and conclusions for the $T = 1.0$ sec are noted for the $T = 3.0$.

Figures 7.15 to 7.18 show the same attenuation plots for $V_{S30} = 760$ m/sec. The same general observations and conclusions noted for $V_{S30} = 400$ m/sec are also applicable to these attenuation curves.

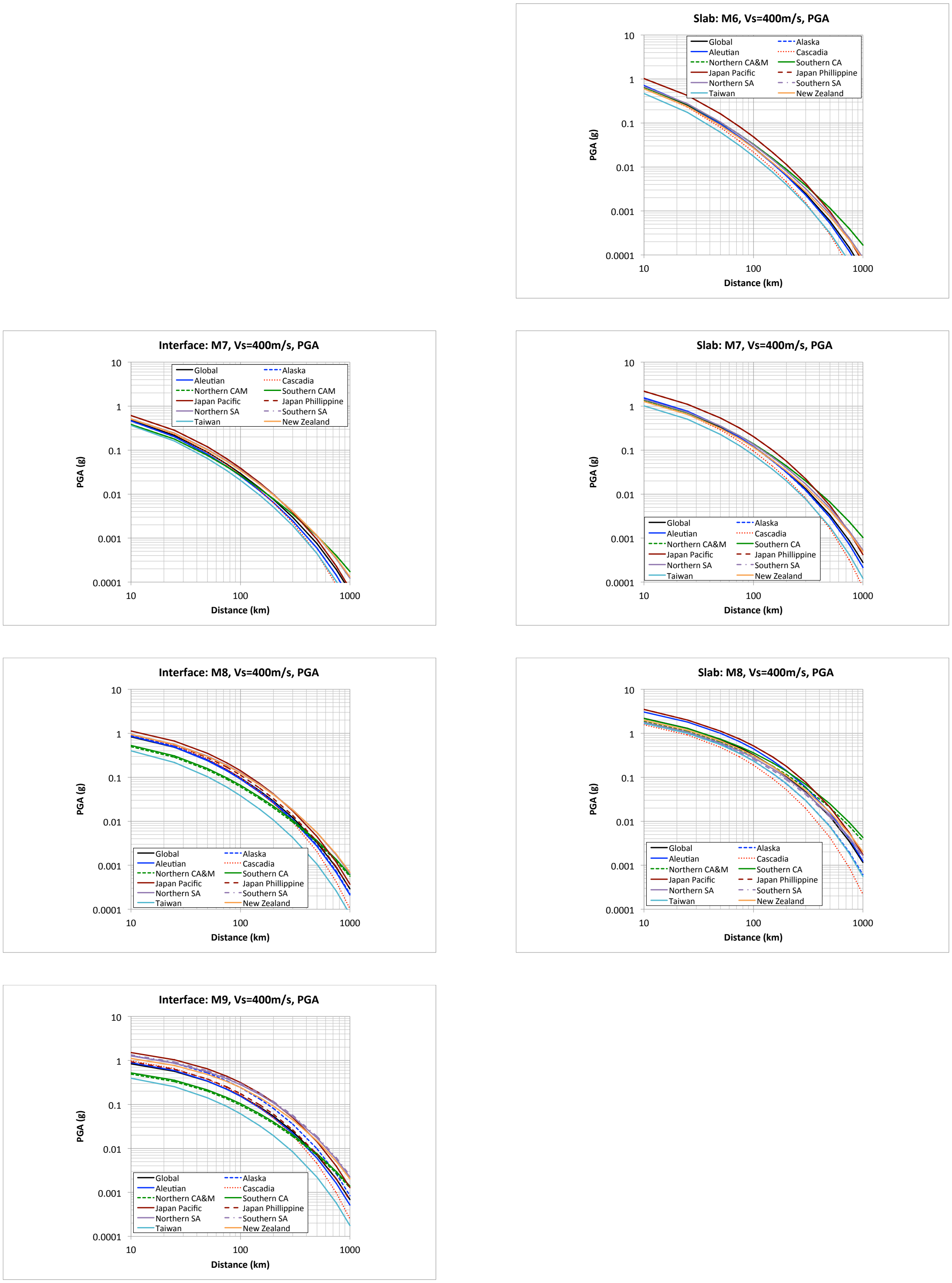

Figure 7.11: Plots of PGA: (left) interface events for M $= 7.0$, 8.0, and 9.0 with $Z_{TOR} = 10$ km; and (right) intraslab events for M $= 6.0$, 7.0, and 8.0 with $Z_{TOR} = 50$ km. For all plots, $V_{S30} = 400$ m/sec and $\delta Z_{1.0} = \delta Z_{2.5} = 0$. The plots are arranged so that interface/intraslab scenarios with the same magnitude are next to each other.

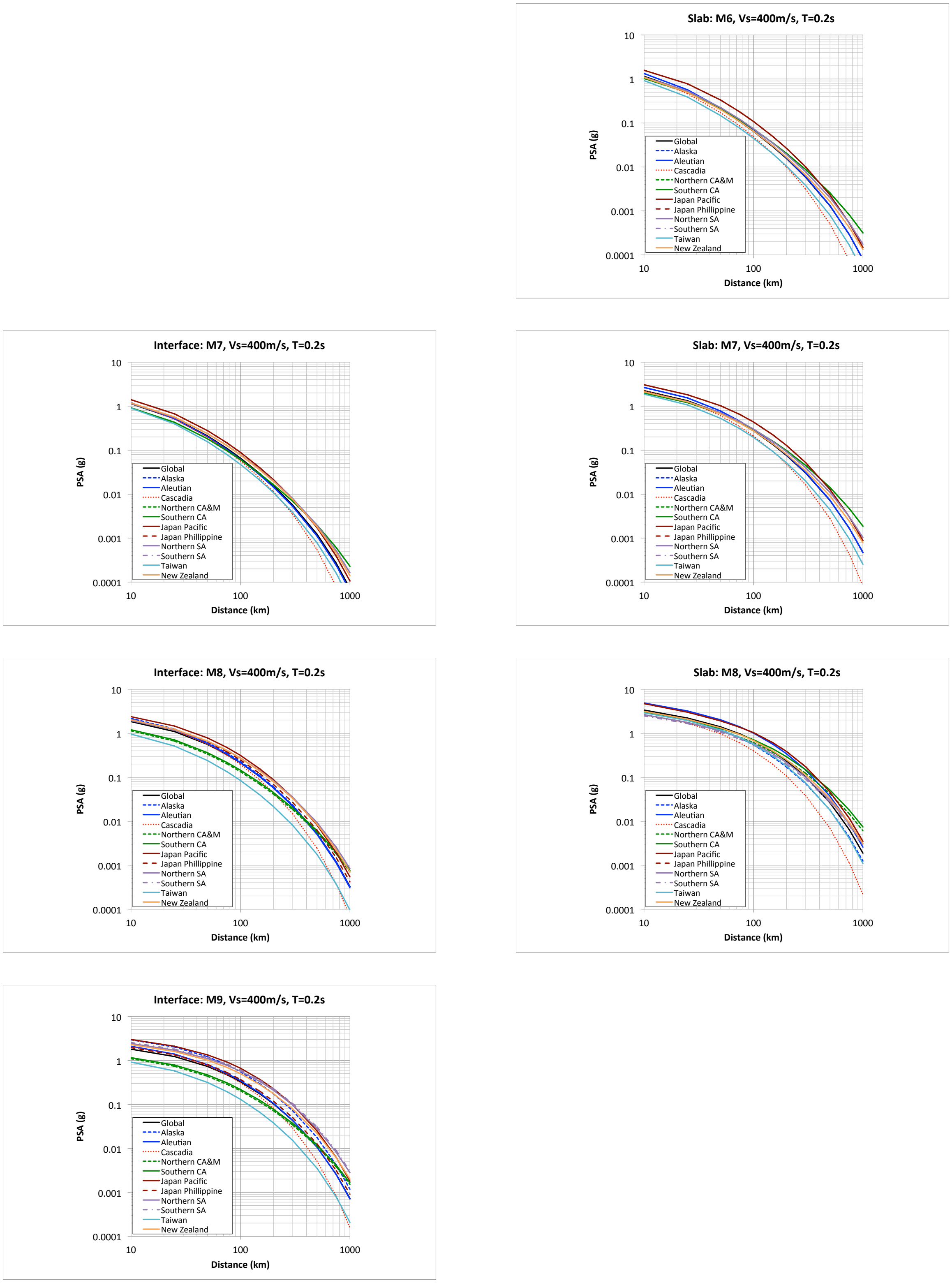

Figure 7.12: Plots of PSA at $T = 0.2$ sec: (left) interface events for M $= 7.0$, 8.0, and 9.0 with $Z_{TOR} = 10$ km; and (right) intraslab events for M $= 6.0$, 7.0, and 8.0 with $Z_{TOR} = 50$ km. For all plots, $V_{S30} = 400$ m/sec and $\delta Z_{1.0} = \delta Z_{2.5} = 0$.

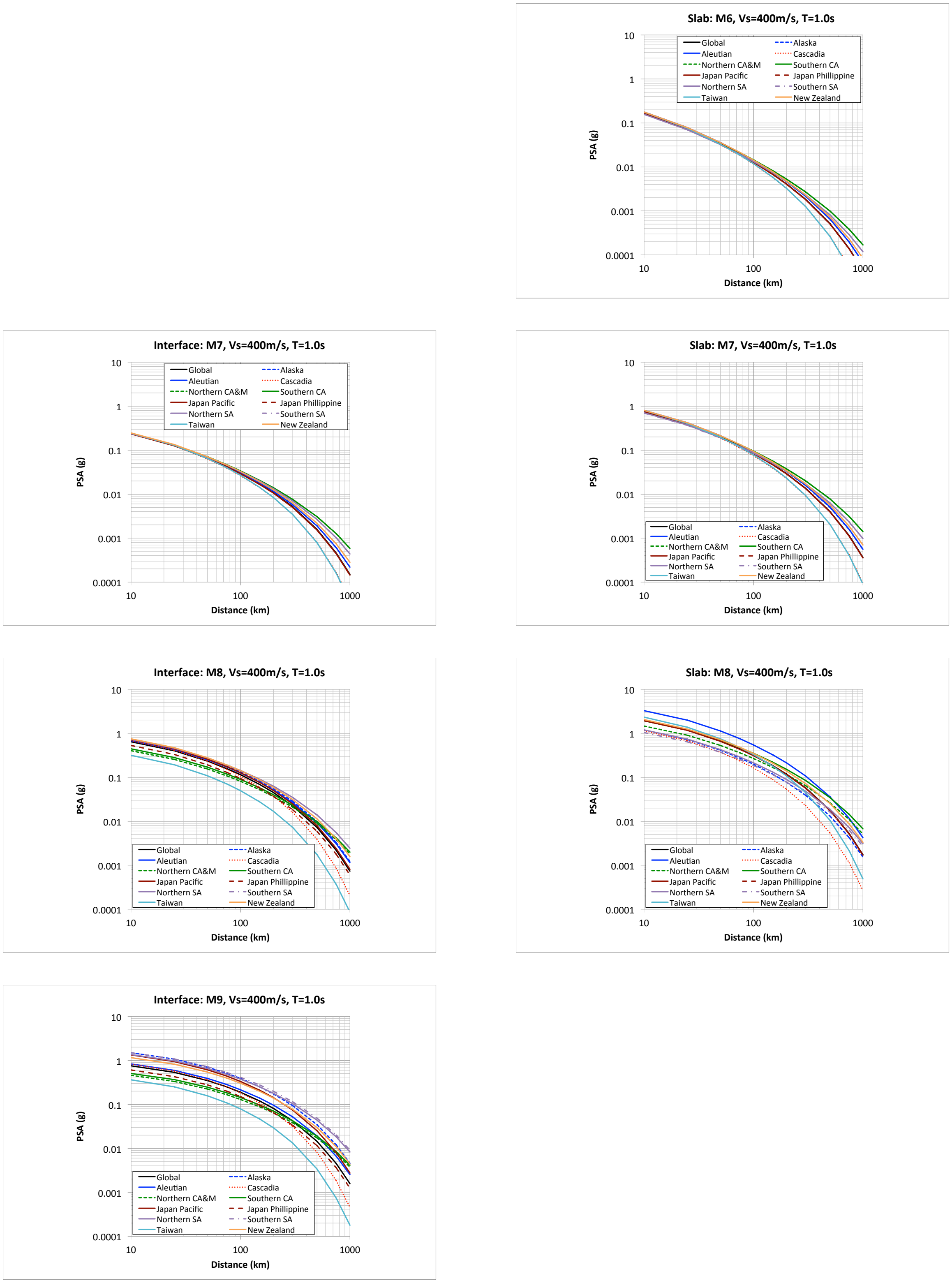

Figure 7.13: Plots of PSA at $T = 1.0$ sec: (left) interface events for M $= 7.0$, 8.0, and 9.0 with $Z_{TOR} = 10$ km; and (right) intraslab events for M $= 6.0$, 7.0, and 8.0 with $Z_{TOR} = 50$ km. For all plots, $V_{S30} = 400$ m/sec and $\delta Z_{1.0} = \delta Z_{2.5} = 0$.

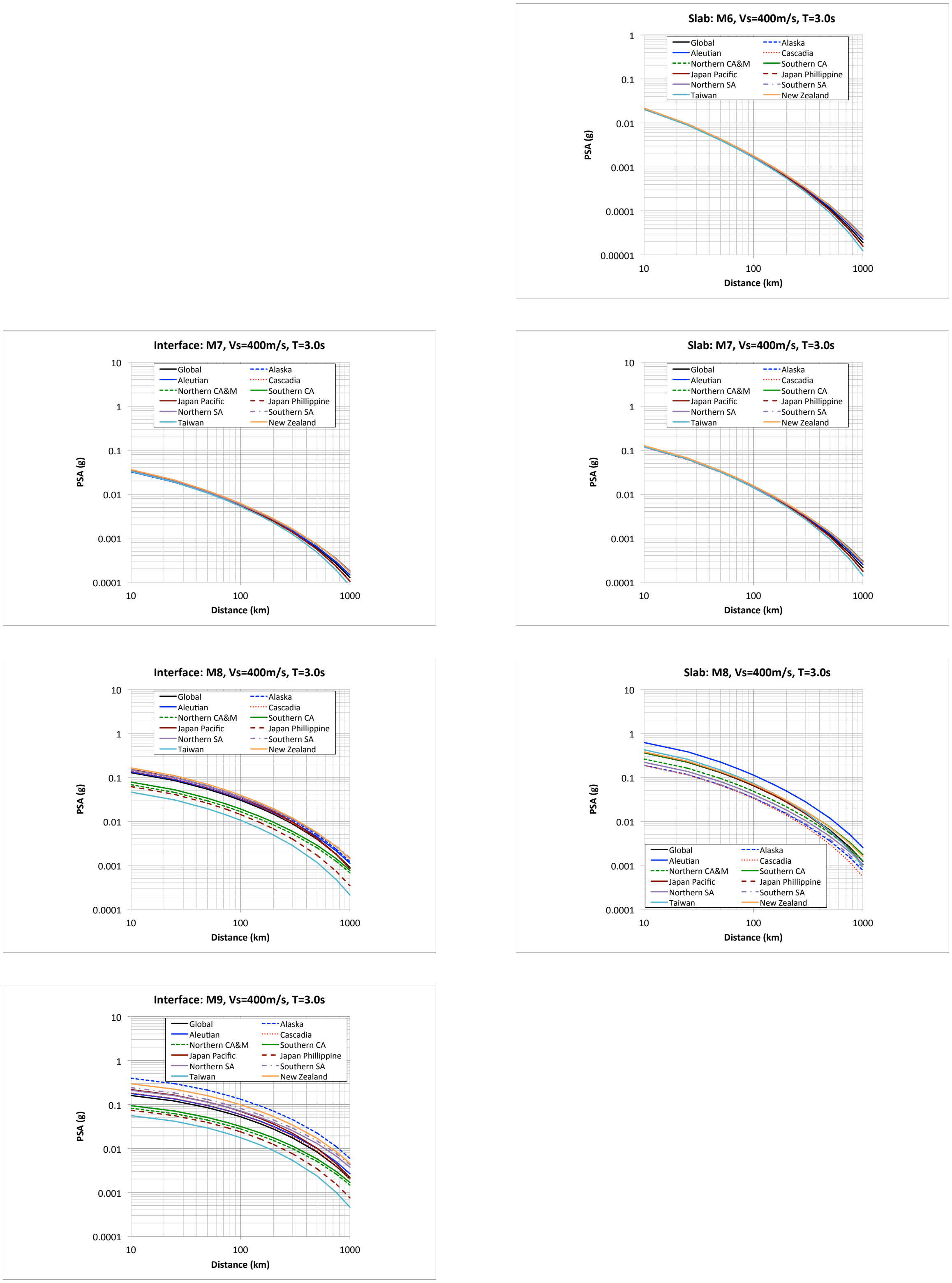

Figure 7.14: Plots of PSA at $T = 3.0$ sec: (left) interface events for M $= 7.0$, 8.0, and 9.0 with $Z_{TOR} = 10$ km; and (right) intraslab events for M $= 6.0$, 7.0, and 8.0 with $Z_{TOR} = 50$ km. For all plots, $V_{S30} = 400$ m/sec and $\delta Z_{1.0} = \delta Z_{2.5} = 0$.

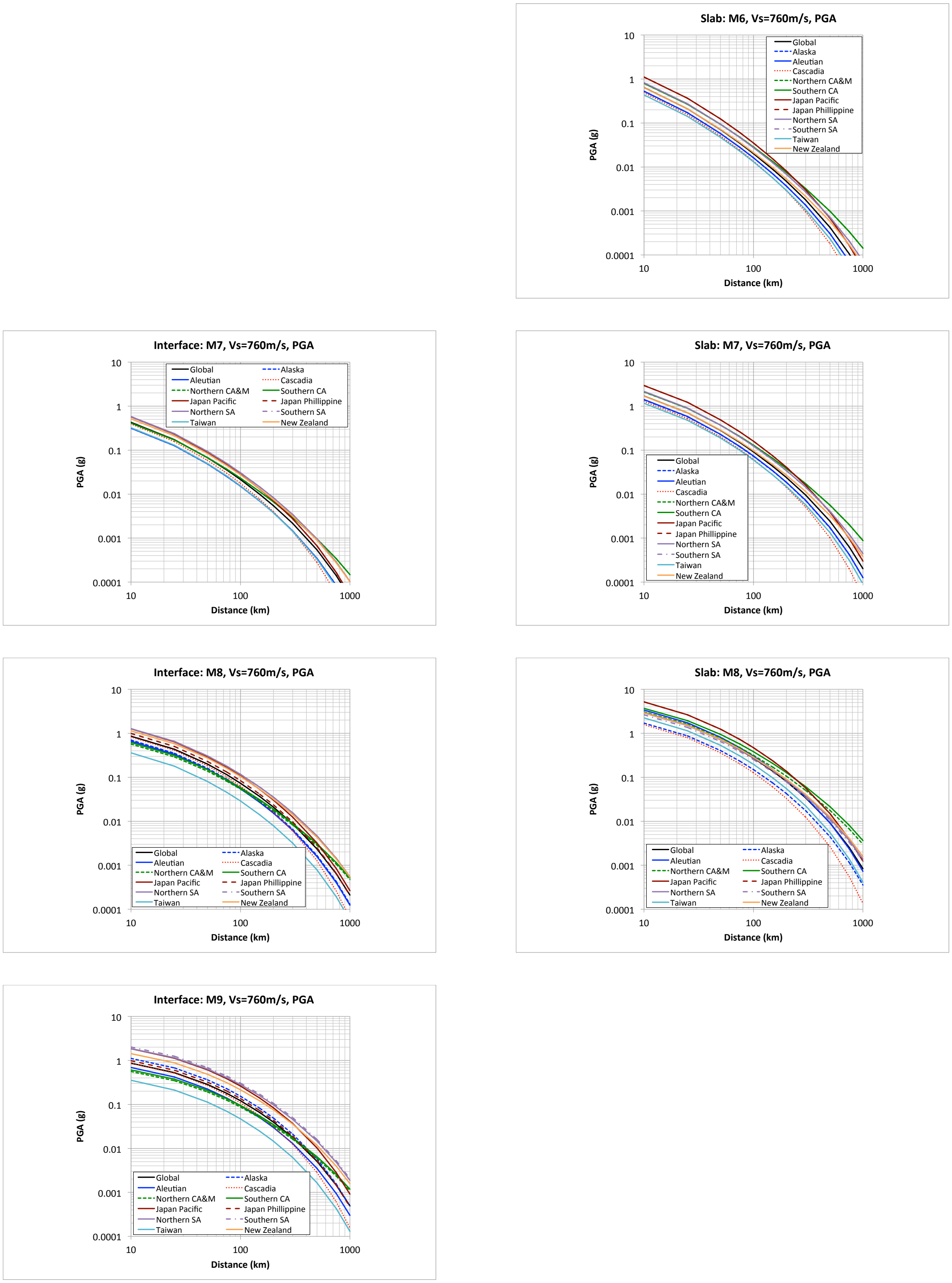

Figure 7.15: Plots of PGA: (left) interface events for M $= 7.0$, 8.0, and 9.0 with $Z_{TOR} = 10$ km; and (right) intraslab events for M $= 6.0$, 7.0, and 8.0 with $Z_{TOR} = 50$ km. For all plots, $V_{S30} = 760$ m/sec and $\delta Z_{1.0} = \delta Z_{2.5} = 0$.

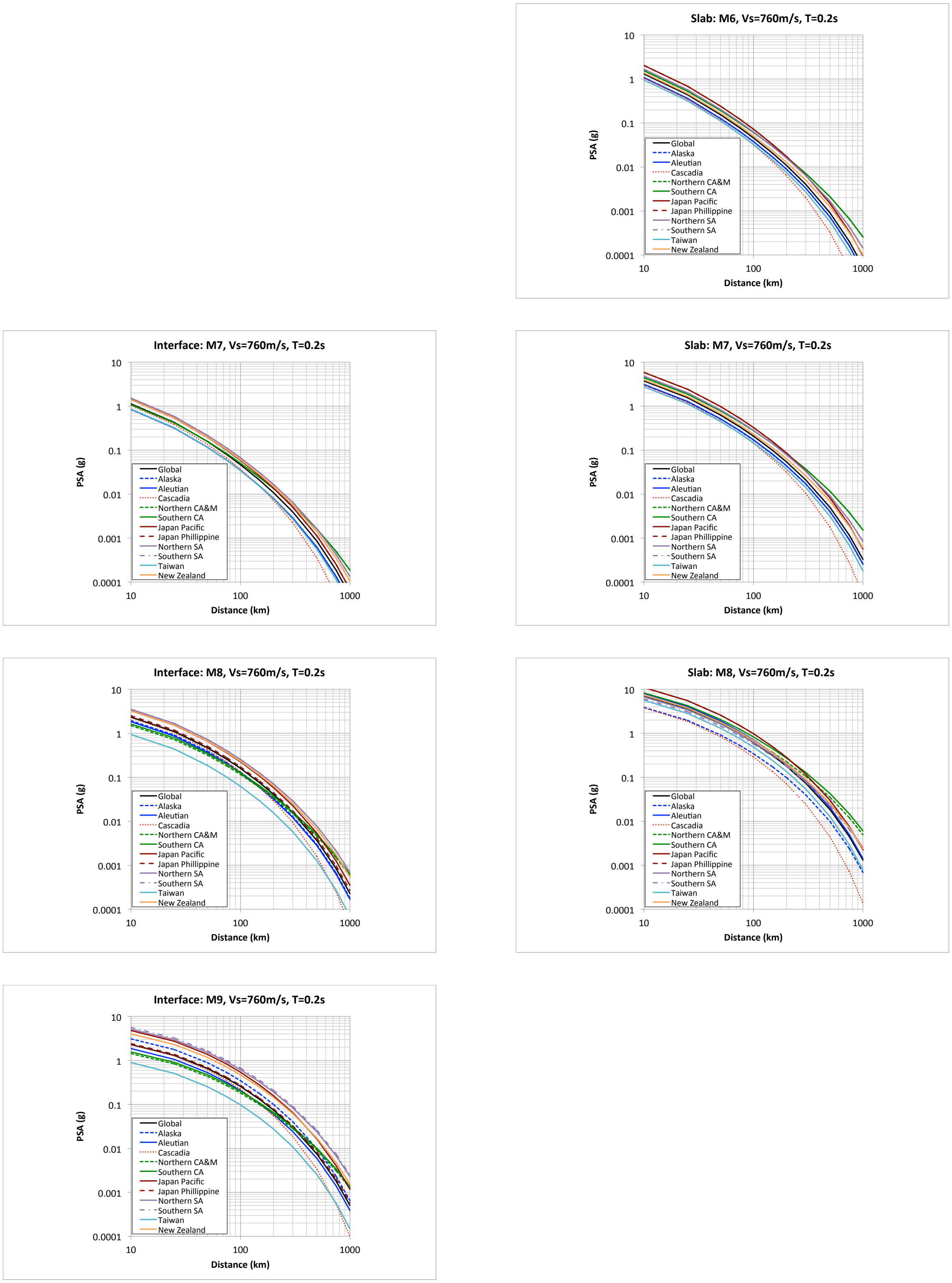

Figure 7.16: Plots of PSA at $T = 0.2$ sec: (left) interface events for M $= 7.0$, 8.0, and 9.0 with $Z_{TOR} = 10$ km; and (right) intraslab events for M $= 6.0$, 7.0, and 8.0 with $Z_{TOR} = 50$ km. For all plots, $V_{S30} = 760$ m/sec and $\delta Z_{1.0} = \delta Z_{2.5} = 0$.

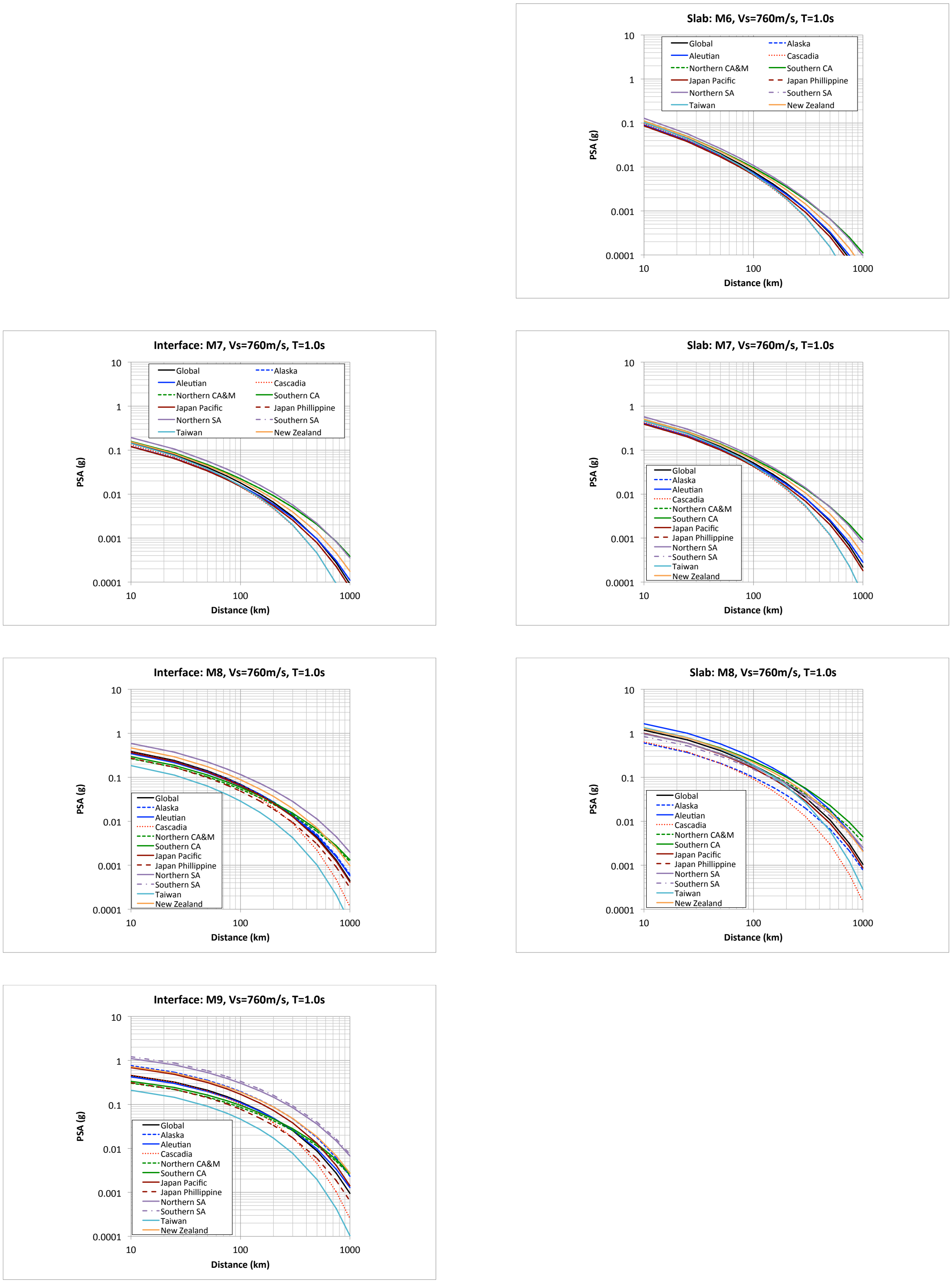

Figure 7.17: Plots of PSA at $T = 1.0$ sec: (left) interface events for M $= 7.0$, 8.0, and $9.0$with $Z_{TOR} = 10$ km; and (right) intraslab events for M $= 6.0$, 7.0, and 8.0 with $Z_{TOR} = 50$ km. For all plots, $V_{S30} = 760$ m/sec and $\delta Z_{1.0} = \delta Z_{2.5} = 0$.

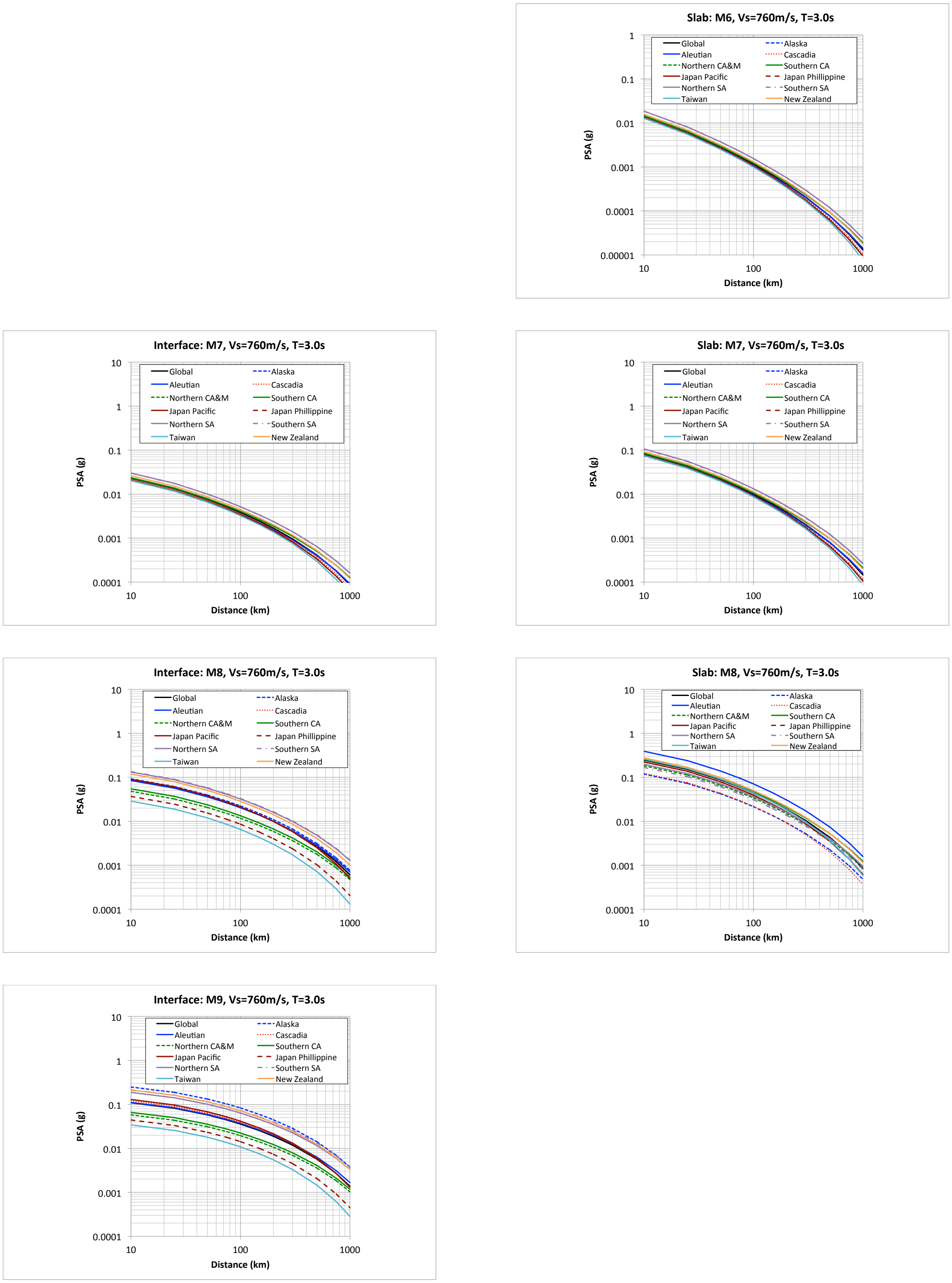

Figure 7.18: Plots of PSA at $T = 3.0$ sec: (left) interface events for M $= 7.0$, 8.0, and 9.0 with $Z_{TOR} = 10$ km; and (right) intraslab events for M $= 6.0$, 7.0, and $8.0$with $Z_{TOR} = 50$ km. For all plots, $V_{S30} = 760$ m/sec and $\delta Z_{1.0} = \delta Z_{2.5} = 0$.

7.2.2 Response Spectra

Figures 7.19 to 7.22 plots the response spectra are plotted for the 12 areas described previously over the full period range of $T = 0.01$ to 10.0 sec. Median predicted values of PSA are plotted for $\mathbf{M} = 7.0$, 8.0, and 9.0 and $Z_{TOR} = 10$ km for interface events and for $\mathbf{M} = 6.0$, 7.0, and 8.0 and $Z_{TOR} = 50$ km for intraslab events. Both types of events are evaluated for $R_{RUP} = 75$ and 200 km, $V_{S30} = 400$ and 760 m/sec, and default basin amplification. As expected, the spectra show a relatively large range in median values as a function of regional area, magnitude, distance, and spectral period. There is closer agreement in the predicted values for the longer periods of the smaller magnitude scenarios than for the intermediate-to-higher periods of the larger magnitude scenarios. Closely associated with this observation is the regional differences in breakpoint magnitude that, for example, leads to the estimates of PSA for TW having the lowest median values for the larger magnitude scenarios. Similar observations are noted for the more distant $R_{RUP} = 200$ km and $V_{S30} = 760$ m/sec scenarios.

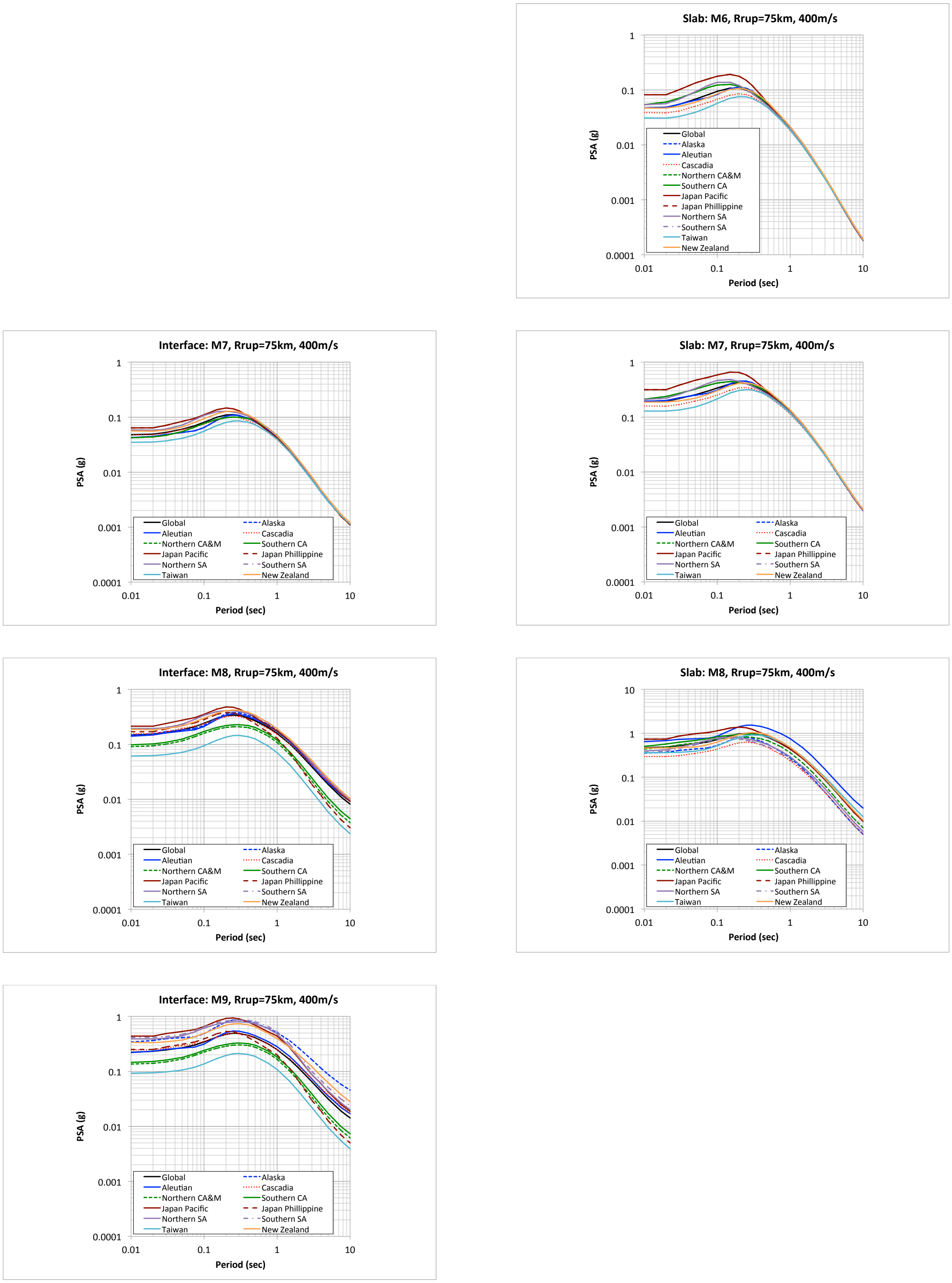

Figure 7.19: Plots of PSA response spectra: (left) interface events for M $= 7.0, 8.0$**, and** 9.0 **with** $Z_{TOR} = 10$ **km; and (right) intraslab events for M** $= 6.0, 7.0$**, and** 8.0 **with** $Z_{TOR} = 50$ **km. For all plots,** $R_{RUP} = 75$ **km,** $V_{S30} = 400$ **m/sec, and** $\delta Z_{1.0} = \delta Z_{2.5} = 0$**.**

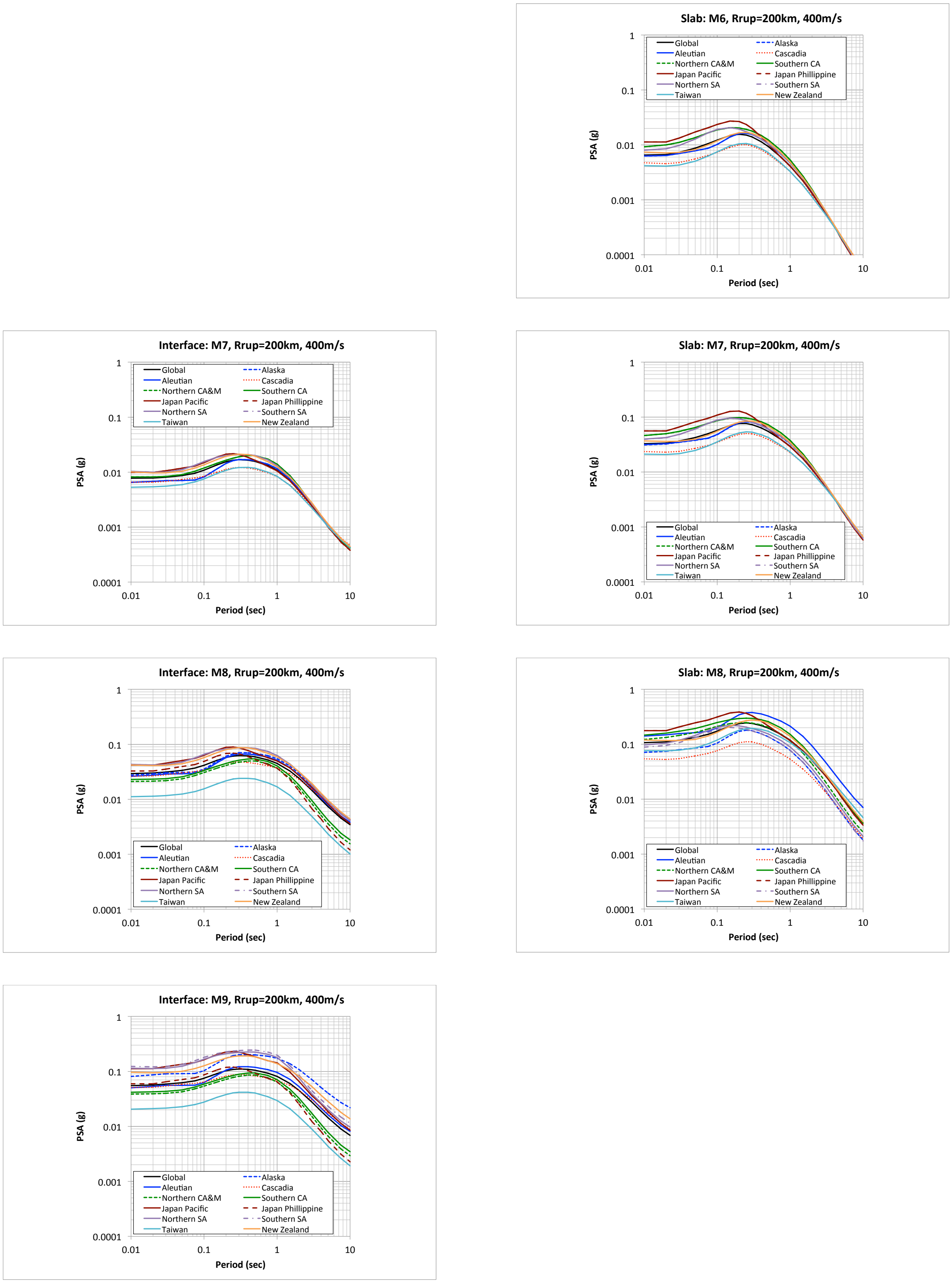

Figure 7.20: Plots of PSA response spectra: (left) interface events for M $= 7.0$, 8.0, and 9.0 with $Z_{TOR} = 10$ km; (right) intraslab events for M $= 6.0$, 7.0, and 8.0 with $Z_{TOR} = 50$ km. For all plots, $R_{RUP} = 200$ km, $V_{S30} = 400$ m/sec, and $\delta Z_{1.0} = \delta Z_{2.5} = 0$.

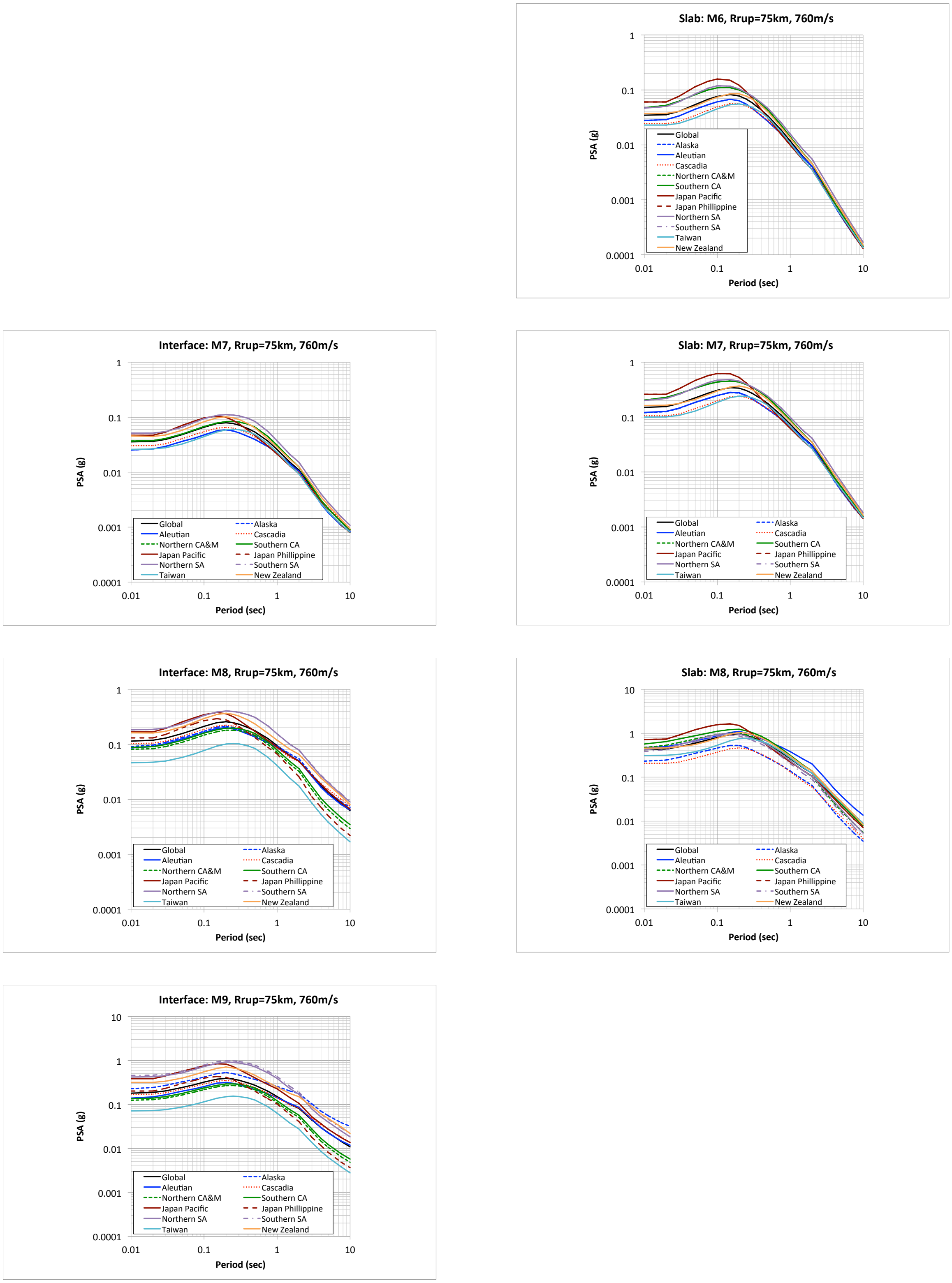

Figure 7.21: Plots of PSA response spectra: (left) interface events for M $= 7.0$, 8.0, and 9.0 with $Z_{TOR} = 10$ km; and (right) intraslab events for M $= 6.0$, 7.0, and 8.0, with $Z_{TOR} = 50$ km. For all plots, $R_{RUP} = 75$ km, $V_{S30} = 760$ m/sec, and $\delta Z_{1.0} = \delta Z_{2.5} = 0$.

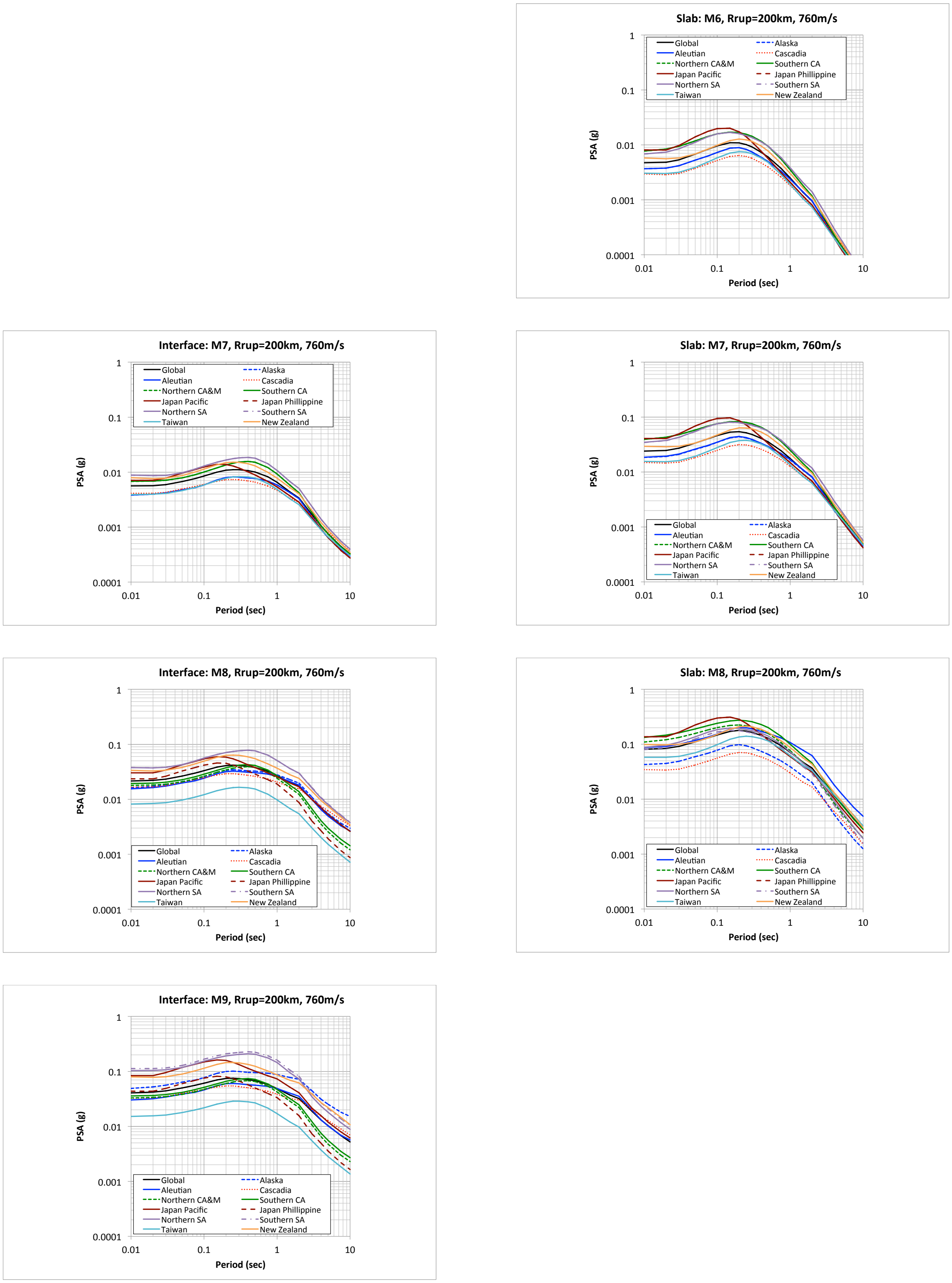

Figure 7.22: Plots of PSA response spectra: (left) interface events for M $= 7.0$**,** 8.0**, and** 9.0 **with** $Z_{TOR} = 10$ **km; and (right) intraslab events for M** $= 6.0$**,** 7.0**, and** 8.0**, with** $Z_{TOR} = 50$ **km. For all plots,** $R_{RUP} = 200$ **km,** $V_{S30} = 760$ **m/sec, and** $\delta Z_{1.0} = \delta Z_{2.5} = 0$**.**

7.2.3 Magnitude

The magnitude scaling of ground motion for the 12 areas is dependent on the regional regression parameters and breakpoint magnitudes. Median ground motions are plotted as a function of magnitude for $\mathbf{M} = 5.0 - 9.5$ for interface events and $\mathbf{M} = 5.0 - 8.5$ for intraslab events to show the impact of this regionalization on magnitude scaling. Plots are presented in Figures 7.23 to 7.26 for PSA at $T = 0.01$, 0.2, 1.0, and 3.0 sec, and $Z_{TOR} = 10$ km for interface events and $Z_{TOR} = 50$ km for intraslab events. For all plots, $R_{RUP} = 75$ km, $V_{S30} = 760$ m/sec, and $\delta Z_{1.0} = \delta Z_{2.5} = 0$ (the default basin amplification). Since the magnitude scaling is not dependent on site amplification, the results are presented only for a single value of V_{S30}.

These plots clearly show the regional dependence and importance of the breakpoint magnitudes on magnitude scaling. As noted earlier, TW has the lowest interface breakpoint magnitude ($\mathbf{M} = 7.1$), and AK and southern SA have the highest ($\mathbf{M} = 8.6$). These regional differences in breakpoint magnitudes lead to relatively large differences in median ground motions for the larger magnitude scenarios at all periods. The period-dependent regionalization of the models also contributes to the observed differences, which leads to the largest predicted ground motions in the southern SA region for $T \leq 1.0$ sec and the largest predicted ground motions in the AK region for the longer $T = 3.0$ sec period. In general, the differences in the median predictions for the regional ground motions are about a factor of 10 at the larger magnitudes.

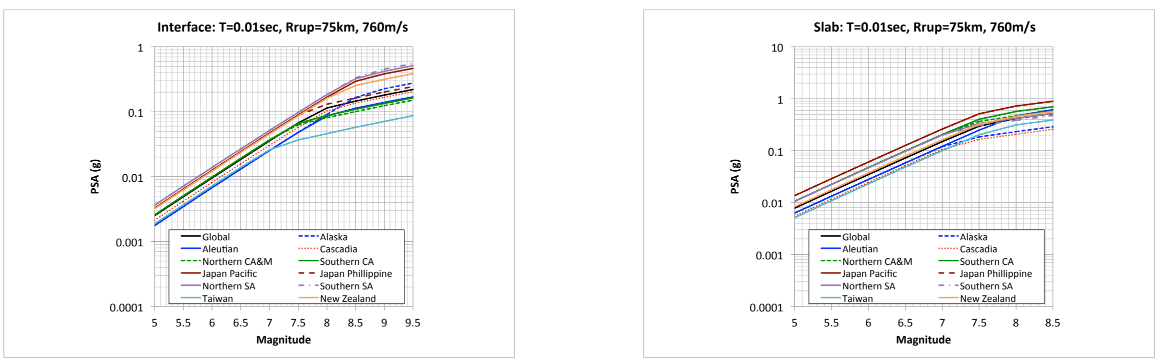

Figure 7.23: Plots of PSA at $T = 0.01$ sec versus magnitude: (left) interface events for $Z_{TOR} = 10$ km; and (right) intraslab events for $Z_{TOR} = 50$ km. For all plots, $R_{RUP} = 75$ km, $V_{S30} = 760$ m/sec, and $\delta Z_{1.0} = \delta Z_{2.5} = 0$.

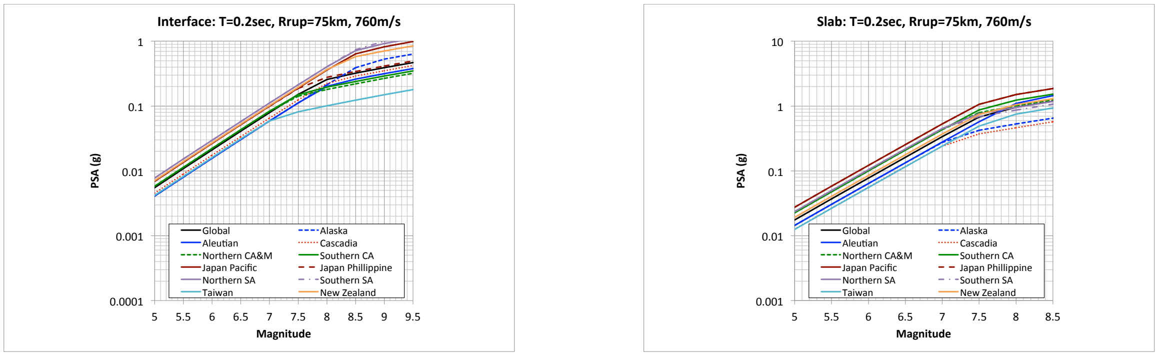

Figure 7.24: Plots of PSA at $T = 0.2$ sec versus magnitude: (left) interface events for $Z_{TOR} = 10$ km; and (right) intraslab events for $Z_{TOR} = 50$ km. For all plots, $R_{RUP} = 75$ km, $V_{S30} = 760$ m/sec, and $\delta Z_{1.0} = \delta Z_{2.5} = 0$.

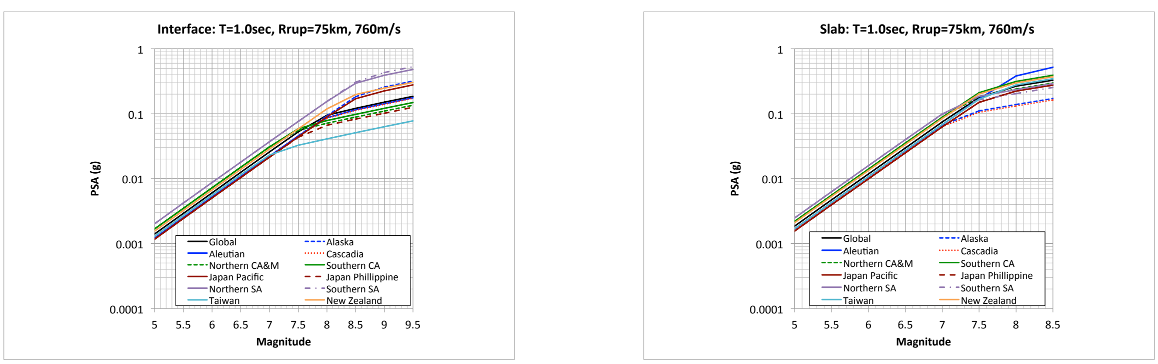

Figure 7.25: Plots of PSA at $T = 1.0$ sec versus magnitude: (left) interface events for $Z_{TOR} = 10$ km; and (right) intraslab events for $Z_{TOR} = 50$ km. For all plots, $R_{RUP} = 75$ km, $V_{S30} = 760$ m/sec, and $\delta Z_{1.0} = \delta Z_{2.5} = 0$.

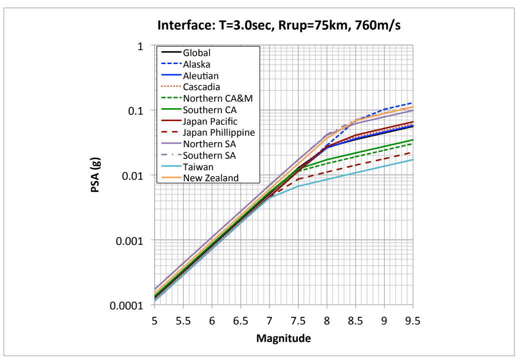

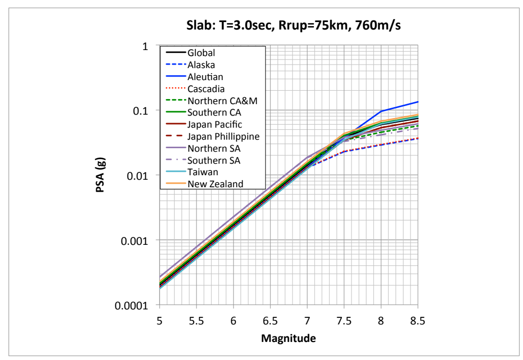

Figure 7.26: Plots of PSA at $T = 3.0$ sec versus magnitude: (left) interface events for $Z_{TOR} = 10$ km; and (right) intraslab events for $Z_{TOR} = 50$ km. For all plots, $R_{RUP} = 75$ km, $V_{S30} = 760$ m/sec, and $\delta Z_{1.0} = \delta Z_{2.5} = 0$.

7.2.4 Source Depth

The source-depth term in KBCG20 is applied globally and is not a regionalized feature of the model. It is also independent of all other predictor variables, which simplifies the plots. For interface events, median ground motions are plotted as a function of depth to the top of rupture, ranging from $Z_{TOR} = 5 - 40$ km for $\mathbf{M} = 8.0$, $R_{RUP} = 75$ km, $V_{S30} = 760$ m/sec, and $\delta Z_{1.0} = \delta Z_{2.5} = 0$. For intraslab events, median ground motions are plotted for $Z_{TOR} = 40 - 100$ km, $\mathbf{M} = 7.0$, $R_{RUP} = 100$ km, $V_{S30} = 760$ m/sec, and $\delta Z_{1.0} = \delta Z_{2.5} = 0$ (the default basin amplification). Results from the global model are presented in Figure 7.27 for PGA and PSA at $T = 0.1$, 0.2, 0.5, 1.0, 2.0, 3.0, and 5.0 sec. Based on these plots, the influence of Z_{TOR} is observed to be stronger for the shorter spectral periods than for the longer spectral periods.

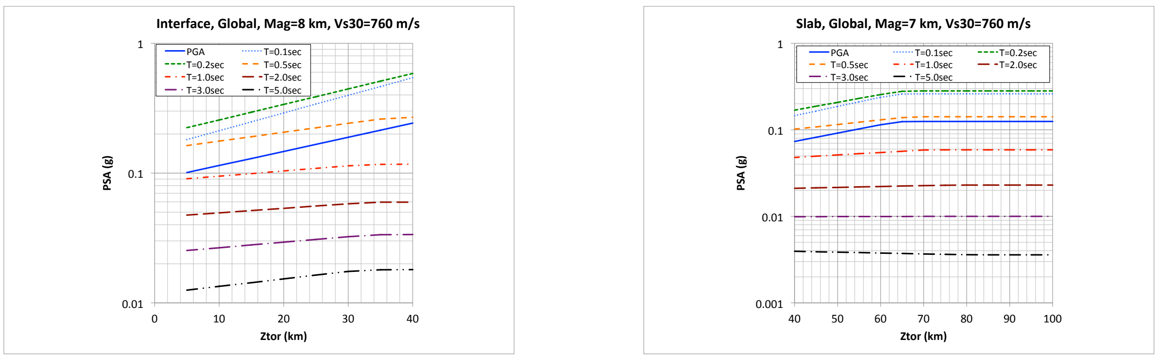

Figure 7.27: Plots of PGA and PSA at $T = 0.1 - 5.0$ sec versus depth to the top of rupture: (left) interface events for M $= 8.0$, $R_{RUP} = 75$ km; and (right) intraslab events for M $= 7.0$ and $R_{RUP} = 100$ km. For all plots, $V_{S30} = 760$ m/sec and $\delta Z_{1.0} = \delta Z_{2.5} = 0$.

7.2.5 Site Amplification

The site-amplification term is regionalized in the regression analysis. Site-amplification effects are shown by plotting response spectra for $V_{S30} = 400$ and 760 m/sec for each of the 12 areas defined previously in Figures 7.28 to 7.39. Because site amplification does not depend on subduction event type, spectra are plotted only for interface events for $\mathbf{M} = 7.0$, 8.0, and 9.0, $Z_{TOR} = 10$ km, $R_{RUP} = 75$ km, and $\delta Z_{1.0} = \delta Z_{2.5} = 0$ (default basin amplification).

These plots show that site amplification is variable across the different areas. For example, in Figure 7.29 for AK, there is amplification at all periods between predicted values of PSA between $V_{S30} = 760$ and 400 m/sec. In contrast, the amplification between the two V_{S30} values is minimal for both the northern and southern SA areas; see Figures 7.36 and 7.37. The observed site amplification for JP Pacific Plate and Philippines Sea Plate (see Figures 7.34 and 7.35) are similar for the shorter periods but increases at longer periods.

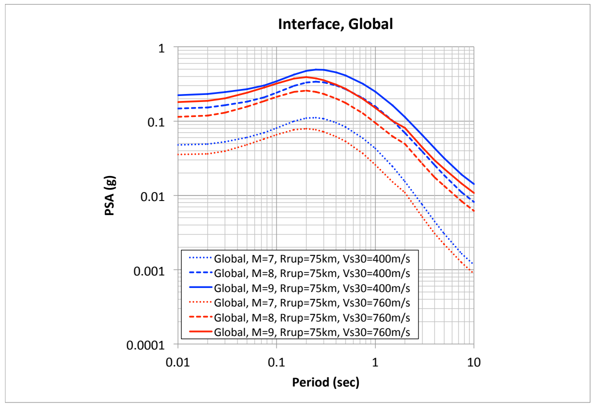

Figure 7.28: Plots of site amplification of PSA response spectra for interface events from the global model for M $= 7.0$**,** 8.0**, and** 9.0**,** $Z_{TOR} = 10$ **km,** $R_{RUP} = 75$ **km,** $V_{S30} = 400$ **and 760 m/sec, and** $\delta Z_{1.0} = \delta Z_{2.5} = 0$**.**

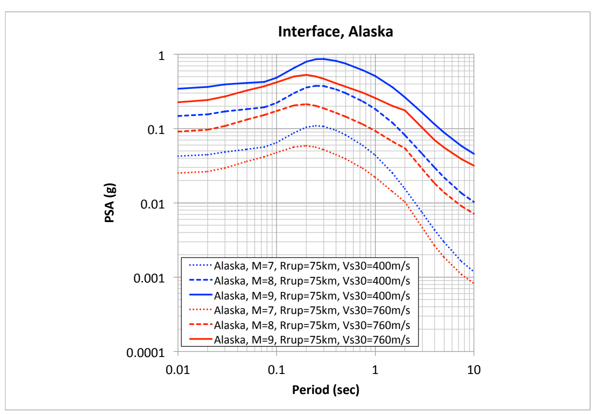

Figure 7.29: Plots of site amplification of PSA response spectra for interface events from the Alaska (AK) area for M $= 7.0$**,** 8.0**, and** 9.0**,** $Z_{TOR} = 10$ **km,** $R_{RUP} = 75$ **km,** $V_{S30} = 400$ **and 760 m/sec, and** $\delta Z_{1.0} = \delta Z_{2.5} = 0$**.**

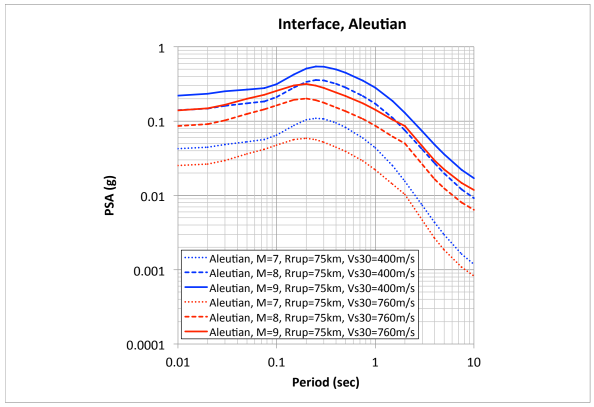

Figure 7.30: Plots of site amplification of PSA response spectra for interface events from the Alaska (AK) Aleutians model for M $= 7.0$**,** 8.0**, and** 9.0**,** $Z_{TOR} = 10$ **km,** $R_{RUP} = 75$ **km,** $V_{S30} = 400$ **and 760 m/sec, and** $\delta Z_{1.0} = \delta Z_{2.5} = 0$**.**

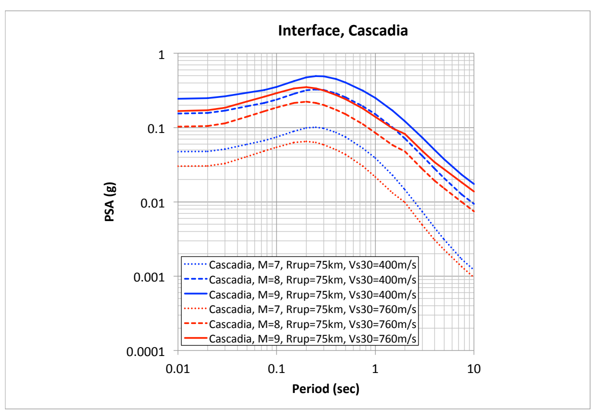

Figure 7.31: Plots of site amplification of PSA response spectra for interface events from the Cascadia (CASC) area for M $= 7.0$**,** 8.0**, and** 9.0**,** $Z_{TOR} = 10$ **km,** $R_{RUP} = 75$ **km,** $V_{S30} = 400$ **and 760 m/sec, and** $\delta Z_{1.0} = \delta Z_{2.5} = 0$**.**

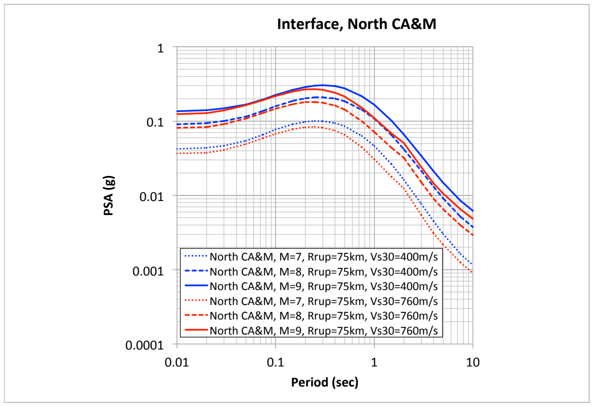

Figure 7.32: Plots of site amplification of PSA response spectra for interface events from the northern Central America and Mexico (CAM) area for M $= 7.0$**,** 8.0 **and** 9.0**,** $Z_{TOR} = 10$ **km,** $R_{RUP} = 75$ **km,** $V_{S30} = 400$ **and 760 m/sec, and** $\delta Z_{1.0} = \delta Z_{2.5} = 0$**.**

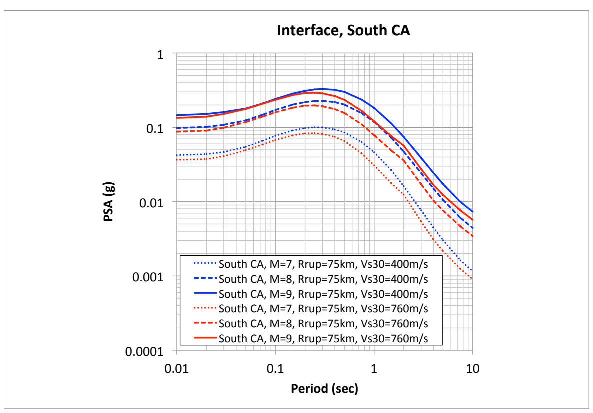

Figure 7.33: Plots of site amplification of PSA response spectra for interface events from the southern Central America (CAM) area for M $= 7.0$**,** 8.0**, and** 9.0**,** $Z_{TOR} = 10$ **km,** $R_{RUP} = 75$ **km,** $V_{S30} = 400$ **and 760 m/sec, and** $\delta Z_{1.0} = \delta Z_{2.5} = 0$**.**

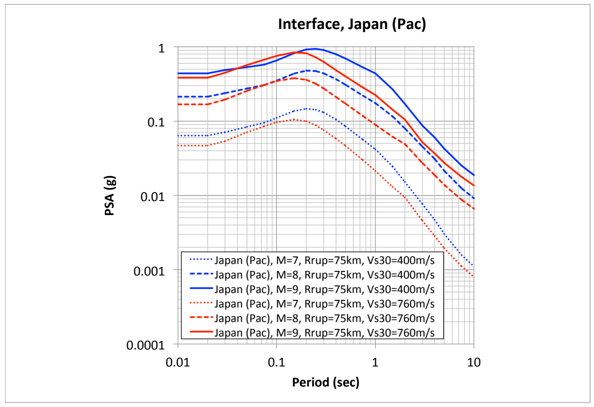

Figure 7.34: Plots of site amplification of PSA response spectra for interface events from the Japan (JP) Pacific Plate area for M $= 7.0$, 8.0, **and** 9.0, $Z_{TOR} = 10$ **km,** $R_{RUP} = 75$ **km,** $V_{S30} = 400$ **and 760 m/sec, and** $\delta Z_{1.0} = \delta Z_{2.5} = 0$.

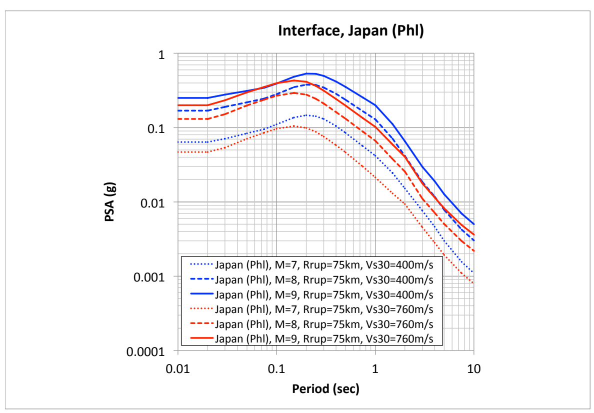

Figure 7.35: Plots of site amplification of PSA response spectra for interface events from the Japan (JP) Philippine Sea Plate area for M $= 7.0$, 8.0, **and** 9.0, $Z_{TOR} = 10$ **km,** $R_{RUP} = 75$ **km,** $V_{S30} = 400$ **and 760 m/sec, and** $\delta Z_{1.0} = \delta Z_{2.5} = 0$.

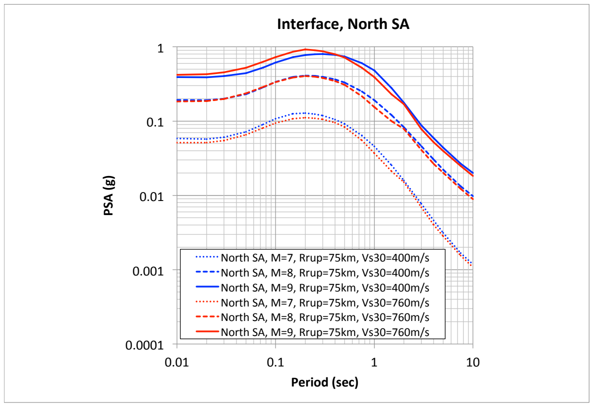

Figure 7.36: Plots of site amplification of PSA response spectra for interface events from the northern South America (SA) area for M $= 7.0$**,** 8.0**, and** 9.0**,** $Z_{TOR} = 10$ **km,** $R_{RUP} = 75$ **km,** $V_{S30} = 400$ **and 760 m/sec, and** $\delta Z_{1.0} = \delta Z_{2.5} = 0$**.**

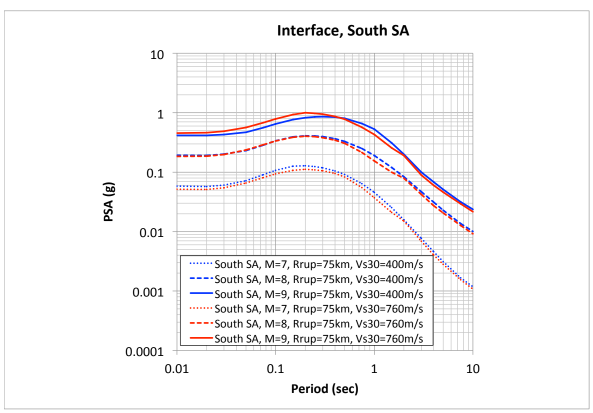

Figure 7.37: Plots of site amplification of PSA response spectra for interface events from the southern South America (SA) area for M $= 7.0$**,** 8.0**, and** 9.0**,** $Z_{TOR} = 10$ **km,** $R_{RUP} = 75$ **km,** $V_{S30} = 400$ **and 760 m/sec, and** $\delta Z_{1.0} = \delta Z_{2.5} = 0$**.**

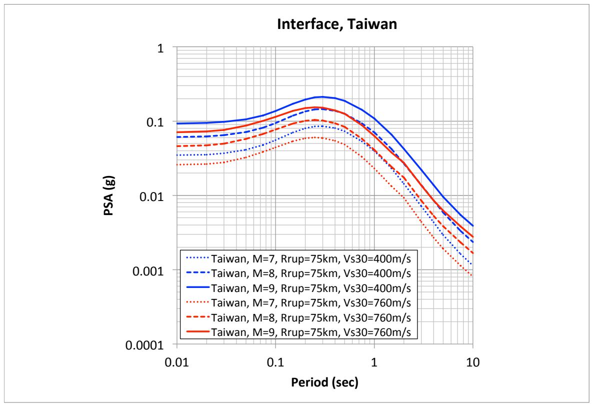

Figure 7.38: Plots of site amplification of PSA response spectra for interface events from the Taiwan (TW) area for M $= 7.0, 8.0$**, and** 9.0**,** $Z_{TOR} = 10$ **km,** $R_{RUP} = 75$ **km,** $V_{S30} = 400$ **and 760 m/sec, and** $\delta Z_{1.0} = \delta Z_{2.5} = 0$**.**

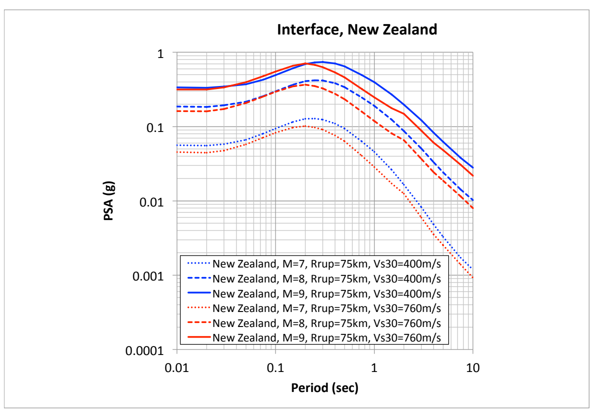

Figure 7.39: Plots of site amplification of PSA response spectra for interface events from the New Zealand (NZ) area for M $= 7.0$, 8.0**, and** 9.0**,** $Z_{TOR} = 10$ **km,** $R_{RUP} = 75$ **km,** $V_{S30} = 400$ **and 760 m/sec, and** $\delta Z_{1.0} = \delta Z_{2.5} = 0$**.**

7.2.6 Basin Amplification

Model KBCG20 includes basin-amplification terms for four regions: CASC, JP, TW, and NZ. For CASC, there is a further refinement of whether a site is located inside or outside of the Seattle Basin. Sites within the Seattle Basin are modeled with a constant basin-amplification factor that is independent of both basin depth and V_{S30} based on the available data but a function of spectral period. For sites located outside of the Seattle Basin and in JP, the basin-amplification factor is a function of $Z_{2.5}$; for NZ and TW, it is a function of $Z_{1.0}$. The model dependency for these four basin zones is shown in Figure 7.40. The basin-amplification factors apply to both interface and intraslab events in these four regions. Except for the Seattle Basin, the only predictor variable that basin amplification is dependent on (other than basin depth) is the value of V_{S30} in the case of default basin effects (i.e., for $\delta Z_{1.0} = \delta Z_{2.5} = 0$).

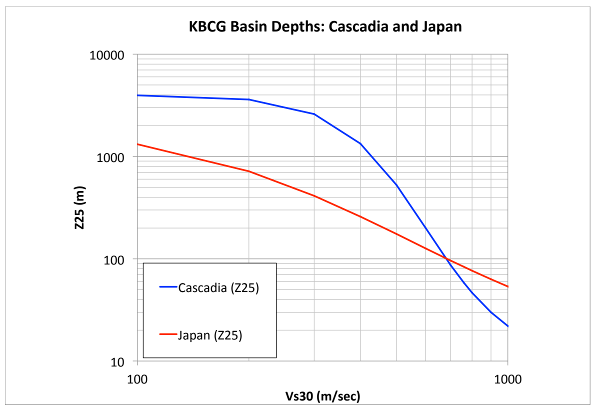

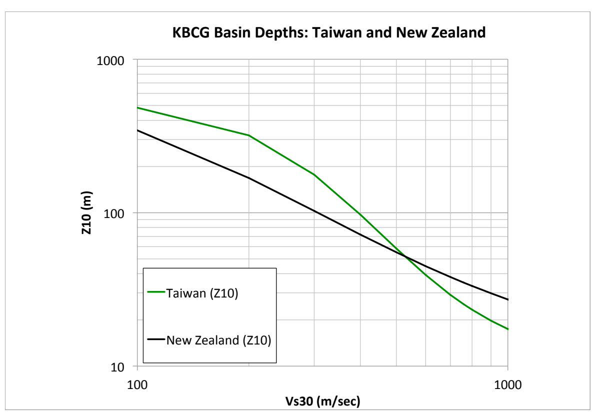

Figure 7.40: Plots of default basin depth as a function of V_{S30}: (top) $Z_{2.5}$ for Cascadia (CASC) and Japan (JP); and (bottom) $Z_{1.0}$ for Taiwan (TW) and New Zealand (NZ).

The following figures show the effects of basin amplifications on PSA response spectra. For CASC, the plots are presented for **M** = 8.0, $Z_{TOR} = 10$ km, $R_{RUP} = 100$ km, $V_{S30} = 400$ m/sec, and $Z_{2.5} = 3.0 - 7.0$ km. The default value of $Z_{2.5}$ is 1.34 km for this value of V_{S30}. The basin-amplification ratios (i.e., the spectral ratios of PSA for a given value of $Z_{2.5}$ divided by that for $Z_{2.5} = 1.34$ km) are shown in Figure 7.41. For $T < 0.4$ sec, the basin-amplification ratios are less than 1.0, indicating a decrease in ground motions. For longer periods, the basin-amplification ratios are greater than 1.0 and are a function of $Z_{2.5}$ for sites not located in the Seattle Basin. For the deepest depths ($Z_{2.5} = 7.0$ km), the basin-amplification ratios for sites located outside of the Seattle Basin approach those located inside the basin as expected, given that all of the Seattle Basin sites in the database are within the deeper parts of the basin.

Ground-motion simulations conducted as part of the "M9 Project" (Wirth and Frankel, 2019; Frankel et al., 2018; Wirth et al., 2018) have indicated that the amplifications influenced by the Seattle Basin can be significant, especially in the longer spectral period range from interface events. Based on the results of these studies and a related USGS workshop (Wirth et al., 2018), the Seattle Department of Construction and Inspections adopted a requirement (SDCI, 2018) that all tall building designs utilizing site-specific ground-motion procedures must incorporate basin effects for those buildings located in the city of Seattle (i.e., within the Seattle Basin). Prior to the NGA-Sub Project, subduction GMMs did not explicitly model basin amplification but several of the NGA-Sub GMMs, including KBCG20, now incorporate a basin-amplification term.

The Seattle Basin amplification factors recommended by SDCI (2018) are plotted in Figure 7.42, along with the basin-amplification factor for Seattle Basin sites from KBCG20. These results are for **M** = 8.0, $Z_{TOR} = 10$ km, $R_{RUP} = 100$ km, and $V_{S30} = 600$ m/sec. This value of V_{S30} corresponds to the value of V_{S30} in the ground-motion simulations used to develop the recommended amplification factors. The KBCG20 basin amplification term for the Seattle Basin is independent of $Z_{2.5}$ as discussed above. Overall, similar amplifications are observed at the longer spectral period range, although the KBCG20 factors are somewhat lower.

For JP, basin-amplification ratios are shown in Figure 7.43 for the same earthquake scenarios used for CASC. In this case, the default value of $Z_{2.5}$ is 0.26 km. Because of the much shallower basin depths compared to CASC, ratios are presented for $Z_{2.5} = 0.5 - 0.7$ km. This region has the same general period dependence of the spectral-amplification ratios as CASC (i.e., less than 1.0 for $T < 0.4$ sec and greater than 1.0 for longer periods). For the longer periods, there is a notable increase in the basin-amplification ratio with increasing values of $Z_{2.5}$.

For TW, basin-amplification ratios are presented in Figure 7.44 for the same earthquake scenarios used for CASC. Unlike CASC and JP, the TW basin-amplification term is based on $Z_{1.0}$ rather than $Z_{2.5}$. In this case, the default value of $Z_{1.0}$ is 0.097 km. Because of the shallower basin depths, ratios are presented for $Z_{1.0} = 0.3 - 0.7$ km. The basin-amplification ratios for TW are greater than 1.0 at all periods. They are approximately constant at a relatively small factor for $T < 0.4$ sec and increase at longer periods and deeper depths.

For NZ, basin-amplification ratios are presented for the same earthquake scenarios as CASC in Figure 7.45. Unlike CASC and JP, the NZ basin-amplification term is based on $Z_{1.0}$ rather than $Z_{2.5}$. In this case, the default value of $Z_{1.0}$ is 0.072 km. Because of the shallower basin depths, ratios are presented for $Z_{1.0} = 0.3 - 0.7$ km. The basin-amplification ratios NZ are greater than 1.0 for spectral periods greater than 0.75 sec. For spectral periods between 0.75 sec to about 0.3 sec, the basin-amplification factor decreases. For spectral periods less than about 0.3 sec, the basin factor is approximately constant.

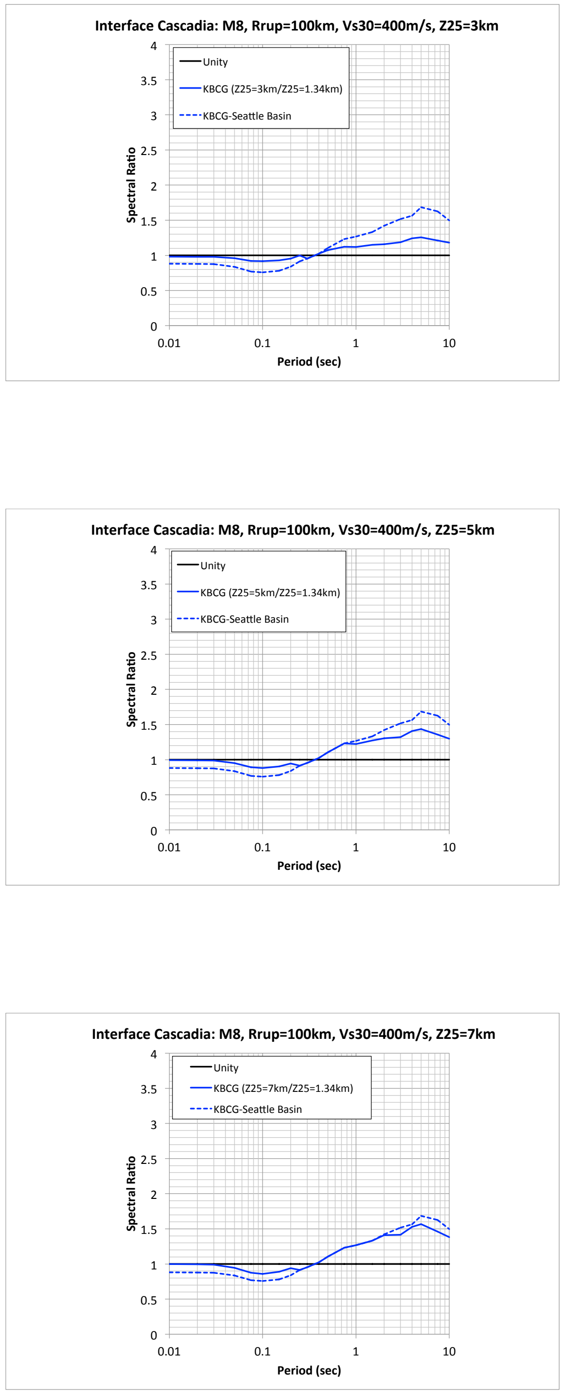

Figure 7.41: Plots of basin-amplification ratios for Cascadia (CASC) with respect to the default basin depth of $Z_{2.5} = 1.34$ km for interface events: (top) $Z_{2.5} = 3.0$ km; (middle) $Z_{2.5} = 5.0$ km; and (bottom) $Z_{2.5} = 7.0$ km. For all plots, M = 8.0, $Z_{TOR} = 10$ km, $R_{RUP} = 100$ km, and $V_{S30} = 400$ m/sec.

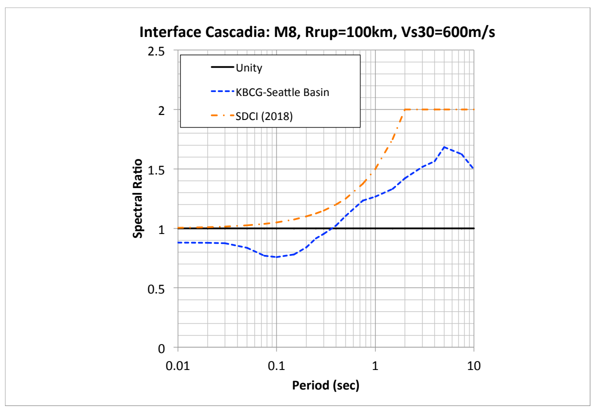

Figure 7.42: Plots of basin-amplification ratios for Cascadia (CASC) Seattle Basin from KBCG20 and SDCI (2018) for interface events, M = 8.0, $Z_{TOR} = 10$ km, $R_{RUP} = 100$ km, and $V_{S30} = 600$ m/sec.

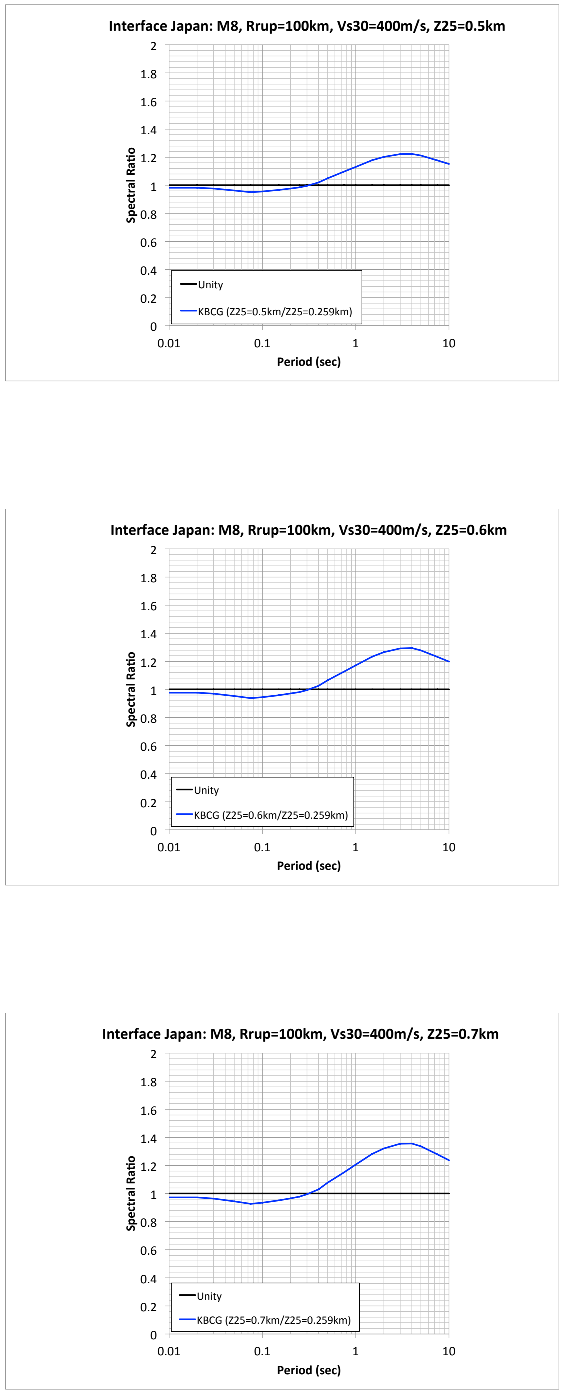

Figure 7.43: Plots of basin amplification ratios for Japan (JP) with respect to the default basin depth of $Z_{2.5} = 0.26$ km for interface events: (top) $Z_{2.5} = 0.5$ km, (middle) $Z_{2.5} = 0.6$ km, and (bottom) $Z_{2.5} = 0.7$ km. For all plots, M = 8.0, $Z_{TOR} = 10$ km, $R_{RUP} = 100$ km, and $V_{S30} = 400$ m/sec.

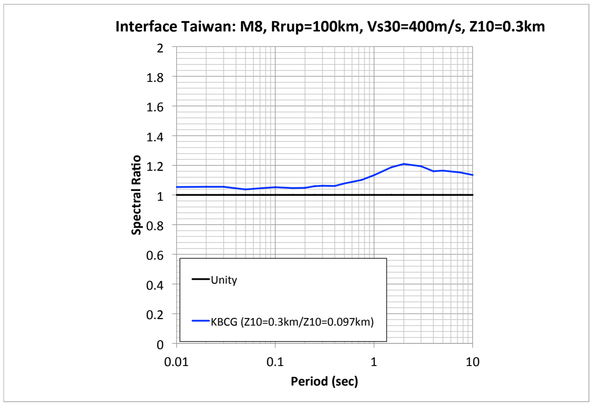

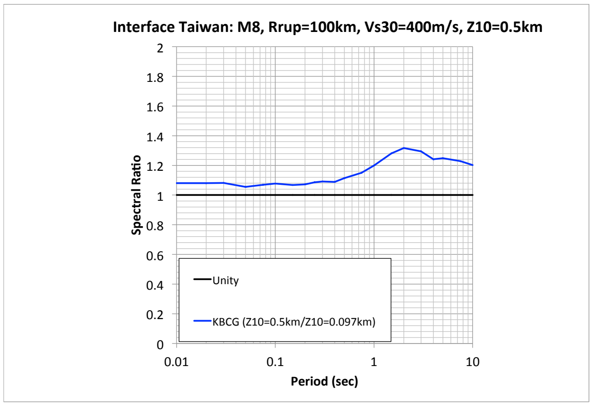

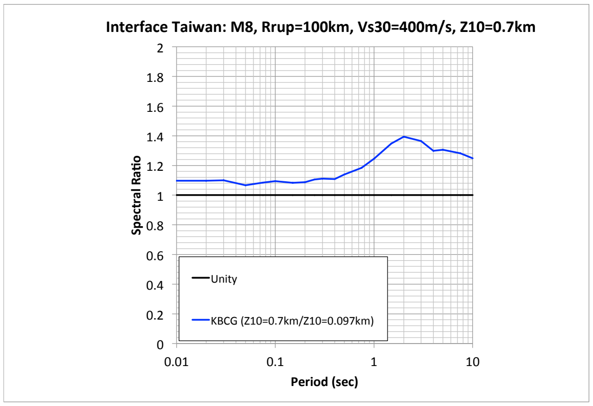

Figure 7.44: Plots of basin-amplification ratios for Taiwan (TW) with respect to the default basin depth of $Z_{1.0} = 0.097$ km for interface events: (top) $Z_{2.5} = 0.3$ km, (middle) $Z_{2.5} = 0.5$ km, and (bottom) $Z_{2.5} = 0.7$ km. For all plots, M = 8.0, $Z_{TOR} = 10$ km, $R_{RUP} = 100$ km, and $V_{S30} = 400$ m/sec.

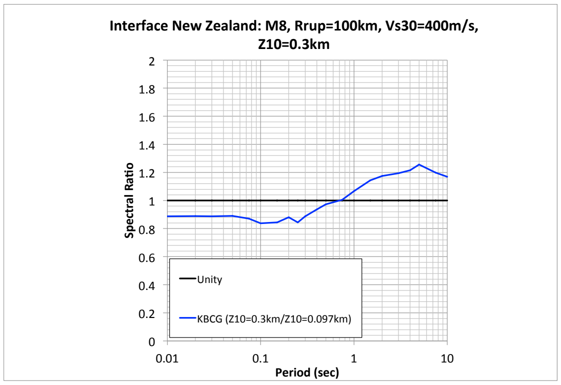

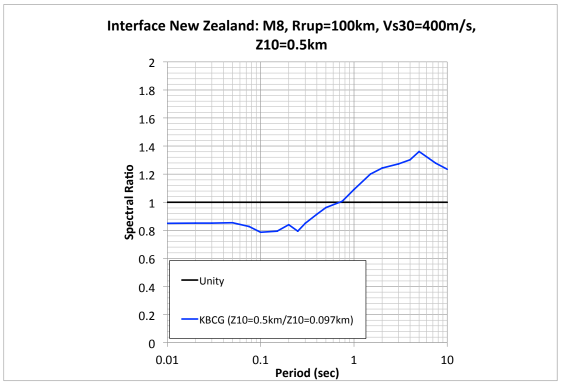

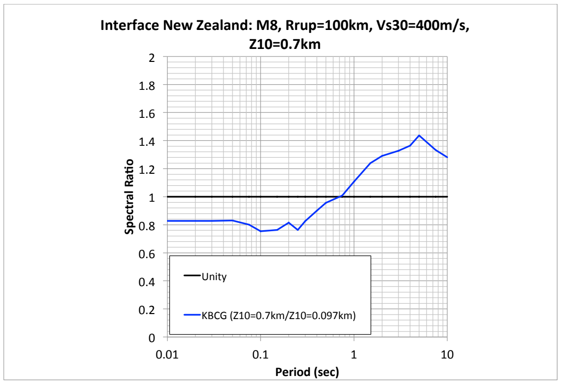

Figure 7.45: Plot of basin-amplification ratios for New Zealand (NZ) with respect to the default basin depth of $Z_{1.0} = 0.072$ km for interface events: (top) $Z_{2.5} = 0.3$ km, (middle) $Z_{2.5} = 0.5$ km, and (bottom) $Z_{2.5} = 0.7$ km. For all plots, M = 8.0, $Z_{TOR} = 10$ km, $R_{RUP} = 100$ km, $V_{S30} = 400$ m/sec, and $Z_{1.0}$ values of (top) 0.3 km, (middle) 0.5 km, and (bottom) 0.7 km.

7.3 COMPARISON WITH PUBLISHED MODELS

This section compares predicted ground motions for interface and intraslab events from KBCG20 with those from a selected set of subduction GMMs. As noted earlier in the report, these selected GMMs consist of those used by the USGS in the development of the 2014 National Seismic Hazard Maps and two additional GMMs published since these maps were released. They do not represent a complete and exhaustive suite of available subduction GMMs, which is beyond the scope of this report. To be consistent with the majority of the GMMs, these comparisons are for forearc regions, which are either only for forearc regions or do not distinguish between forearc and backarc regions.

The following published models are presented in the comparisons:

- Atkinson and Boore (2003, 2008) [AB08]
- Atkinson and Macias (2009) [AM09]
- Zhao et al. (2006) [Zea06]
- Zhao et al. (2016) [Zea16]
- BCHydro (Abrahamson et al., 2016) [BCH]
- BCHydro Update for USGS (Abrahamson et al., 2018) [BCHU]

Model AM09 is only valid for interface events and where $V_{S30} = 760$ m/sec. The development and applicability of these selected GMMs was presented earlier in the report. A selected set of comparisons is presented that is similar to the previously presented plots for KBCG20. It is expected that prior to use of the KBCG20 model in any seismic hazard study, similar types of comparisons should be made and considered based on the region of interest and the site-specific seismic sources expected to control the seismic hazard.

7.3.1 Attenuation

Figures 7.46 to 7.49 plot the median interface and intraslab event attenuation curves for PGA and PSA at $T = 0.2$, 1.0, and 3.0 sec, $V_{S30} = 400$ and 760 m/sec, and $\delta Z_{1.0} = \delta Z_{2.5} = 0$ (the default basin amplification). For interface events, $\mathbf{M} = 7.0$, 8.0, and 9.0 and $Z_{TOR} = 10$ km, and for intraslab events, $\mathbf{M} = 6.0$, 7.0, and 8.0 and $Z_{TOR} = 50$ km, Note that the older GMMs are not defined as a continuous function of V_{S30}; for these comparisons an applicable site category is selected. In addition, these attenuation curves are shown for distances up to 1000 km, which falls outside of the recommended distance range for the older GMMs. They are plotted to these distances to show what happens when they are extrapolated beyond their recommended distance range.

KBCG20 predictions are evaluated for the following four geographic regions: Global (blue line with squares), CASC (green line with circles), JP Pacific Plate (red line with diamonds), and

JP Philippine Sea Plate (black line with triangles). These four regional predictions are the closest comparison to the previous models based on their predominate datasets (e.g., Zea06 and Zea16 for use in JP) or their development for application in a specific region (e.g., AM09 and BCHU for use in CASC).

For PGA and $T = 0.2$ sec, the attenuation curves are comparable among all of the GMMs for the smaller magnitude scenarios and for distances of about 60 to 100 km. For larger magnitudes and distances outside of this range, there are notable differences between the attenuation curves. Similar observations are noted for the longer periods, with a large variation in the rate of attenuation between AB08 and BCH at larger distances. Also, the smaller breakpoint magnitude for the KBCG20 JP Philippine Sea Plate area leads to overall lower ground motions for the larger magnitude scenario at all distances.

Figures 7.50 to 7.53 show similar plots for $V_{S30} = 760$ m/sec. Similar observations are noted for these comparisons as were found for the $V_{S30} = 400$ m/sec scenarios.

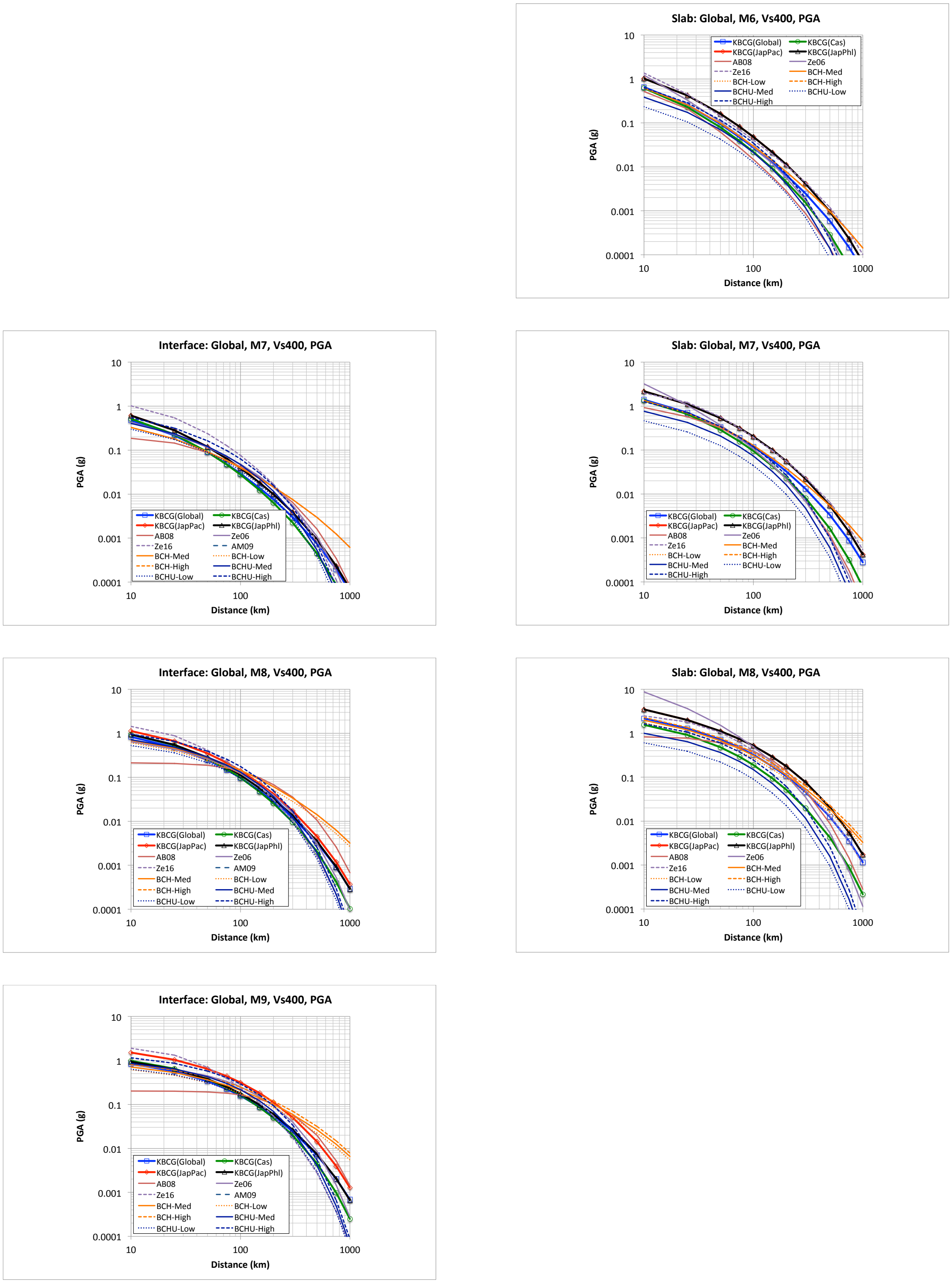

Figure 7.46: Plots of PGA ($T = 0$) versus distance comparing KBCG20 with selected published models: (left) interface events for M $= 7.0$, 8.0, and 9.0 with $Z_{TOR} = 10$ km; and (right) intraslab events for M $= 6.0$, 7.0, and 8.0 with $Z_{TOR} = 50$ km. For all plots, $V_{S30} = 400$ m/sec and $\delta Z_{1.0} = \delta Z_{2.5} = 0$.

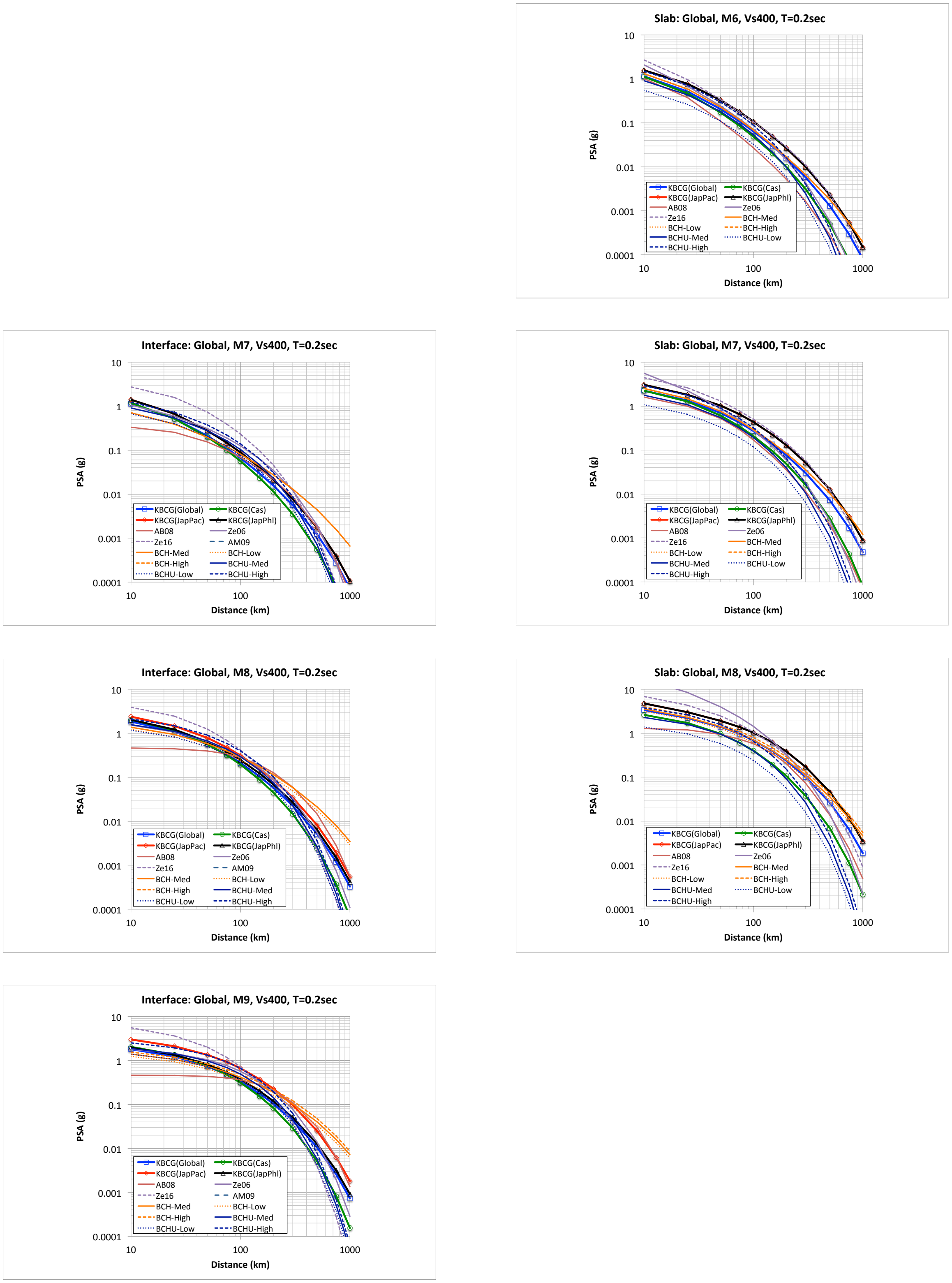

Figure 7.47: Plots of PSA at $T = 0.2$ sec versus distance comparing KBCG20 with selected published models: (left) interface events for **M** $= 7.0$, 8.0, and 9.0 with $Z_{TOR} = 10$ km; and (right) intraslab events for **M** $= 6.0$, 7.0, and 8.0 with $Z_{TOR} = 50$ km. For all plots, $V_{S30} = 400$ m/sec and $\delta Z_{1.0} = \delta Z_{2.5} = 0$.

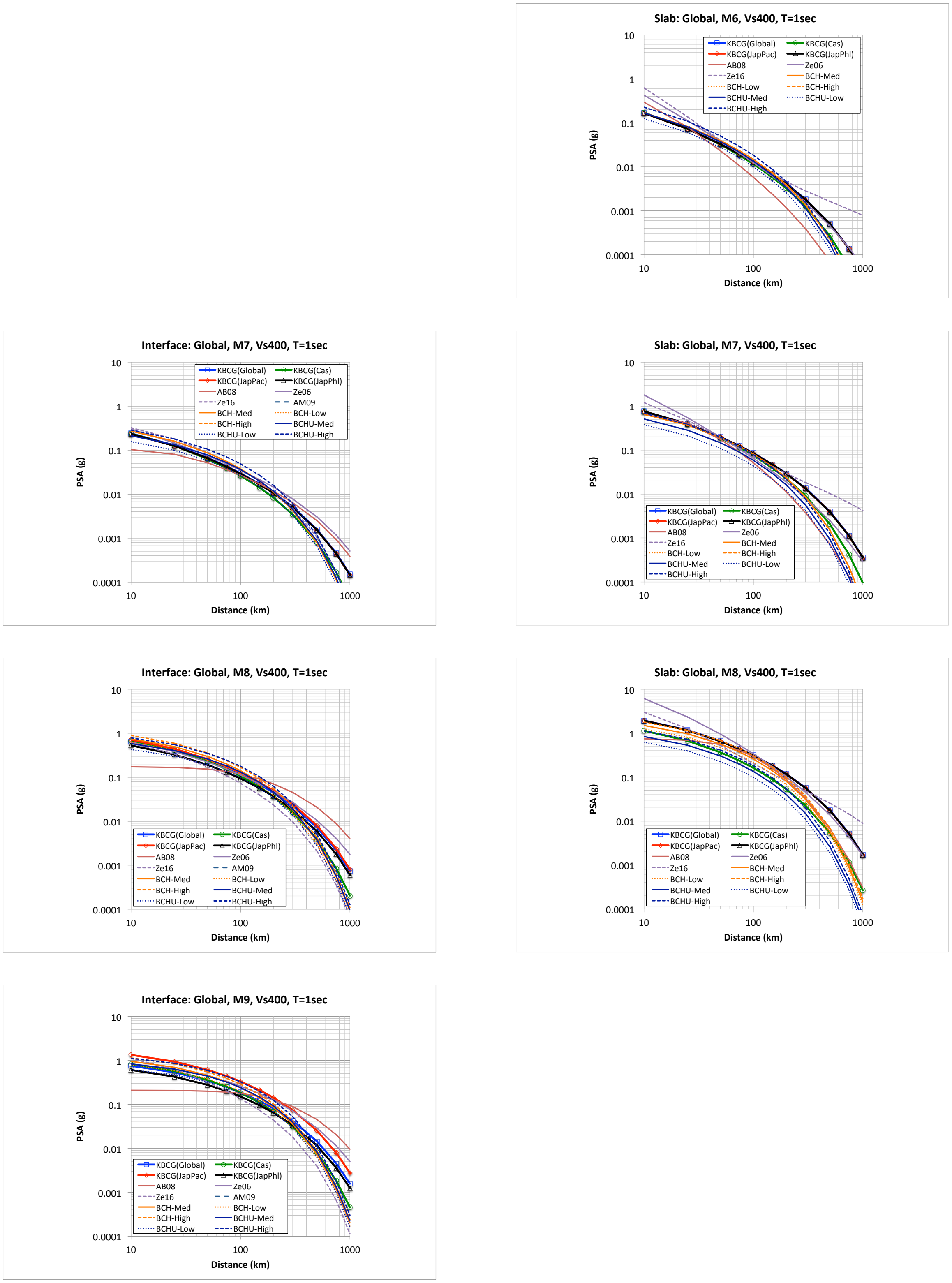

Figure 7.48: Plots of PSA at $T = 1.0$ sec versus distance comparing KBCG20 with selected published models: (left) interface events for M $= 7.0$, 8.0, and 9.0 with $Z_{TOR} = 10$ km; and (right) intraslab events for M $= 6.0$, 7.0, and 8.0 with $Z_{TOR} = 50$ km. For all plots, $V_{S30} = 400$ m/sec and $\delta Z_{1.0} = \delta Z_{2.5} = 0$.

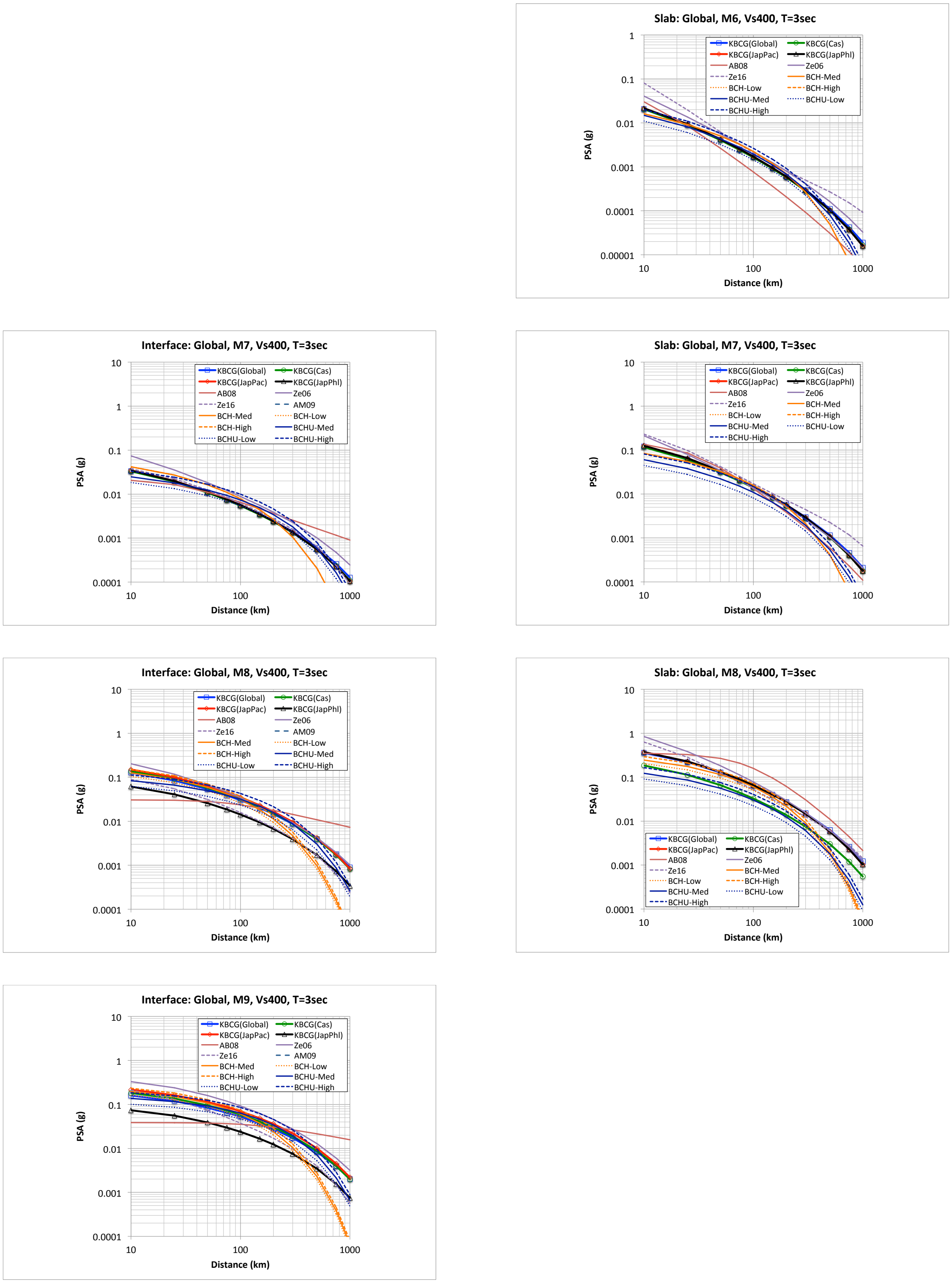

Figure 7.49: Plots of PSA at $T = 3.0$ sec versus distance comparing KBCG20 with selected published models: (left) interface events for M $= 7.0$, 8.0, and 9.0 with $Z_{TOR} = 10$ km; and (right) intraslab events for M $= 6.0$, 7.0, and 8.0 with $Z_{TOR} = 50$ km. For all plots, $V_{S30} = 400$ m/sec and $\delta Z_{1.0} = \delta Z_{2.5} = 0$.

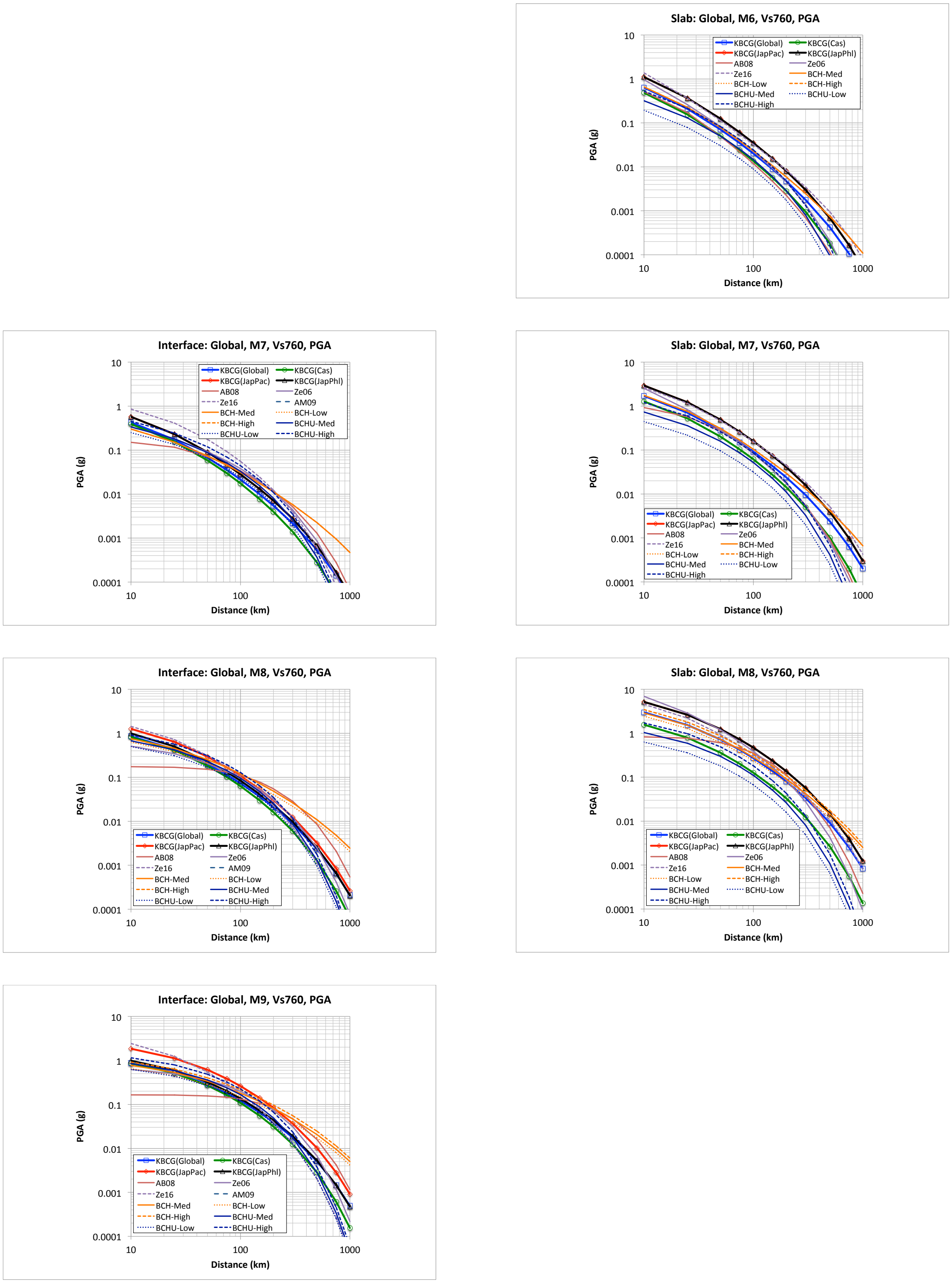

Figure 7.50: Plots of PGA ($T = 0$) versus distance comparing KBCG20 with selected published models: (left) interface events for M $= 7.0$, 8.0, and 9.0 with $Z_{TOR} = 10$ km; and (right) intraslab events for M $= 6.0$, 7.0, and 8.0 with $Z_{TOR} = 50$ km. For all plots, $V_{S30} = 760$ m/sec and $\delta Z_{1.0} = \delta Z_{2.5} = 0$.

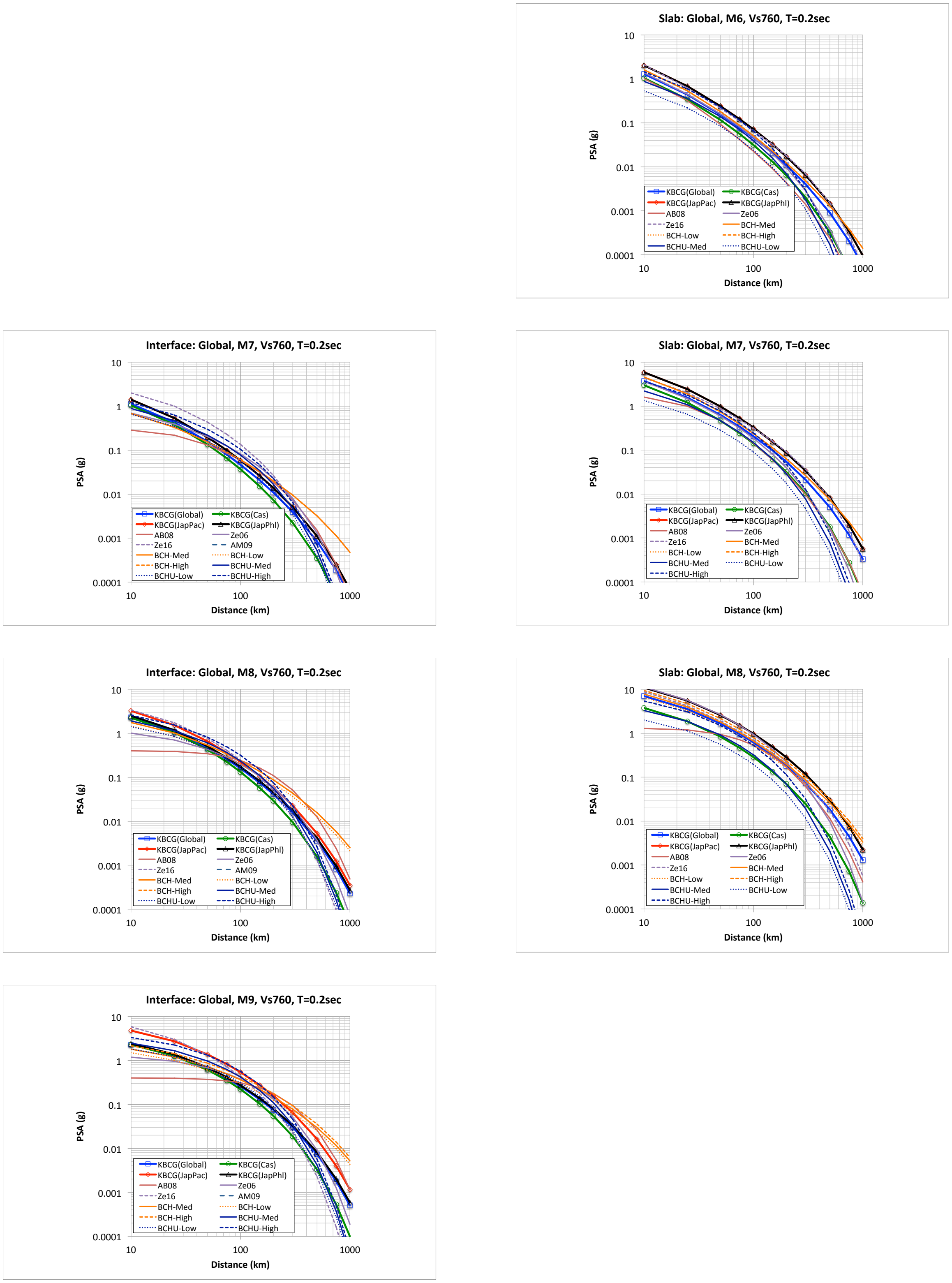

Figure 7.51: Plots of PSA at $T = 0.2$ sec versus distance comparing KBCG20 with selected published models: (left) interface events for M $= 7.0$, 8.0, and 9.0 with $Z_{TOR} = 10$ km; and (right) intraslab events for M $= 6.0$, 7.0, and 8.0 with $Z_{TOR} = 50$ km. For all plots, $V_{S30} = 760$ m/sec and $\delta Z_{1.0} = \delta Z_{2.5} = 0$.

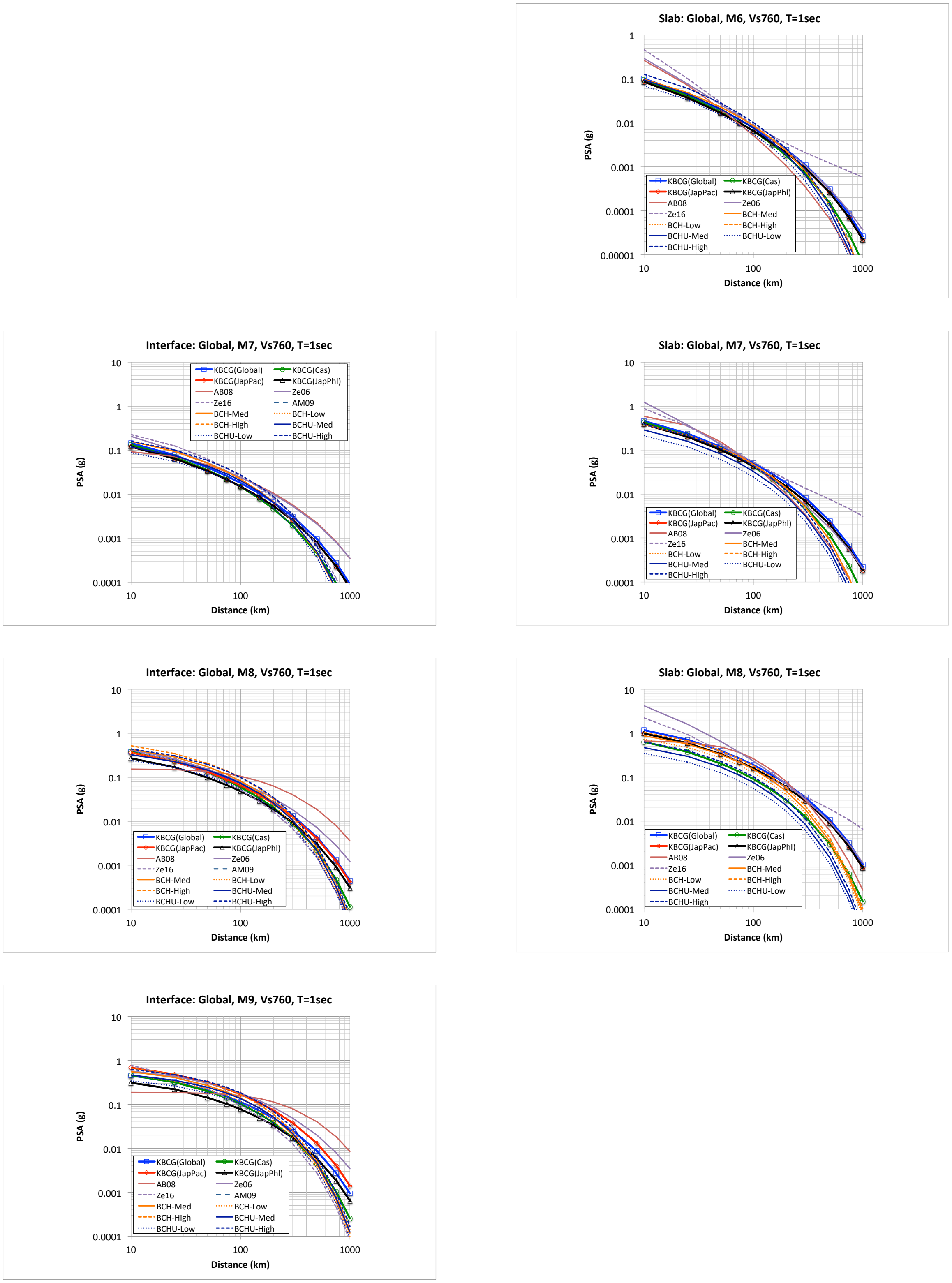

Figure 7.52: Plots of PSA at $T = 1.0$ sec versus distance comparing KBCG20 with selected published models: (left) interface events for M $= 7.0$, 8.0, and 9.0 with $Z_{TOR} = 10$ km; and (right) intraslab events for M $= 6.0$, 7.0, and 8.0 with $Z_{TOR} = 50$ km. For all plots, $V_{S30} = 760$ m/sec and $\delta Z_{1.0} = \delta Z_{2.5} = 0$.

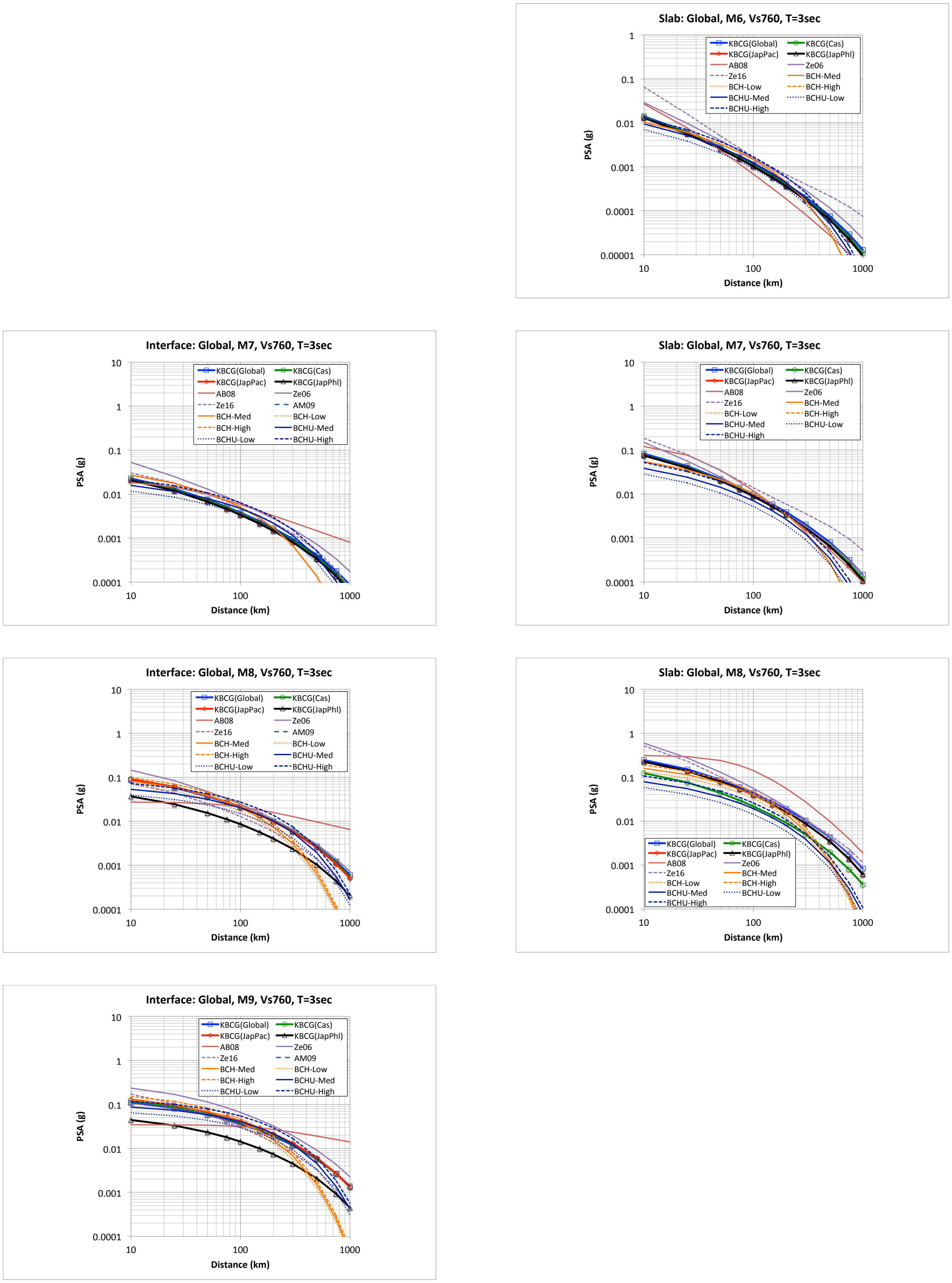

Figure 7.53: Plots of PSA at $T = 3.0$ sec versus distance comparing KBCG20 with selected published models: (left) interface events for **M** $= 7.0$, 8.0, and 9.0 with $Z_{TOR} = 10$ km; and (right) intraslab events for **M** $= 6.0$, 7.0, and 8.0 with $Z_{TOR} = 50$ km. For all plots, $V_{S30} = 760$ m/sec and $\delta Z_{1.0} = \delta Z_{2.5} = 0$.

7.3.2 Response Spectra

Figures 7.54 to 7.57 compare predicted median PSA response spectra between KBCG20 and the published GMMs. The comparisons are made for the same scenarios as in the previous section for distances of $R_{RUP} = 75$ and 100 km. In general, the range in the suite of response spectra among the GMMs falls within a factor of less than about 10 and closer, on average, to a factor of about 3 to 5.

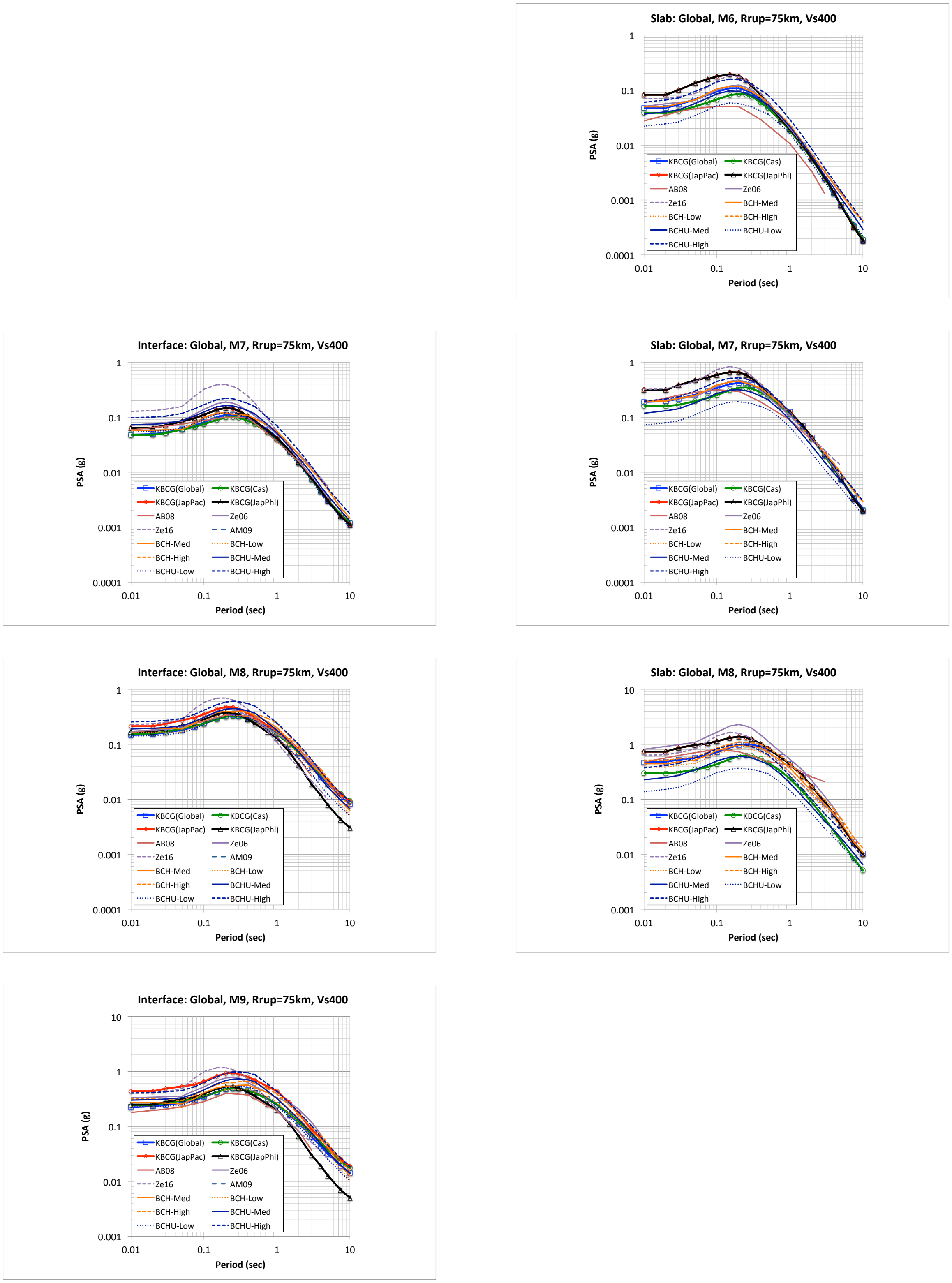

Figure 7.54: Plots of PSA response spectra comparing KBCG20 with published models: (left) interface events for M $= 7.0, 8.0$**, and** 9.0 **with** $Z_{TOR} = 10$ **km; and (right) intraslab events for M** $= 6.0, 7.0$**, and** 8.0 **with** $Z_{TOR} = 50$ **km. For all plots,** $V_{S30} = 400$ **m/sec,** $R_{RUP} = 75$ **km, and** $\delta Z_{1.0} = \delta Z_{2.5} = 0$**.**

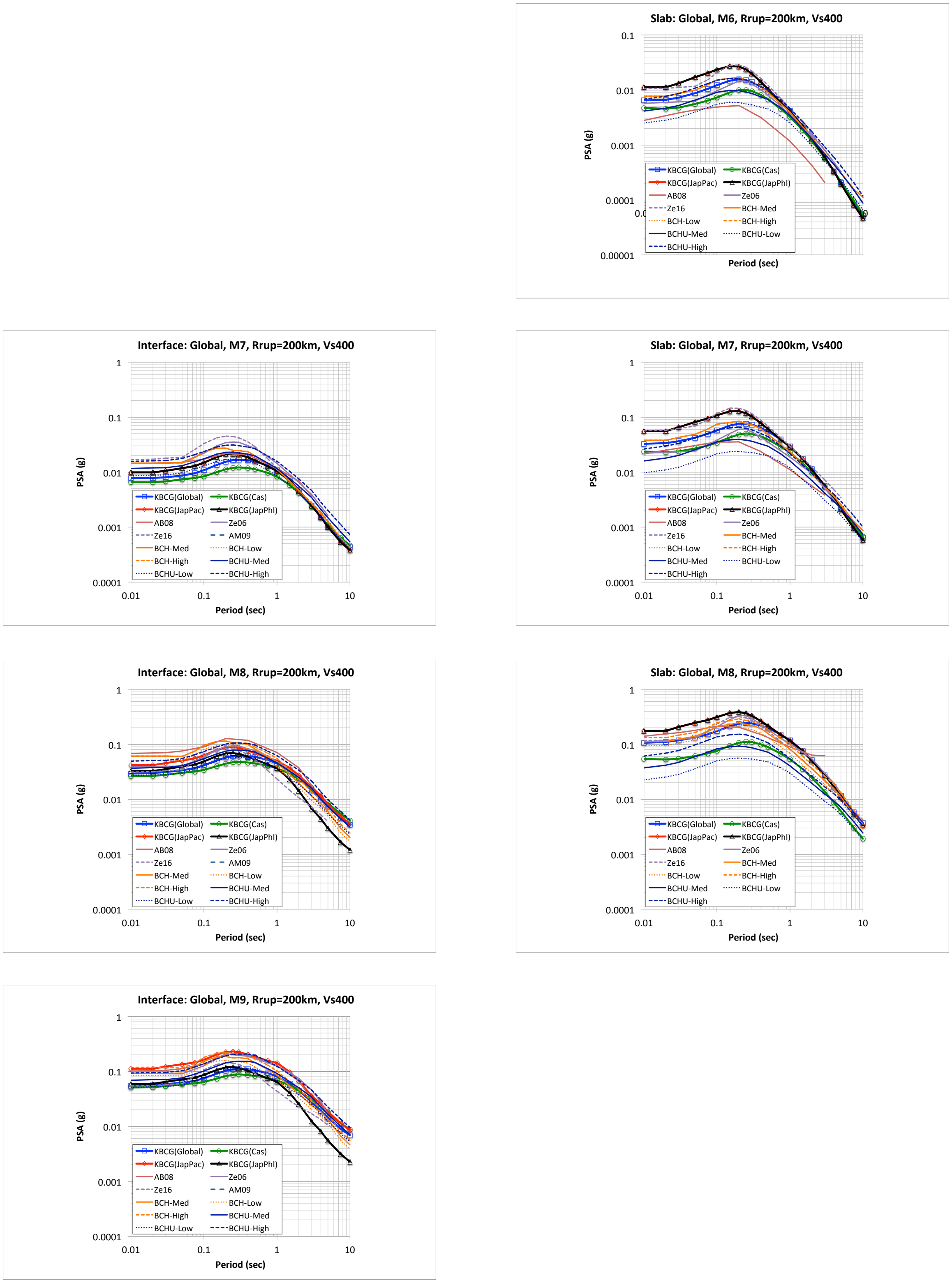

Figure 7.55: Plots of PSA response spectra comparing KBCG20 with published models: (left) interface events for M $= 7.0$, 8.0, and 9.0 with $Z_{TOR} = 10$ km; and (right) intraslab events for M $= 6.0$, 7.0, and 8.0 with $Z_{TOR} = 50$ km. For all plots, $V_{S30} = 400$ m/sec, $R_{RUP} = 200$ km, and $\delta Z_{1.0} = \delta Z_{2.5} = 0$.

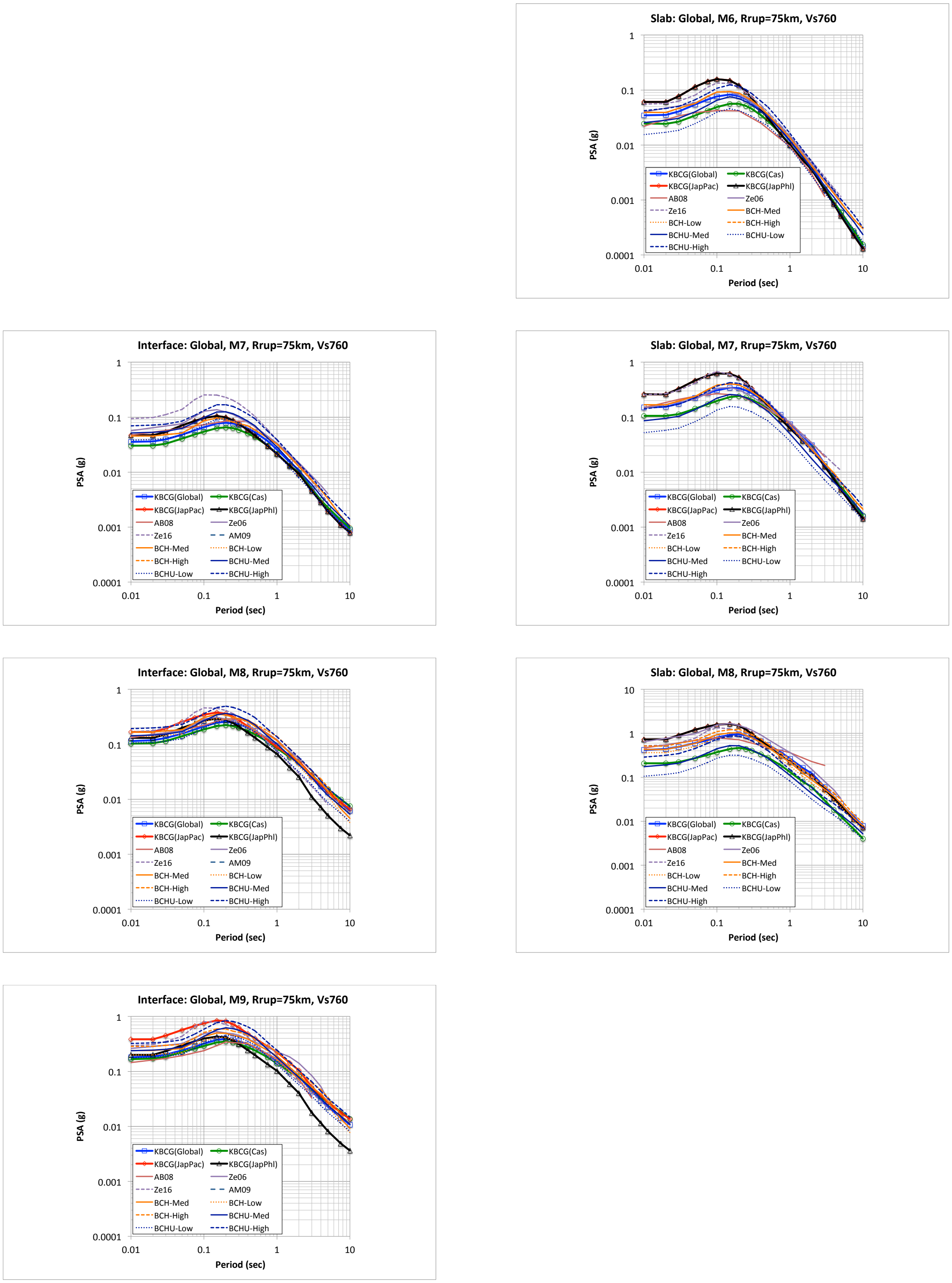

Figure 7.56: Plots of PSA response spectra comparing KBCG20 with published models: (left) interface events for M $= 7.0, 8.0$**, and** 9.0 **with** $Z_{TOR} = 10$ **km; and (right) intraslab events for M** $= 6.0, 7.0$**, and** 8.0 **with** $Z_{TOR} = 50$ **km. For all plots,** $V_{S30} = 760$ **m/sec,** $R_{RUP} = 75$ **km, and** $\delta Z_{1.0} = \delta Z_{2.5} = 0$**.**

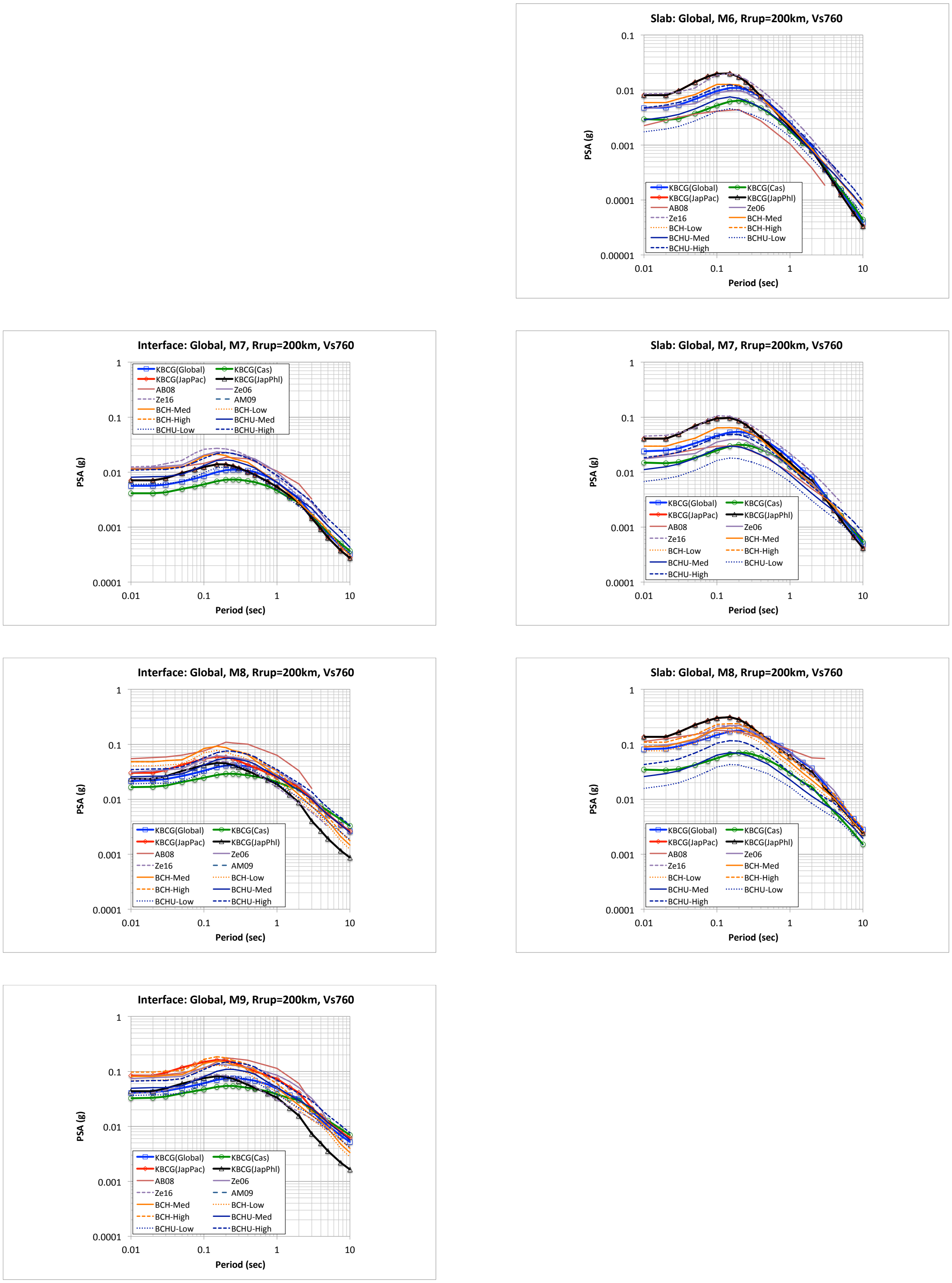

Figure 7.57: Plots of PSA response spectra comparing KBCG20 with published models: (left) interface events for M $= 7.0, 8.0$**, and** 9.0 **with** $Z_{TOR} = 10$ **km; and (right) intraslab events for M** $= 6.0, 7.0$**, and** 8.0 **with** $Z_{TOR} = 50$ **km. For all plots,** $V_{S30} = 760$ **m/sec,** $R_{RUP} = 200$ **km, and** $\delta Z_{1.0} = \delta Z_{2.5} = 0$**.**

7.3.3 Magnitude

Figures 7.58 to 7.61 compare the predicted ground motions as a function of magnitude between KBCG20 and the selected GMMs described previously for PSA at $T = 0.01$, 0.2, 1.0, and 3.0 sec, interface and intraslab events, $R_{RUP} = 75$ km, $V_{S30} = 760$ m/sec, and $\delta Z_{1.0} = \delta Z_{2.5} = 0$ (default basin amplification). For interface events, $Z_{TOR} = 10$ km and for intraslab events, $Z_{TOR} = 50$ km. The magnitude scaling is similar for magnitudes less than the breakpoint magnitudes except for AM09 and AB08.Note: AM09 was developed using ground-motion simulations based on a limited range of magnitudes; its extrapolation to the smaller magnitudes used in our comparison is outside its recommended range. Similarly, the dataset used in the AB08 model was not as extensive as the other models for the smaller magnitudes used in our comparison; therefore, its extrapolation is not well constrained by data. These GMMs are plotted for these smaller magnitudes to show what happens when they are extrapolated beyond their recommended ranges.

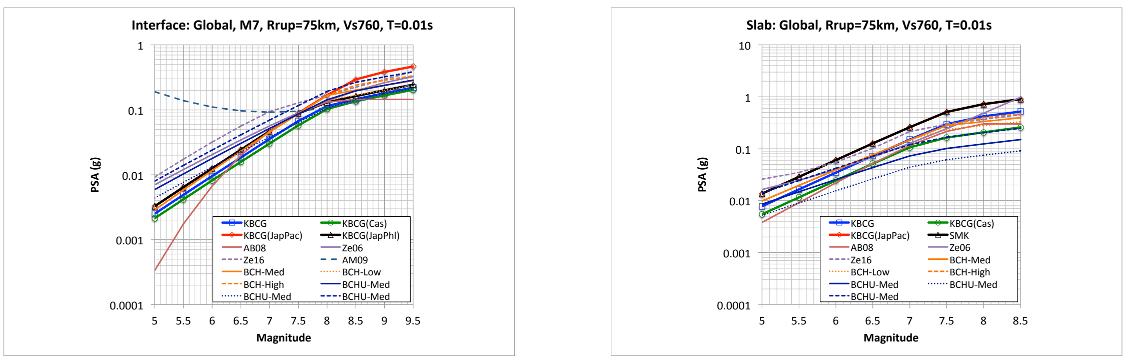

Figure 7.58: Plots of PSA at $T = 0.01$ sec versus magnitude comparing KBCG20 with published models: (left) interface events for $Z_{TOR} = 10$ km and (right) intraslab events for $Z_{TOR} = 50$ km. For all plots, $R_{RUP} = 75$ km, $V_{S30} = 760$ m/sec, and $\delta Z_{1.0} = \delta Z_{2.5} = 0$.

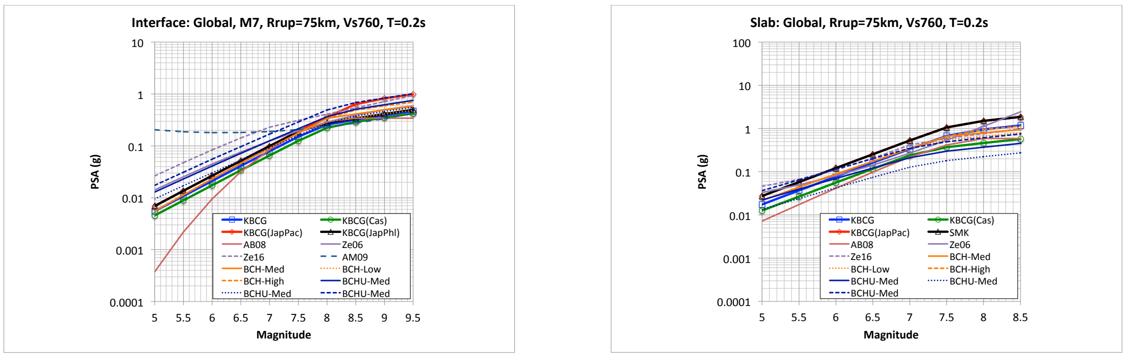

Figure 7.59: Plots of PSA at $T = 0.2$ sec versus magnitude comparing KBCG20 with published models: (left) interface events for $Z_{TOR} = 10$ km and (right) intraslab events for $Z_{TOR} = 50$ km. For all plots, $R_{RUP} = 75$ km, $V_{S30} = 760$ m/sec, and $\delta Z_{1.0} = \delta Z_{2.5} = 0$.

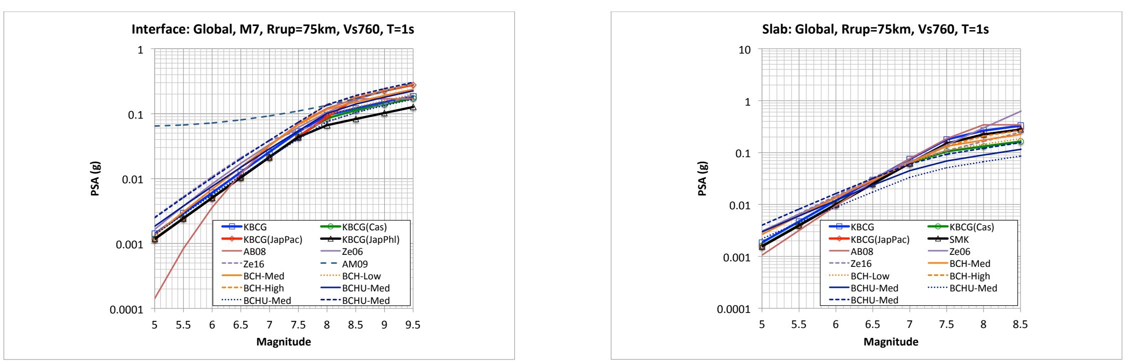

Figure 7.60: Plots of PSA at $T = 1.0$ sec versus magnitude comparing KBCG20 with published models: (left) interface events for $Z_{TOR} = 10$ km and (right) intraslab events for $Z_{TOR} = 50$ km. For all plots, $R_{RUP} = 75$ km, $V_{S30} = 760$ m/sec, and $\delta Z_{1.0} = \delta Z_{2.5} = 0$.

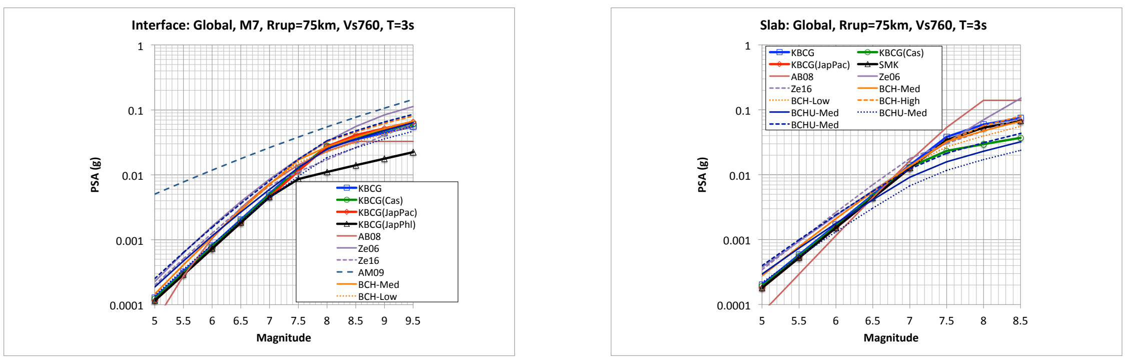

Figure 7.61: Plots of PSA at $T = 3.0$ sec versus magnitude comparing KBCG20 with published models: (left) interface events for $Z_{TOR} = 10$ km and (right) intraslab events for $Z_{TOR} = 50$ km. For all plots, $R_{RUP} = 75$ km, $V_{S30} = 760$ m/sec, and $\delta Z_{1.0} = \delta Z_{2.5} = 0$.

7.3.4 Source Depth

Figures 7.62 to 7.65 compare the predicted ground motions as a function of source depth between KBCG20 and the selected GMMs described previously for PGA and PSA at $T = 0.2$, 1.0, and 3.0 sec, interface $\mathbf{M} = 8.0$, $R_{RUP} = 75$ km, $V_{S30} = 760$ m/sec, and $\delta Z_{1.0} = \delta Z_{2.5} = 0$ (default basin amplification) and intraslab events, $\mathbf{M} = 7.0$, $R_{RUP} = 100$ km, $V_{S30} = 760$ m/sec, and $\delta Z_{1.0} = \delta Z_{2.5} = 0$ (default basin amplification). Depths are plotted from $Z_{TOR} = 5 - 40$ km for interface events and from $Z_{TOR} = 40 - 100$ km for intraslab events. Unlike KBCG20, none of the selected GMMs for interface events include source depth as a predictor variable, which is why they have the same predictions at all values of Z_{TOR}. For the intraslab events, the previous models contain a stronger linear function when compared the KBCG20 model which has a saturation for deeper intraslab events. These comparisons show that there can be a relatively large difference in source-depth scaling among the various GMMs, especially for deeper intraslab events.

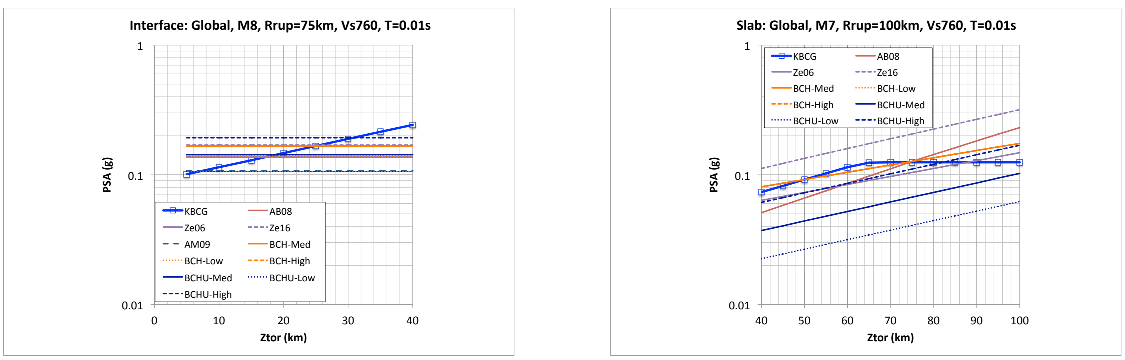

Figure 7.62: Plots of PGA versus source depth comparing KBCG20 with published models: (left) interface events and (right) intraslab events. For all plots, M $= 8.0$, $R_{RUP} = 75$ km, $V_{S30} = 760$ m/sec, and $\delta Z_{1.0} = \delta Z_{2.5} = 0$.

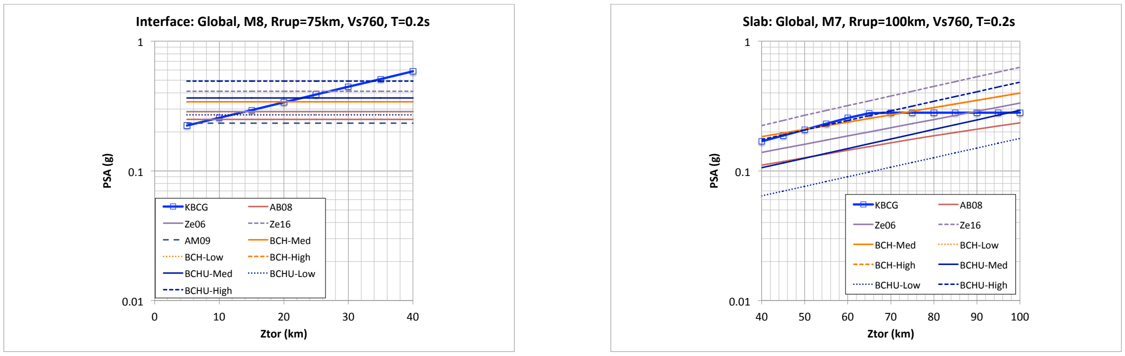

Figure 7.63: Plots of PSA at $T = 0.2$ sec versus source depth comparing KBCG20 with published models: (left) interface events and (right) intraslab events. For all plots, M $= 8.0$, $R_{RUP} = 75$ km, $V_{S30} = 760$ m/sec, and $\delta Z_{1.0} = \delta Z_{2.5} = 0$.

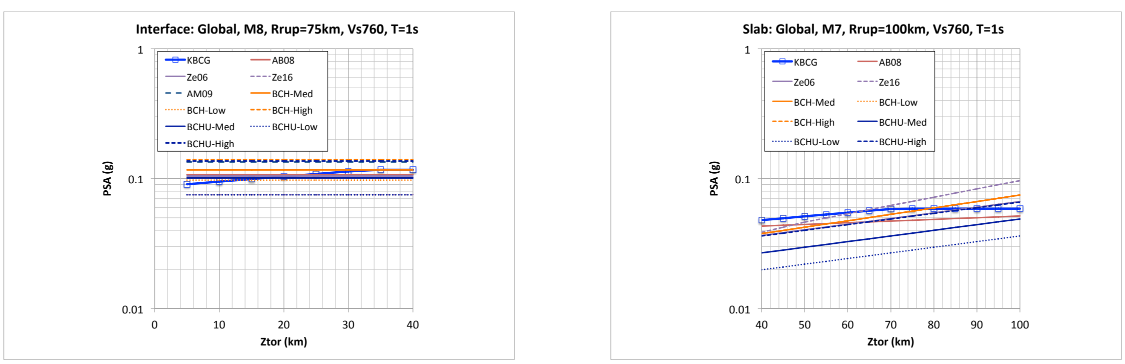

Figure 7.64: Plots of PSA at $T = 1.0$ sec versus source depth comparing KBCG20 with published models: (left) interface events and (right) intraslab events. For all plots, M $= 8.0$, $R_{RUP} = 75$ km, $V_{S30} = 760$ m/sec, and $\delta Z_{1.0} = \delta Z_{2.5} = 0$.

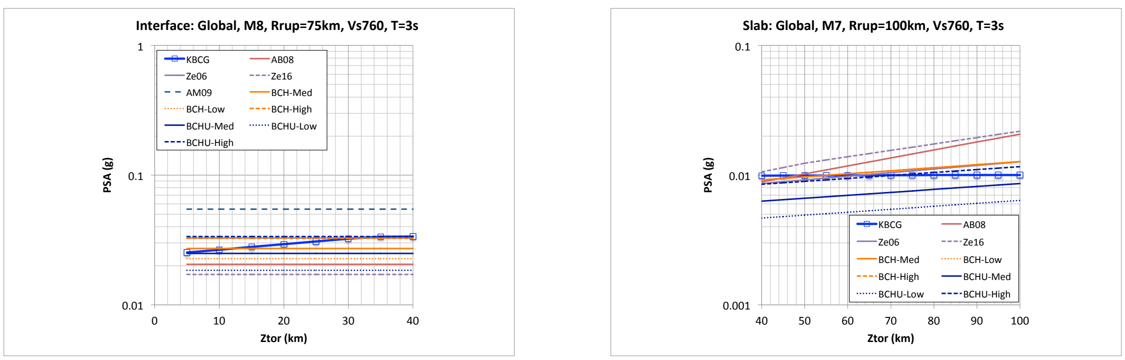

Figure 7.65: Plots of PSA at $T = 3.0$ sec versus source depth comparing KBCG20 with published models: (left) interface events and (right) intraslab events. For all plots, M $= 8.0$, $R_{RUP} = 75$ km, $V_{S30} = 760$ m/sec, and $\delta Z_{1.0} = \delta Z_{2.5} = 0$.

7.3.5 Site Amplification

Figures 7.66 to 7.68 show response spectral ratios between soft rock and rock comparing KBCG20 with published models. For the KBCG20 model, results are shown for the Global, CASC, and JP regionalized models since they are most consistent with the data used to develop the other GMMs. The spectral ratios are shown for interface events, **M** = 7.0, 8.0, and 9.0, $Z_{TOR} = 10$ km, $R_{RUP} = 75$ km, and $\delta Z_{1.0} = \delta Z_{2.5} = 0$ (default basin effects). The ratios are similar for intraslab events.

For GMMs defined in terms of V_{S30}, values of 400 and 760 m/sec were used to represent soft rock and rock, respectively. For the other GMMs, rock-site conditions were defined as either NEHRP B/C (AB08) or "rock" (Zea06 and Zea16), and soft-rock site conditions were defined as either NEHRP C (AB08) or "hard soil" (Zea06 and Zea16). Note that AM09 is only defined for $V_{S30} = 760$ m/sec and is not included in the figures.

Except for the long-period ratios from AB08, the shapes of the spectral ratios are similar among the GMMs; however, there is a relatively large difference in the amplitudes of the spectral ratios among many of the models. The periods at which the spectral ratios reach their minimum at short periods and their maximum at moderate periods also varies among the GMMs.

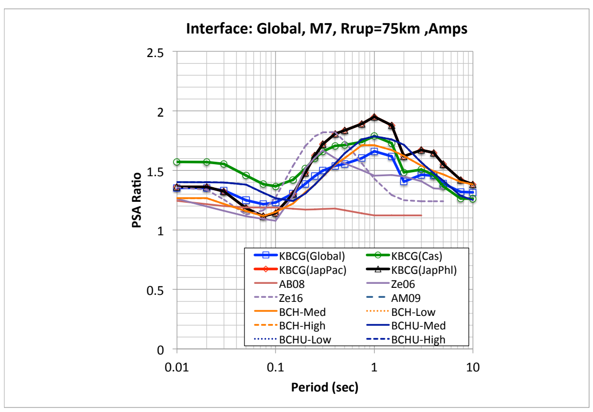

Figure 7.66: Plots of PSA response spectral ratios between soft rock ($V_{S30} = 400$ m/sec) and rock ($V_{S30} = 760$ m/sec) comparing KBCG20 (Global, CASC and JP) with published models: interface events, M = 7.0, $Z_{TOR} = 10$ km, $R_{RUP} = 75$ km, and $\delta Z_{1.0} = \delta Z_{2.5} = 0$.

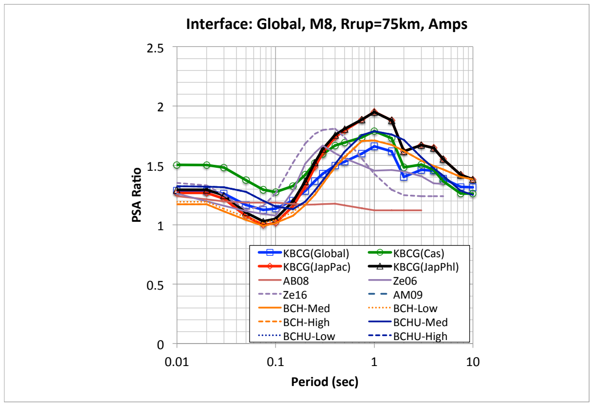

Figure 7.67: Plots of PSA response spectral ratios between soft rock ($V_{S30} = 400$ m/sec) and rock ($V_{S30} = 760$ m/sec) comparing KBCG20 (Global, CASC and JP) with published models: interface events, M $= 8.0$, $Z_{TOR} = 10$ km, $R_{RUP} = 75$ km, and $\delta Z_{1.0} = \delta Z_{2.5} = 0$.

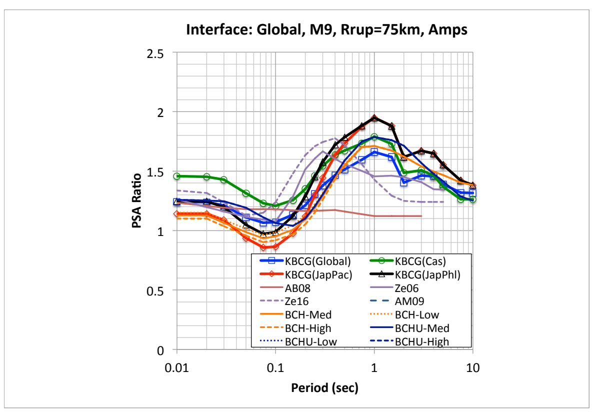

Figure 7.68: Plots of PSA response spectral ratios between soft rock ($V_{S30} = 400$ m/sec) and rock ($V_{S30} = 760$ m/sec) comparing KBCG20 (Global, CASC and JP) with published models: interface events, M $= 9.0$, $Z_{TOR} = 10$ km, $R_{RUP} = 75$ km, and $\delta Z_{1.0} = \delta Z_{2.5} = 0$.

7.3.6 Standard Deviation

In this section, we compared aleatory standard deviations between KBCG20 and the selected GMMs described previously. Figure 7.69 shows comparisons of between-event (τ), within-event (ϕ), and total (σ) standard deviations as a function of spectral period. Note that not all of the GMMs separate standard deviations into between-event and within-event terms, in which case they only appear on the total standard deviation plot.

For spectral periods between about 0.1 and 4 sec, σ from KBCG20 is similar to that from BCHU. This is not surprising because both are based on the NGA-Sub database. However, for shorter and longer periods, the two GMMs differ, with KBCG20 having smaller values of σ. In comparison to BCH (the original BCHydro GMM), both the KBCG20 and BCHU total standard deviations are larger, especially at short periods. The relatively large differences in standard deviations among all of the models, especially for τ and σ, can result in relatively large differences in probabilistic estimates of ground motions.

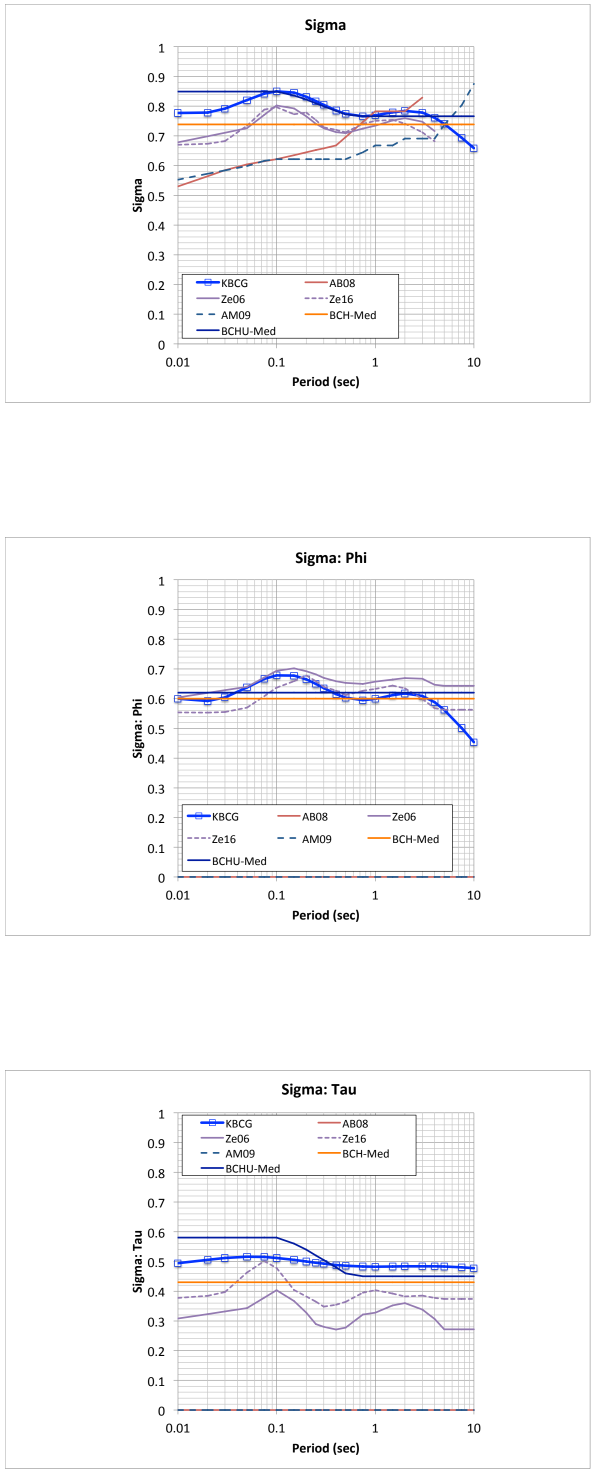

Figure 7.69: Plots of aleatory standard deviations versus spectral period comparing KBCG20 with published models: (top) total standard deviation (σ); (middle) within-event standard deviation (ϕ); and (bottom) between-event standard deviation (τ)

8 ENGINEERING APPLICATION GUIDELINES

We recognize that our NGA-Sub ground-motion model is relatively complex due to its geographical regionalization and the nonuniform density of ground-motion observations in the seven modeled regions. Therefore, in this chapter, we provide guidelines to potential users on how to use KBCG20 in seismic hazard and engineering applications. We cover the model's general limits of applicability, its application to subduction zones not included in the model, and its specific application to the Cascadia Subduction Zone.

8.1 MODEL APPLICABILITY

We consider KBCG20 to be applicable for estimating peak ground motion parameters and 5%-damped pseudo-spectral acceleration (PSA) for subduction interface and intraslab earthquakes. The range of predictor variables for which the GMM is reliable depends on the region of interest because of the different numbers of earthquakes, seismographs, and recordings for each of the seven regions included in the model. We recommend that the user to use the computer program that is distributed with this report to evaluate the median predictions, between-event and within-event aleatory variabilities, and within-model epistemic uncertainty described in Chapter 6 for a specific set of predictor variables (i.e., a specific earthquake scenario). The epistemic standard deviation will increase (possibly considerably) if one or more of the predictor variables are near or beyond the limit of their observed values for that region. If the user considers the resulting epistemic standard deviation to be too large, s/he can decide whether the GMM should be considered reliable for that particular scenario.

8.1.1 General Applicability

The ranges of variables for which our GMM can be considered generally reliable are as follows:

- Ground-motion parameters:
  - Peak parameters: PGA (g), PGV (cm/sec)
  - Spectral parameters: PSA (g) at $T = 0.01 - 10$ sec
- Minimum magnitude:

  - All earthquakes: $\mathbf{M} \geq 5.0$

- Maximum magnitude:
  - Interface earthquakes: $\mathbf{M} \leq 9.5$
  - Intraslab earthquakes: $\mathbf{M} \leq 8.5$

- Breakpoint magnitude:
  - See Regional Applicability section

- Source depth:
  - Interface earthquakes: $Z_{TOR} \leq 50$ km
  - Intraslab earthquakes: $Z_{TOR} \leq 200$ km (except Colombia; see Section 8.1.2, Regional Applicability).

- Closest distance to fault rupture:
  - All earthquakes: $10 \leq R_{RUP} \leq 1000$ km

- Anelastic attenuation:
  - See Regional Applicability section

- Shear-wave velocity:
  - All sites: $150 \leq V_{S30} \leq 1500$ m/sec

- Basin (sediment) depth:
  - See Regional Applicability section

8.1.2 Regional Applicability

Major aspects of the regional terms for which the GMM can be considered generally reliable are as follows:

- Magnitude breakpoint:
  - Global:
    * Interface earthquakes: $\bar{\mathbf{M}}_{B,if} = 7.9$
    * Intraslab earthquakes: $\bar{\mathbf{M}}_{B,slab} = 7.6$
  - Other regions:
    * Interface earthquakes: See Table 8.2, Campbell (2020)
    * Intraslab earthquakes: See Table 8.1, Ji and Archuleta (2018)

- Source depth:
  - Colombia intraslab earthquakes: $Z_{TOR} \leq 150$ km
- Attenuation subregions:
  - Forearc: Global, AK, CAM, CASC, NZ, JP, SA, and TW
  - Backarc: AK, JP, and NZ
  - Backarc: Global, CAM, CASC, SA, and TW (same as forearc)
- Basin (sediment) depth:
  - CASC, JP: $Z_{2.5} \leq 10$ km
  - NZ, TW: $Z_{1.0} \leq 2.2$ km

8.2 EPISTEMIC UNCERTAINTY

8.2.1 Median Ground Motion

As noted previously in this report, KBCG20 was developed for seven regional subduction zones (plus a global model) for which sufficient data are available in the NGA-Sub database to develop regionalized constant (amplitude), anelastic attenuation, site-amplification and basin-amplification terms and, in some cases, sub-regional differences in anelastic attenuation (e.g., forearc versus backarc). Chapter 6 describes how epistemic uncertainty in the median estimates of ground motion for these regions, as well as for the global model, can be estimated using 800 samples taken from the posterior distributions of median ground motion. A computer program written in "R" (statistical computing and graphics language) is provided as an electronic supplement to this report, that calculates KBCG20 median estimates of the modeled ground-motion parameters, their aleatory standard deviations, and their epistemic uncertainty.

As indicated in Figure 6.3, regions with the least amount of data have the largest epistemic standard deviations at short-to-moderate spectral periods, with CASC having the largest and JP the smallest. The coalescence of the epistemic standard deviations to a relatively small value at long periods represents the increased consistency and similarity in long wavelength ground motion, possibly due to the similarity in the gross tectonic structure of subduction zones globally. The epistemic uncertainty in the median estimates of ground motion for the KBCG20 global model is found to be the highest, since it should only be used for those subduction zones with no available regional terms.

There are other subduction zones located throughout the world—other than the seven addressed in this study—for which GMMs might be needed to perform a PSHA or other engineering applications. Some of these subduction zones might have limited ground-motion data and some no data at all. If ground-motion data are not available—or are not used even if available—the KBCG20 global median model along with its aleatory standard deviations should be used; however, epistemic uncertainty should be increased due to the application of the model to a new region similar to that recommended in Chapter 12.8 of Gelman and Hill (2006). This requires sampling regional adjustment coefficients from their joint distribution [Equation 4.13]; see also Chapter 6), and adding them to the global coefficient values. This additional epistemic uncertainty is included in the computer program distributed with this report. For the seven explicitly subduction zones modeled in our GMM, the computer program will give smaller epistemic uncertainty for those regions with the largest amount of data.

If there are data available for the subduction zone of interest and the user is willing to compile and process them, the median ground motions predicted from the global model could be taken as a prior distribution of the median predictions of the new subduction zone and the data used to develop a posterior distribution, as proposed by Stafford (2019). If the user is not willing or able to develop a local ground-motion model, an assessment of the applicability of KBCG20 could also be performed by calculating and reviewing residuals with respect to the KBCG20 global predictions. Note: any statistical approach should be used with caution to ensure that the results are not contaminated by unintended bias or uncertainty in the local data that are used.

The epistemic uncertainty discussed above and in Chapter 6 represents within-model uncertainty since it only addresses uncertainty in the median estimates of ground motion due to uncertainty in the model coefficients. Although one would hope that such within-model uncertainty would capture the epistemic uncertainty in the predicted ground motions from other GMMs, that is not necessarily the case (e.g., Al-Atik and Youngs, 2014). The use of additional GMMs, such as those developed as part of the NGA-Sub project (Bozorgnia et al., 2018) or other published GMMs, such as those presented in Sections 1.2 and 7.3, could be used to account for additional between-model epistemic uncertainty not addressed by the KBCG20 within-model uncertainty. The user should be careful not to double count these two estimates of uncertainty (e.g., Al-Atik and Youngs, 2014). Stochastic-based and physics-based GMMs can also be used for this purpose.

8.2.2 Breakpoint Magnitude

It is clear from modern empirical subduction interface GMMs (e.g., Abrahamson et al., 2018, 2016; Zhao et al., 2016b; Morikawa and Fujiwara, 2013) and other literature reviews (Campbell, 2020; Stewart et al., 2013) that there is a magnitude at which the magnitude scaling rate of ground-motion parameters (MSR) from subduction interface events must become smaller. This breakpoint magnitude is only controlled by two megathrust events: the 2010 (**M**8.8) Maule, Chile, earthquake and the 2011 (**M** 9.0) Tohoku-oki, Japan, earthquake. The breakpoint magnitude for intraslab earthquakes is only slightly better constrained empirically (Abrahamson et al., 2018). This makes the empirical determination of breakpoint magnitude for both types of earthquakes highly uncertain.

One of the issues facing all of the GMM developers in the NGA-Sub project was what breakpoint magnitudes should be used. An important feature in KBCG20 is the incorporation of a regionalized breakpoint magnitude based on the physical attributes of subducting slabs (Archuleta and Ji, 2018; Ji and Archuleta, 2018) and subduction megathrust interfaces (Campbell, 2020). Both of these studies are based on the concept that MSR decreases when the rupture width of an event saturates the thickness of the oceanic slab (in the case of intraslab earthquakes) or the seismogenic width of the subduction interface (in the case of megathrust earthquakes). The breakpoint magnitudes used in KBCG20 for those subduction zones that were included in the model–as well as

Table 8.1: Subduction intraslab breakpoint magnitudes.

Subduction Zone		Plate Unbending		Slab Breakoff	
JA18[1]	**Bea15**[2]	W_{MAX} (km)	$\mathbf{M}_{B,slab}$	W_{MAX} (km)	$\mathbf{M}_{B,slab}$
Alaska					
Alaska	Kodiak–Prince William Sound	20–25	7.1–7.3	40–50	7.7–7.9
Aleutian	Komandorski–Semidi	—	—	50–54	7.9
Cascadia					
Cascadia	Cascadia	9–11	6.3–6.5	17–21	6.9–7.1
CAM					
Central America N.	Jalisco-Guatemala	11–14	6.6–6.8	22–28	7.2–7.4
Central America S.	El Salvador–West Panama	—	—	36	7.6
Japan					
Japan Pac.	Japan	36–38	7.6	72–76	8.2
Japan Phi.	Nankai	17–20	6.9–7.1	33–40	7.5–7.7
Northern Mariana	Marianas	38	7.6	76	8.2
New Zealand					
New Zealand N.	Hikurangi	36–38	7.6	72–75	8.2
New Zealand S.	Puysegur	30–31	7.5	60–62	8.0
South America					
South America N.	Ecuador–Colombia	9-18	6.3–7.0	17–36	6.9–7.6
South America S.	Peru–Central Chile	20–27	7.1–7.4	40–54	7.7–8.0
Taiwan					
Taiwan	Ryukyu	21	7.1	42	7.7

[1] JA18, Ji and Archuleta (2018)
[2] Bea15, Berryman et al. (2015)

others that are not–are summarized in Table 8.1 for intraslab events (Ji and Archuleta, 2018) and Table 8.2 for interface events Campbell (2020). Two reference names for each subduction zone are listed in these tables: those assigned by Ji and Archuleta (2018) and the approximate corresponding subduction zone segments designated by Berryman et al. (2015). The subduction zone segments designated by each study are not necessarily the same but should be generally similar.

Table 8.1 lists the estimated ranges of slab widths (W_{MAX}) and breakpoint magnitudes ($\mathbf{M}_{B,slab}$) for the "plate unbending" and "slab breakoff" scenarios proposed by Ji and Archuleta (2018).

Table 8.2: Subduction interface breakpoint magnitudes.

Subduction Zone (JA18)	Subduction Zone (Bea15)	$\bar{W}_{MAX}$	$\bar{\mathbf{M}}_{B,if}$	$\mathbf{M}^{5\%}_{B,if}$	$\mathbf{M}^{95\%}_{B,if}$
Alaska					
Alaska	Kodiak–Prince William Sound	133–263	8.3–8.9	8.0–8.4	8.9–9.7
Aleutian	Komandorski–Semidi	62–123	7.6–8.3	7.2–7.9	8.1–8.8
Cascadia					
Cascadia	Cascadia	68	7.7	7.3	8.2
Central America & Mexico					
Central America N.	Jalisco–Guatemala	40–58	7.2–7.6	6.7–7.2	7.6–8.0
Central America S.	El Salvador–West Panama	42–68	7.3–7.7	6.8–7.3	7.7–8.2
Japan					
Japan Pac.	Japan	166	8.5	8.1	9.2
Japan Phi.	Nankai	64	7.7	7.3	8.1
Northern Mariana	Marianas	85	7.9	7.6	8.4
New Zealand					
New Zealand N.	Hikurangi	130	8.3	7.9	8.9
New Zealand S.	Puysegur	97	8.0	7.7	8.5
South America					
South America N.	Ecuador–Colombia	162	8.5	8.1	9.2
South America S.	Peru–Central Chile	178–192	8.4–8.7	8.1–8.3	9.1-9.3
Taiwan					
Taiwan	Ryukyu	35	7.1	6.5	7.5

Table 8.2 lists the mean interface widths ($\bar{W}_{MAX}$), mean epistemic breakpoint magnitudes ($\bar{\mathbf{M}}_{B,if}$), and breakpoint magnitudes corresponding to the epistemic 5% ($\mathbf{M}^{5\%}_{B,if}$) and 95% ($\mathbf{M}^{95\%}_{B,if}$) confidence limits for the same subduction zones given in Table 8.1. Ranges are given when multiple subduction segments from Berryman et al. (2015) correspond to the subduction zones listed by Ji and Archuleta (2018). Campbell (2020) provides a full listing of breakpoint magnitudes for all 79 subduction zones characterized in Berryman et al. (2015).

Because of the large uncertainty in breakpoint magnitude, epistemic uncertainty in this parameter should be an integral part of any seismic hazard analysis that incorporates subduction zone sources, whether or not they are modeled in KBCG20. KBGC19 used the midpoint between the "plate unbending" and "slab breakoff" estimates of Ji and Archuleta (2018) listed in Table 8.1. Ji and Archuleta (2018) did not formally develop means and epistemic standard deviations for their estimates of breakpoint magnitude, although Ji (*Personal Communication*) suggested that estimates using either method could be considered equally likely. The user should develop a logic tree from these estimates and other information obtained from the published literature to incorporate epistemic uncertainty in the value of intraslab breakpoint magnitude in his or her PSHA or other engineering application.

Campbell (2020) provides both mean estimates and 90% confidence bounds of interface breakpoint magnitudes for 79 global subduction zones that can be used to capture epistemic uncertainty in this parameter (e.g., Table 8.2). These estimates can be used directly in a seismic hazard analysis using a logic tree. One method of incorporating uncertainty in interface breakpoint magnitude is to assign the 5% and 95% confidence limits weights of 0.185 each and the mean value a weight of 0.630. This is the best three-point discrete representation of a normal distribution recommended by Keefer and Bodily (1983). As noted for CASC in Section 8.3, one should review the literature on the tectonics, geophysics, and geometry of the subduction zone of interest before using these estimates, which might indicate that other values should be considered.

8.2.3 Magnitude Scaling Rate (MSR)

Like breakpoint magnitude, there are few empirical data to determine the MSR of ground-motion parameters for moderate-to-large intraslab earthquakes or large-to-great subduction megathrust earthquakes. This was particularly true for megathrust events prior to the occurrence of the Maule and Tohoku-oki earthquakes, when large-magnitude scaling was based primarily on a linear or quadratic extrapolation of the MSR of $\mathbf{M} < 8.0$ events (Campbell, 2020; Stewart et al., 2013).

There are five GMMs for interface events that have been developed since the occurrence of the Maule and Tohoku-oki earthquakes. Nonetheless, the large uncertainty in the empirical determination of MSR continues to exist. In their empirical GMM based on Japanese recordings, Morikawa and Fujiwara (2013) proposed complete saturation of magnitude scaling (i.e., MSR = 0) of PGA and PGV for $\mathbf{M} > 8.1$–8.2, driven entirely by recordings from the Tohoku-oki earthquake. Also using Japanese data, Ghofrani and Atkinson (2014) developed a GMM for $\mathbf{M} > 7.0$ earthquakes that has a relatively shallow MSR for magnitudes up to $\mathbf{M}9.0$. They show that their empirical MSR is similar to that derived from the ground-motion simulations of Atkinson and Macias (2009). Zhao et al. (2016b) used a breakpoint magnitude of 7.1 in the development of their GMM for Japanese earthquakes of $\mathbf{M} > 5.0$ based on an empirical study by Zhao and Xu (2012). They note that their large-magnitude MSR is similar to that derived from the ground-motion simulations of Gregor et al. (2002) at near-source distances.

Using global earthquakes, Abrahamson et al. (2018) and Abrahamson et al. (2016) used a large-magnitude MSR for interface events that is consistent with the ground-motion simulations of Gregor et al. (2002) and Atkinson and Macias (2009). There is more empirical evidence for a break in MSR for intraslab events than for interface events because of their larger rate of occurrence. There remains a large degree of uncertainty in determining MSR, even for those regions with a large number of earthquakes (Abrahamson et al., 2018) . Therefore, any GMM–including ours–that uses the empirical or physically-based MSRs suggested by the studies summarized above should properly account for epistemic uncertainty in MSR when used in a PSHA or other engineering application.

8.3 CASCADIA SUBDUCTION ZONE

8.3.1 Regional Adjustments to Constant Term

There have been very few significant earthquakes on CASC, which makes the prediction of ground motion challenging for this subduction zone. There have been no $\mathbf{M} > 5$ interface earthquakes recorded instrumentally on CASC except at its highly seismic southern end (the Gorda sub-plate deformation zone located off Cape Mendocino in northern California) and northern end (Explorer sub-plate deformation zone located off central Vancouer Island). The southern end of CASC was the location of the April 25, 1992 Petrolia (**M**7.1), California, earthquake that occurred along the Gorda deformation zone between the Gorda segment of CASC and the North American plate. The NGA-Sub database attributes the Petrolia earthquake to shallow crustal thrust faulting within the overriding North American plate; however, this interpretation is not universal (e.g., Oppenheimer et al., 1993) and some scientists believe that it was an interface event (e.g., Tanioka et al., 1995b; Cascadia Region Earthquake Workgroup, 2013).

A comparison of residuals between ground-motion recordings from the Petrolia earthquake and predicted ground motions from the proposed CASC GMM of KBCG20 indicates that KBCG20 overestimates short-period ground motions and underestimates long-period ground motions. The overestimation at short periods is in addition the downward adjustment already incorporated in the CASC regional constant (Figure 4.18). The underestimation at long periods might be due to the rock-site conditions in the Cape Mendocino area, although many small-to-moderate magnitude intraslab events in the Puget Sound and northern California regions exhibit the same behavior. It could also be due to there being no CASC regional adjustment for long-period ground motions.

There have been many more intraslab earthquakes than interface earthquakes on CASC. They have primarily occurred within the Juan de Fuca Plate in the Puget Sound, Washington, and Georgia Straight, British Columbia, regions and the Gorda sub-plate in northern California. The largest and best-recorded of these is the February 28, 2001, Nisqually (**M** 6.8), Washington, earthquake. Other smaller, yet still relatively well-recorded, events are the January 10, 2010, Ferndale (**M** 6.5), California, earthquake, and two **M** 6.5 and 6.7 aftershocks of the 1992 Petrolia earthquake. Although other large earthquakes have occurred in these regions, there are too few strong-motion recordings to include them in the NGA-Sub database.

We used the Nisqually and Ferndale earthquakes to help constrain our CASC regional intraslab constant term (Figure 4.18), and because of correlation, the interface constant term (Figure 4.18) results in smaller predicted short-period amplitudes than predicted by our global GMM. However, short-period ground motions for these two events are still overestimated and the long-period ground motions underestimated. Had smaller intraslab events in the NGA-Sub database been used to adjust the regional constant, an even larger negative adjustment in the global constant would have been required, leading to even smaller CASC predicted short-period amplitudes. The short-period amplitudes of the Petrolia aftershocks exhibit a positive bias (underestimation), which is the opposite of that found for the Petrolia, Nisqually, and Ferndale earthquakes.

The regional downward adjustments to the global short-period constants for CASC events are consistent with the results presented in Chapter 4 (Figure 4.18). Practically all other GMMs that have evaluated CASC ground motions have found reductions in short-period amplitudes and increases in long-period amplitudes compared to GMMs based on global or Japanese recordings (e.g., Atkinson and Boore, 2003, 2008; Ghofrani and Atkinson, 2014; Abrahamson et al., 2016, 2018). However, for $T > 0.2$ sec, the CASC adjustment in KBCG20 goes to zero even though the empirical evidence indicates there should be a positive adjustment. The reason for this is the relatively small standard deviation of the global constant term, which prevents the posterior distribution from "pushing" the regional constant from its global prior unless there is a lot of data supporting the adjustment, which is not the case for CASC.

The above discussion emphasizes that, like other subduction zones with little or no ground-motion data, the application of any GMM to CASC is fraught with uncertainty, notwithstanding the issue with respect to the appropriate breakpoint magnitude to use as discussed in the next section. We refer the reader to Section 8.2 for a discussion of how to include appropriate epistemic uncertainty in regional estimates of ground motion for subduction zones with little or no ground-motion recordings. Given the discrepancy between the short-period residuals of the Petrolia aftershocks and the Nisqually and Ferndale earthquakes that were used to adjust the global model, it would appear that the CASC adjustments to the global constant terms are appropriate and consistent with smaller stress drops and greater attenuation expected for the young, warm, and narrow Cascadia oceanic slab (e.g. Hyndman, 2013; Wang and Tréhu, 2016; Campbell, 2020).

8.3.2 Selection of Breakpoint Magnitude

As discussed in Campbell (2020), Berryman et al. (2015) estimated a relatively narrow preferred average seismogenic interface width of 68 km for CASC based primarily on the most likely down-dip limit of co-seismic rupture defined by the mid-point of the transition zone determined from geodetic and thermal data. This resulted in a relatively small estimate of mean breakpoint magnitude of $\bar{\mathbf{M}}_{B,if} = 7.7$ and epistemic 5% and 95% confidence limits of $\mathbf{M}_{B,if}^{5\%} = 7.3$ and $\mathbf{M}_{B,if}^{95\%} = 8.2$. respectively.

According to Campbell (2020), a similar interface width and breakpoint magnitude was derived for the Nankai segment of the Nankai-Ryukyu subduction zone by Berryman et al. (2015), which is consistent with it being analogous to CASC due to its similar age of subducting oceanic crust (~10 million years old) and rate of convergence (4-8 cm/yr) (Satake and Atwater, 2007). Furthermore, Frankel et al. (2018) found that their broadband ground-motion simulations of a $\mathbf{M} \approx 9$ mega-earthquake on CASC were consistent with predictions from the empirical GMM of Abrahamson et al. (2016), which has a central breakpoint magnitude of 8.0 at short periods and decreasing to 7.6 at long periods, which is similar to the mean estimate of breakpoint magnitude determined by Campbell (2020) and within its epistemic uncertainty bounds. The preferred seismogenic width and resulting breakpoint magnitude for CASC is also consistent with the mean magnitude and slip estimated by Satake et al. (2003) for the 1700 Cascadia earthquake (Campbell, 2020).

The Cascadia seismogenic interface shallows and widens in the Puget Sound region where the North American plate bends to a more northwesterly direction. Campbell (2020) suggests that the most likely seismogenic interface width in this region is ~140 km according to Frankel and Petersen (2008); Frankel et al. (2015) revised this to ~170 km based on the inferred 1 cm/yr locking depth recommended at a regional workshop of experts convened as part of the National Seismic Hazard Mapping Program. The 200 km maximum seismogenic width used by Frankel and Petersen (2008) might be considered an upper bound for earthquakes that initiate in the Puget Sound region given that it represents a rupture width extending to the top of episodic tremor and slip (ETS) events (Frankel and Petersen, 2008); however, both Hyndman (2013) and Wirth and Frankel (2019) argue that co-seismic rupture to this depth is not likely given thermal, geologic, and geodetic constraints from past mega-earthquakes and ground-motion simulations.

Campbell (2020) poses the question of whether an earthquake that originates on the wider section of the CASC interface in the Puget Sound region will exhibit a larger breakpoint magnitude. This might be the case if rupture were to extend the full width of the fault before extending along strike rather than rupturing along the strike before "filling in" the full width of the seismogenic interface in this region. To account for this uncertainty, a larger breakpoint magnitude could be used for hypocenters located in the Puget Sound region and a smaller one for hypocenters originating along the narrower sections of the CASC interface.

Alternatively, epistemic uncertainty could be modeled using a single set of breakpoint magnitudes regardless of hypocenter location. For example per Campbell (2020), if this latter alternative is used, one possible set of values would be 7.7 (5% confidence limit), 8.0 (mean), and 8.5 (95% confidence limit) with weights of 0.185, 0.630, and 0.185, respectively. The central value of 8.0 was used in the KBCG20 Cascadia regionalized GMM. We used the breakpoint magnitudes from the study of Ji and Archuleta (2018) for intraslab events on CASC.

8.3.3 Basin-Depth Model

The basin-depth model in Cascadia is different for sites in the Seattle Basin and other basins. As seen in Figure 4.7, there is almost no correlation between $Z_{2.5}$ and V_{S30} for the Seattle Basin, with all sites in the Seattle Basin having an almost constant $Z_{2.5}$ value of about 7000 m. Thus, we use a constant value to model the basin amplification for the Seattle Basin. This has the disadvantage that there is a sharp discontinuity at the boundary of the basin, but there is not enough information in the database to fully resolve this issue. For other sites in Cascadia, the normal basin-depth model can be used, which depends on the difference of the observed $Z_{2.5}$ value from the reference $Z_{2.5}$ value for a given V_{S30} value.

8.4 ALEATORY VARIABILITY

The aleatory variability is described in Chapter 5. The application is straightforward: the value of the aleatory variability (standard deviation) is a constant for each period and can be calculated as $\sigma^2 = \tau^2 + \phi^2$. As with all other parameters of our model, ϕ and τ are associated with epistemic uncertainty. Thus, the user should think about whether to include this epistemic uncertainty.Note that the range of epistemic uncertainty is not large; therefore, its effect on final hazard calculations is probably small.

We do not partition the within-event residuals into a systematic site term δS and within-event/within-site residual because due to the narrow azimuthal range of the data, potential unmodeled path effects can easily be mapped into systematic site terms. If one needs to use a single-station sigma model in PSHA calculations, one possibility is to use ratios between ϕ and ϕ_{SS} from existing studies [see e.g., Lin et al. (2011) and references therein] to partition ϕ into ϕ_{SS} and ϕ_{S2S}. Such an approach assumes that these ratios (which will typically be estimated for shallow active crustal data) are applicable to subduction data as well.

The value of the within-event standard deviation ϕ is estimated during the regression before taking into account basin effects. Hence, the value of ϕ includes additional uncertainty due to differences in basin depths. If one includes $Z_{1.0}$ of $Z_{2.5}$ as a predictor, then one should use a lower value of ϕ to avoid double-counting. The ratios of ϕ with and without basin-depth scaling are shown in Figure 5.2. Since the values for Cascadia, New Zealand, and Taiwan are based on a small number of records, we recommend using the ratio for Japan. If the value of $Z_{1.0}$ or $Z_{2.5}$ is unknown, then one can either use the reference value calculated from V_{S30} together with the larger value of ϕ, or include $Z_{1.0}$/$Z_{2.5}$ with uncertainty together with the smaller value of ϕ. The latter approach is preferred.

9 Discussion and Conclusions

9.1 MAIN CONCLUSIONS

KBCG20 was developed as part of the NGA-Sub research program using a comprehensive compilation of subduction interface and intraslab ground-motion recordings and metadata available in the NGA-Sub database. It includes ground-motion scaling terms for magnitude, distance, site amplification, and basin amplification, with some of these terms being adjustable to accommodate differences between interface and intraslab events, and differences among seven subduction zone regions, including Alaska (AK), Central America and Mexico (CAM), Cascadia (CASC), Japan (JP), New Zealand (NZ), South America (SA), and Taiwan (TW). Some of these regions are further divided into subregions to account for differences in anelastic attenuation between forearc and backarc, and differences in breakpoint magnitude between segments of a larger subduction zone. We believe that our new GMM, which includes median, aleatory variability, and epistemic uncertainty models, represents a significant improvement in the understanding and estimation of subduction ground motions. The Bayesian approach used to develop the model will facilitate the update of the GMM as new data become available. Some of the more important technical issues that were addressed in our study and how we addressed them are described in the remainder of this chapter.

9.2 BREAKPOINT MAGNITUDE

There are only a few subduction zones for which earthquakes larger than the estimated breakpoint magnitude have occurred. Even fewer of these mega-earthquakes have ground-motion recordings, which make them among the least sampled in our global empirical database. KBCG20 incorporates a decrease in ground-motion magnitude-scaling rate (MSR) beyond the breakpoint magnitude for a particular subduction zone based primarily on ground-motion simulations as implemented in Abrahamson et al. (2016, 2018), which make the values of breakpoint magnitude and MSR beyond this magnitude uncertain. Yet, both of these parameters have a large impact on predicted ground motions from large intraslab earthquakes and great-to-giant interface events. Although the breakpoint magnitudes are estimated from scientific studies, there is still a great deal of uncertainty associated with them [e.g., Tables 8.1 and 8.2; Campbell (2020)]. Figure 4.13 shows that the uncertainty in the MSR above the breakpoint magnitude—defined by the regression coefficient θ_5—is relatively large. Its posterior estimates are similar to its prior estimates because of the large uncertainty in its prior values and the paucity of earthquakes that contribute to its estimate. Therefore, epistemic uncertainty should be incorporated in both the breakpoint magnitude and large-magnitude MSR in the engineering application of KBCG20.

9.3 ANELASTIC ATTENUATION

Anelastic attenuation of subduction ground motion depends on many factors, including the type of earthquake (interface or intraslab), the fracturing and density of the crust, the location of the site with respect to a volcanic arc (forearc or backarc), and the frequency or period of the ground motion. The KBCG20 anelastic attenuation terms account for many of these factors on a global and regional scale, although not necessarily in a consistent way because of the non-uniform geographic distribution of the recordings. The difference in anelastic attenuation between interface and intraslab earthquakes potentially accounts for the unique travel paths that ground motions from these two types of events must traverse due to their interaction with the dense oceanic slab; however, KBGC19 does not find such differences, possibly because of trade-offs between anelastic attenuation and other terms that involve these two types of earthquakes.

All seven regions had a sufficient number of recordings to model differences in forearc anelastic attenuation among the regions. The global model used all of these data for its forearc anelastic attenuation term. Although some regions had enough recordings to distinguish between the forearc and backarc (AK, CASC, and JP), other regions either did not have enough data to distinguish between these two attenuation subregions or the data did not indicate that there was a difference. Although the global model included a backarc anelastic attenuation term in the regression, we recommend that it not be used in a forward prediction unless it is known that the subduction zone has different anelastic attenuation in the forearc and backarc from, e.g., regional Q estimates. JP is unique in that it has two forearc subregions (the Japan Trench associated with the Pacific plate and the Nankai Trough associated with the Philippine Sea plate) as well as a backarc sub-region. Thus, there was sufficient data in JP to distinguish between all three subregions and account for travel paths that cross the volcanic arc from one sub-region to another.

9.4 SITE AMPLIFICATION

Linear site amplification is modeled using the predictor variable V_{S30}. Ideally, V_{S30} should be measured at every site included in the analysis. Unfortunately, this is not possible because of the prohibitively large computing costs required to make such measurements. Instead, the NGA-Sub program relied on existing measurements available in the literature or provided by regional scientists and engineers (Bozorgnia et al., 2020). As a result, the majority of V_{S30} values in the database are estimated using a variety of geologic, geomorphologic, and topographic proxies. The use of proxies increases the uncertainty in the value of V_{S30}, which is generally taken into account in the Bayesian regression analysis. We do not include a station term in the regression because of its trade-off with other predictor variables, such as anelastic attenuation within the backarc. If we had included a station term, the value of the standard deviation of this term (traditionally defined as ϕ_{S2S}) would account for such factors, depending on whether V_{S30} is measured or estimated.

Since we do not include a station term, epistemic uncertainty should be incorporated in V_{S30} if it is not measured, or if there is some other reason to believe that it is uncertain in the engineering application of KBCG20.

Another issue related to site amplification is its nonlinearity. As is usually the case, there are very few recordings with amplitudes high enough to cause observable nonlinear soil effects in the ground motion. Instead, we adopted the nonlinear site formulation used by Campbell and Bozorgnia (2014) in their NGA-West2 shallow crustal GMM for both interface and intraslab earthquakes and all subduction zone regions. By doing this we inherently make the assumption that a site will exhibit similar site response for all earthquake sources and geographic regions. This assumption is likely not true, but it is the only means of including nonlinear soil effects in our GMM at the present time.

9.5 BASIN AMPLIFICATION

An important issue for the design of long-period structures worldwide is the effect of sedimentary-basin amplification. One example of this is the Puget Sound, Washington, region. Ground-motion simulations conducted as part of the "M9 Project" (Wirth and Frankel, 2019; Frankel et al., 2018; Wirth et al., 2018) have shown that long-period ground motions can be significantly amplified at sites located in the Seattle basin from interface, intraslab, and crustal earthquakes. Based on the results of these studies and a related USGS workshop (Wirth et al., 2018), the Seattle Department of Construction and Inspections adopted a requirement (SDCI (2018)) that all tall building designs utilizing site-specific ground-motion procedures must incorporate basin effects for those buildings located in the city of Seattle.

Basin-amplification effects for the Seattle basin and other basin and non-basin locations in the Pacific Northwest are included in KBCG20 using a basin-depth term that utilizes site-specific estimates of the basin-depth parameter $Z_{2.5}$. A comparison of the basin-amplification factors for the Seattle basin estimated by our GMM and those proposed by SDCI (2018) are shown in Figure 7.42. KBCG20 also includes basin-amplification terms for JP using values $Z_{2.5}$ and for NZ and TW using values of $Z_{1.0}$. There is insufficient information on basin depths for the remaining regions (AK, CAM, and SA) to include a basin-depth term. A basin-depth term was not included in the global model because of the site- and region-specific nature of this term.

9.6 EPISTEMIC UNCERTAINTY

KBGC19 is partially non-ergodic because of its regionalization of terms involving the overall amplitude of ground shaking (constants), anelastic attenuation, site amplification (terms involving V_{S30}), and basin amplification (terms involving $Z_{1.0}$ and $Z_{2.5}$). That said, the degree of non-ergodicity is limited based on available data compiled to date, but there are still several subduction zone regions around the world with limited or no empirical data at all. Even some of the regions included in our GMM have very limited usable data (e.g., CASC) due to either a paucity of earthquakes for the region or, if there are earthquakes, the paucity of seismographs and recordings.

Before KBCG20 is used to estimate ground motions for a region not modeled as part of KBCG20, an analysis of the applicability of the model should be performed. If data are available, this evaluation can be in the form of a simple residual analysis or a more sophisticated Bayesian update. It can also include an evaluation of an applicable breakpoint magnitude at which the MSR is expected to decrease based on the overall tectonic characteristics of the subduction zone (see Section 8.4). If a regional evaluation or update is not possible, the global model should be used along with its associated epistemic standard deviation; see Chapter 6. Because of a lack of any empirical constraints, the epistemic standard deviation associated with the global GMM is larger than that for any of the modeled regional models. Of course, it is possible to reduce the epistemic standard deviations for the global and regional models with additional investigations and data.

An important feature of our model is that the within-model epistemic uncertainty is explicitly quantified to account for differences in available data for each of the seven modeled subduction zone regions as well as those regions for which data are unavailable. To capture the epistemic uncertainty associated with the ground-motion predictions, we developed 800 sets of regression parameters (coefficients and aleatory standard deviations) through our Bayesian modeling approach. The 800 sets of coefficients are provided in an electronic supplement to this report. In theory, the complete set of 800 cases could be used in a PSHA to account for the complete distribution of epistemic uncertainty, but the necessary effort and computing time to do so is only possible for the most important studies with sufficient resources. Of course, one could always down-sample the 800 cases in an attempt to capture a realistic estimate of the epistemic uncertainty associated with the ground-motion predictions, but studies would need to be done to ensure that accuracy is not being sacrificed.

A computer program distributed as part of this study allows the user to estimate median ground motions, between-earthquake standard deviations, within-earthquake standard deviations, and epistemic standard deviations for PGA, PGV, and 5%-damped PSA at periods of 0.01, 0.02, 0.03, 0.05, 0.075, 0.1, 0.15, 0.2, 0.25, 0.3, 0.4, 0.5, 0.75, 1.0, 1.5, 2.0, 3.0, 4.0, 5.0, 7.5 and 10 sec. The epistemic uncertainty calculated in this way only applies to KBCG20 (i.e., intra-model uncertainty). Therefore, we recommend that the user also considers modeling epistemic uncertainty by employing multiple GMMs, either developed as part of the NGA-Sub program or available in the literature.

REFERENCES

Abrahamson N., Gregor N., Addo, K. (2016). BC hydro ground motion prediction equations for subduction earthquakes, *Earthq. Spectra*, 32(1): 23–44.

Abrahamson N.A., Kuehn N., Gregor N., Bozorgnia Y., Parker G.A., Stewart J.P, Chiou B.-J., Campbell K.W., Youngs R. (2018). Update of the BC Hydro subduction ground-motion model using the NGA-Subduction Dataset, *Report No. 2018*.

Abrahamson N.A., Kuehn N., Walling M., Landwehr N. (2019). Probabilistic seismic hazard analysis in California using nonergodic ground motion models, *Bull. Seismol. Soc. Am.*, 109(4): 1235–1249.

Abrahamson N.A., Silva W.J., Kamai R. (2014). Summary of the ASK14 ground motion relation for active crustal regions, *Earthq. Spectra*, 30(3): 1025–1055.

Ahdi S.K., Ancheta T.D., Contreras V., Kishida T., Kwak D.Y., Kwok O.L., Parker G.A., Ruz F., Stewart J.P. (2020). Chapter 5: Site Condition Parameters, in *Data Resources for NGA- Subduction Project*, *PEER Report No. 2020/02*, J.P. Stewart (ed.), Pacific Earthquake Engineering Research Center, University of California, Berkeley, CA.

Al-Atik L., Youngs R.R. (2014). Epistemic uncertainty for NGA-West2 models, *Earthq. Spectra*, 30(3): 1301–1318.

Ancheta T.D., Darragh R.B., Stewart J.P., Seyhan E., Silva W.J., Chiou B.S.-J., Wooddell K.E., Graves R.W., Kottke A.R., Boore D.M., Kishida T., Donahue J.L. (2014). NGA-West2 database, *Earthq. Spectra*, 30(3): 989–1005.

Anderson J.G., Brune J.N. (1999). Probabilistic seismic hazard analysis without the ergodic assumption, *Seismol. Res. Lett.*, 70(1): 19–28.

Archuleta R.J,. Ji C. (2018). A look at scaling of ground motion with magnitude." *Proceedings of the 11th U.S. National Conference on Earthquake Engineering*, Los Angeles, CA.

Atkinson G.M. (1997). Empirical ground motion relations for earthquakes in the Cascadia region, *Can. J. Civil Eng.*, 24(1): 64–77.

Atkinson G.M., Bommer J.J., Abrahamson N.A. (2014). Alternative approaches to modeling epistemic uncertainty in ground motions in probabilistic seismic-hazard analysis, *Seismol. Res. Lett.*, 85(6): 1141–1144.

Atkinson G.M., Boore D.M. (2003). Empirical ground-motion relations for subduction-zone earthquakes and their application to Cascadia and other regions, *Bull. Seismol. Soc. Am.*, 93(4): 1703–1729.

Atkinson G.M., Boore D.M. (2008). Erratum to 'Empirical ground-notion relations for subduction aone earthquakes and their application to Cascadia and other regions', *Bull. Seismol. Soc. Am.*, 98(5): 2567–2569.

Atkinson G.M., Macias M. (2009). Predicted ground motions for great interface earthquakes in the Cascadia subduction zone, *Bull. Seismol. Soc. Am.*, 99(3): 1552–1578.

Atkinson G.M., Morrison M. (2009). Observations on regional variability in ground-mMotion amplitudes for small-to-moderate earthquakes in North America, *Bull. Seismol. Soc. Am.*, 99(4): 2393–2409.

BC Hydro (2012). *Dam Safety Probabilistic Seismic Hazard Analysis (PSHA) Model*, Report, Vancouver, British Columbia, <papers3://publication/uuid/676C6BA7-37CC-4A72-848C-3DF341C88B19>.

Berryman, K., Wallace L., Hayes G.P., Bird P., Wang K., Basili R., Lay T., Stein R.S., Sagiya T., Rubin A.M., Barrientos S., Kreemer C., Litchfield N., Pagani M., Gledhill K., Haller K., Costa C. (2015). *The GEM Faulted Earth Subduction Characterisation Project Report (Version 1.0)*, <http://www.nexus.globalquakemodel.org/gem-faulted-earth/posts>.

Betancourt M. (2017). A conceptual introduction to Hamiltonian Monte Carlo, arXiv:1701.02434v2.

Betancourt M., Girolami M. (2015). Hamiltonian Monte Carlo for hierarchical models, in *Current Trends in Bayesian Methodology with Applications*, CRC Press, Boca Raton, FL, pp. 79–101.

Boore D.M., Stewart J.P., Seyhan E., Atkinson G.M. (2014). NGA-West2 equations for predicting PGA, PGV, and 5% damped PSA for shallow crustal earthquakes, *Earthq. Spectra*, 30(3): 1057–1085.

Bozorgnia Y., Abrahamson N.A., Atik L.A., Ancheta T.D., Atkinson G.M., Baker J.W., Baltay A., Boore D.M., Campbell K.W., Chiou B.S.-J., Darragh R., Day S., Donahue J., Graves R.W., Gregor N., Hanks T., Idriss I.M., Kamai R., Kishida T., Kottke A., Mahin S.A., Rezaeian S., Rowshandel B., Seyhan E., Shahi S., Shantz T., Silva W.J., Spudich P., Stewart J.P., Watson-Lamprey J., Wooddell K.E., Youngs R.R. (2014). NGA-West2 research project, *Earthq. Spectra*, 30(3): 973–987.

Bozorgnia Y., Kishida T., Abrahamson N.A., Ahdi S. K., Ancheta T.D., Archuleta J., Atkinson G.M., Boore D.M., Campbell K.W., Chiou B.S.-J., Contreras V., Darragh R., Gregor N., Gulerce Z., Idriss I. M., Ji C., Kamai R., Kuehn N., Kwak D. Y., Kwok A., Lin P.-S., Magistrale H., Mazzoni S., Muin S., Parker G.A., Si H., Silva W.J., Stewart J.P., Walling M., Wooddell K.E., Youngs R.R. (2018). NGA-Subduction research program, *Proceedings of the 11th U.S. National Conference on Earthquake Engineering*, Los Angeles, CA.

Bozorgnia Y., Stewart J.P., Abrahamson N.A., Ahdi S.K., Ancheta T.D., Archuleta R.J., Atkinson G.M., Boore D.M., Boroschek R, Campbell K.W., Chiou B.S.-J., Contreras V., Darragh R.B., Gregor N., Gulerce Z., Idriss I.M., Ji C., Kamai R., Kishida T., Kuehn N., Kwak D.Y., Kwok A.O., Lin P.S., Magistrale H., Mazzoni S., Muin S., Midorikawa S., Parker G.A., Si H., Silva

W.J., Walling M., Wooddell K.E., Youngs R.R., (2020). "Chapter 1: Introduction." in *Data Resources for NGA- Subduction Project*, *PEER Report No. 2020/02*, J.P. Stewart (ed.), Pacific Earthquake Engineering Research Center, University of California, Berkeley, Ca.

Building Seismic Safety Council (2001). *The 2000 NEHRP Recommended Provisions for New Buildings and Other Structures, Part I (Provisions) and Part II (Commentary), FEMA 369*, Federal Emergency Management Agency, Washington, D.C.

Campbell K.W. (2020). Proposed methodology for estimating the magnitude at which subduction megathrust ground motions and source dimensions exhibit a break in magnitude scaling: Example for 79 global subduction zones, *Earthq. Spectra*, 36(3), doi.org/10.1177/8755293019899957.

Campbell K.W., Bozorgnia Y. (2008). NGA ground motion model for the geometric mean horizontal component of PGA, PGV, PGD and 5% damped linear elastic response spectra fo periods Ranging from 0.01 to 10 s, *Earthq. Spectra*, 24(1): 139–171.

Campbell K.W., Bozorgnia Y. (2014). "NGA-West2 ground motion model for the average horizontal components of PGA, PGV, and 5% damped linear acceleration response Sspectra, *Earthq. Spectra*, 30(3): 1087–1115.

Carpenter B., Gelman A., Hoffman M.D., Lee D., Goodrich B., Betancourt M., Brubaker M., Guo J., Li P., Riddell, A. (2017). Stan : A probabilistic programming language, *J. Stat. Softw.*, 76(1): 1–32.

Cascadia Region Earthquake Workgroup (2013). "Cascadia Subduction Zone Earthquakes: A Magnitude 9.0 Earthquake Scenario.." *Report no.*, Washington Division of Geology and Earth Resources Information Circular 116, Oregon Department of Geology and Mineral Industries Open-File Report 0-13-22, and British Columbia Geological Survey Information Circular 2013-3.

Chiou B.S-J., Darragh R., Gregor N., Silva W.J. (2008). NGA project strong-motion database, *Earthq. Spectra*, 24(1): 23.

Chiou B.S.-J., Youngs R.R. (2014). Update of the Chiou and Youngs NGA model for the average horizontal component of peak ground motion and response spectra, *Earthq. Spectra*, 30(3): 1117–1153.

Contreras V., Stewart J.P., Kishida T., Darragh R.B., Chiou B.S.-J., Mazzoni S., Kuehn N.M., Ahdi S.K., Wooddell K., Youngs R.R., Bozorgnia, Y., Boroschek, R., Rojas, F., Órdenes, J. (2020). Chapter 4: Source and Path Metadata, in *Data Resources for NGA-Subduction Project*, *PEER Report 2020/02*, J.P. Stewart (ed,), Pacific Earthquake Engineering Research Center, University of California, Berkeley, CA.

Dawood H.M., Rodriguez-Marek A. (2013). A method for including path effects in ground-motion prediction equations: An example using the Mw 9.0 Tohoku earthquake aftershocks, *Bull. Seismol. Soc. Am.*, 103(2B): 1360–1372.

Frankel A.D., Chen R., Petersen M., Moschetti M., Sherrod B. (2015). 2014 update of the Pacific Northwest portion of the U.S. National Seismic Hazard Maps, *Earthq. Spectra*, 31(S1): S131–S148.

Frankel A.D., Wirth E., Marafi N., Vidale J., Stephenson W. (2018). Broadband synthetic seismograms for magnitude 9 earthquakes on the Cascadia Megathrust based on 3D simulations and stochastic synthetics, Part 1: Methodology and overall results, *Bull. Seismol. Soc. Am.*, 108(5A): 2347–2369.

Frankel A.D., Petersen M.D. (2008). Cascadia Subduction Zone." *U.S.G.S. Open-File Report 2007-1437- L*, U.S. Geological Survey, Reston, VA.

García-Fernández M., Gehl P., Jiménez M.-J., D'Ayala D. (2019). Modelling Pan-European ground motions for seismic hazard applications, *Bull. Earthq. Eng.*, 17(6): 2821–2840.

Gelman A. (2006). Prior distributions for variance parameters in hierarchical models, *Bayesian Anal.*, 1(3): 515–534.

Gelman A., Hill J. (2006). *Data Analysis Using Regression and Multilevel/Hierarchical Models*. Cambridge University Press.

Ghofrani H., Atkinson G.M. (2014). "Ground-motion prediction equations for interface earthquakes of M7 to M9 based on empirical data from Japan, *Bull. Earthq. Eng.*, 12(2): 549–571.

Gregor N., Silva W.J., Wong I.G., Youngs R. R. (2002). Ground-motion attenuation relationships for Cascadia subduction zone megathrust earthquakes based on a stochastic finite-fault model, *Bull. Seismol. Soc. Am.*, 92(5): 1923–1932.

Hjort N.L., Holmes C., Müller P., Walker S.G., Ghosal S., Lijoi A., Prünster I., Teh, Y.W., Jordan M.I., Griffin J., Dunson D.B. Quintana, F. (2010). *Bayesian Nonparametrics*. Cambridge University Press, <http://www.cambridge.org/catalogue/catalogue.asp?isbn=9780521513463>.

Hyndman R.D. (2013). Downdip landward limit of Cascadia great earthquake rupture, *J. Geophys. Res.: Solid Earth*, 118(10): 5530–5549.

Ji C., Archuleta R.J. (2018). *Scaling of PGA and PGV deduced from numerical simulations of intraslab earthquakes*, PEER Report, in preparation, Pacific Earthquake Engineering Research Center, University of California, Berkeley, Ca.

Juárez M.A., Steel M.F.J. (2010). Model-based clustering of non-Gaussian panel data based on Skew- t distributions, *J. Bus. Econ. Stat.*, 28(1): 52–66.

Keefer D.L. Bodily S.E. (1983). Three-point approximations for continuous random variables, *Management Science*, 29(5), 519–637, https://doi.org/10.1287/mnsc.29.5.595.

Kishida T., Contreras V., Bozorgnia Y., Abrahamson N.A., Ahdi S.K., Boore D.M., Campbell K.W., Chiou B.S-J., Darragh R., Gregor N., Kwak D.Y., Kwok A.O., Lin P., Magistrale, H. Mazzoni S., Midorikawa S., Si H., Silva W.J., Stewart J.P., Wooddell K.E., Youngs R.R. (2018). Nga-Sub ground motion database, *Proceedings of the 11th U.S. National Conference on Earthquake Engineering*, Los Angeles, CA.

Kotha S.R., Bindi D., Cotton F. (2016). Partially non-ergodic region specific GMPE for Europe and Middle-East, *Bull. Earthq. Eng.*, 14(4): 1245–1263.

Kuehn N.M., Abrahamson N.A., Walling M.A. (2019). Incorporating nonergodic path effects into the NGA-West2 ground-motion prediction equations, *Bull. Seismol. Soc. Am.*, 109(2): 575–585.

Lacour M., Abrahamson N.A. (2019). Efficient propagation of epistemic uncertainty in the median groundâĂŘmotion model in probabilistic aazard calculations, *Bull. Seismol. Soc. Am.*, 109(5): 2063–2072.

Lanzano G., Luzi L., Pacor F., Felicetta C., Puglia R., Sgobba S., DâĂŹAmico M. (2019). A revised groundâĂŘmotion prediction nodel for shallow crustal earthquakes in Italy, *Bull. Seismol. Soc. Am.*, 109(2): 525–540.

Lewandowski D., Kurowicka D., Joe H. (2009). Generating random correlation matrices based on vines and extended onion method, *J. Multivariate Anal.*, 100(9): 1989–2001.

Lin, P.-S., Chiou, B., Abrahamson, N., Walling, M., Lee, C.-T., and Cheng, C.-T. (2011). "Repeatable Source, Site, and Path Effects on the Standard Deviation for Empirical Ground-Motion Prediction Models." *Bulletin of the Seismological Society of America*, 101(5), 2281–2295.

Montalva G.A., Bastías N., RodriguezâĂŘMarek A. (2017). GroundâĂŘmotion prediction equation for the Chilean subduction zone, *Bull. Seismol. Soc. Am.*, 107(2): 901–911.

Morikawa N., Fujiwara H. (2013). A new ground motion prediction equation for Japan applicable up to M9 mega-earthquake, *J. Disaster Res.*, 8(5): 878–888.

Neal R.M. (2011). MCMC using Hamiltonian dynamics, *Handbook of Markov Chain Monte Carlo*, pp. 113–162, CRC Press, Boca Raton, FL.

Oppenheimer D., Eaton J., Jayko A., Lisowski M., Marshall G., Murray M., Simpson R., Stein R., Beroza G., Magee M., Carver G., Dengler L., McPherson R., Gee L., Romanowicz B., Gonzalez F., Li W. H., Satake K., Somerville P.G., Valentine D. (1993). The Cape Mendocino, California, earthquakes of April 1992: Subduction at the triple junction, *Science*, 261(5120): 433–438.

Petersen M.D., Moschetti M.P., Powers P.M., Mueller C.S., Haller K.M., Frankel A.D., Zeng Y., Rezaeian S., Harmsen S.C., Boyd O.S., Field N., Chen R., Rukstales K.S., Luco N., Wheeler R.L., Williams R.A., Olsen A.H. (2014). "Documentation for the 2014 Update of the United States National Seismic Hazard Maps, *U.S.G.S. Open-File Report 2014âĂŞ1091*, U.S. Geological Survey, 243 pgs., Reston, VA, https://dx.doi.org/10.3133/ofr20141091.

Rasmussen C.E., Williams C.K.I. (2006). *Gaussian Processes for Machine Learning.* MIT Press, Cambridge, http://www.gaussianprocess.org/gpml/.

Satake K., Atwater B.F. (2007). Long-term perspectives on giant earthquakes and tsunamis at subduction zones, *Annu. Rev. Earth Pl. Sc.*, 35(1): 349–374.

Satake K., Wang K., Atwater B.F. (2003). Fault slip and seismic moment of the 1700 Cascadia earthquake inferred from Japanese tsunami descriptions, *J. Geophys. Res.*, 108(B11): 2535.

SDCI (2018). Implementation of March 22, 2018 USGS/SDCI basin ampligication workshop results, *Director's Rule 20-2018*." *Report no.*, City of Seattle Department of Construction and Inspections, Seattle, WA.

Sedaghati F., Pezeshk S. (2017). Partially nonergodic empirical groundâĂŘmotion models for predicting horizontal and vertical PGV, PGA, and 5% damped linear acceleration response spectra using data from the Iranian Plateau, *Bull. Seismol. Soc. Am.*, 107(2): 934–948.

Spiegelhalter D., Rice, K. (2009). Bayesian statistics, *Scholarpedia*, 4(8): 5230, doi:10.4249/scholarpedia.5230.

Stafford P.J. (2014). Crossed and nested mixed-effects approaches for enhanced model development and removal of the ergodic assumption in empirical ground-motion models, *Bull. Seismol. Soc. Am.*, 104(2): 702–719.

Stafford P.J. (2019). Continuous integration of data into ground-motion models using Bayesian updating, *J. Seismol.*, 23(1): 39–57.A

Stewart, J.P. (ed.) (2020). Data resources for NGA-Subduction Project, *PEER Report No. 2020/02*, Pacific Earthquake Engineering Research Center, University of California, Berkeley, CA.

Stewart J.P., Midorikawa S., Graves R.W., Khodaverdi K., Kishida T., Miura H., Bozorgnia Y., Campbell K.W. (2013). Implications of the M w 9.0 Tohoku-Oki earthquake for ground motion scaling with source, path, and site parameters, *Earthq. Spectra*, 29(S1): S1–S21.

Tanioka Y., Ruff L., Satake K. (1995a). The great Kurile Earthquake of October 4, 1994 tore the slab, *Geophys. Res. Lett.*, 22(13): 1661–1664.

Tanioka Y., Satake K., Ruff L. (1995b). Seismotectonics of the April 25, 1992, Petrolia earthquake and the Mendocino triple junction region, *Tectonics*, 14(5): 1095–1103.

Walling M., Silva W.J., Abrahamson N.A. (2008). Nonlinear site amplification factors for constraining the NGA models, *Earthq. Spectra*, 24(1): 243–255.

Wang K., Tréhu A.M. (2016). Invited review paper: Some outstanding issues in the study of great megathrust earthquakesâĂŤThe Cascadia example, *J. Geodyn.*, 98: 1–18.

Wirth E.A., Chang S.W., Frankel A.D. (2018). 2018 report on incorporating sedimentary basin response into the design of tall buildings in Seattle, Washington:, *Open File Report 2018âĂŞ1149*, U.S. Geological Survey, Reston, VA.

Wirth E.A., Frankel A.D. (2019). Impact of down-dip rupture limit and high-stress drop subevents on coseismic land-level change during Cascadia megathrust earthquakes, *Bull. Seismol. Soc. Am.*, 109(6): 2187–2197.

Wooddell K.E., Abrahamson N.A. (2014). Classification of main shocks and aftershocks in the NGA-West2 database, *Earthq. Spectra*, 30(3): 1257–1267.

Zhao J.X., Jiang F., Shi P., Xing H., Huang H., Hou R., Zhang Y., Yu P., Lan X., Rhoades D.A., Somerville P.G., Irikura K., Fukushima Y. (2016a). GroundâĂŘmotion prediction equations for subduction slab earthquakes in Japan ssing site class and simple geometric attenuation functions. *Bull. Seismol. Soc. Am.*, 106(4): 1535–1551.

Zhao J.X., Liang X., Jiang F., Xing H., Zhu M., Hou R., Zhang Y., Lan X., Rhoades D.A., Irikura K., Fukushima Y., Somerville P.G. (2016b). GroundâĂŘmotion prediction equations for subduction interface earthquakes in Japan using site class and simple geometric attenuation functions, *Bull. Seismol. Soc. Am.*, 106(4): 1518–1534.

Zhao J.X. Xu H. (2012). Magnitude-scaling rate in ground-motion prediction equations for response spectra from large subduction interface earthquakes in Japan, *Bull. Seismol. Soc. Am.*, 102(1): 222–235.

Zhao J.X., Zhang J., Asano A., Ohno Y., Oouchi T., Takahashi T., Ogawa H., Irikura K., Thio H. K., Somerville P.G., Fukushima Y. (2006). Attenuation relations of strong ground motion in Japan using site classification based on predominant period, *Bull. Seismol. Soc. Am.*, 96(3): 898–913.

PEER REPORTS

PEER reports are available as a free PDF download from https://peer.berkeley.edu/peer-reports. In addition, printed hard copies of PEER reports can be ordered directly from our printer by following the instructions at https://peer.berkeley.edu/peer-reports. For other related questions about the PEER Report Series, contact the Pacific Earthquake Engineering Research Center, 325 Davis Hall, Mail Code 1792, Berkeley, CA 94720. Tel.: (510) 642-3437; and Email: peer_center@berkeley.edu.

PEER 2020/03 *NGA-Subduction Global Ground-Motion Models with Regional Adjustment Factors.* Grace A. Parker, Jonathan P. Stewart, David M. Boore, Gail M. Atkinson, and Behzad Hassani. September 2020.

PEER 2020/02 *Data Resources for NGA-Subduction Project.* Yousef Bozorgnia (PI) and Jonathan P. Stewart (Editor). March 2020.

PEER 2020/01 *Modeling Viscous Damping in Nonlinear Response History Analysis for Steel Moment-Frame Buildings.* Xin Qian, Anil K. Chopra, and Frank McKenna. June 2020.

PEER 2019/09 Seismic Behavior of Special Concentric Braced Frames under Short- and Long-Duration Ground Motions. Ali Hammad and Mohamed A. Moustafa. December 2019.

PEER 2019/08 Influence of Vertical Ground Motion on Bridges Isolated with Spherical Sliding Bearings. Rushil Mojidra and Keri L. Ryan. December 2019.

PEER 2019/07 *PEER Hub ImageNet* (*ϕ*-Net): *A Large-Scale Multi-Attribute Benchmark Dataset of Structural Images*. Yuqing Gao, and Khalid. M. Mosalam. November 2019.

PEER 2019/06 *Fluid-Structure Interaction and Python-Scripting Capabilities in OpenSees*. Minjie Zhu and Michael H. Scott. August 2019.

PEER 2019/05 *Expected Earthquake Performance of Buildings Designed to the California Building Code (California Alfred E. Alquist Seismic Safety Publication 19-01).* Grace S. Kang, Sifat Muin, Jorge Archbold, Bitanoosh Woods, and Khalid Mosalam. July 2019.

PEER 2019/04 *Aftershock Seismic Vulnerability and Time-Dependent Risk Assessment of Bridges*. Sujith Mangalathu, Mehrdad Shokrabadi, and Henry V. Burton. May 2019.

PEER 2019/03 *Ground-Motion Directivity Modeling for Seismic Hazard Applications.* Jennifer L. Donahue, Jonathan P. Stewart, Nicolas Gregor, and Yousef Bozorgnia. Review Panel: Jonathan D. Bray, Stephen A. Mahin, I. M. Idriss, Robert W. Graves, and Tom Shantz. May 2019.

PEER 2019/02 *Direct-Finite-Element Method for Nonlinear Earthquake Analysis of Concrete Dams Including Dam–Water–Foundation Rock Interaction.* Arnkjell Løkke and Anil K. Chopra. March 2019.

PEER 2019/01 *Flow-Failure Case History of the Las Palmas, Chile, Tailings Dam.* R. E. S. Moss, T. R. Gebhart, D. J. Frost, and C. Ledezma. January 2019.

PEER 2018/08 *Central and Eastern North America Ground-Motion Characterization: NGA-East Final Report*. Christine Goulet, Yousef Bozorgnia, Norman Abrahamson, Nicolas Kuehn, Linda Al Atik, Robert Youngs, Robert Graves, and Gail Atkinson. December 2018.

PEER 2018/07 *An Empirical Model for Fourier Amplitude Spectra using the NGA-West2 Database*. Jeff Bayless, and Norman A. Abrahamson. December 2018.

PEER 2018/06 *Estimation of Shear Demands on Rock-Socketed Drilled Shafts subjected to Lateral Loading*. Pedro Arduino, Long Chen, and Christopher R. McGann. December 2018.

PEER 2018/05 *Selection of Random Vibration Procedures for the NGA-East Project*. Albert Kottke, Norman A. Abrahamson, David M. Boore, Yousef Bozorgnia, Christine Goulet, Justin Hollenback, Tadahiro Kishida, Armen Der Kiureghian, Olga-Joan Ktenidou, Nicolas Kuehn, Ellen M. Rathje, Walter J. Silva, Eric Thompson, and Xiaoyue Wang. December 2018.

PEER 2018/04 *Capturing Directivity Effects in the Mean and Aleatory Variability of the NGA-West 2 Ground Motion Prediction Equations.* Jennie A. Watson-Lamprey. November 2018.

PEER 2018/03 *Probabilistic Seismic Hazard Analysis Code Verification*. Christie Hale, Norman Abrahamson, and Yousef Bozorgnia. July 2018.

PEER 2018/02 *Update of the BCHydro Subduction Ground-Motion Model using the NGA-Subduction Dataset.* Norman Abrahamson, Nicolas Kuehn, Zeynep Gulerce, Nicholas Gregor, Yousef Bozorgnia, Grace Parker, Jonathan Stewart, Brian Chiou, I. M. Idriss, Kenneth Campbell, and Robert Youngs. June 2018.

PEER 2018/01 *PEER Annual Report 2017–2018*. Khalid Mosalam, Amarnath Kasalanati, and Selim Günay. June 2018.

PEER 2017/12 *Experimental Investigation of the Behavior of Vintage and Retrofit Concentrically Braced Steel Frames under Cyclic Loading*. Barbara G. Simpson, Stephen A. Mahin, and Jiun-Wei Lai, December 2017.

PEER 2017/11 *Preliminary Studies on the Dynamic Response of a Seismically Isolated Prototype Gen-IV Sodium-Cooled Fast Reactor* (*PGSFR*). Benshun Shao, Andreas H. Schellenberg, Matthew J. Schoettler, and Stephen A. Mahin. December 2017.

PEER 2017/10 *Development of Time Histories for IEEE693 Testing and Analysis (including Seismically Isolated Equipment).* Shakhzod M. Takhirov, Eric Fujisaki, Leon Kempner, Michael Riley, and Brian Low. December 2017.

PEER 2017/09 *“”R” Package for Computation of Earthquake Ground-Motion Response Spectra.* Pengfei Wang, Jonathan P. Stewart, Yousef Bozorgnia, David M. Boore, and Tadahiro Kishida. December 2017.

PEER 2017/08 *Influence of Kinematic SSI on Foundation Input Motions for Bridges on Deep Foundations*. Benjamin J. Turner, Scott J. Brandenberg, and Jonathan P. Stewart. November 2017.

PEER 2017/07 *A Nonlinear Kinetic Model for Multi-Stage Friction Pendulum Systems*. Paul L. Drazin and Sanjay Govindjee. September 2017.

PEER 2017/06 *Guidelines for Performance-Based Seismic Design of Tall Buildings, Version 2.02*. TBI Working Group led by co-chairs Ron Hamburger and Jack Moehle: Jack Baker, Jonathan Bray, C.B. Crouse, Greg Deierlein, John Hooper, Marshall Lew, Joe Maffei, Stephen Mahin, James Malley, Farzad Naeim, Jonathan Stewart, and John Wallace. May 2017.

PEER 2017/05 *Recommendations for Ergodic Nonlinear Site Amplification in Central and Eastern North America*. Youssef M.A. Hashash, Joseph A. Harmon, Okan Ilhan, Grace A. Parker, and Jonathan P. Stewart. March 2017.

PEER 2017/04 *Expert Panel Recommendations for Ergodic Site Amplification in Central and Eastern North America*. Jonathan P. Stewart, Grace A. Parker, Joseph P. Harmon, Gail M. Atkinson, David M. Boore, Robert B. Darragh, Walter J. Silva, and Youssef M.A. Hashash. March 2017.

PEER 2017/03 *NGA-East Ground-Motion Models for the U.S. Geological Survey National Seismic Hazard Maps*. Christine A. Goulet, Yousef Bozorgnia, Nicolas Kuehn, Linda Al Atik, Robert R. Youngs, Robert W. Graves, and Gail M. Atkinson. March 2017.

PEER 2017/02 *U.S.–New Zealand–Japan Workshop: Liquefaction-Induced Ground Movements Effects, University of California, Berkeley, California, 2–4 November 2016.* Jonathan D. Bray, Ross W. Boulanger, Misko Cubrinovski, Kohji Tokimatsu, Steven L. Kramer, Thomas O’Rourke, Ellen Rathje, Russell A. Green, Peter K. Robinson, and Christine Z. Beyzaei. March 2017.

PEER 2017/01 *2016 PEER Annual Report*. Khalid M. Mosalam, Amarnath Kasalanati, and Grace Kang. March 2017.

PEER 2016/10 *Performance-Based Robust Nonlinear Seismic Analysis with Application to Reinforced Concrete Bridge Systems*. Xiao Ling and Khalid M. Mosalam. December 2016.

PEER 2017/09 *Detailing Requirements for Column Plastic Hinges subjected to Combined Flexural, Axial, and Torsional Seismic Loading.* Gabriel Hurtado and Jack P. Moehle. December 2016.

PEER 2016/08 *Resilience of Critical Structures, Infrastructure, and Communities*. Gian Paolo Cimellaro, Ali Zamani-Noori, Omar Kamouh, Vesna Terzic, and Stephen A. Mahin. December 2016.

PEER 2016/07 *Hybrid Simulation Theory for a Classical Nonlinear Dynamical System*. Paul L. Drazin and Sanjay Govindjee. September 2016.

PEER 2016/06 *California Earthquake Early Warning System Benefit Study*. Laurie A. Johnson, Sharyl Rabinovici, Grace S. Kang, and Stephen A. Mahin. July 2006.

PEER 2016/05 *Ground-Motion Prediction Equations for Arias Intensity Consistent with the NGA-West2 Ground-Motion Models.* Charlotte Abrahamson, Hao-Jun Michael Shi, and Brian Yang. July 2016.

PEER 2016/04 *The M_W 6.0 South Napa Earthquake of August 24, 2014: A Wake-Up Call for Renewed Investment in Seismic Resilience Across California.* Prepared for the California Seismic Safety Commission, Laurie A. Johnson and Stephen A. Mahin. May 2016.

PEER 2016/03 *Simulation Confidence in Tsunami-Driven Overland Flow.* Patrick Lynett. May 2016.

PEER 2016/02 *Semi-Automated Procedure for Windowing time Series and Computing Fourier Amplitude Spectra for the NGA-West2 Database.* Tadahiro Kishida, Olga-Joan Ktenidou, Robert B. Darragh, and Walter J. Silva. May 2016.

PEER 2016/01 *A Methodology for the Estimation of Kappa (κ) from Large Datasets: Example Application to Rock Sites in the NGA-East Database and Implications on Design Motions.* Olga-Joan Ktenidou, Norman A. Abrahamson, Robert B. Darragh, and Walter J. Silva. April 2016.

PEER 2015/13 *Self-Centering Precast Concrete Dual-Steel-Shell Columns for Accelerated Bridge Construction: Seismic Performance, Analysis, and Design*. Gabriele Guerrini, José I. Restrepo, Athanassios Vervelidis, and Milena Massari. December 2015.

PEER 2015/12 *Shear-Flexure Interaction Modeling for Reinforced Concrete Structural Walls and Columns under Reversed Cyclic Loading*. Kristijan Kolozvari, Kutay Orakcal, and John Wallace. December 2015.

PEER 2015/11 *Selection and Scaling of Ground Motions for Nonlinear Response History Analysis of Buildings in Performance-Based Earthquake Engineering*. N. Simon Kwong and Anil K. Chopra. December 2015.

PEER 2015/10 *Structural Behavior of Column-Bent Cap Beam-Box Girder Systems in Reinforced Concrete Bridges Subjected to Gravity and Seismic Loads. Part II: Hybrid Simulation and Post-Test Analysis*. Mohamed A. Moustafa and Khalid M. Mosalam. November 2015.

PEER 2015/09 *Structural Behavior of Column-Bent Cap Beam-Box Girder Systems in Reinforced Concrete Bridges Subjected to Gravity and Seismic Loads. Part I: Pre-Test Analysis and Quasi-Static Experiments*. Mohamed A. Moustafa and Khalid M. Mosalam. September 2015.

PEER 2015/08 *NGA-East: Adjustments to Median Ground-Motion Models for Center and Eastern North America*. August 2015.

PEER 2015/07 *NGA-East: Ground-Motion Standard-Deviation Models for Central and Eastern North America*. Linda Al Atik. June 2015.

PEER 2015/06 *Adjusting Ground-Motion Intensity Measures to a Reference Site for which V_{S30} = 3000 m/sec*. David M. Boore. May 2015.

PEER 2015/05 *Hybrid Simulation of Seismic Isolation Systems Applied to an APR-1400 Nuclear Power Plant.* Andreas H. Schellenberg, Alireza Sarebanha, Matthew J. Schoettler, Gilberto Mosqueda, Gianmario Benzoni, and Stephen A. Mahin. April 2015.

PEER 2015/04 *NGA-East: Median Ground-Motion Models for the Central and Eastern North America Region*. April 2015.

PEER 2015/03 *Single Series Solution for the Rectangular Fiber-Reinforced Elastomeric Isolator Compression Modulus*. James M. Kelly and Niel C. Van Engelen. March 2015.

PEER 2015/02 *A Full-Scale, Single-Column Bridge Bent Tested by Shake-Table Excitation.* Matthew J. Schoettler, José I. Restrepo, Gabriele Guerrini, David E. Duck, and Francesco Carrea. March 2015.

PEER 2015/01 *Concrete Column Blind Prediction Contest 2010: Outcomes and Observations.* Vesna Terzic, Matthew J. Schoettler, José I. Restrepo, and Stephen A Mahin. March 2015.

PEER 2014/20 *Stochastic Modeling and Simulation of Near-Fault Ground Motions for Performance-Based Earthquake Engineering*. Mayssa Dabaghi and Armen Der Kiureghian. December 2014.

PEER 2014/19 *Seismic Response of a Hybrid Fiber-Reinforced Concrete Bridge Column Detailed for Accelerated Bridge Construction*. Wilson Nguyen, William Trono, Marios Panagiotou, and Claudia P. Ostertag. December 2014.

PEER 2014/18 *Three-Dimensional Beam-Truss Model for Reinforced Concrete Walls and Slabs Subjected to Cyclic Static or Dynamic Loading*. Yuan Lu, Marios Panagiotou, and Ioannis Koutromanos. December 2014.

PEER 2014/17 *PEER NGA-East Database.* Christine A. Goulet, Tadahiro Kishida, Timothy D. Ancheta, Chris H. Cramer, Robert B. Darragh, Walter J. Silva, Youssef M.A. Hashash, Joseph Harmon, Jonathan P. Stewart, Katie E. Wooddell, and Robert R. Youngs. October 2014.

PEER 2014/16 *Guidelines for Performing Hazard-Consistent One-Dimensional Ground Response Analysis for Ground Motion Prediction*. Jonathan P. Stewart, Kioumars Afshari, and Youssef M.A. Hashash. October 2014.

PEER 2014/15 *NGA-East Regionalization Report: Comparison of Four Crustal Regions within Central and Eastern North America using Waveform Modeling and 5%-Damped Pseudo-Spectral Acceleration Response*. Jennifer Dreiling, Marius P. Isken, Walter D. Mooney, Martin C. Chapman, and Richard W. Godbee. October 2014.

PEER 2014/14 *Scaling Relations between Seismic Moment and Rupture Area of Earthquakes in Stable Continental Regions*. Paul Somerville. August 2014.

PEER 2014/13 *PEER Preliminary Notes and Observations on the August 24, 2014, South Napa Earthquake*. Grace S. Kang and Stephen A. Mahin, Editors. September 2014.

PEER 2014/12 *Reference-Rock Site Conditions for Central and Eastern North America: Part II – Attenuation (Kappa) Definition*. Kenneth W. Campbell, Youssef M.A. Hashash, Byungmin Kim, Albert R. Kottke, Ellen M. Rathje, Walter J. Silva, and Jonathan P. Stewart. August 2014.

PEER 2014/11 *Reference-Rock Site Conditions for Central and Eastern North America: Part I - Velocity Definition*. Youssef M.A. Hashash, Albert R. Kottke, Jonathan P. Stewart, Kenneth W. Campbell, Byungmin Kim, Ellen M. Rathje, Walter J. Silva, Sissy Nikolaou, and Cheryl Moss. August 2014.

PEER 2014/10 *Evaluation of Collapse and Non-Collapse of Parallel Bridges Affected by Liquefaction and Lateral Spreading*. Benjamin Turner, Scott J. Brandenberg, and Jonathan P. Stewart. August 2014.

PEER 2014/09 *PEER Arizona Strong-Motion Database and GMPEs Evaluation*. Tadahiro Kishida, Robert E. Kayen, Olga-Joan Ktenidou, Walter J. Silva, Robert B. Darragh, and Jennie Watson-Lamprey. June 2014.

PEER 2014/08 *Unbonded Pretensioned Bridge Columns with Rocking Detail*. Jeffrey A. Schaefer, Bryan Kennedy, Marc O. Eberhard, and John F. Stanton. June 2014.

PEER 2014/07 *Northridge 20 Symposium Summary Report: Impacts, Outcomes, and Next Steps*. May 2014.

PEER 2014/06 *Report of the Tenth Planning Meeting of NEES/E-Defense Collaborative Research on Earthquake Engineering*. December 2013.

PEER 2014/05 *Seismic Velocity Site Characterization of Thirty-One Chilean Seismometer Stations by Spectral Analysis of Surface Wave Dispersion*. Robert Kayen, Brad D. Carkin, Skye Corbet, Camilo Pinilla, Allan Ng, Edward Gorbis, and Christine Truong. April 2014.

PEER 2014/04 Effect of Vertical Acceleration on Shear Strength of Reinforced Concrete Columns. Hyerin Lee and Khalid M. Mosalam. April 2014.

PEER 2014/03 *Retest of Thirty-Year-Old Neoprene Isolation Bearings.* James M. Kelly and Niel C. Van Engelen. March 2014.

PEER 2014/02 *Theoretical Development of Hybrid Simulation Applied to Plate Structures.* Ahmed A. Bakhaty, Khalid M. Mosalam, and Sanjay Govindjee. January 2014.

PEER 2014/01 *Performance-Based Seismic Assessment of Skewed Bridges.* Peyman Kaviani, Farzin Zareian, and Ertugrul Taciroglu. January 2014.

PEER 2013/26 *Urban Earthquake Engineerin*g. Proceedings of the U.S.-Iran Seismic Workshop. December 2013.

PEER 2013/25 *Earthquake Engineering for Resilient Communities: 2013 PEER Internship Program Research Report Collection.* Heidi Tremayne (Editor), Stephen A. Mahin (Editor), Jorge Archbold Monterossa, Matt Brosman, Shelly Dean, Katherine deLaveaga, Curtis Fong, Donovan Holder, Rakeeb Khan, Elizabeth Jachens, David Lam, Daniela Martinez Lopez, Mara Minner, Geffen Oren, Julia Pavicic, Melissa Quinonez, Lorena Rodriguez, Sean Salazar, Kelli Slaven, Vivian Steyert, Jenny Taing, and Salvador Tena. December 2013.

PEER 2013/24 *NGA-West2 Ground Motion Prediction Equations for Vertical Ground Motions*. September 2013.

PEER 2013/23 *Coordinated Planning and Preparedness for Fire Following Major Earthquakes*. Charles Scawthorn. November 2013.

PEER 2013/22 *GEM-PEER Task 3 Project: Selection of a Global Set of Ground Motion Prediction Equations.* Jonathan P. Stewart, John Douglas, Mohammad B. Javanbarg, Carola Di Alessandro, Yousef Bozorgnia, Norman A. Abrahamson, David M. Boore, Kenneth W. Campbell, Elise Delavaud, Mustafa Erdik, and Peter J. Stafford. December 2013.

PEER 2013/21 *Seismic Design and Performance of Bridges with Columns on Rocking Foundations*. Grigorios Antonellis and Marios Panagiotou. September 2013.

PEER 2013/20 *Experimental and Analytical Studies on the Seismic Behavior of Conventional and Hybrid Braced Frames*. Jiun-Wei Lai and Stephen A. Mahin. September 2013.

PEER 2013/19 *Toward Resilient Communities: A Performance-Based Engineering Framework for Design and Evaluation of the Built Environment.* Michael William Mieler, Bozidar Stojadinovic, Robert J. Budnitz, Stephen A. Mahin, and Mary C. Comerio. September 2013.

PEER 2013/18 *Identification of Site Parameters that Improve Predictions of Site Amplification*. Ellen M. Rathje and Sara Navidi. July 2013.

PEER 2013/17 *Response Spectrum Analysis of Concrete Gravity Dams Including Dam-Water-Foundation Interaction*. Arnkjell Løkke and Anil K. Chopra. July 2013.

PEER 2013/16 *Effect of Hoop Reinforcement Spacing on the Cyclic Response of Large Reinforced Concrete Special Moment Frame Beams.* Marios Panagiotou, Tea Visnjic, Grigorios Antonellis, Panagiotis Galanis, and Jack P. Moehle. June 2013.

PEER 2013/15 *A Probabilistic Framework to Include the Effects of Near-Fault Directivity in Seismic Hazard Assessment*. Shrey Kumar Shahi, Jack W. Baker. October 2013.

PEER 2013/14 *Hanging-Wall Scaling using Finite-Fault Simulations.* Jennifer L. Donahue and Norman A. Abrahamson. September 2013.

PEER 2013/13 *Semi-Empirical Nonlinear Site Amplification and its Application in NEHRP Site Factors*. Jonathan P. Stewart and Emel Seyhan. November 2013.

PEER 2013/12 *Nonlinear Horizontal Site Response for the NGA-West2 Project.* Ronnie Kamai, Norman A. Abramson, Walter J. Silva. May 2013.

PEER 2013/11 *Epistemic Uncertainty for NGA-West2 Models.* Linda Al Atik and Robert R. Youngs. May 2013.

PEER 2013/10 *NGA-West 2 Models for Ground-Motion Directionality.* Shrey K. Shahi and Jack W. Baker. May 2013.

PEER 2013/09 *Final Report of the NGA-West2 Directivity Working Group.* Paul Spudich, Jeffrey R. Bayless, Jack W. Baker, Brian S.J. Chiou, Badie Rowshandel, Shrey Shahi, and Paul Somerville. May 2013.

PEER 2013/08 *NGA-West2 Model for Estimating Average Horizontal Values of Pseudo-Absolute Spectral Accelerations Generated by Crustal Earthquakes*. I. M. Idriss. May 2013.

PEER 2013/07 *Update of the Chiou and Youngs NGA Ground Motion Model for Average Horizontal Component of Peak Ground Motion and Response Spectra*. Brian Chiou and Robert Youngs. May 2013.

PEER 2013/06 *NGA-West2 Campbell-Bozorgnia Ground Motion Model for the Horizontal Components of PGA, PGV, and 5%-Damped Elastic Pseudo-Acceleration Response Spectra for Periods Ranging from 0.01 to 10 sec.* Kenneth W. Campbell and Yousef Bozorgnia. May 2013.

PEER 2013/05 *NGA-West 2 Equations for Predicting Response Spectral Accelerations for Shallow Crustal Earthquakes*. David M. Boore, Jonathan P. Stewart, Emel Seyhan, and Gail M. Atkinson. May 2013.

PEER 2013/04 *Update of the AS08 Ground-Motion Prediction Equations Based on the NGA-West2 Data Set*. Norman Abrahamson, Walter Silva, and Ronnie Kamai. May 2013.

PEER 2013/03 *PEER NGA-West2 Database.* Timothy D. Ancheta, Robert B. Darragh, Jonathan P. Stewart, Emel Seyhan, Walter J. Silva, Brian S.J. Chiou, Katie E. Wooddell, Robert W. Graves, Albert R. Kottke, David M. Boore, Tadahiro Kishida, and Jennifer L. Donahue. May 2013.

PEER 2013/02 *Hybrid Simulation of the Seismic Response of Squat Reinforced Concrete Shear Walls*. Catherine A. Whyte and Bozidar Stojadinovic. May 2013.

PEER 2013/01 *Housing Recovery in Chile: A Qualitative Mid-program Review*. Mary C. Comerio. February 2013.

PEER 2012/08 *Guidelines for Estimation of Shear Wave Velocity.* Bernard R. Wair, Jason T. DeJong, and Thomas Shantz. December 2012.

PEER 2012/07 *Earthquake Engineering for Resilient Communities: 2012 PEER Internship Program Research Report Collection.* Heidi Tremayne (Editor), Stephen A. Mahin (Editor), Collin Anderson, Dustin Cook, Michael Erceg, Carlos Esparza, Jose Jimenez, Dorian Krausz, Andrew Lo, Stephanie Lopez, Nicole McCurdy, Paul Shipman, Alexander Strum, Eduardo Vega. December 2012.

PEER 2012/06 *Fragilities for Precarious Rocks at Yucca Mountain.* Matthew D. Purvance, Rasool Anooshehpoor, and James N. Brune. December 2012.

PEER 2012/05 *Development of Simplified Analysis Procedure for Piles in Laterally Spreading Layered Soils.* Christopher R. McGann, Pedro Arduino, and Peter Mackenzie–Helnwein. December 2012.

PEER 2012/04 *Unbonded Pre-Tensioned Columns for Bridges in Seismic Regions.* Phillip M. Davis, Todd M. Janes, Marc O. Eberhard, and John F. Stanton. December 2012.

PEER 2012/03 *Experimental and Analytical Studies on Reinforced Concrete Buildings with Seismically Vulnerable Beam-Column Joints*. Sangjoon Park and Khalid M. Mosalam. October 2012.

PEER 2012/02 *Seismic Performance of Reinforced Concrete Bridges Allowed to Uplift during Multi-Directional Excitation*. Andres Oscar Espinoza and Stephen A. Mahin. July 2012.

PEER 2012/01 *Spectral Damping Scaling Factors for Shallow Crustal Earthquakes in Active Tectonic Regions.* Sanaz Rezaeian, Yousef Bozorgnia, I. M. Idriss, Kenneth Campbell, Norman Abrahamson, and Walter Silva. July 2012.

PEER 2011/10 *Earthquake Engineering for Resilient Communities: 2011 PEER Internship Program Research Report Collection*. Heidi Faison and Stephen A. Mahin, Editors. December 2011.

PEER 2011/09 *Calibration of Semi-Stochastic Procedure for Simulating High-Frequency Ground Motions*. Jonathan P. Stewart, Emel Seyhan, and Robert W. Graves. December 2011.

PEER 2011/08 *Water Supply in regard to Fire Following Earthquake*. Charles Scawthorn. November 2011.

PEER 2011/07 *Seismic Risk Management in Urban Areas*. Proceedings of a U.S.-Iran-Turkey Seismic Workshop. September 2011.

PEER 2011/06 *The Use of Base Isolation Systems to Achieve Complex Seismic Performance Objectives*. Troy A. Morgan and Stephen A. Mahin. July 2011.

PEER 2011/05 *Case Studies of the Seismic Performance of Tall Buildings Designed by Alternative Means.* Task 12 Report for the Tall Buildings Initiative. Jack Moehle, Yousef Bozorgnia, Nirmal Jayaram, Pierson Jones, Mohsen Rahnama, Nilesh Shome, Zeynep Tuna, John Wallace, Tony Yang, and Farzin Zareian. July 2011.

PEER 2011/04 *Recommended Design Practice for Pile Foundations in Laterally Spreading Ground.* Scott A. Ashford, Ross W. Boulanger, and Scott J. Brandenberg. June 2011.

PEER 2011/03 *New Ground Motion Selection Procedures and Selected Motions for the PEER Transportation Research Program*. Jack W. Baker, Ting Lin, Shrey K. Shahi, and Nirmal Jayaram. March 2011.

PEER 2011/02 *A Bayesian Network Methodology for Infrastructure Seismic Risk Assessment and Decision Support*. Michelle T. Bensi, Armen Der Kiureghian, and Daniel Straub. March 2011.

PEER 2011/01 *Demand Fragility Surfaces for Bridges in Liquefied and Laterally Spreading Ground*. Scott J. Brandenberg, Jian Zhang, Pirooz Kashighandi, Yili Huo, and Minxing Zhao. March 2011.

PEER 2010/05 *Guidelines for Performance-Based Seismic Design of Tall Buildings.* Developed by the Tall Buildings Initiative. November 2010.

PEER 2010/04 *Application Guide for the Design of Flexible and Rigid Bus Connections between Substation Equipment Subjected to Earthquakes.* Jean-Bernard Dastous and Armen Der Kiureghian. September 2010.

PEER 2010/03 *Shear Wave Velocity as a Statistical Function of Standard Penetration Test Resistance and Vertical Effective Stress at Caltrans Bridge Sites.* Scott J. Brandenberg, Naresh Bellana, and Thomas Shantz. June 2010.

PEER 2010/02 *Stochastic Modeling and Simulation of Ground Motions for Performance-Based Earthquake Engineering.* Sanaz Rezaeian and Armen Der Kiureghian. June 2010.

PEER 2010/01 *Structural Response and Cost Characterization of Bridge Construction Using Seismic Performance Enhancement Strategies.* Ady Aviram, Božidar Stojadinović, Gustavo J. Parra-Montesinos, and Kevin R. Mackie. March 2010.

PEER 2009/03 *The Integration of Experimental and Simulation Data in the Study of Reinforced Concrete Bridge Systems Including Soil-Foundation-Structure Interaction.* Matthew Dryden and Gregory L. Fenves. November 2009.

PEER 2009/02 *Improving Earthquake Mitigation through Innovations and Applications in Seismic Science, Engineering, Communication, and Response*. Proceedings of a U.S.-Iran Seismic Workshop. October 2009.

PEER 2009/01 *Evaluation of Ground Motion Selection and Modification Methods: Predicting Median Interstory Drift Response of Buildings*. Curt B. Haselton, Editor. June 2009.

PEER 2008/10 *Technical Manual for Strata.* Albert R. Kottke and Ellen M. Rathje. February 2009.

PEER 2008/09 *NGA Model for Average Horizontal Component of Peak Ground Motion and Response Spectra.* Brian S.-J. Chiou and Robert R. Youngs. November 2008.

PEER 2008/08 *Toward Earthquake-Resistant Design of Concentrically Braced Steel Structures*. Patxi Uriz and Stephen A. Mahin. November 2008.

PEER 2008/07 *Using OpenSees for Performance-Based Evaluation of Bridges on Liquefiable Soils*. Stephen L. Kramer, Pedro Arduino, and HyungSuk Shin. November 2008.

PEER 2008/06 *Shaking Table Tests and Numerical Investigation of Self-Centering Reinforced Concrete Bridge Columns*. Hyung IL Jeong, Junichi Sakai, and Stephen A. Mahin. September 2008.

PEER 2008/05 *Performance-Based Earthquake Engineering Design Evaluation Procedure for Bridge Foundations Undergoing Liquefaction-Induced Lateral Ground Displacement*. Christian A. Ledezma and Jonathan D. Bray. August 2008.

PEER 2008/04 *Benchmarking of Nonlinear Geotechnical Ground Response Analysis Procedures.* Jonathan P. Stewart, Annie On-Lei Kwok, Youssef M. A. Hashash, Neven Matasovic, Robert Pyke, Zhiliang Wang, and Zhaohui Yang. August 2008.

PEER 2008/03 *Guidelines for Nonlinear Analysis of Bridge Structures in California.* Ady Aviram, Kevin R. Mackie, and Božidar Stojadinović. August 2008.

PEER 2008/02 *Treatment of Uncertainties in Seismic-Risk Analysis of Transportation Systems*. Evangelos Stergiou and Anne S. Kiremidjian. July 2008.

PEER 2008/01 *Seismic Performance Objectives for Tall Buildings.* William T. Holmes, Charles Kircher, William Petak, and Nabih Youssef. August 2008.

PEER 2007/12 *An Assessment to Benchmark the Seismic Performance of a Code-Conforming Reinforced Concrete Moment-Frame Building.* Curt Haselton, Christine A. Goulet, Judith Mitrani-Reiser, James L. Beck, Gregory G. Deierlein, Keith A. Porter, Jonathan P. Stewart, and Ertugrul Taciroglu. August 2008.

PEER 2007/11 *Bar Buckling in Reinforced Concrete Bridge Columns.* Wayne A. Brown, Dawn E. Lehman, and John F. Stanton. February 2008.

PEER 2007/10 *Computational Modeling of Progressive Collapse in Reinforced Concrete Frame Structures*. Mohamed M. Talaat and Khalid M. Mosalam. May 2008.

PEER 2007/09 *Integrated Probabilistic Performance-Based Evaluation of Benchmark Reinforced Concrete Bridges*. Kevin R. Mackie, John-Michael Wong, and Božidar Stojadinović. January 2008.

PEER 2007/08 *Assessing Seismic Collapse Safety of Modern Reinforced Concrete Moment-Frame Buildings*. Curt B. Haselton and Gregory G. Deierlein. February 2008.

PEER 2007/07 *Performance Modeling Strategies for Modern Reinforced Concrete Bridge Columns*. Michael P. Berry and Marc O. Eberhard. April 2008.

PEER 2007/06 *Development of Improved Procedures for Seismic Design of Buried and Partially Buried Structures*. Linda Al Atik and Nicholas Sitar. June 2007.

PEER 2007/05 *Uncertainty and Correlation in Seismic Risk Assessment of Transportation Systems*. Renee G. Lee and Anne S. Kiremidjian. July 2007.

PEER 2007/04 *Numerical Models for Analysis and Performance-Based Design of Shallow Foundations Subjected to Seismic Loading.* Sivapalan Gajan, Tara C. Hutchinson, Bruce L. Kutter, Prishati Raychowdhury, José A. Ugalde, and Jonathan P. Stewart. May 2008.

PEER 2007/03 *Beam-Column Element Model Calibrated for Predicting Flexural Response Leading to Global Collapse of RC Frame Buildings*. Curt B. Haselton, Abbie B. Liel, Sarah Taylor Lange, and Gregory G. Deierlein. May 2008.

PEER 2007/02 *Campbell-Bozorgnia NGA Ground Motion Relations for the Geometric Mean Horizontal Component of Peak and Spectral Ground Motion Parameters*. Kenneth W. Campbell and Yousef Bozorgnia. May 2007.

PEER 2007/01 *Boore-Atkinson NGA Ground Motion Relations for the Geometric Mean Horizontal Component of Peak and Spectral Ground Motion Parameters*. David M. Boore and Gail M. Atkinson. May 2007.

PEER 2006/12 Societal Implications of Performance-Based Earthquake Engineering. Peter J. May. May 2007.

PEER 2006/11 *Probabilistic Seismic Demand Analysis Using Advanced Ground Motion Intensity Measures, Attenuation Relationships, and Near-Fault Effects*. Polsak Tothong and C. Allin Cornell. March 2007.

PEER 2006/10 *Application of the PEER PBEE Methodology to the I-880 Viaduct*. Sashi Kunnath. February 2007.

PEER 2006/09 *Quantifying Economic Losses from Travel Forgone Following a Large Metropolitan Earthquake*. James Moore, Sungbin Cho, Yue Yue Fan, and Stuart Werner. November 2006.

PEER 2006/08 *Vector-Valued Ground Motion Intensity Measures for Probabilistic Seismic Demand Analysis*. Jack W. Baker and C. Allin Cornell. October 2006.

PEER 2006/07 *Analytical Modeling of Reinforced Concrete Walls for Predicting Flexural and Coupled–Shear-Flexural Responses*. Kutay Orakcal, Leonardo M. Massone, and John W. Wallace. October 2006.

PEER 2006/06 *Nonlinear Analysis of a Soil-Drilled Pier System under Static and Dynamic Axial Loading*. Gang Wang and Nicholas Sitar. November 2006.

PEER 2006/05 *Advanced Seismic Assessment Guidelines.* Paolo Bazzurro, C. Allin Cornell, Charles Menun, Maziar Motahari, and Nicolas Luco. September 2006.

PEER 2006/04 *Probabilistic Seismic Evaluation of Reinforced Concrete Structural Components and Systems*. Tae Hyung Lee and Khalid M. Mosalam. August 2006.

PEER 2006/03 *Performance of Lifelines Subjected to Lateral Spreading.* Scott A. Ashford and Teerawut Juirnarongrit. July 2006.

PEER 2006/02 *Pacific Earthquake Engineering Research Center Highway Demonstration Project.* Anne Kiremidjian, James Moore, Yue Yue Fan, Nesrin Basoz, Ozgur Yazali, and Meredith Williams. April 2006.

PEER 2006/01 *Bracing Berkeley. A Guide to Seismic Safety on the UC Berkeley Campus.* Mary C. Comerio, Stephen Tobriner, and Ariane Fehrenkamp. January 2006.

PEER 2005/17 *Earthquake Simulation Tests on Reducing Residual Displacements of Reinforced Concrete Bridges.* Junichi Sakai, Stephen A Mahin, and Andres Espinoza. December 2005.

PEER 2005/16 *Seismic Response and Reliability of Electrical Substation Equipment and Systems.* Junho Song, Armen Der Kiureghian, and Jerome L. Sackman. April 2006.

PEER 2005/15 *CPT-Based Probabilistic Assessment of Seismic Soil Liquefaction Initiation.* R. E. S. Moss, R. B. Seed, R. E. Kayen, J. P. Stewart, and A. Der Kiureghian. April 2006.

PEER 2005/14 *Workshop on Modeling of Nonlinear Cyclic Load-Deformation Behavior of Shallow Foundations.* Bruce L. Kutter, Geoffrey Martin, Tara Hutchinson, Chad Harden, Sivapalan Gajan, and Justin Phalen. March 2006.

PEER 2005/13 *Stochastic Characterization and Decision Bases under Time-Dependent Aftershock Risk in Performance-Based Earthquake Engineering*. Gee Liek Yeo and C. Allin Cornell. July 2005.

PEER 2005/12 *PEER Testbed Study on a Laboratory Building: Exercising Seismic Performance Assessment.* Mary C. Comerio, Editor. November 2005.

PEER 2005/11 *Van Nuys Hotel Building Testbed Report: Exercising Seismic Performance Assessment.* Helmut Krawinkler, Editor. October 2005.

PEER 2005/10 *First NEES/E-Defense Workshop on Collapse Simulation of Reinforced Concrete Building Structures.* September 2005.

PEER 2005/09 *Test Applications of Advanced Seismic Assessment Guidelines.* Joe Maffei, Karl Telleen, Danya Mohr, William Holmes, and Yuki Nakayama. August 2006.

PEER 2005/08 *Damage Accumulation in Lightly Confined Reinforced Concrete Bridge Columns.* R. Tyler Ranf, Jared M. Nelson, Zach Price, Marc O. Eberhard, and John F. Stanton. April 2006.

PEER 2005/07 *Experimental and Analytical Studies on the Seismic Response of Freestanding and Anchored Laboratory Equipment.* Dimitrios Konstantinidis and Nicos Makris. January 2005.

PEER 2005/06 *Global Collapse of Frame Structures under Seismic Excitations*. Luis F. Ibarra and Helmut Krawinkler. September 2005.

PEER 2005//05 *Performance Characterization of Bench- and Shelf-Mounted Equipment.* Samit Ray Chaudhuri and Tara C. Hutchinson. May 2006.

PEER 2005/04 *Numerical Modeling of the Nonlinear Cyclic Response of Shallow Foundations.* Chad Harden, Tara Hutchinson, Geoffrey R. Martin, and Bruce L. Kutter. August 2005.

PEER 2005/03 *A Taxonomy of Building Components for Performance-Based Earthquake Engineering.* Keith A. Porter. September 2005.

PEER 2005/02 *Fragility Basis for California Highway Overpass Bridge Seismic Decision Making*. Kevin R. Mackie and Božidar Stojadinović. June 2005.

PEER 2005/01 *Empirical Characterization of Site Conditions on Strong Ground Motion.* Jonathan P. Stewart, Yoojoong Choi, and Robert W. Graves. June 2005.

PEER 2004/09 *Electrical Substation Equipment Interaction: Experimental Rigid Conductor Studies.* Christopher Stearns and André Filiatrault. February 2005.

PEER 2004/08 *Seismic Qualification and Fragility Testing of Line Break 550-kV Disconnect Switches.* Shakhzod M. Takhirov, Gregory L. Fenves, and Eric Fujisaki. January 2005.

PEER 2004/07 *Ground Motions for Earthquake Simulator Qualification of Electrical Substation Equipment.* Shakhzod M. Takhirov, Gregory L. Fenves, Eric Fujisaki, and Don Clyde. January 2005.

PEER 2004/06 *Performance-Based Regulation and Regulatory Regimes.* Peter J. May and Chris Koski. September 2004.

PEER 2004/05 *Performance-Based Seismic Design Concepts and Implementation: Proceedings of an International Workshop.* Peter Fajfar and Helmut Krawinkler, Editors. September 2004.

PEER 2004/04 *Seismic Performance of an Instrumented Tilt-up Wall Building.* James C. Anderson and Vitelmo V. Bertero. July 2004.

PEER 2004/03 *Evaluation and Application of Concrete Tilt-up Assessment Methodologies.* Timothy Graf and James O. Malley. October 2004.

PEER 2004/02 *Analytical Investigations of New Methods for Reducing Residual Displacements of Reinforced Concrete Bridge Columns.* Junichi Sakai and Stephen A. Mahin. August 2004.

PEER 2004/01 *Seismic Performance of Masonry Buildings and Design Implications.* Kerri Anne Taeko Tokoro, James C. Anderson, and Vitelmo V. Bertero. February 2004.

PEER 2003/18 *Performance Models for Flexural Damage in Reinforced Concrete Columns.* Michael Berry and Marc Eberhard. August 2003.

PEER 2003/17 *Predicting Earthquake Damage in Older Reinforced Concrete Beam-Column Joints.* Catherine Pagni and Laura Lowes. October 2004.

PEER 2003/16 *Seismic Demands for Performance-Based Design of Bridges.* Kevin Mackie and Božidar Stojadinović. August 2003.

PEER 2003/15 *Seismic Demands for Nondeteriorating Frame Structures and Their Dependence on Ground Motions.* Ricardo Antonio Medina and Helmut Krawinkler. May 2004.

PEER 2003/14 *Finite Element Reliability and Sensitivity Methods for Performance-Based Earthquake Engineering*. Terje Haukaas and Armen Der Kiureghian. April 2004.

PEER 2003/13 *Effects of Connection Hysteretic Degradation on the Seismic Behavior of Steel Moment-Resisting Frames.* Janise E. Rodgers and Stephen A. Mahin. March 2004.

PEER 2003/12 *Implementation Manual for the Seismic Protection of Laboratory Contents: Format and Case Studies*. William T. Holmes and Mary C. Comerio. October 2003.

PEER 2003/11 *Fifth U.S.-Japan Workshop on Performance-Based Earthquake Engineering Methodology for Reinforced Concrete Building Structures*. February 2004.

PEER 2003/10 *A Beam-Column Joint Model for Simulating the Earthquake Response of Reinforced Concrete Frames.* Laura N. Lowes, Nilanjan Mitra, and Arash Altoontash. February 2004.

PEER 2003/09 *Sequencing Repairs after an Earthquake: An Economic Approach.* Marco Casari and Simon J. Wilkie. April 2004.

PEER 2003/08 *A Technical Framework for Probability-Based Demand and Capacity Factor Design (DCFD) Seismic Formats*. Fatemeh Jalayer and C. Allin Cornell. November 2003.

PEER 2003/07 *Uncertainty Specification and Propagation for Loss Estimation Using FOSM Methods.* Jack W. Baker and C. Allin Cornell. September 2003.

PEER 2003/06 *Performance of Circular Reinforced Concrete Bridge Columns under Bidirectional Earthquake Loading*. Mahmoud M. Hachem, Stephen A. Mahin, and Jack P. Moehle. February 2003.

PEER 2003/05 *Response Assessment for Building-Specific Loss Estimation.* Eduardo Miranda and Shahram Taghavi. September 2003.

PEER 2003/04 *Experimental Assessment of Columns with Short Lap Splices Subjected to Cyclic Loads*. Murat Melek, John W. Wallace, and Joel Conte. April 2003.

PEER 2003/03 *Probabilistic Response Assessment for Building-Specific Loss Estimation*. Eduardo Miranda and Hesameddin Aslani. September 2003.

PEER 2003/02 *Software Framework for Collaborative Development of Nonlinear Dynamic Analysis Program*. Jun Peng and Kincho H. Law. September 2003.

PEER 2003/01 *Shake Table Tests and Analytical Studies on the Gravity Load Collapse of Reinforced Concrete Frames.* Kenneth John Elwood and Jack P. Moehle. November 2003.

PEER 2002/24 *Performance of Beam to Column Bridge Joints Subjected to a Large Velocity Pulse.* Natalie Gibson, André Filiatrault, and Scott A. Ashford. April 2002.

PEER 2002/23 *Effects of Large Velocity Pulses on Reinforced Concrete Bridge Columns.* Greg L. Orozco and Scott A. Ashford. April 2002.

PEER 2002/22 *Characterization of Large Velocity Pulses for Laboratory Testing.* Kenneth E. Cox and Scott A. Ashford. April 2002.

PEER 2002/21 *Fourth U.S.-Japan Workshop on Performance-Based Earthquake Engineering Methodology for Reinforced Concrete Building Structures.* December 2002.

PEER 2002/20 *Barriers to Adoption and Implementation of PBEE Innovations.* Peter J. May. August 2002.

PEER 2002/19 *Economic-Engineered Integrated Models for Earthquakes: Socioeconomic Impacts.* Peter Gordon, James E. Moore II, and Harry W. Richardson. July 2002.

PEER 2002/18 *Assessment of Reinforced Concrete Building Exterior Joints with Substandard Details.* Chris P. Pantelides, Jon Hansen, Justin Nadauld, and Lawrence D. Reaveley. May 2002.

PEER 2002/17 *Structural Characterization and Seismic Response Analysis of a Highway Overcrossing Equipped with Elastomeric Bearings and Fluid Dampers: A Case Study*. Nicos Makris and Jian Zhang. November 2002.

PEER 2002/16 *Estimation of Uncertainty in Geotechnical Properties for Performance-Based Earthquake Engineering*. Allen L. Jones, Steven L. Kramer, and Pedro Arduino. December 2002.

PEER 2002/15 *Seismic Behavior of Bridge Columns Subjected to Various Loading Patterns*. Asadollah Esmaeily-Gh. and Yan Xiao. December 2002.

PEER 2002/14 *Inelastic Seismic Response of Extended Pile Shaft Supported Bridge Structures.* T.C. Hutchinson, R.W. Boulanger, Y.H. Chai, and I.M. Idriss. December 2002.

PEER 2002/13 *Probabilistic Models and Fragility Estimates for Bridge Components and Systems.* Paolo Gardoni, Armen Der Kiureghian, and Khalid M. Mosalam. June 2002.

PEER 2002/12 *Effects of Fault Dip and Slip Rake on Near-Source Ground Motions: Why Chi-Chi Was a Relatively Mild M7.6 Earthquake*. Brad T. Aagaard, John F. Hall, and Thomas H. Heaton. December 2002.

PEER 2002/11 *Analytical and Experimental Study of Fiber-Reinforced Strip Isolators*. James M. Kelly and Shakhzod M. Takhirov. September 2002.

PEER 2002/10 *Centrifuge Modeling of Settlement and Lateral Spreading with Comparisons to Numerical Analyses***.** Sivapalan Gajan and Bruce L. Kutter. January 2003.

PEER 2002/09 *Documentation and Analysis of Field Case Histories of Seismic Compression during the 1994 Northridge, California, Earthquake*. Jonathan P. Stewart, Patrick M. Smith, Daniel H. Whang, and Jonathan D. Bray. October 2002.

PEER 2002/08 *Component Testing, Stability Analysis and Characterization of Buckling-Restrained Unbonded Braces^{TM}*. Cameron Black, Nicos Makris, and Ian Aiken. September 2002.

PEER 2002/07 *Seismic Performance of Pile-Wharf Connections.* Charles W. Roeder, Robert Graff, Jennifer Soderstrom, and Jun Han Yoo. December 2001.

PEER 2002/06 *The Use of Benefit-Cost Analysis for Evaluation of Performance-Based Earthquake Engineering Decisions*. Richard O. Zerbe and Anthony Falit-Baiamonte. September 2001.

PEER 2002/05 *Guidelines, Specifications, and Seismic Performance Characterization of Nonstructural Building Components and Equipment*. André Filiatrault, Constantin Christopoulos, and Christopher Stearns. September 2001.

PEER 2002/04 *Consortium of Organizations for Strong-Motion Observation Systems and the Pacific Earthquake Engineering Research Center Lifelines Program: Invited Workshop on Archiving and Web Dissemination of Geotechnical Data, 4–5 October 2001*. September 2002.

PEER 2002/03 *Investigation of Sensitivity of Building Loss Estimates to Major Uncertain Variables for the Van Nuys Testbed*. Keith A. Porter, James L. Beck, and Rustem V. Shaikhutdinov. August 2002.

PEER 2002/02 *The Third U.S.-Japan Workshop on Performance-Based Earthquake Engineering Methodology for Reinforced Concrete Building Structures*. July 2002.

PEER 2002/01 *Nonstructural Loss Estimation: The UC Berkeley Case Study.* Mary C. Comerio and John C. Stallmeyer. December 2001.

PEER 2001/16 *Statistics of SDF-System Estimate of Roof Displacement for Pushover Analysis of Buildings.* Anil K. Chopra, Rakesh K. Goel, and Chatpan Chintanapakdee. December 2001.

PEER 2001/15 *Damage to Bridges during the 2001 Nisqually Earthquake.* R. Tyler Ranf, Marc O. Eberhard, and Michael P. Berry. November 2001.

PEER 2001/14 *Rocking Response of Equipment Anchored to a Base Foundation.* Nicos Makris and Cameron J. Black. September 2001.

PEER 2001/13 *Modeling Soil Liquefaction Hazards for Performance-Based Earthquake Engineering*. Steven L. Kramer and Ahmed-W. Elgamal. February 2001.

PEER 2001/12 *Development of Geotechnical Capabilities in OpenSees*. Boris Jeremić. September 2001.

PEER 2001/11 *Analytical and Experimental Study of Fiber-Reinforced Elastomeric Isolators*. James M. Kelly and Shakhzod M. Takhirov. September 2001.

PEER 2001/10 *Amplification Factors for Spectral Acceleration in Active Regions.* Jonathan P. Stewart, Andrew H. Liu, Yoojoong Choi, and Mehmet B. Baturay. December 2001.

PEER 2001/09 *Ground Motion Evaluation Procedures for Performance-Based Design.* Jonathan P. Stewart, Shyh-Jeng Chiou, Jonathan D. Bray, Robert W. Graves, Paul G. Somerville, and Norman A. Abrahamson. September 2001.

PEER 2001/08 *Experimental and Computational Evaluation of Reinforced Concrete Bridge Beam-Column Connections for Seismic Performance*. Clay J. Naito, Jack P. Moehle, and Khalid M. Mosalam. November 2001.

PEER 2001/07 *The Rocking Spectrum and the Shortcomings of Design Guidelines.* Nicos Makris and Dimitrios Konstantinidis. August 2001.

PEER 2001/06 *Development of an Electrical Substation Equipment Performance Database for Evaluation of Equipment Fragilities*. Thalia Agnanos. April 1999.

PEER 2001/05 *Stiffness Analysis of Fiber-Reinforced Elastomeric Isolators.* Hsiang-Chuan Tsai and James M. Kelly. May 2001.

PEER 2001/04 *Organizational and Societal Considerations for Performance-Based Earthquake Engineering*. Peter J. May. April 2001.

PEER 2001/03 *A Modal Pushover Analysis Procedure to Estimate Seismic Demands for Buildings: Theory and Preliminary Evaluation*. Anil K. Chopra and Rakesh K. Goel. January 2001.

PEER 2001/02 *Seismic Response Analysis of Highway Overcrossings Including Soil-Structure Interaction*. Jian Zhang and Nicos Makris. March 2001.

PEER 2001/01 *Experimental Study of Large Seismic Steel Beam-to-Column Connections.* Egor P. Popov and Shakhzod M. Takhirov. November 2000.

PEER 2000/10 *The Second U.S.-Japan Workshop on Performance-Based Earthquake Engineering Methodology for Reinforced Concrete Building Structures*. March 2000.

PEER 2000/09 *Structural Engineering Reconnaissance of the August 17, 1999 Earthquake: Kocaeli (Izmit), Turkey.* Halil Sezen, Kenneth J. Elwood, Andrew S. Whittaker, Khalid Mosalam, John J. Wallace, and John F. Stanton. December 2000.

PEER 2000/08 *Behavior of Reinforced Concrete Bridge Columns Having Varying Aspect Ratios and Varying Lengths of Confinement*. Anthony J. Calderone, Dawn E. Lehman, and Jack P. Moehle. January 2001.

PEER 2000/07 *Cover-Plate and Flange-Plate Reinforced Steel Moment-Resisting Connections.* Taejin Kim, Andrew S. Whittaker, Amir S. Gilani, Vitelmo V. Bertero, and Shakhzod M. Takhirov. September 2000.

PEER 2000/06 *Seismic Evaluation and Analysis of 230-kV Disconnect Switches.* Amir S. J. Gilani, Andrew S. Whittaker, Gregory L. Fenves, Chun-Hao Chen, Henry Ho, and Eric Fujisaki. July 2000.

PEER 2000/05 *Performance-Based Evaluation of Exterior Reinforced Concrete Building Joints for Seismic Excitation*. Chandra Clyde, Chris P. Pantelides, and Lawrence D. Reaveley. July 2000.

PEER 2000/04 *An Evaluation of Seismic Energy Demand: An Attenuation Approach*. Chung-Che Chou and Chia-Ming Uang. July 1999.

PEER 2000/03 *Framing Earthquake Retrofitting Decisions: The Case of Hillside Homes in Los Angeles.* Detlof von Winterfeldt, Nels Roselund, and Alicia Kitsuse. March 2000.

PEER 2000/02 *U.S.-Japan Workshop on the Effects of Near-Field Earthquake Shaking*. Andrew Whittaker, Editor. July 2000.

PEER 2000/01 *Further Studies on Seismic Interaction in Interconnected Electrical Substation Equipment.* Armen Der Kiureghian, Kee-Jeung Hong, and Jerome L. Sackman. November 1999.

PEER 1999/14 *Seismic Evaluation and Retrofit of 230-kV Porcelain Transformer Bushings*. Amir S. Gilani, Andrew S. Whittaker, Gregory L. Fenves, and Eric Fujisaki. December 1999.

PEER 1999/13 *Building Vulnerability Studies: Modeling and Evaluation of Tilt-up and Steel Reinforced Concrete Buildings*. John W. Wallace, Jonathan P. Stewart, and Andrew S. Whittaker, Editors. December 1999.

PEER 1999/12 *Rehabilitation of Nonductile RC Frame Building Using Encasement Plates and Energy-Dissipating Devices*. Mehrdad Sasani, Vitelmo V. Bertero, James C. Anderson. December 1999.

PEER 1999/11 *Performance Evaluation Database for Concrete Bridge Components and Systems under Simulated Seismic Loads*. Yael D. Hose and Frieder Seible. November 1999.

PEER 1999/10 *U.S.-Japan Workshop on Performance-Based Earthquake Engineering Methodology for Reinforced Concrete Building Structures*. December 1999.

PEER 1999/09 *Performance Improvement of Long Period Building Structures Subjected to Severe Pulse-Type Ground Motions*. James C. Anderson, Vitelmo V. Bertero, and Raul Bertero. October 1999.

PEER 1999/08 *Envelopes for Seismic Response Vectors.* Charles Menun and Armen Der Kiureghian. July 1999.

PEER 1999/07 *Documentation of Strengths and Weaknesses of Current Computer Analysis Methods for Seismic Performance of Reinforced Concrete Members*. William F. Cofer. November 1999.

PEER 1999/06 *Rocking Response and Overturning of Anchored Equipment under Seismic Excitations*. Nicos Makris and Jian Zhang. November 1999.

PEER 1999/05 *Seismic Evaluation of 550 kV Porcelain Transformer Bushings.* Amir S. Gilani, Andrew S. Whittaker, Gregory L. Fenves, and Eric Fujisaki. October 1999.

PEER 1999/04 *Adoption and Enforcement of Earthquake Risk-Reduction Measures.* Peter J. May, Raymond J. Burby, T. Jens Feeley, and Robert Wood. August 1999.

PEER 1999/03 *Task 3 Characterization of Site Response General Site Categories*. Adrian Rodriguez-Marek, Jonathan D. Bray and Norman Abrahamson. February 1999.

PEER 1999/02 *Capacity-Demand-Diagram Methods for Estimating Seismic Deformation of Inelastic Structures: SDF Systems*. Anil K. Chopra and Rakesh Goel. April 1999.

PEER 1999/01 *Interaction in Interconnected Electrical Substation Equipment Subjected to Earthquake Ground Motions*. Armen Der Kiureghian, Jerome L. Sackman, and Kee-Jeung Hong. February 1999.

PEER 1998/08 *Behavior and Failure Analysis of a Multiple-Frame Highway Bridge in the 1994 Northridge Earthquake*. Gregory L. Fenves and Michael Ellery. December 1998.

PEER 1998/07 *Empirical Evaluation of Inertial Soil-Structure Interaction Effects.* Jonathan P. Stewart, Raymond B. Seed, and Gregory L. Fenves. November 1998.

PEER 1998/06 *Effect of Damping Mechanisms on the Response of Seismic Isolated Structures*. Nicos Makris and Shih-Po Chang. November 1998.

PEER 1998/05 *Rocking Response and Overturning of Equipment under Horizontal Pulse-Type Motions*. Nicos Makris and Yiannis Roussos. October 1998.

PEER 1998/04 *Pacific Earthquake Engineering Research Invitational Workshop Proceedings, May 14–15, 1998: Defining the Links between Planning, Policy Analysis, Economics and Earthquake Engineering*. Mary Comerio and Peter Gordon. September 1998.

PEER 1998/03 *Repair/Upgrade Procedures for Welded Beam to Column Connections*. James C. Anderson and Xiaojing Duan. May 1998.

PEER 1998/02 *Seismic Evaluation of 196 kV Porcelain Transformer Bushings.* Amir S. Gilani, Juan W. Chavez, Gregory L. Fenves, and Andrew S. Whittaker. May 1998.

PEER 1998/01 *Seismic Performance of Well-Confined Concrete Bridge Columns.* Dawn E. Lehman and Jack P. Moehle. December 2000.

PEER REPORTS: ONE HUNDRED SERIES

PEER 2012/103 *Performance-Based Seismic Demand Assessment of Concentrically Braced Steel Frame Buildings.* Chui-Hsin Chen and Stephen A. Mahin. December 2012.

PEER 2012/102 *Procedure to Restart an Interrupted Hybrid Simulation: Addendum to PEER Report 2010/103.* Vesna Terzic and Bozidar Stojadinovic. October 2012.

PEER 2012/101 *Mechanics of Fiber Reinforced Bearings.* James M. Kelly and Andrea Calabrese. February 2012.

PEER 2011/107 *Nonlinear Site Response and Seismic Compression at Vertical Array Strongly Shaken by 2007 Niigata-ken Chuetsu-oki Earthquake.* Eric Yee, Jonathan P. Stewart, and Kohji Tokimatsu. December 2011.

PEER 2011/106 *Self Compacting Hybrid Fiber Reinforced Concrete Composites for Bridge Columns.* Pardeep Kumar, Gabriel Jen, William Trono, Marios Panagiotou, and Claudia Ostertag. September 2011.

PEER 2011/105 *Stochastic Dynamic Analysis of Bridges Subjected to Spacially Varying Ground Motions.* Katerina Konakli and Armen Der Kiureghian. August 2011.

PEER 2011/104 *Design and Instrumentation of the 2010 E-Defense Four-Story Reinforced Concrete and Post-Tensioned Concrete Buildings.* Takuya Nagae, Kenichi Tahara, Taizo Matsumori, Hitoshi Shiohara, Toshimi Kabeyasawa, Susumu Kono, Minehiro Nishiyama (Japanese Research Team) and John Wallace, Wassim Ghannoum, Jack Moehle, Richard Sause, Wesley Keller, Zeynep Tuna (U.S. Research Team). June 2011.

PEER 2011/103 *In-Situ Monitoring of the Force Output of Fluid Dampers: Experimental Investigation.* Dimitrios Konstantinidis, James M. Kelly, and Nicos Makris. April 2011.

PEER 2011/102 *Ground-Motion Prediction Equations 1964–2010.* John Douglas. April 2011.

PEER 2011/101 *Report of the Eighth Planning Meeting of NEES/E-Defense Collaborative Research on Earthquake Engineering.* Convened by the Hyogo Earthquake Engineering Research Center (NIED), NEES Consortium, Inc. February 2011.

PEER 2010/111 *Modeling and Acceptance Criteria for Seismic Design and Analysis of Tall Buildings.* Task 7 Report for the Tall Buildings Initiative - Published jointly by the Applied Technology Council. October 2010.

PEER 2010/110 *Seismic Performance Assessment and Probabilistic Repair Cost Analysis of Precast Concrete Cladding Systems for Multistory Buildlings.* Jeffrey P. Hunt and Božidar Stojadinovic. November 2010.

PEER 2010/109 *Report of the Seventh Joint Planning Meeting of NEES/E-Defense Collaboration on Earthquake Engineering. Held at the E-Defense, Miki, and Shin-Kobe, Japan, September 18–19, 2009.* August 2010.

PEER 2010/108 *Probabilistic Tsunami Hazard in California.* Hong Kie Thio, Paul Somerville, and Jascha Polet, preparers. October 2010.

PEER 2010/107 *Performance and Reliability of Exposed Column Base Plate Connections for Steel Moment-Resisting Frames.* Ady Aviram, Božidar Stojadinovic, and Armen Der Kiureghian. August 2010.

PEER 2010/106 *Verification of Probabilistic Seismic Hazard Analysis Computer Programs.* Patricia Thomas, Ivan Wong, and Norman Abrahamson. May 2010.

PEER 2010/105 *Structural Engineering Reconnaissance of the April 6, 2009, Abruzzo, Italy, Earthquake, and Lessons Learned.* M. Selim Günay and Khalid M. Mosalam. April 2010.

PEER 2010/104 *Simulating the Inelastic Seismic Behavior of Steel Braced Frames, Including the Effects of Low-Cycle Fatigue.* Yuli Huang and Stephen A. Mahin. April 2010.

PEER 2010/103 *Post-Earthquake Traffic Capacity of Modern Bridges in California.* Vesna Terzic and Božidar Stojadinović. March 2010.

PEER 2010/102 *Analysis of Cumulative Absolute Velocity (CAV) and JMA Instrumental Seismic Intensity (I_{JMA}) Using the PEER–NGA Strong Motion Database.* Kenneth W. Campbell and Yousef Bozorgnia. February 2010.

PEER 2010/101 *Rocking Response of Bridges on Shallow Foundations.* Jose A. Ugalde, Bruce L. Kutter, and Boris Jeremic. April 2010.

PEER 2009/109 *Simulation and Performance-Based Earthquake Engineering Assessment of Self-Centering Post-Tensioned Concrete Bridge Systems.* Won K. Lee and Sarah L. Billington. December 2009.

PEER 2009/108 *PEER Lifelines Geotechnical Virtual Data Center.* J. Carl Stepp, Daniel J. Ponti, Loren L. Turner, Jennifer N. Swift, Sean Devlin, Yang Zhu, Jean Benoit, and John Bobbitt. September 2009.

PEER 2009/107 *Experimental and Computational Evaluation of Current and Innovative In-Span Hinge Details in Reinforced Concrete Box-Girder Bridges: Part 2: Post-Test Analysis and Design Recommendations.* Matias A. Hube and Khalid M. Mosalam. December 2009.

PEER 2009/106 *Shear Strength Models of Exterior Beam-Column Joints without Transverse Reinforcement.* Sangjoon Park and Khalid M. Mosalam. November 2009.

PEER 2009/105 *Reduced Uncertainty of Ground Motion Prediction Equations through Bayesian Variance Analysis.* Robb Eric S. Moss. November 2009.

PEER 2009/104 *Advanced Implementation of Hybrid Simulation.* Andreas H. Schellenberg, Stephen A. Mahin, Gregory L. Fenves. November 2009.

PEER 2009/103 *Performance Evaluation of Innovative Steel Braced Frames.* T. Y. Yang, Jack P. Moehle, and Božidar Stojadinovic. August 2009.

PEER 2009/102 *Reinvestigation of Liquefaction and Nonliquefaction Case Histories from the 1976 Tangshan Earthquake.* Robb Eric Moss, Robert E. Kayen, Liyuan Tong, Songyu Liu, Guojun Cai, and Jiaer Wu. August 2009.

PEER 2009/101 *Report of the First Joint Planning Meeting for the Second Phase of NEES/E-Defense Collaborative Research on Earthquake Engineering.* Stephen A. Mahin et al. July 2009.

PEER 2008/104 *Experimental and Analytical Study of the Seismic Performance of Retaining Structures.* Linda Al Atik and Nicholas Sitar. January 2009.

PEER 2008/103 *Experimental and Computational Evaluation of Current and Innovative In-Span Hinge Details in Reinforced Concrete Box-Girder Bridges. Part 1: Experimental Findings and Pre-Test Analysis.* Matias A. Hube and Khalid M. Mosalam. January 2009.

PEER 2008/102 *Modeling of Unreinforced Masonry Infill Walls Considering In-Plane and Out-of-Plane Interaction.* Stephen Kadysiewski and Khalid M. Mosalam. January 2009.

PEER 2008/101 *Seismic Performance Objectives for Tall Buildings.* William T. Holmes, Charles Kircher, William Petak, and Nabih Youssef. August 2008.

PEER 2007/101 *Generalized Hybrid Simulation Framework for Structural Systems Subjected to Seismic Loading*. Tarek Elkhoraibi and Khalid M. Mosalam. July 2007.

PEER 2007/100 *Seismic Evaluation of Reinforced Concrete Buildings Including Effects of Masonry Infill Walls*. Alidad Hashemi and Khalid M. Mosalam. July 2007.

The Pacifi c Earthquake Engineering Research Center (PEER) is a multi-institutional research and education center with headquarters at the University of California, Berkeley. Investigators from over 20 universities, several consulting companies, and researchers at various state and federal government agencies contribute to research programs focused on performance-based earthquake engineering.

These research programs aim to identify and reduce the risks from major earthquakes to life safety and to the economy by including research in a wide variety of disciplines including structural and geotechnical engineering, geology/ seismology, lifelines, transportation, architecture, economics, risk management, and public policy.

PEER is supported by federal, state, local, and regional agencies, together with industry partners.

PEER Core Institutions

University of California, Berkeley (Lead Institution)
California Institute of Technology
Oregon State University
Stanford University
University of California, Davis
University of California, Irvine
University of California, Los Angeles
University of California, San Diego
University of Nevada, Reno
University of Southern California
University of Washington

PEER reports can be ordered at https://peer.berkeley.edu/peer-reports or by contacting

Pacific Earthquake Engineering Research Center
University of California, Berkeley
325 Davis Hall, Mail Code 1792
Berkeley, CA 94720-1792
Tel: 510-642-3437
Email: peer_center@berkeley.edu

ISSN 2770-8314
https://doi.org/10.55461/NZZW1930